

**CO₂-CH₄ REFORMING OVER LANTHANIDE
PROMOTED COBALT/MESOPOROUS
ALUMINA CATALYST FOR SYNGAS
PRODUCTION**



MAHADI BIN BAHARI

اونيورسيتي ملايسيا قهغ

UNIVERSITI MALAYSIA PAHANG

DOCTOR OF PHILOSOPHY

UNIVERSITI MALAYSIA PAHANG

UNIVERSITI MALAYSIA PAHANG

DECLARATION OF THESIS AND COPYRIGHT

Author's Full Name : MAHADI BIN BAHARI

Date of Birth : 18th DECEMBER 1990

Title : CO₂-CH₄ REFORMING OVER LANTHANIDE
PROMOTED COBALT/MESOPOROUS ALUMINA
CATALYST FOR SYNGAS PRODUCTION

Academic Session : SEMESTER 1 2020/2021

I declare that this thesis is classified as:

- CONFIDENTIAL (Contains confidential information under the Official Secret Act 1997)*
- RESTRICTED (Contains restricted information as specified by the organization where research was done)*
- OPEN ACCESS I agree that my thesis to be published as online open access (Full Text)

I acknowledge that Universiti Malaysia Pahang reserves the following rights:

1. The Thesis is the Property of Universiti Malaysia Pahang
2. The Library of Universiti Malaysia Pahang has the right to make copies of the thesis for the purpose of research only.
3. The Library has the right to make copies of the thesis for academic exchange.

Certified by:


(Student's Signature)


(Supervisor's Signature)

901218-06-5367
New IC/Passport Number
Date: 25 JANUARY 2021

Prof. Madya Ts. Dr.
Herma Dina Setiabudi
Name of Supervisor
Date: 25 JANUARY 2021

SUPERVISOR'S DECLARATION

We hereby declare that we have checked this thesis and in our opinion, this thesis is adequate in terms of scope and quality for the award of the degree of Doctor of Philosophy.



(Supervisor's Signature)

Full Name : Prof. Madya Ts. Dr. Herma Dina Setiabudi

Position : Senior Lecturer

Date : 25 JANUARY 2021



(Co-supervisor's Signature)

Full Name : Dr. Nurul Aini Mohamed Razali

Position : Senior Lecturer

Date : 25/01/2021

STUDENT'S DECLARATION

I hereby declare that the work in this thesis is based on my original work except for quotations and citations which have been duly acknowledged. I also declare that it has not been previously or concurrently submitted for any other degree at Universiti Malaysia Pahang or any other institutions.



(Student's Signature)

Full Name : Mahadi Bahari

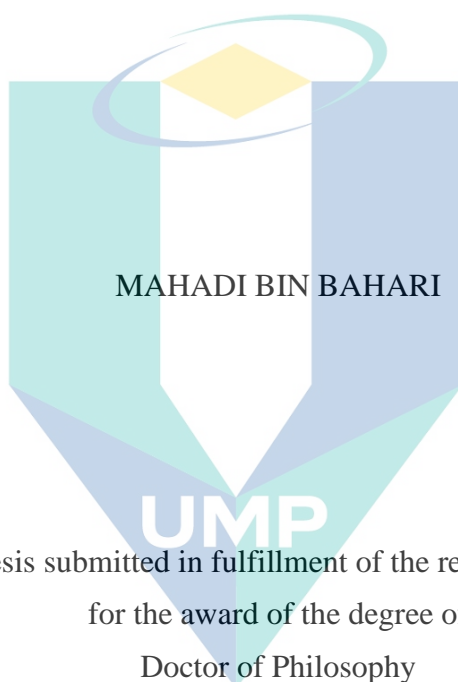
ID Number : PKG 17001

Date : 25 JANUARY 2021

اونيورسيتي ملايسيا قهغ

UNIVERSITI MALAYSIA PAHANG

CO₂-CH₄ REFORMING OVER LANTHANIDE PROMOTED
COBALT/MESOPOROUS ALUMINA CATALYSTS FOR SYNGAS
PRODUCTION



Thesis submitted in fulfillment of the requirements
for the award of the degree of
Doctor of Philosophy

اونيورسيتي ملايسيا قهغ

UNIVERSITI MALAYSIA PAHANG

Faculty of Chemical & Process Engineering Technology

UNIVERSITI MALAYSIA PAHANG

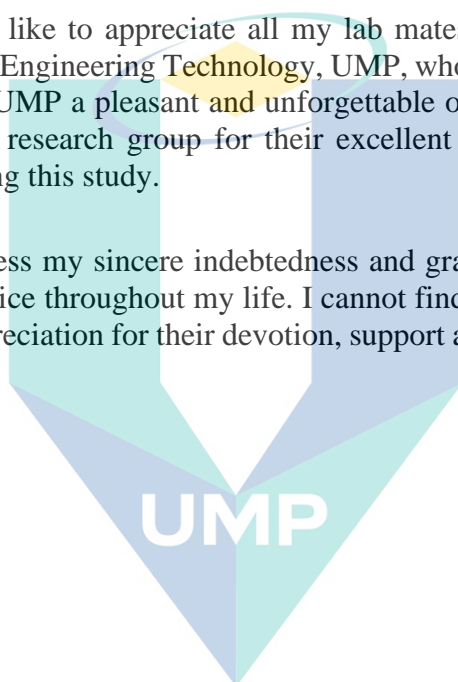
JANUARY 2021

ACKNOWLEDGEMENTS

I would like to express my sincere gratitude to my supervisor, Prof. Madya Ts. Dr. Herma Dina Setiabudi for her invaluable guidance and continuous encouragement. She has always impressed me with her outstanding professional conduct and valuable knowledge in the field of reaction engineering. I also would like to thank my ex-supervisor Dr. Vo Nguyen Dai Viet for his constant support throughout the duration of this research even though after moving to Vietnam. I would also like to thank my co-supervisor, Dr. Nurul Aini Mohamed Razali for her suggestions and co-operation given throughout the study. I also sincerely thank her for her time spent on proofreading and correcting my thesis.

Additionally, I would like to appreciate all my lab mates and staffs of the Faculty of Chemical and Process Engineering Technology, UMP, who had helped me in many ways and made my stay at UMP a pleasant and unforgettable one. I also would like to thank my colleagues in our research group for their excellent co-operation, inspiration and support rendered during this study.

Lastly, I wish to express my sincere indebtedness and gratitude to my parents for their love, dream and sacrifice throughout my life. I cannot find appropriate words that could aptly describe my appreciation for their devotion, support and faith in my ability to attain my goals.



اونيورسيتي مليسيا قهغ

UNIVERSITI MALAYSIA PAHANG

ABSTRAK

Pembaharuan $\text{CO}_2\text{-CH}_4$ telah menarik perhatian kerana teknologi ini mampu menukar gas yang menipiskan ozon yang tidak diinginkan, CO_2 dan CH_4 sebagai bahan suapan kepada syngas ekuimolar yang diinginkan untuk sintesis Fischer-Tropsch. Pada masa ini, masih ada cabaran dalam menghasilkan pemangkin yang sangat stabil dan aktif untuk pembaharuan $\text{CO}_2\text{-CH}_4$ serta ketahanan yang lebih baik terhadap pemendapan karbon. Oleh itu, idea utama kerja kami untuk menghasilkan sokongan mesopore alumina (MA) menggunakan Teknik pembentukan sendiri Bersama hidroterma (SAHA) sebelum diimpregnasi dengan Co. Kemudian, hubungan antara parameter operasi, seperti suhu (923-1073 K) dan tekanan separa reaktan (10-40 kPa) terhadap prestasi pemangkin dan pembentukan karbon dinilai dalam kerja ini, serta kinetik dan mekanisme bagi pemangkin 10%Co/MA dalam pembaharuan $\text{CO}_2\text{-CH}_4$. Kesan pengalok lanthanida (lanthanum (La), cerium (Ce), yttrium (Y) dan samarium (Sm)) dan kuantiti pengalok (1, 2, 3 dan 5wt.%) terhadap sifat fizikokimia pemangkin 10%Co/MA juga dikaji dalam projek ini. 10%Co/MA menunjukkan prestasi pemangkin yang bagus (penukaran $\text{CH}_4 = 70.9\%$, penukaran $\text{CO}_2 = 71.7\%$ dan kadar penyahaktifan = 1.3%), disebabkan oleh penyebaran zarah Co yang baik kedalam pori MA, interaksi sokongan-logam yang kuat, dan kebolehan pengurangan MA. Penyebaran zarah Co pada sokongan MA terbukti bertambah baik setelah penggabungan pengalok, menghasilkan ukuran kristalit yang lebih kecil dan pengumpulan Co yang lebih rendah. Penukaran reaktan bertambah baik mengikut urutan $\text{YCo/MA} > \text{LaCo/MA} > \text{CeCo/MA} > \text{SmCo/MA} > \text{Co/MA}$, sementara jumlah pemendapan karbon dicatatkan dengan urutan $\text{Co/MA} > \text{SmCo/MA} > \text{LaCo/MA} > \text{CeCo/MA} > \text{YCo/MA}$. Selain itu, pemangkin YCo/MA mencapai prestasi pemangkin terbaik (penukaran $\text{CH}_4 = 85.8\%$, penukaran $\text{CO}_2 = 92.2\%$, Kadar penyahaktifan = 0.57%) dan memiliki pemendapan karbon terendah (7.02%) kerana penyebaran zarah Co yang bagus, saiz Co yang kecil dengan interaksi Co-MA yang kuat dan keupayaan penyimpanan oksigen yang lebih tinggi. Nisbah H_2/CO diperolehi dalam 0.78-0.86, sedikit lebih rendah daripada 1 akibat peralihan air-gas terbalik. Prestasi pemangkin unggul ditunjukkan oleh pemuatan 3wt.% Y_2O_3 (penukaran $\text{CH}_4 = 85.8\%$, dan penukaran $\text{CO}_2 = 90.5\%$), diikuti oleh 2wt.% > 5wt.% > 1wt.% > 0wt.% muatan Y_2O_3 . Hasil ini disebabkan sifat pemangkin yang bagus oleh 3% Y-10%Co/MA termasuk saiz zarah Co kecil, penyebaran Co tinggi, jumlah nisbah atom yang tinggi (Co/Al), dan jumlah kekosongan oksigen kisi yang tinggi. Lebihan kandungan Y_2O_3 (>3wt.%) menyebabkan halangan terhadap aktif Co yang tidak dapat dielakkan dan mengakibatkan penurunan prestasi pemangkin. Pemuatan 3wt.% Y_2O_3 mencatat karbon pemendapan paling rendah (7.0%) kerana kekosongan oksigen tertinggi (78.1%) berbanding 1, 2 dan 5wt.% Y_2O_3 . Kesimpulannya, penggunaan sokongan MA dan penambahan pengalok Y_2O_3 (3wt.%) berkesan dalam meningkatkan prestasi Co dalam pembaharuan $\text{CO}_2\text{-CH}_4$ termasuk menghalang pemendapan karbon diatas permukaan pemangkin berbanding pengalok yang lain (Ce, La, dan Sm) dan kandungan Y_2O_3 (1, 2, 5wt. %) disebabkan penambahbaikan terhadap struktur dan sifat fizikimia pemangkin.

ABSTRACT

CO₂-CH₄ reforming has caught significant attention since this technology is able to convert undesirable ozone-depleting gases, CO₂ and CH₄, as feedstocks into the desired equimolar syngas for Fisher-Tropsch synthesis. At present, there is still a challenge in developing the highly stable and active catalysts for CO₂-CH₄ reforming as well as better resistance to carbon deposition. Therefore, the main idea of our work is to synthesize mesoporous alumina (MA) support using self-assembly hydrothermal approach (SAHA) technique before being impregnated with cobalt (Co). Then, the relationship between operating parameters, such as reforming temperature (923–1073 K) and reactant partial pressure (10-40 kPa) on catalytic performance and coke formation was evaluated in this work. The effect of lanthanide promoters (lanthanum (La), cerium (Ce), yttrium (Y), and samarium (Sm)) and promoter loading (1, 2, 3, and 5wt.%) on the physicochemical properties of 10%Co/MA catalyst was also studied in this project. 10%Co/MA exhibited great catalytic performance (CH₄ conversion = 70.9%, CO₂ conversion = 71.7% and Rate of deactivation = 1.3%), credited to the well dispersed Co within pore MA, strong metal-support interaction, and MA confinement ability. The Co particle dispersion on MA support evidently improved after promoter incorporation, resulting in smaller crystallite size and lesser Co agglomeration. The reactant conversions improved in the order of YCo/MA > LaCo/MA > CeCo/MA > SmCo/MA > Co/MA, while the amount of carbon deposit was recorded with the sequence of Co/MA > SmCo/MA > LaCo/MA > CeCo/MA > YCo/MA. Additionally, YCo/MA catalyst attained the highest catalytic performance (CH₄ conversion = 85.8%, CO₂ conversion = 92.2%, Rate of deactivation = 0.57%) and possessed the lowest carbon deposition (7.02%) due to great Co dispersion, small Co particle size with strong Co-MA interaction and higher oxygen storage capacity. H₂/CO ratios were obtained within 0.78-0.86, which is slightly lower than 1 due to the reverse water-gas shift. A superior catalytic performance was shown by 3wt.% Y₂O₃ loading (CH₄ conversion = 85.8%, and CO₂ conversion = 90.5%), followed by 2wt.% > 5 wt.% > 1 wt.% > 0 wt.% Y₂O₃ loading. This result was attributed to the favorable catalytic properties of 3%Y-10%Co/MA including small Co particle size, high Co dispersion, high amount of atomic ratio (Co/Al), and a high number of lattice oxygen vacancies. The excess Y₂O₃ addition (>3 wt.%) led to inevitably blocked Co active sites and resulted in decreasing catalytic performance. The 3wt.% Y₂O₃ promoter loading recorded the lowest carbon deposited (7.0%) due to the highest oxygen vacancies (78.1%) as compared to 1, 2 and 5 wt.% Y₂O₃. As a conclusion, the employment of MA support and incorporation of Y₂O₃ (3wt.) effectively boosted the Co performance in CO₂-CH₄ reforming along with suppressing the deposition of carbon on the catalyst surface as compared with other promoted catalysts (Ce, La, and Sm) and Y₂O₃ loadings (1, 2, 5wt.) owing to the improvement in catalysts structure and physicochemical attributes.

TABLE OF CONTENT

DECLARATION	
TITLE PAGE	
ACKNOWLEDGEMENTS	ii
ABSTRAK	iii
ABSTRACT	iv
TABLE OF CONTENT	v
LIST OF TABLES	ix
LIST OF FIGURES	x
LIST OF APPENDICES	xiv
LIST OF SYMBOLS	xv
LIST OF ABBREVIATIONS	xvi
CHAPTER 1 INTRODUCTION	1
1.1 Introduction	1
1.2 Problem Statement	3
1.3 Objectives	5
1.4 Scope of Study	5
1.5 Overview of Thesis	6
CHAPTER 2 LITERATURE REVIEW	8
2.1 Introduction	8
2.2 Overview of Syngas	8
2.3 Methane Reforming Technologies	9
2.3.1 Steam Reforming	9
2.3.2 Partial Oxidation	10

2.3.3	Autothermal Reforming	11
2.4	CO ₂ -CH ₄ reforming	12
2.4.1	Overview	12
2.4.2	Reaction Mechanism	13
2.4.3	Effect of Operating Condition	14
2.5	The Catalyst Development for CO ₂ -CH ₄ reforming	20
2.5.1	Overview of Catalyst	20
2.5.2	Noble Metals as Active Sites	20
2.5.3	Non-Noble Metals as Active Site	21
2.5.4	Mesoporous Support	27
2.5.5	Catalyst Promoter	37
2.6	Catalyst Deactivation	42
2.6.1	Fouling Phenomena	43
2.6.2	Sintering Phenomena	46
2.7	Research Gaps	49
2.8	Concluding Remarks	49
CHAPTER 3 METHODOLOGY		51
3.1	Introduction	51
3.2	Materials and Equipment	51
3.2.1	Chemical and Gases	51
3.2.2	Equipment	53
3.3	Catalyst Preparation	53
3.3.1	Mesoporous Alumina	53
3.3.2	Unpromoted Catalysts	54
3.3.3	Promoted Catalyst	54

3.4	Catalyst Characterization	56
3.4.1	Textural Measurement	56
3.4.2	X-ray Diffraction	56
3.4.3	Temperature-programmed Reduction	57
3.4.4	X-ray Photoelectron Spectroscopy	57
3.4.5	Scanning Electron Microscopy	57
3.4.6	High-Resolution Transmission Electron Microscopy	58
3.4.7	Temperature-programmed Oxidation	58
3.5	Experimental Set-up	58
3.6	Gaseous Product Analysis	60
3.7	Mass Flow Controller Calibration	60
3.8	Reaction Metrics	60
3.9	Preliminary Experiments	62
3.9.1	Blank Test	62
3.9.2	Thermodynamic Consideration	62
3.9.3	Elimination of Transport Intrusions	64
3.10	Concluding Remarks	71
CHAPTER 4 RESULTS AND DISCUSSIONS		72
4.1	Introduction	72
4.2	Evaluation of Co/MA Catalyst for CO ₂ -CH ₄ Reforming	72
4.2.1	Catalyst Characterization	72
4.2.2	CO ₂ -CH ₄ Reforming Analysis	75
4.2.3	Post-Reaction Characterizations	84
4.3	Effect of Lanthanides Promoters on Co/MA Catalyst for CO ₂ -CH ₄ Reforming	87
4.3.1	Catalyst Characterizations	87

4.3.2	CO ₂ -CH ₄ Reforming Analysis	91
4.3.3	Post-Reaction Characterizations	94
4.4	Impact of Yttrium Promoter Loading on Co/MA Catalyst for CO ₂ -CH ₄ Reforming	103
4.4.1	Catalyst Characterizations	103
4.4.2	Reaction Analysis	107
4.4.3	Post-Reaction Characterizations	110
4.4.4	Longevity Test	120
4.5	Concluding Remarks	121
CHAPTER 5 CONCLUSIONS AND RECOMMENDATIONS		123
5.1	Conclusions	123
5.2	Recommendations	125
APPENDIX A CALCULATIONS FOR SUPPORT AND CATALYST PREPARATION		150
APPENDIX B TRANSPORT RESISTANCE ESTIMATION		153
APPENDIX C CALIBRATION CURVES		161
APPENDIX D LIST OF PUBLICATIONS & CONFERENCE PROCEEDINGS		163

اوتیور سینی ملیسیا فہق

UNIVERSITI MALAYSIA PAHANG

LIST OF TABLES

Table 2.1	Comparison of technology for syngas production from methane.	12
Table 2.2	List of cobalt based catalysts which have been examined in CO ₂ -CH ₄ reforming.	24
Table 2.3	Bibliographic listing of CO ₂ -CH ₄ reforming with mesoporous alumina support.	35
Table 2.4	Mechanisms of catalyst deactivation	42
Table 2.5	Details of carbon formed in CO ₂ -CH ₄ reforming.	45
Table 3.1	List of used chemicals	52
Table 3.2	List of consumed gases	52
Table 3.3	List of equipment used for the synthesis of support and catalysts	53
Table 3.4	Standard gas data.	60
Table 3.5	Summary of thermodynamic findings for CO ₂ -CH ₄ reforming.	64
Table 3.6	Properties used in the calculation of transport resistances	65
Table 4.1	Summary of the catalytic performance of catalysts for CO ₂ -CH ₄ reforming	82
Table 4.2	Textural properties of promoted and unpromoted catalysts.	89
Table 4.3	Binding energies, atomic ratios and oxygen vacancies values obtained from the XPS analysis of all spent catalysts.	98
Table 4.4	Textural properties of MA support δ %Y-10%Ni/MA ($\delta = 0-5$ wt%) catalyst.	104
Table 4.5	Binding energies, atomic ratios, and oxygen vacancies values obtained from the XPS analysis of all spent catalysts.	114

اونيورسيتي ملايسيا قهغ

UNIVERSITI MALAYSIA PAHANG

LIST OF FIGURES

Figure 2.1	The application of syngas according to the H ₂ /CO ratio (*).	9
Figure 2.2	The effect of operating pressure on reactant conversions and products distribution at stoichiometric condition and T = 1173 K.	14
Figure 2.3	The conversion of CH ₄ and CO ₂ as a function of temperature with stoichiometric condition.	16
Figure 2.4	Effect of temperature on product yields at stoichiometric condition and under atmospheric pressure.	17
Figure 2.5	Effect of temperature on H ₂ /CO ratio at stoichiometric condition and under atmospheric pressure.	17
Figure 2.6	The influence of reaction temperature on the moles of carbon generated during CO ₂ -CH ₄ reforming reaction at 1 atm.	18
Figure 2.7	Reactant conversion, product yields and H ₂ /CO ratio as function of CH ₄ /CO ₂ molar ratio at reaction temperature of 1123 K and under atmospheric pressure.	19
Figure 2.8	The catalytic performance of CoAl catalyst supported on different metal oxides; (a) Al ₂ O ₃ , (b) CeO ₂ , (c) MgAl ₂ O ₄ , (d) SiO ₂ , and (e) ZrO ₂ .	23
Figure 2.9	Schematic illustration of the self-templating mechanism.	28
Figure 2.10	Steps for the preparation of mesoporous crystalline γ -alumina using MOF-5.	30
Figure 2.11	The mechanism for the formation of MA from boehmite using block copolymer.	33
Figure 2.12	Schematic coke formation for CO ₂ -CH ₄ reforming on the catalysts synthesised via EISA and impregnation (IMP).	34
Figure 2.13	Illustration represents the effect of Ce promoter addition.	38
Figure 2.14	La ₂ O ₃ redox cycle for surface carbon removal during CO ₂ -CH ₄ reforming.	39
Figure 2.15	Scheme of carbon deposition and carbon removal over Ni-based catalysts.	40
Figure 2.16	a) SEM images of 10Ni-SBA-15 and 3Sm-10Ni-SBA-15 catalysts and b) FESEM images of the 3Sm-10Ni-SBA-15 catalyst after 12 h of the reaction.	41
Figure 2.17	Thermodynamic equilibrium profiles for CO ₂ -CH ₄ reforming at pressure of 1 atm, temperature range from 0 to 1000 °C and at CO ₂ /CH ₄ feed ratio = 1	44
Figure 2.18	The deposition of carbon resulted in encapsulation of active metal sites and pore plugging of a supported metal catalyst.	45
Figure 2.19	The mechanism of carbon formation in CO ₂ -CH ₄ reforming.	45

Figure 2.20	The illustration of atomic migration and crystallite migration models.	46
Figure 2.21	The correlation between carbon deposition and deactivation as a function of Co loading.	48
Figure 2.22	CH ₄ conversion versus time on stream for different Co:Ni ratio.	49
Figure 3.1	Overall flowchart of this study.	55
Figure 3.2	Experimental set-up for CO ₂ -CH ₄ reforming reaction.	59
Figure 3.3	Effect of operating temperature on the variation of the Gibbs free energy for main and side reactions in CO ₂ -CH ₄ reforming.	63
Figure 4.1	The physisorption isotherms and pore size distribution profile of MA support and 10%Co/MA catalyst	73
Figure 4.2	XRD patterns of (a) MA support and (b) 10%Co/MA catalyst.	74
Figure 4.3	H ₂ -TPR profile of 10%Co/MA catalyst.	75
Figure 4.4	Influence of P_{CO_2} on (a) CH ₄ conversion and (b) CO ₂ conversion for 10%Co/MA catalyst at $P_{CH_4} = 20$ kPa and T = 923-1023 K.	76
Figure 4.5	Influence of P_{CO_2} on H ₂ :CO ratio for 10%Co/MA catalyst at $P_{CH_4} = 20$ kPa and T = 923-1023 K.	78
Figure 4.6	Effect of P_{CH_4} on CH ₄ conversion for 10%Co/MA catalyst at $P_{CO_2} = 20$ kPa and T = 923-1023 K.	79
Figure 4.7	Effect of P_{CH_4} on CO ₂ conversion and (c) H ₂ :CO ratio for 10%Co/MA catalyst at $P_{CO_2} = 20$ kPa and T = 923-1023 K.	80
Figure 4.8	Effect of P_{CH_4} on H ₂ :CO ratio for 10%Co/MA catalyst at $P_{CO_2} = 20$ kPa and T = 923-1023 K.	80
Figure 4.9	XRD patterns of 10%Co/MA-F and spent 10%Co/MA after 8 h CO ₂ -CH ₄ reforming at temperature of 923-1073 K and $P_{CO_2} = P_{CH_4} = 20$ kPa.	84
Figure 4.10	(a) Derivative weight profiles and (b) weight loss profile of spent 10%Co/MA catalyst attained from TPO after 8 h CO ₂ -CH ₄ reforming at temperature of 923-1073 K and $P_{CH_4} = P_{CO_2} = 20$ kPa.	85
Figure 4.11	TEM image and particle size distribution of (a) 10%Co/MA-F and (b) spent 10%Co/MA catalyst after 8 h CO ₂ -CH ₄ reforming at temperature of 1023 K and $P_{CH_4} = P_{CO_2} = 20$ kPa.	86
Figure 4.12	X-ray diffractograms of MA support, Co/MA and promoted Co/MA catalysts.	88

Figure 4.13	H ₂ temperature-programmed reduction of promoted and unpromoted Co-based catalysts.	90
Figure 4.14	CH ₄ conversion of promoted and unpromoted catalysts as a function of time.	91
Figure 4.15	CO ₂ conversion of promoted and unpromoted catalysts as a function of time	92
Figure 4.16	H ₂ /CO ratio of promoted and unpromoted catalysts as a function of time.	93
Figure 4.17	Catalytic performance comparison for all catalysts at steady state condition.	94
Figure 4.18	XRD patterns of spent Co/MA and promoted Co/MA catalysts after 8 h CO ₂ -CH ₄ at T = 1023 K, GHSV = 36000 mL g _{cat} ⁻¹ h ⁻¹ , and CO ₂ :CH ₄ :N ₂ = 1:1:3.1.	95
Figure 4.19	(a) Co 2p and (b) O 1s XPS spectra of used promoted and unpromoted catalysts after 8 h CO ₂ -CH ₄ reforming at T = 1023 K, GHSV = 36000 mL g _{cat} ⁻¹ h ⁻¹ and CO ₂ :CH ₄ :N ₂ = 1:1:3.1.	97
Figure 4.20	C 1s XPS spectra of used promoted and unpromoted catalysts after 8 h CO ₂ -CH ₄ reforming at T = 1023 K, GHSV = 36000 mL g _{cat} ⁻¹ h ⁻¹ and CO ₂ :CH ₄ :N ₂ = 1:1:3.1.	99
Figure 4.21	TPO profiles and weight loss of the spent catalysts after 8 h CO ₂ -CH ₄ reforming at T = 1023 K, GHSV = 36000 mL g _{cat} ⁻¹ h ⁻¹ and CO ₂ :CH ₄ :N ₂ = 1:1:3.1.	101
Figure 4.22	HRTEM images of (a) MA support, spent (b) Co/MA, (c) LaCo/MA, (d) CeCo/MA, (e) YCo/MA and (f) SmCo/MA catalysts after 8 h of CO ₂ -CH ₄ reforming at T = 1023 K, GHSV = 36000 mL g _{cat} ⁻¹ h ⁻¹ and CO ₂ :CH ₄ :N ₂ = 1:1:3.1.	102
Figure 4.23	XRD patterns of (a) MA support, (b) 10%Co/MA, (c) 1%Y-10%Co/MA, (d) 2%Y-10%Co/MA, (e) 3%Y-10%Co/MA and (f) 5%Y-10%Co/MA.	105
Figure 4.24	H ₂ temperature-programmed reduction of (a) 10%Co/MA, (b) 1%Y-10%Co/MA, (c) 2%Y-10%Co/MA, (d) 3%Y-10%Co/MA and (e) 5%Y-10%Co/MA.	106
Figure 4.25	Effect of yttrium loading on (A) CH ₄ and (B) CO ₂ conversions during CO ₂ -CH ₄ reforming at 1023 K and molar ratio of CH ₄ /CO ₂ = 1:1 for 8 h time-on-stream.	107
Figure 4.26	Effect of yttrium loadings on H ₂ /CO ratio during CO ₂ -CH ₄ reforming at 1023 K and molar ratio of CH ₄ /CO ₂ = 1:1 for 8 h time-on-stream.	109
Figure 4.27	Effect of yttrium loading on (A) H ₂ and (B) CO yields during CO ₂ -CH ₄ reforming at 1023 K and molar ratio of CH ₄ /CO ₂ = 1:1 for 8 h time-on-stream.	110
Figure 4.28	X-ray diffractograms of spent (a) 10%Co/MA, (b) 1%Y-10%Co/MA, (c) 2%Y-10%Co/MA, (d) 3%Y-10%Co/MA and (e) 5%Y-10%Co/MA.	111

- Figure 4.29 HRTEM images of (a) MA support, spent (b) 10%Co/MA, (c) 1%Y-10%Co/MA, (d) 2%Y-10%Co/MA, (e) 3%Y-10%Co/MA and (f) 5%Y-10%Co/MA. 112
- Figure 4.30 TPO profiles and weight loss of the spent catalysts after 8 h CO₂-CH₄ reforming reaction at 1023 K, GHSV = 36000 cm³ g_{cat}⁻¹ h⁻¹ and CH₄: CO₂ = 1:1. 113
- Figure 4.31 XPS Co 2p spectra of the spent (a) 10%Co/MA, (b) 1%Y-10%Co/MA, (c) 2%Y-10%Co/MA, (d) 3%Y-10%Co/MA and (e) 5%Y-10%Co/MA catalysts after 8 h CO₂-CH₄ reforming reaction at 1023 K, GHSV = 36000 cm³ g_{cat}⁻¹ h⁻¹ and CH₄: CO₂ = 1:1. 116
- Figure 4.32 XPS O 1s spectra of the spent (a) 10%Co/MA, (b) 1%Y-10%Co/MA, (c) 2%Y-10%Co/MA, (d) 3%Y-10%Co/MA and (e) 5%Y-10%Co/MA catalysts after 8 h CO₂-CH₄ reforming reaction at 1023 K, GHSV = 36000 cm³ g_{cat}⁻¹ h⁻¹ and CH₄:CO₂ = 1:1. 117
- Figure 4.33 XPS C 1s spectra of the spent (a) 10%Co/MA, (b) 1%Y-10%Co/MA, (c) 2%Y-10%Co/MA, (d) 3%Y-10%Co/MA and (e) 5%Y-10%Co/MA catalysts after 8 h CO₂-CH₄ reforming reaction at 1023 K, GHSV = 36000 cm³ g_{cat}⁻¹ h⁻¹ and CH₄: CO₂ = 1:1. 118
- Figure 4.34 Summary on the relationship between promoter loading with catalyst properties and catalytic performances in CO₂-CH₄ reforming. 119
- Figure 4.35 Time-on-stream profile for reactant conversions and product yields attained from longevity test of 3%Y-10%Co/MA at 1023 K and molar ratio of CH₄/CO₂ = 1:1. 120

اونيورسيتي ملايسيا قهغ

UNIVERSITI MALAYSIA PAHANG

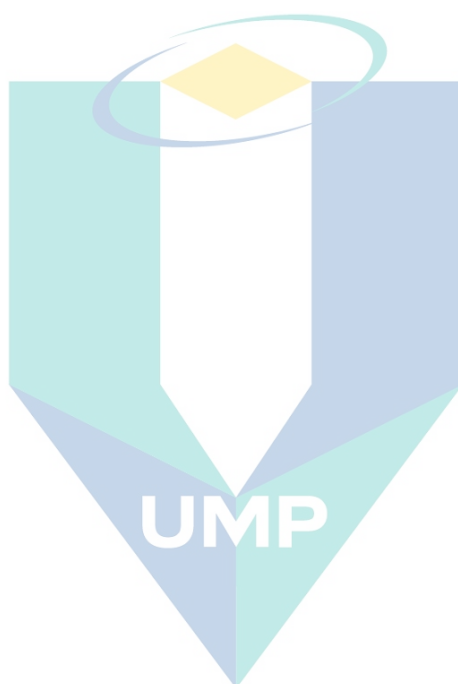
LIST OF APPENDICES

APPENDIX A CALCULATIONS FOR SUPPORT AND CATALYST PREPARATION

APPENDIX B TRANSPORT RESISTANCE ESTIMATION

APPENDIX C CALIBRATION CURVES

APPENDIX D LIST OF PUBLICATIONS & CONFERENCE PROCEEDINGS



اونيورسيتي ملايسيا قهغ

UNIVERSITI MALAYSIA PAHANG

LIST OF SYMBOLS

P_{CH_4}	Partial pressure of CH ₄
P_{CO_2}	Partial pressure of CO ₂
ΔG	The changes in the standard Gibbs free energy
n	Number of moles
D_d	Deactivation degree
wt%	weight percent
C_{Ab}	Bulk gas-phase concentration
c_p	Specific heat capacity
C_d	Carbon deposition
k_c	Mass transfer coefficient
h_w	Heat transfer coefficient
R	Ideal gas constant
μ	Viscosity
D_{eff}	Effective diffusivity
D_g	Diffusivity in mixture
E_A	Activation energy
$-\Delta H_r$	Heat of reaction
r	Rate of reaction
R_p	Catalyst particle radius
T	Temperature
V	Volume
ε	Void fraction on the catalyst bed
ρ_c	Density of catalyst pellet
ρ_b	Bulk density of catalyst bed
σ_c	Construction factor
$\tilde{\tau}$	Tortuosity
ω_p	Catalyst pellet porosity
n	Reaction order
j_D	Colburn's mass transfer factor
Sc	Schmidt number
U	Superficial gas velocity
\dot{n}	Molar flow rates
$W_{cat.}$	Weight of catalyst
β	full width at half maximum of peaks
λ	XRD wavelength
θ	Bragg angle
C_α	Adsorbed. atomic carbon (surface carbide)
C_β	Polymers, amorphous films
C_γ	Ni carbide (bulk)
C_v	Vermicular filaments/ whiskers
C_c	Graphite (crystalline) platelets film
X_i	Conversion

LIST OF ABBREVIATIONS

BET	Brunauer-Emmett-Teller
BP	British Petroleum
Ce	Cerium
Co	Cobalt
CTAB	Cetyl-trimethyl ammonium bromide
EISA	Evaporation-induced self-assembly
FTS	Fischer-Tropsch synthesis
FWHM	Full width at half maximum of peaks
GHSV	Gas hourly speed velocity
HRTEM	High-resolution transmission electron microscopy
I.D.	Inner diameter
Ir	Iridium
IUPAC	International Union of Pure and Applied Chemistry
IWI	Incipient wetness impregnation
JCPDS	Joint Committee on Powder Diffraction Standards
La	Lanthanum
MA	Mesoporous alumina
MCM-41	Mobil Composition of Matter No. 41
MSR	Methane steam reforming
n.a.	Not available
O.D.	Outer diameter
Pd	Palladium
PPO	Polypropylene oxide
Pt	Platinum
RBR	Reverse Boudouard reaction
Rh	Rhodium
Ru	Ruthenium
RWGS	Reverse water gas shift
SA	Surface area
SAHA	Self-assembly hydrothermal approach
SBA-15	Santa Barbara Amorphous-15
S:C	Steam to carbon ratio
SDA	Structure directing agent
SEM	Scanning electron microscopy
SIWI	Sequential incipient wetness impregnation
Sm	Samarium
SOFCs	Solid oxide fuel cells
TPR	Temperature-programmed reduction
TPO	Temperature-programmed oxidation
US	United States
WGS	Water gas shift
XPS	X-ray photoelectron spectroscopy
XRD	X-ray diffraction

CHAPTER 1

INTRODUCTION

1.1 Introduction

World's energy utilization depends largely on fossil fuels. According to the statistical data reported in the literature, approximately more than 80% of the energy consumed around the world was obtained from fossil fuels (BP Statistical Review, 2019; Global Energy Statistical Yearbook, 2019; Johnsson, Kjärstad, and Rootzén (2019). The reliance on fossil fuels to meet energy demand has created environmental problems by significant emission of greenhouse gases which are CO₂, and CH₄. Besides, depleting reserves of fossil fuels also is one of the concerning issues which the world is currently facing (Abas, Kalair, & Khan, 2015; Martins, Felgueiras, Smitkova, & Caetano, 2019). Thus, syngas (a mixture of CO and H₂) has been acknowledged as a potential option to replace fossil fuels since it holds many valuable uses including its usage as source of energy for power engines, fuel for solid oxide fuel cells (SOFCs) and feedstock for Fischer-Tropsch synthesis (FTS) (Abdul Mujeebu, 2016; Peng et al., 2017).

The most common and economical method for syngas production is either through steam reforming (I. Iglesias, Baronetti, Alemany, & Mariño, 2019), partial oxidation (Singha, Shukla, Yadav, Sivakumar Konathala, & Bal, 2017) or autothermal reforming (Luneau et al., 2017). However, these well-established technologies have their drawbacks related to anthropogenic CO₂ emission. Therefore, the development of alternative synthesis routes for syngas generation are important. Recently, there has been increasing interests in the CO₂-CH₄ reforming since this route convert the two kinds of greenhouse gases (CH₄ and CO₂) (da Fonseca, Rabelo-Neto, Simões, Mattos, & Noronha, 2020; Moura-Nickel et al., 2019; Padi et al., 2020) into syngas. Moreover, the reforming process produces syngas with a lower H₂:CO molar ratio, making it an ideal feed for FTS and for highly selective syntheses of chemical compounds (Usman, Wan Daud, & Abbas, 2015).

Although CO₂-CH₄ reforming reaction has been extensively studied for syngas production, there are several real challenges related to the deposition of carbon which often leads to catalyst bed clogging, high-pressure drop or limited lifetime of existing catalysts due to the sintering of the active phase (Estephane et al., 2015). Therefore, the selection of a suitable catalyst is significantly important for minimizing this challenge. Noble metal-based and non-noble catalysts are generally applied in the CO₂-CH₄ reforming reaction. It is well-known that CO₂-CH₄ reforming over noble metal catalysts such as Rh (Drif et al., 2015), Ru (Whang et al., 2017), Pd (Singha, Yadav, Shukla, Kumar, & Bal, 2017), and Pt (Niu, Du, Ran, & Wang, 2016) exhibited high conversion and hydrogen formation rate. However, the low availability and high price of these precious metals make them unsuitable for industrial applications. Hence, the utilization of non-noble metal catalysts such as Ni and Co-based for CO₂-CH₄ reforming has received considerable interest.

Cobalt (Co)-based catalysts gained good reputation in reforming reaction since it reveals higher stability and lower carbon deposition. Indeed, Ayodele, Khan, and Cheng (2016) reported that a Co-based catalyst are less susceptible to catalyst deactivation. However, it is stated that the disadvantages of Co are due to the lower activities in reaction (Budiman, Song, Chang, Shin, & Choi, 2012). G. Zhang, Su, Du, Qu, and Xu (2014) stated that the catalytic performance of Co-based catalysts can be improved by choosing appropriate support materials. Indeed, S. Li and Gong (2014) specified that the employment of high surface area support could resolve low-performance issues by improving the dispersion of active metal particles. Thus, mesoporous materials with high surface area were introduced to improve the catalytic performance. Among the mesoporous materials, mesoporous Al₂O₃ (MA) has drawn a great attention as it provides high specific surface areas (207.0-310.0 m² g⁻¹), tuneable pore sizes (8.3-10.1 nm), and narrow pore size distribution (Huseyin Arbag, 2018; Aw, Dražić, Djinović, & Pintar, 2016; Q. Ma et al., 2016). Moreover, mesoporous Al₂O₃ could confine the active nanoparticles inside the pore channels and prevent the metal particles from sintering, which leads to catalyst deactivation (Fang et al., 2015; N. Wang et al., 2014).

Apart from support selection, the low activity of Co-based catalysts can be positively tackled by introducing lanthanide metals such as Cerium (Ce), Lanthanum (La), Yttrium (Y), and Samarium (Sm) as catalyst promoters, since these metals are also

capable of improving active metal dispersion. Various studies reported the positive influence of promoter addition on catalytic performance. Recently, Y. Sun, Zhang, Liu, Xu, and Lv (2020) found that the addition of Ce promoter made a great contribution in improving CO₂-CH₄ reforming activity by increasing the number of active sites through improving metal dispersion. Similar findings were attained by Rahbar Shamskar, Meshkani, and Rezaei (2017) and Taherian, Yousefpour, Tajally, and Khoshandam (2017a) during the employment of La and Sm promoters, respectively in CO₂-CH₄ reforming reaction. Indeed, it was reported that the promoter incorporation as one crucial approach to preventing catalyst deactivation owing to these metals' properties such as basic attributes and high oxygen storage/release capability (Rahbar Shamskar et al., 2017; L. Zhang et al., 2017).

As a result, the aim of this study is to extensively investigate the effect of MA employment as a support for Co in CO₂-CH₄ reforming activity at various operating conditions. In addition, the influence of lanthanide promoters (Ce, La, Sm, and Y) incorporation towards the structure of the Co/MA and catalytic performance in CO₂-CH₄ reforming, as well as carbon deposition were studied. Finally, the correlation between physicochemical properties and catalytic performance of all prepared catalysts will be thoroughly elucidated. This work was highly interesting since to the best of our knowledge, there is almost no report on MA with Co catalyst during CO₂-CH₄ reforming and there is no study about the role lanthanide promoters on Co/MA catalyst.

1.2 Problem Statement

CO₂-CH₄ reforming has been considered as a better alternative approach in converting the two most important greenhouse gases, CH₄ and CO₂, into syngas (CO+H₂) which could be further utilized in chemical industries. Nevertheless, CO₂-CH₄ reforming is encountered by several challenges; deactivation and value of syngas ratio, which will be resolved in this research.

Firstly, there is still the challenge in developing the highly stable and active catalysts for CO₂-CH₄ reforming as well as better resistance to catalyst deactivation. Recently, non-noble metal-based catalysts metal such as Ni-based catalysts currently emerged as potential catalysts for CO₂-CH₄ reforming owing to its cost-effectiveness and abundance in availability (Chong et al., 2019; Dou et al., 2019). However, the rapid

deactivation of Ni-based catalysts resulting from coke formation is the main drawback in CO₂-CH₄ reforming. Thus, Co has gained interest as an active metal for CO₂-CH₄ reforming due to its capability to decrease the rate of carbon deposition by oxidizing the surface carbon. Nevertheless, the reforming performances of this metal are slightly lower as compared to Ni-based catalysts (Nishimoto et al., 2004). Therefore, several approaches in enhancing the catalytic performance of Co-based catalyst, such as the effect of support and the addition of lanthanide promoters have been employed in this study. The employment of appropriate support materials was found to be capable in improving the catalytic performances (G. Zhang et al., 2014). In fact, the use of support with high surface area resulted in the enhancement of active metal dispersion, hence boosting the catalytic activity (S. Li & Gong, 2014). Mesoporous materials such as MA gained a growing interest in the field of reforming as a support material since this material has high surface area, tuneable pore size, and narrow pore size distribution (Leilei Xu, Song, & Chou, 2013). All these features may increase the number of accessible Co active sites which in turn enhance the catalytic activity.

Apart from that, the addition of promoters also could effectively assist in improving Co catalytic activity through enhancing the dispersion of active metals. Various types of promoter had been employed in literature for improving the catalytic performance. Among those metal oxide promoters, the rare earth metal oxides such as CeO₂, La₂O₃, Sm₂O₃ and Y₂O₃ are potential candidates for improving the catalytic performances (Rahbar Shamskar et al., 2017; Taherian, Yousefpour, Tajally, & Khoshandam, 2017b). Fascinatingly, these metals are also well known for suppressing the carbon deposition during reaction accredited to their high rates of oxygen release and storage. Therefore, in this work, catalytic activity values for the CO₂-CH₄ reforming reaction will be determined by utilizing MA support prepared through the self-assembly hydrothermal approach (SAHA). Indeed, examining the effect of those lanthanide promoters on both textural properties and activities of Co/MA catalyst is vital to develop novel promising catalysts for CO₂-CH₄ reforming. Interestingly, till now, to the best of our knowledge, there are no previous experimental research about the impact of MA employment as a support for Co-based catalyst in CO₂-CH₄ reforming along with the incorporation of rare earth promoters (Ce, La, Sm, and Y).

Secondly, the molar ratio of H₂/CO close to unity is needed from the CO₂-CH₄ reforming reaction to achieve an appropriate feedstock amount for downstream FTS. Therefore, screening reaction conditions by adjusting reaction temperature or feed ratio is necessary in CO₂-CH₄ reforming for obtaining the optimal operating conditions.

1.3 Objectives

The specific aims of this research project may be described as:

- i. To synthesize the mesoporous alumina support, promoted and unpromoted Co/MA catalysts, and to determine their physicochemical properties using various characterization techniques.
- ii. To evaluate the catalytic performance of as-synthesized catalysts for CO₂-CH₄ reforming at various operation conditions.
- iii. To investigate the effects of promoter types and loadings on the physicochemical properties of catalyst and catalytic performance during CO₂-CH₄ reforming.

1.4 Scope of Study

Work scopes for objective 1:

- i. Preparation of MA support using the self-assembly hydrothermal approach (SAHA).
- ii. Determination of the physicochemical properties of the MA support such as crystallinity using X-ray diffraction (XRD), textural properties (including surface area, pore volume and pore diameter) using Brunauer-Emmett-Teller (BET) method, N₂ adsorption-desorption analysis, surface morphology via high-resolution transmission electron microscopy (HRTEM).
- iii. Preparation of the 10%Co/MA and M%-10%Co/MA (M = La, Sm, Y, and Ce) catalysts through sequential incipient wetness impregnation method.
- iv. Characterization of the as-synthesized catalysts by XRD, BET, H₂-temperature-programmed reduction (H₂-TPR), X-ray photoelectron spectroscopy (XPS), HRTEM, and temperature-programmed oxidation (TPO) measurements.

Work scopes for objective 2:

- i. Evaluation of the catalytic performance 10%Co/MA catalyst for CO₂-CH₄ reforming using a stainless-steel fixed bed reactor for 8 h under several independent variables including reaction temperature (923-1073 K), reactant partial pressure (10-40 kPa), and gas hourly space velocity (GHSV) of 36 L g_{cat}⁻¹ h⁻¹ under atmospheric pressure.
- ii. Investigation of the effect of the promoter on the catalytic activity of 10%Co/MA catalyst in CO₂-CH₄ reforming under reaction temperature of 1023 K, at stoichiometric feed ratio (CH₄/CO₂ = 1), GHSV of 36 L g_{cat}⁻¹ h⁻¹ under atmospheric condition. Evaluation of the activities in terms of the reactant conversions, yield of product, and H₂/CO ratio. A comparative investigation on the catalyst's activity was conducted to determine the best-promoted catalyst.

Work scopes for objective 3:

- i. Investigation of the influence of promoter loading (1, 2, 3, and 5wt%) on the physicochemical properties of the selected promoted catalyst using XRD, BET, H₂-TPR, XPS, HRTEM and TPO analysis.
- ii. Investigation of the effect of promoter loading (1, 2, 3, and 5wt%) on the CO₂-CH₄ reforming performance using temperature of 1023 K and at CH₄:CO₂ molar ratio of 1:1.
- iii. Evaluation of the stability of the optimal catalyst in CO₂-CH₄ reforming under a reaction temperature of 1023 K and CH₄/CO₂ ratio of 1 for 72 h. The extent of stability was determined as a function of the conversion with time on stream and the percentage of deactivation.

1.5 Overview of Thesis

This research work contains 4 main sections which are background information of research topic, catalysts preparation, characterization, and catalytic evaluation for CO₂-CH₄ reforming. This thesis is divided into eight chapters and outlined as follows:

Chapter 1 presents the background related to the CO₂-CH₄ reforming research project, including the description of problem statements, objectives, and the scope of the research. The complete outline of the thesis is also provided in this chapter.

Chapter 2 provides a detailed literature review on syngas energy and applications in order to recognize its capabilities. The various reforming technologies employed for syngas production using methane are also given in this chapter for comparison purposes. Additionally, the literature review on catalyst for CO₂-CH₄ reforming in previous studies is reviewed in depth in this chapter in terms of catalyst support, metal, promoter, and deactivation.

Chapter 3 explains the methodology employed in this research work for preparing support, unpromoted, and promoted catalysts. The detailed characterizations and experimental set-up for CO₂-CH₄ reforming reaction in a fixed-bed reactor at various operation conditions are also included. The preliminary work to be conducted necessarily such as the blank test analysis, heat and mass transport resistances calculation, and instrument calibration also is explained in this chapter. The reaction metrics for evaluating the performance of CO₂-CH₄ reforming is also listed in this chapter.

Chapter 4 reveals the characterization and catalytic performance of 10%Co/MA catalyst at various operation conditions namely, reactant partial pressure and temperature. The influence of different promoters from lanthanide groups (Ce, La, and Sm) on the physicochemical properties of catalysts and their performances in CO₂-CH₄ reforming also is covered in this chapter. Indeed, the effect of promoter loading on the physicochemical properties of catalyst and its performances in CO₂-CH₄ reforming is also listed in this chapter. The optimal catalyst is further employed to investigate stability via longevity test. In addition, the physicochemical attributes of the spent catalysts after CO₂-CH₄ reforming are analysed in this chapter to study the morphology and the amount of carbonaceous deposition on the spent catalyst surface.

Chapter 5 summaries the overall results achieved in this research project. In addition, the relevant recommendations for future work related to CO₂-CH₄ reforming are also included at the end of this chapter.

CHAPTER 2

LITERATURE REVIEW

2.1 Introduction

This chapter provides a detailed review of syngas energy, the existing literature on methane reforming technologies for syngas production, thermodynamic study, reaction mechanisms, catalyst development, and catalyst deactivation during the CO₂-CH₄ reforming.

2.2 Overview of Syngas

Syngas (a mixture of CO and H₂) is an intermediate product in the chemical industry. This promising replacement energy for fossil fuels was initially discovered by Franz Fischers and Hans Tropsch in 1920s during the invention of FTS technology. The discovery of syngas led to the transition of world's energy demand from fossil fuels to syngas energy since it is capable of reducing the reliance on non-renewable resources and decreasing greenhouse gas emissions. Syngas is mainly used as a feedstock for producing a wide range of chemicals such as ammonia, methanol, and dimethyl ether as well as synthetic fuels via FTS (Capodaglio & Bolognesi, 2019; da Rosa, 2013; D. J. Wilhelm, Simbeck, Karp, & Dickenson, 2001). According to the study of L. Yang and Ge (2016) the synthesis of ammonia for fertilizer production recorded the highest consumption of syngas produced (~55%); followed by oil refining processes (22%) and then methanol production (12%). The detailed application of syngas based on the ratio of H₂/CO is depicted in Figure 2.1.

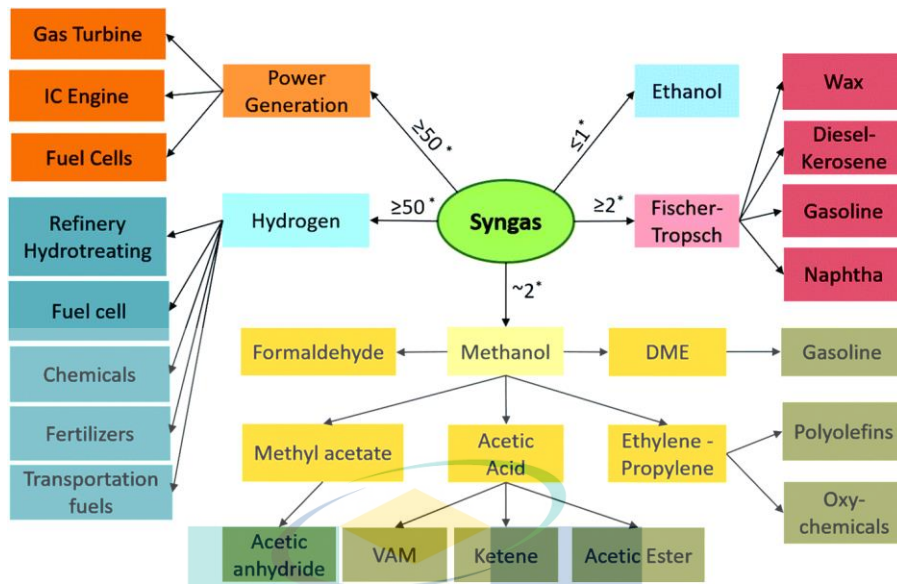


Figure 2.1 The application of syngas according to the H_2/CO ratio (*).

Source : Hernández et al. (2017)

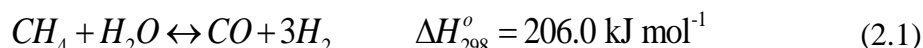
Recently, a lot of efforts on the utilization of natural gas reserves to produce syngas have been invested either in both industry and academics. According to Pakhare and Spivey (2014), Energy Information Administration of the United States reported that there is about 280 million cubic feet of proven natural gas reserves and 850 trillion cubic feet of estimated recoverable resources in the United States. They claimed that these huge reserves could offer a reasonable clean fuel and a dependable feedstock for reforming reaction, hence boosting the global economy. So far, CH_4 can be utilized as feedstock in steam reforming, partial oxidation, and autothermal reforming. These reforming techniques will be discussed in the subsequent subsections.

2.3 Methane Reforming Technologies

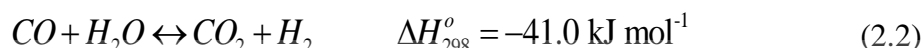
2.3.1 Steam Reforming

In 1868, Tessie du Motay and Marechal introduced the steam reforming process of hydrocarbons in the presence of steam over calcium oxide (Adris, Pruden, Lim, & Grace, 1996). Then, the steam reforming process was early established in 1930 for a large-scale application with the installation of a tubular natural gas steam reformer. Steam reforming of natural gas is currently one of the most widely employed techniques for syngas production, by contributing approximately 50% of the syngas production globally (Iulianelli, Liguori, Wilcox, & Basile, 2016). The steam reforming process for converting methane into syngas with a H_2/CO ratio of 3 involves the following reaction:

Methane steam reforming (MSR) reaction:



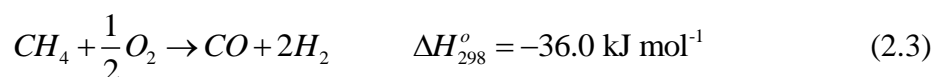
and water gas shift (WGS) reaction:



Due to endothermic nature, MSR is usually performed at the high temperature region about 1073-1373 K with a steam to carbon feed ratio (S:C) of 2-5 (Di Giuliano & Gallucci, 2018; I. D. Iglesias, Baronetti, & Mariño, 2017; Nawfal et al., 2015). In addition, WGS reaction (cf. Eq. (2.2)) occurring simultaneously in steam reforming may result in additional H₂ production. Thus, the steam reforming process offers more advantages over partial oxidation and auto thermal reforming, especially when considering hydrogen yield (Palo, Dagle, & Holladay, 2007). Nickel-based catalyst was widely used as catalysts for steam reforming since other metals have their own drawbacks; cobalt cannot endure with high pressure steam, iron could be easily oxidized and the high cost of noble metals is the main issue related to the usage of noble metals (Angeli, Monteleone, Giaconia, & Lemonidou, 2014).

2.3.2 Partial Oxidation

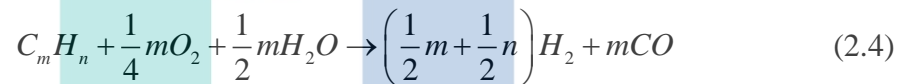
Liander (1929) was the first researcher in investigating syngas production through catalytic partial oxidation. The author reported that a high yield of synthesis gas could be achieved at a temperature of about 1123 K. In a stoichiometric partial oxidation reaction, the ratio of H₂/CO produced is about 2, which is ideal for downstream processes and carbon dioxide content generated is relatively low (Dedov et al., 2015; Singha, Shukla, et al., 2017). Therefore, research on partial oxidation is rapidly increased per year, especially for the utilization of methane as feedstock and nickel as catalyst (Figen & Baykara, 2015; Peymani, Alavi, & Rezaei, 2016). Generally, partial oxidation of methane is a process that consumes a limited amount of oxygen for partially oxidizing methane to CO and H₂ (cf. Eq. (2.3)).



Partial oxidation technology avoids the need for large amounts of expensive superheated steam required in a steam reforming reaction. However, an oxygen separation plant, which is also costly, may be required in cases where nitrogen (from air) is undesirable in high-pressure downstream processes.

2.3.3 Autothermal Reforming

Autothermal reforming process is a combination of steam reforming and partial oxidation process (cf. Eq. (2.4)). Generally, this reforming process requires CH₄, H₂O, and O₂ as the main feedstock to generate favourable H₂/CO ratio ranges about 1 to 2 (Yan et al., 2015).



Additionally, all the heat generated by the partial oxidation reaction is fully utilized to drive steam reforming reaction. Hence, autothermal reformers usually offer higher system efficiency than partial oxidation system, where excess heat is not easily recovered (Ogden, 2001). According to Padban and Becher (2005), autothermal reforming reaction also provides the reduction of emissions due to internal heat supply and high conversion of methane. However, autothermal reforming reaction carries higher risks of explosion due to the presence of oxygen. Ni-based catalysts have been widely employed in autothermal reforming, though this metal suffer from sintering and coke deposition (Ismagilov et al., 2015; Sepehri, Rezaei, Garbarino, & Busca, 2016b).

Table 2.1 was provided in order to summarize and clearly compare the synthesis routes of syngas production for CH₄. SR is the predominant commercial technology for producing syngas from methane, while partial oxidation and autothermal are the alternative approaches which still have limited commercial usage. Recently, CO₂-CH₄ reforming has gained considerable interest since it utilizes CO₂ and converts it into syngas with lower H₂/CO ratio (approaching to 1), suitable for many chemical synthesis such as the synthesis of oxygenated chemicals and FTS for producing synthetic fuels (Delgado Dobladez, Águeda Maté, Torrellas, Larriba, & Brea, 2020; Monteiro, Vieira, Calgaro, Perez-Lopez, & Ligabue, 2019). Noble and non-noble metal-based catalysts were widely employed in CO₂-CH₄ reforming. However, nickel-based catalysts are more economic and suitable for this reaction as compared to noble metal-based catalysts due to its low

cost and comparable activity (Dou et al., 2019; Movasati, Alavi, & Mazloom, 2019; Vizcaíno, Lindo, Carrero, & Calles, 2012). The details about CO₂-CH₄ reforming will be reviewed in the subsequent sections.

Table 2.1 Comparison of technology for syngas production from methane.

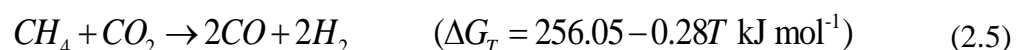
Synthesis routes	Process description	Advantages	Disadvantages
Steam reforming	T = 973-1973 K P = 3-25 bar CH ₄ /H ₂ O = 1:1 H ₂ /CO = 3:1	*High efficiency	*Consumes high energy *Expensive operating cost *Complicated system
Partial oxidation	T = 1223-1373 K P = 100 bar CH ₄ /O ₂ = 2:1 H ₂ /CO = 2:1	*High reactant conversions *High syngas selectivity *Short residence time	*The inevitable hot spot induction *Expensive operating cost related to oxygen separation
Autothermal	T = 700-1200 K CH ₄ /O ₂ = 1:0.6 CH ₄ /H ₂ O = 2:1 H ₂ /CO = 1:1-2:1	*Low temperature and energy require *Produce wide range of syngas ratio *Reduce hot spot induction	*Limited commercial experience due to complicated system * Expensive operating cost since it involves oxygen

Source : Abdullah, Abd Ghani, and Vo (2017); Souza and Schmal (2005); D. J. Wilhelm et al. (2001)

2.4 CO₂-CH₄ reforming

2.4.1 Overview

CO₂-CH₄ reforming or known as methane dry reforming is an alternative route that converts two abundantly available greenhouse gases (CH₄ and CO₂) into syngas (with H₂/CO ratio of 1) (cf. Eq. (2.5)). This lower H₂/CO ratio could be further consumed in the production of oxygenated chemicals and hydrocarbons from FTS (Delgado Dobladez et al., 2020). Typically, CO₂-CH₄ reforming is a favourably endothermic reaction demanding high operating temperature (above 930 K) to attain high CH₄ and CO₂ conversions.

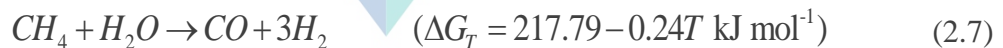
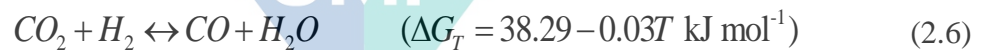


In 1928, Fischer and Tropsch were the first to conduct research about CO₂-CH₄ reforming over Ni and Co catalysts for generating syngas (Pakhare & Spivey, 2014). They found that Ni and Co catalysts employed during the reaction were severely

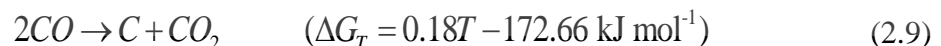
deactivated due to carbon deposition. Therefore, further reaction research was continued by Reitmeier, Atwood, Bennett, and Baugh (1948) in 1949, to unravel deactivation issue on Ni-based catalysts at reaction temperature of 700-1256 K. They successfully discovered that operating conditions (viz. temperature, pressure, and feed ratio of CH₄/CO₂) could be manipulated during CO₂-CH₄ reforming to generate favourable H₂/CO ratio with relatively low carbon deposition. The new constraints, i.e., catalyst synthesis methods, active metal types, metal-support interaction, and basic promoters have been implemented in CO₂-CH₄ reforming reaction several years later to suppress the formation of carbon (Pakhare & Spivey, 2014).

2.4.2 Reaction Mechanism

Theoretically, CO₂-CH₄ reforming yields a syngas with a H₂/CO ratio close to unity. However, the ratio of H₂/CO that could be obtained is less than 1 during CO₂-CH₄ reforming due to the instantaneous occurrence of reverse water gas shift (RWGS) (cf. Eq. (2.6)). Nevertheless, the existence of intermediate H₂O by-product through RWGS also could lead to methane steam reforming reaction (cf. Eq. (2.7)) resulting in H₂/CO ratio >1.



Apart from H₂O, H₂ and CO, carbon could also be simultaneously generated during CO₂-CH₄ reforming via methane decomposition (cf. Eq. (2.8)) and Boudouard reaction (cf. Eq. (2.9)).



2.4.3 Effect of Operating Condition

In CO₂-CH₄ reforming, the effect of reaction condition (i.e., temperature, pressure, and feed composition) have been extensively studied in academic research in order to optimise CO₂-CH₄ reforming for obtaining desired H₂/CO ratio with relatively low coke formation. Thus, all those factors are further discussed in detail in the following subsections.

2.4.3.1 Pressure

Nikoo and Amin (2011) have provided a thermodynamic equilibrium analysis on CO₂-CH₄ reforming as a function of operating pressure at a stoichiometric molar ratio ($n_{\text{CH}_4}:n_{\text{CO}_2} = 1$ mol) and reaction temperature of 1173 K (cf. Figure 2.2). They revealed that the highest conversion of CO₂ and CH₄ was obtained under atmospheric pressure condition within the range of 97.4-99.0 %. However, both conversions were significantly decreased with an increase in operating pressure from 1 to 25 atm due to the position of equilibrium system that was shifted towards the left side (cf. Eq. (2.5)) in order to counteract the increment of pressure, in agreement with Le Chatelier's principle.

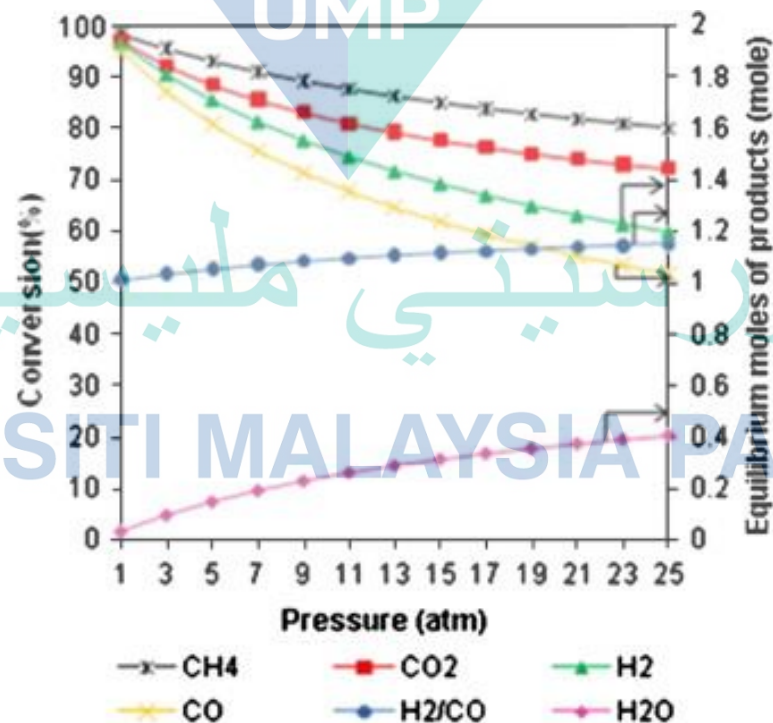


Figure 2.2 The effect of operating pressure on reactant conversions and products distribution at stoichiometric condition and T = 1173 K.

Source: Nikoo and Amin (2011)

A similar trend for product distribution (H_2 and CO) vs. pressure (cf. Figure 2.2) was also observed with the rise of pressure implying that the rate of dry reforming was decreased. Indeed, the decline in CO and H_2 formation at the higher pressures also was assisted by the back reaction of methane decomposition (cf. Eq. (2.8)) and CO disproportionation (cf. Eq. (2.9)), in turn lowering the conversion of CH_4 and CO_2 . However, the production of water was considerably enhanced from 0.03 to 0.4 mol with the growth of operating pressure from 1 to 25 atm. Nikoo and Amin (2011) reported that this observation reasonably resulted from the existence of reverse water gas shift reaction at high-pressure conditions, which is consistent with results obtained by Shamsi and Johnson (2007).

In another literature, Shamsi and Johnson (2007) investigated the influence of operating pressure on carbon formation in CO_2 - CH_4 reforming using a thermodynamic approach. They stated that the carbon generated from the Boudouard reaction was increased with the rise of operating pressure but decrease in methane decomposition. They further explained that these results that verified Boudouard reaction is the most desirable route for carbon generation at high operating pressure as compared with the cracking of methane.

2.4.3.2 Temperature

Ayodele, Khan, and Cheng (2016) conducted CO_2 - CH_4 reforming at a temperature of 873-1173 K to examine the effect of the reaction temperature on reactant conversions, product yields, and H_2/CO molar ratio. The authors carried out CO_2 - CH_4 reforming using 20%Co/CeO₂ catalyst at a stoichiometric feed ratio. As seen in Figure 2.3, CH_4 and CO_2 conversion levels improved significantly about 132.2% and 96.4%, respectively with an increase in reaction temperature. They justified that this trend may be attributed to the endothermic character of CO_2 - CH_4 reforming. In addition, the conversion of CO_2 was superior to CH_4 conversion over the entire range of operating temperatures. They implied that this behaviour resulted from the co-occurrence of parallel side reaction i.e., RWGS and Reverse Boudouard. A similar observation was also reported by Paksoy, Caglayan, and Aksoylu (2015) and Luisetto, Tuti, Battocchio, Lo Mastro, and Sodo (2015), with the increment of reaction temperature.

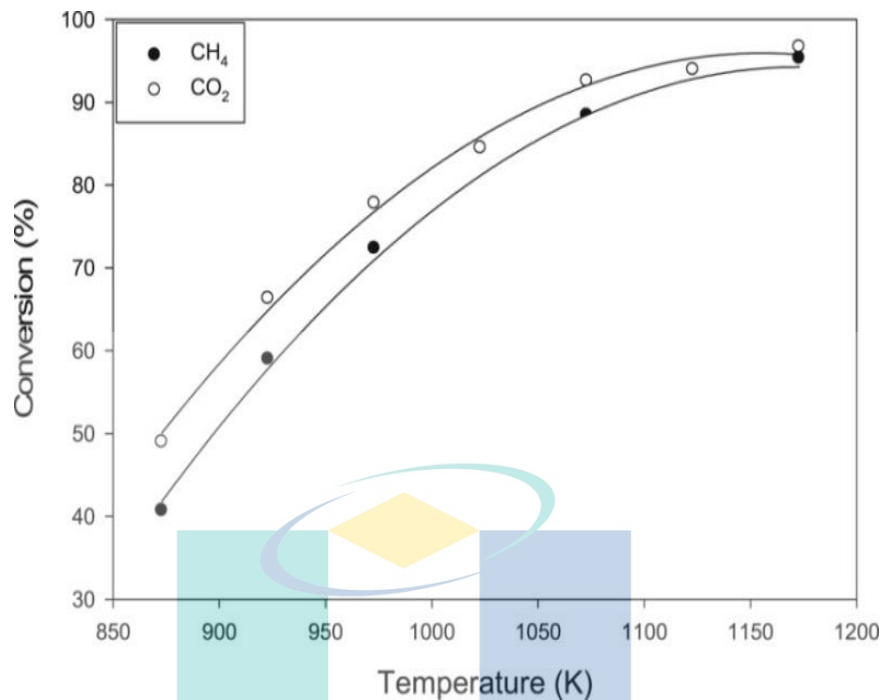


Figure 2.3 The conversion of CH₄ and CO₂ as a function of temperature with stoichiometric condition.

Source: Ayodele, Khan, and Cheng (2016)

In that CO₂-CH₄ reforming evaluation, Ayodele, Khan, and Cheng (2016) also found that H₂ and CO yield was improved and reached the maximum value of 30.11% and 42.11%, respectively at a temperature of 1173 K (cf. Figure 2.4). The enrichment of both yields with reaction temperature is consistent with other studies (Hassani Rad, Haghghi, Alizadeh Eslami, Rahmani, & Rahemi, 2016; N. Wang, Yu, Wang, Chu, & Liu, 2013). However, the yield of H₂ obtained in that experiment was greater than the CO yield beyond the temperature of 1023 K because of the improvement of CO₂-CH₄ reforming. As presented in Figure 2.5, the H₂/CO ratio also experienced a nonlinear ascent from 0.73 to 1.40 with the rise of temperature from 873 to 1173 K. From the results, the author suggested that it is favourable to conduct CO₂-CH₄ reforming within a temperature of 948 to 1023 K in order to generate the desirable syngas ratio for Fischer-Tropsch synthesis.

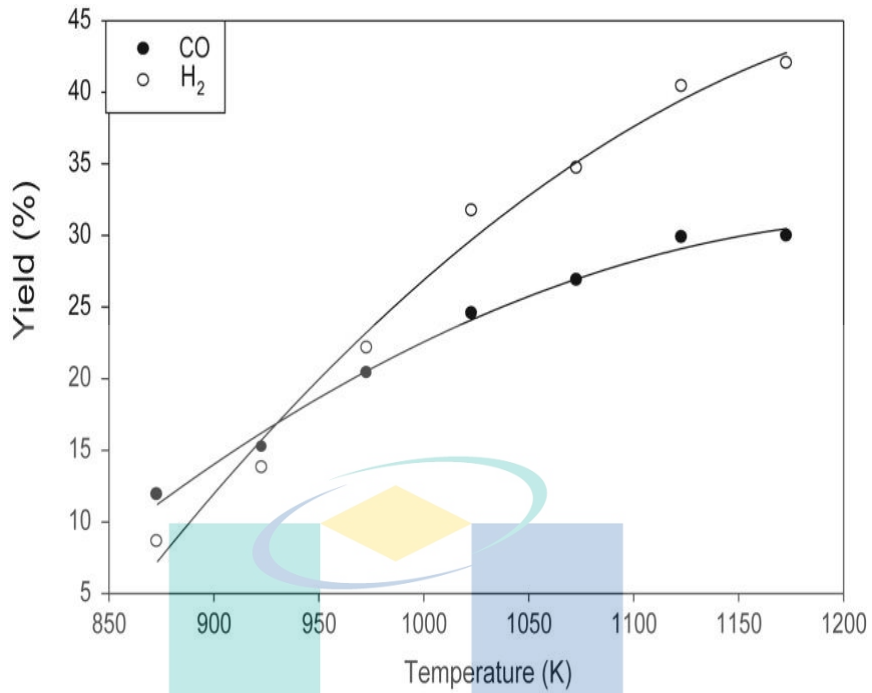


Figure 2.4 Effect of temperature on product yields at stoichiometric condition and under atmospheric pressure.

Source: Ayodele, Khan, and Cheng (2016)

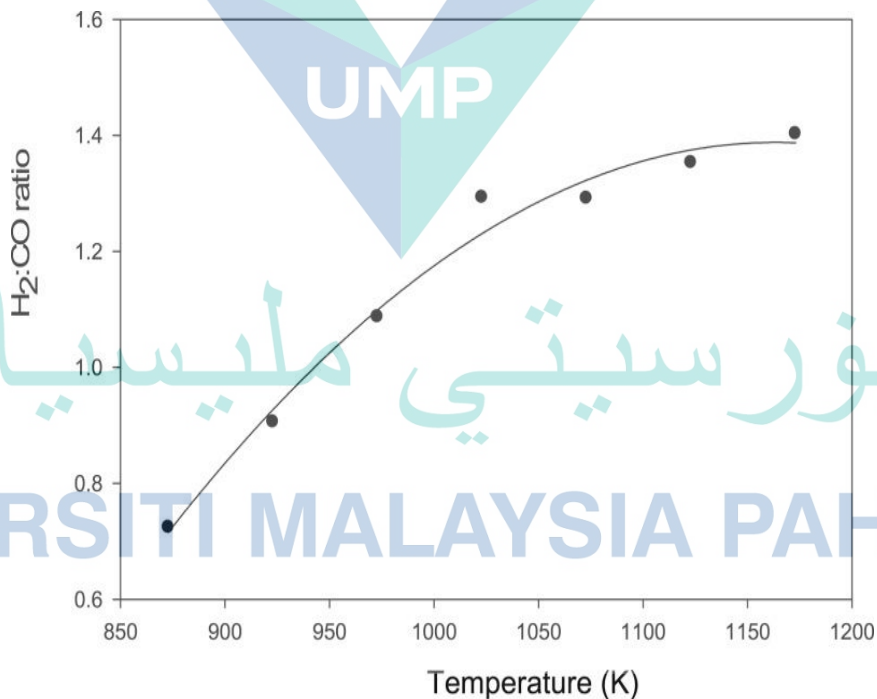


Figure 2.5 Effect of temperature on H₂/CO ratio at stoichiometric condition and under atmospheric pressure.

Source: Ayodele, Khan, and Cheng (2016)

The thermodynamic study taken from research by Nikoo and Amin (2011) as seen in Figure 2.6, displayed that carbon deposition was reduced significantly with the growth of reaction temperature from 873-1173 K. They explained that the employment of high temperature during CO₂-CH₄ reforming acting as a carbon-removal by enhancing the reverse Boudouard reaction ($2CO \rightarrow C + CO_2$) and carbon gasification reaction ($C + H_2O \rightarrow CO + H_2$). The results achieved here are in agreement with the previous study by Ginsburg, Piña, El Solh, and de Lasa (2005) on a 20%Ni/USY-zeolite catalyst. Although higher reaction temperature could lead to catalyst sintering, it is necessary to employ reaction temperature above those carbon formation limits (>1073 K) in order to minimize the rate of coke formation and avoid the occurrence of reactor blockage.

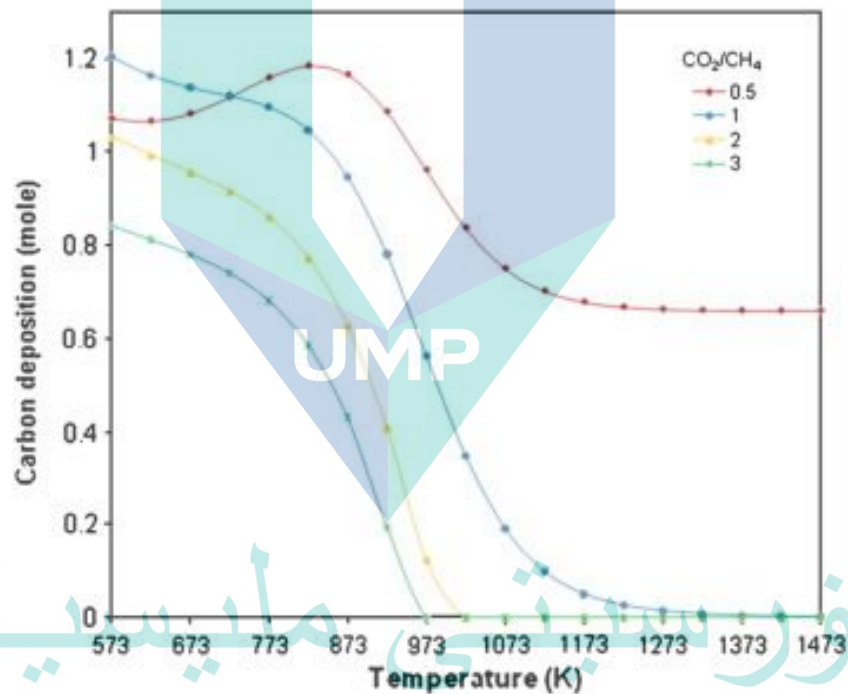


Figure 2.6 The influence of reaction temperature on the moles of carbon generated during CO₂-CH₄ reforming reaction at 1 atm.

Source: Nikoo and Amin (2011)

2.4.3.3 CH₄/CO₂ Feed Composition

Figure 2.7 shows reactant conversions, product yield, and H₂/CO molar ratio as a function of CH₄/CO₂ feed composition reported by Hassani Rad et al. (2016) using Ni/Al₂O₃-CeO₂ catalyst. They found that the conversion of CO₂ improved about 33.81%, whilst CH₄ decreased about 22.70% as a result of the increment of CH₄/CO₂ feed composition from 0.5 to 2.0. They suggested that this trend was observed during CO₂-CH₄ reforming evaluation owing to the accumulated carbon generated through the decomposition of excess CH₄. The noticed reduction of CH₄ conversion for CH₄/CO₂ > 1 is in agreement with results reported by Paksoy et al. (2015) and Wisniewski, Boréave, and Gélin (2005) and with CO₂-CH₄ reforming reaction over Co-Ce/ZrO₂ and Ir/Ce_{0.9}Gd_{0.1}O_{2-x} catalysts, respectively.

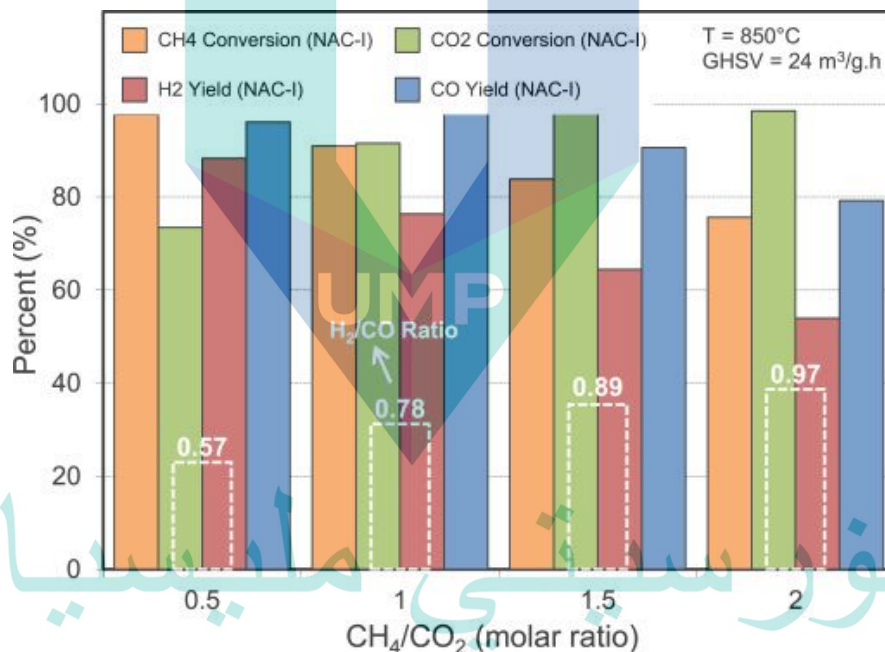


Figure 2.7 Reactant conversion, product yields and H₂/CO ratio as function of CH₄/CO₂ molar ratio at reaction temperature of 1123 K and under atmospheric pressure.

Source: Wisniewski et al. (2005)

In another CO₂-CH₄ reforming evaluation, Omoregbe et al. (2017) investigated the effect of CH₄/CO₂ feed composition on the catalytic performance of 10%Ni/SBA-15 catalyst by varying both partial pressures within the range of 20-60 kPa. However, they obtained dissimilar CO₂ conversion trends with the aforementioned results when CH₄ partial pressure increased from 20-60 kPa. According to the authors, the increase in CH₄ partial pressure did not assist the conversion rates of both reactants. On the contrary, it

promotes the coke formation on the catalyst surface. Although the existence of CO₂ could act as an oxidant agent for carbon removal, they assumed that the carbon gasification rate could be inferior to the carbon formation rate during CH₄-rich environment. The increment of CO₂ partial pressure resulted in a rise in CH₄ conversion, and a decline in CO₂ conversion. Omoregbe et al. (2017) concluded that the improvement in CH₄ conversion is due to the enhancement of parallel RBR, whilst the drop in CH₄ conversion is owing to deficient amount of CH₄-limiting reactant. From the results of all previous researchers, it is necessary to carry out the CO₂-CH₄ reforming reaction at CH₄/CO₂ ratio of 1:1 for the rest of the catalytic tests.

2.5 The Catalyst Development for CO₂-CH₄ reforming

2.5.1 Overview of Catalyst

In general, catalyst is a material that enhances the rate of a chemical reaction by offering an easier path with less activation energy as compared to the uncatalyzed reaction. In CO₂-CH₄ reforming, an ideal composition of heterogeneous catalyst could be designed based on the types of active metals, catalyst supports and promoters in order to ensure that catalyst created has the following attributes i.e., excellent and stable catalytic activities, high coke resistance, negligible sintering and high tolerance against deactivation. Therefore, the subsequent section gives an overview of active metals, supports, and promoters that have been employed in previous studies of CO₂-CH₄ reforming.

2.5.2 Noble Metals as Active Sites

The employment of noble metals as catalysts has been widely explored for CO₂-CH₄ reforming. Hou, Chen, Fang, Zheng, and Yashima (2006) investigated the catalytic performance of several noble metals (Ru, Rh, Pt, Pd, and Ir) over Al₂O₃ support during the CO₂-CH₄ reforming at the reaction temperature of 1073 K under CH₄/CO₂ feed ratio of 1.0. They reported that all those metals exhibited stable catalytic performance with no coke formation during 240 min on stream, except Pd which contributed to coke formation at about 4.9 mg coke g_{cat}⁻¹ h⁻¹. This observation strongly reflects the excellent coke-resistant capability of those metals in CO₂-CH₄ reforming. In addition, they concluded that the catalytic activity and stability increased in the order; Pt > Pd > Ir > Ru > Rh. In another study by Whang et al. (2017), the catalytic evaluation of Ru-based catalysts

prepared by the impregnation method was investigated in CO₂-CH₄ reforming at stoichiometric molar ratio and reaction temperature 1073 K. They stated that the Ru/ZrO₂-SiO₂ catalyst not only revealed excellent activity and stability in 20 h CO₂-CH₄ reforming but also presented no carbon formation after reaction. In fact, the superior catalytic activities and coke resistance of those catalysts were also verified by other studies (Anil, Modak, & Madras, 2020; Cimino, Lisi, & Mancino, 2017; de Caprariis et al., 2016). Although those metals exhibited superior CO₂-CH₄ reforming performance and resisted carbon formation, they are rarely used for industrial purpose owing to their expensive cost and limited availability. Thus, non-noble catalysts have gained significant attention for dry CH₄ reforming reaction.

2.5.3 Non-Noble Metals as Active Site

Non-noble catalysts such as Ni and Fe were preferred for CO₂-CH₄ reforming since they are relatively cheap, have excellent capacity of C-H bond scission and possess high catalytic activity (X. Li et al., 2017; Tsoukalou et al., 2016). Shang, Li, Li, Liu, and Liang (2017) reported that CO₂-CH₄ reforming over Ni nanoparticle catalyst exhibited both high activity and stability using a stoichiometric feed ratio (1:1) at the reaction temperature ranging from 973-1123 K. However, high coke formation is the main problem in the utilization of non-noble catalyst especially nickel for CO₂-CH₄ reforming, which resulted from the inevitable CH₄ decomposition and CO disproportionation side reactions (Ay & Üner, 2015; Usman et al., 2015). Then, cobalt was appointed as a potential catalyst owing to its higher stability and lower carbon deposition. In a previous study, Koh et al. (2007) found that the rate of coke formation was considerably reduced by using a Co-based catalyst. Although this catalyst showed excellent carbon resistance and stability, their lower catalytic performances are the main reasons for less application as compared to Ni-based catalysts. Therefore, a lot of research recently was focused on improving the metal dispersion, reducing the crystallite size of metal particles on the catalyst surface, and increasing the basic properties of catalysts. The summary of the previous findings related to the employment of Co-based catalysts in CO₂-CH₄ reforming attained from literature is presented in Table 2.2.

Support modification had been extensively reported in literature for improving the reforming activity of Co-based catalyst in CO₂-CH₄ reforming. In fact, the selection of basic supports for Co-based catalysts is important since it could provide thermal

stability to Co-active metals as well as suppress the deposition of carbon. Bouarab, Akdim, Auroux, Cherifi, and Mirodatos (2004) investigated the effect of support modification by adding MgO to Co/SiO₂ catalyst towards catalyst's properties and performance in CO₂-CH₄ reforming within the temperature range of 773-1023 K. The authors noticed the positive influence arising in reforming activity with this modification, accredited to the increment in alkaline properties and the formation of small metallic cobalt particles. Omata, Nukui, Hottai, Showa, and Yamada (2004) evaluated the performance of Co catalyst in CO₂-CH₄ reforming at 1023 K and stoichiometric feed ratio by using strontium carbonate as support (SrCO₃). The author attained superior catalytic activity with SrCO₃ employment as compared to other Co-based catalysts supported with MgO, CaO, CeO₂ and La₂O₃, which are synthesized using similar oxalate co-precipitation technique.

In different works, J.-H. Park, Yeo, and Chang (2018) examined the influence of different supports (Al₂O₃, CeO₂, MgAl₂O₄, SiO₂, and ZrO₂) on the catalytic performance of CoAl catalyst in CO₂-CH₄ reforming at 1123 K and stoichiometric condition. The authors stated that the superior performance exhibited by CoAl supported on MgAl₂O₄ as compared to that of on Al₂O₃, ZrO₂, CeO₂, and SiO₂ (cf. Figure 2.8), owing to the strong Co-MgAl₂O₄ interaction. Indeed, the authors justified that the great improvement was accredited to the balance between the rates of coke formation from CH₄ cracking and surface oxidation via CO₂ dissociation. Besides, Ayodele, Khan, and Cheng (2016) verified that the employment of CeO₂ support for Co induced high activity towards CO₂-CH₄ reforming which was proven from the high reactant conversion (CH₄ Conv. = 79.5% and CO₂ Conv. = 87.6%), attributed to the high capacity of oxygen retention and great dispersion of Co particles on the catalyst surface. Apart from that, the employment of mesoporous materials such as SBA-15 and mesoporous alumina is also capable of resolving the low-performance of Co through improving the dispersion of active metal particles accredited to their high surface area (El Hassan et al., 2016; Taherian et al., 2017a).

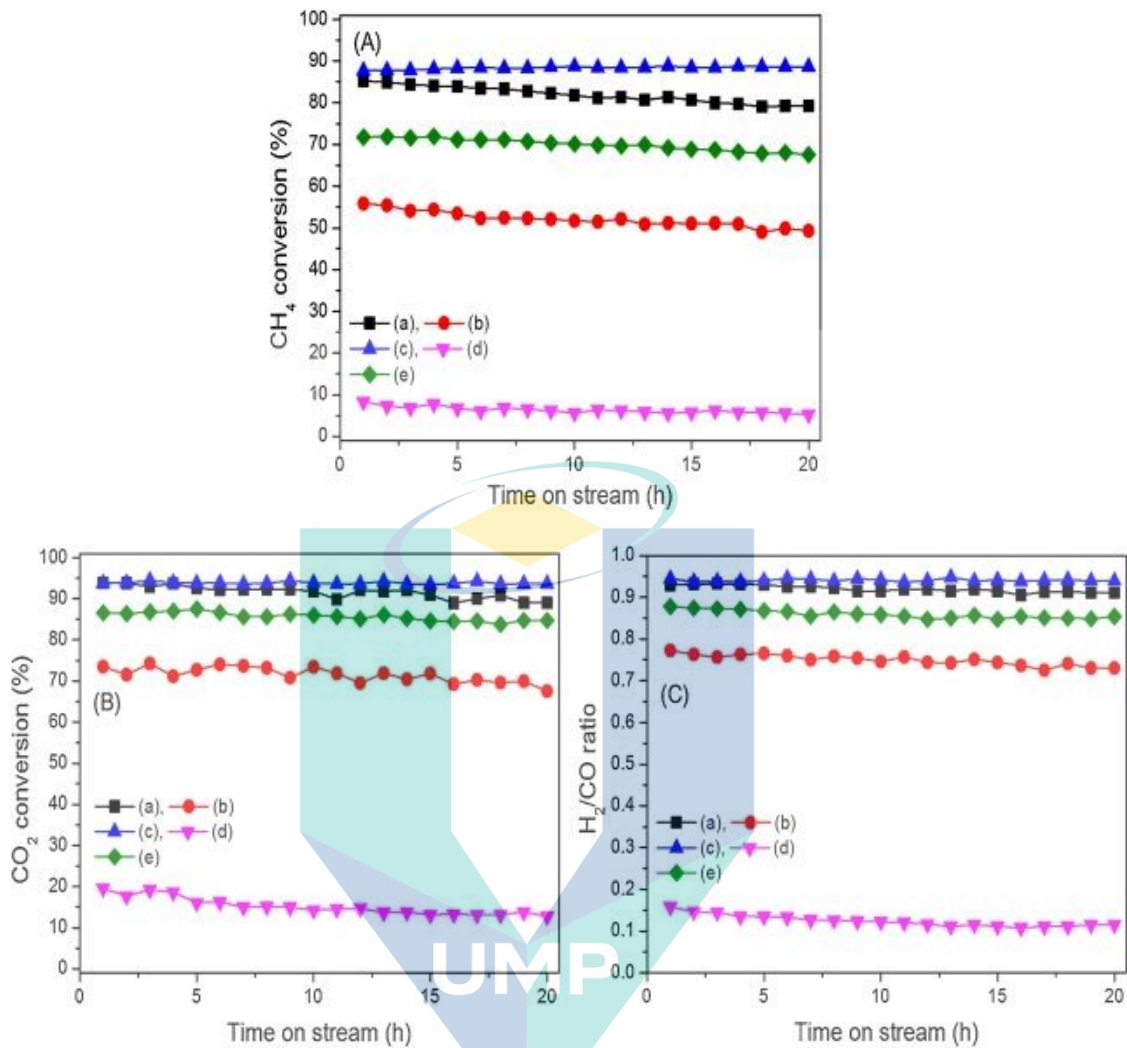


Figure 2.8 The catalytic performance of CoAl catalyst supported on different metal oxides; (a) Al₂O₃, (b) CeO₂, (c) MgAl₂O₄, (d) SiO₂, and (e) ZrO₂.

Source : J.-H. Park et al. (2018).

Additionally, catalyst synthesis plays a significant role in enhancing the catalytic performance since the structural properties of catalysts including their reduction properties could be changed by using different approaches. Ewbank, Kovarik, Kenvin, and Sievers (2014) compared two kinds of catalyst synthesis, namely the controlled adsorption and dry impregnation in preparing Co/Al₂O₃ for CO₂-CH₄ reforming. As a result, Co/Al₂O₃ synthesized via controlled adsorption achieved superior CO₂-CH₄ reforming activity and slower deactivation as compared to its counterpart, owing to the smaller average particle size and higher dispersions of Co. Even though catalyst prepared by controlled adsorption attained higher activity than the dry impregnation, the deactivation rate for both techniques are considerably high since both techniques recorded about 21.9% and 37.4% within 6 h reaction (cf. Table 2.2).

Table 2.2 List of cobalt based catalysts which have been examined in CO₂-CH₄ reforming.

Catalyst	Co (wt%)	Method	T (K)	GHSV (L g _{cat} ⁻¹ h ⁻¹)	Conversion (%)		D _d (%)	H ₂ yield (%)	Cd (%)	SA (m ² g ⁻¹)	Pore Diameter (nm)	Ref.
					CH ₄	CO ₂						
CoAl/Al ₂ O ₃					79.3	89.0	6.9	73.2	4.2	105.7	9.8	
CoAl/CeO ₂					49.3	67.5	11.6	35.5	1.4	8.9	>40.0	
CoAl/MgAl ₂ O ₄	5	Wet impregnation	1123	60	87.6	93.7	0.1	84.2	3.4	94.9	12.0	J.-H. Park et al. (2018)
CoAl/ SiO ₂					5.3	12.8	36.1	8.3	1.5	264.0	13.7	
CoAl/ ZrO ₂					67.6	84.8	5.8	71.8	26.2	13.2	>40.0	
Co/SBA-15					24.0	38.0	11.7	n.a.	n.a.	628.0	1.3	
Sm ₂ O ₃ /Co/SBA-15	10	Two-solvents impregnation	973	n.a.	11.4	29.1	2.1	n.a.	56.9	564.0	0.9	Taherian et al. (2017a)
Co/SBA-15					16.91		0.3			639	3.7	
Co/SiO ₂	12	Two-solvents impregnation	823	67	4.97	n.a.	1.8	n.a.	n.a.	171	n.a.	El Hassan et al. (2016)
RhCo/ SBA-15					48.8		0.1			448	3.7	
Co/CeO ₂		Wet impregnation	1023	30000 ^a	87.6	79.5		37.6		39.4	1.2	(Ayodele, Khan, & Cheng, 2016)
Co/La ₂ O ₃	20					n.a.	50.0	60.0	n.a.	45.0	n.a.	
Co/CeO ₂	8	Incipient wetness impregnation	973	n.a.	0.62	0.82	96.0	0.01	0	18.9	n.a.	Ay and Üner (2015)
Ni-Co/CeO ₂	4				64.2	71.0	16.2	39.5	17.0	18.3		
Co/ZrO ₂	5	Wet impregnation	973	3.8		n.a.		75.8	28.2	3.6	27.7	Abasaheed, Al-Fatesh, Naeem, Ibrahim, and Fakeeha (2015)
Co/CeO ₂					59.4	11.0	7.4	18.9				
	5				25.8	33.5	26.5	23.0		80.7	14.8	
	10				66.8	74.5	1.0	60.7		97.5	13.8	
CoMgO	15	Co-precipitation	973	12	22.1	31.4	60.1	33.7	n.a.	100.1	11.2	Mirzaei, Rezaei, Meshkani, and Fattah (2015)
	20				26.5	29.0	43.7	31.5		88.3	14.1	
	30				24.2	36.6	52.7	43.7		78.2	12.9	
Co/ZSM5					52.8	64.1	n.a.		20.6	247.0		
1Ni1Co/ZSM5	n.a.	Wet impregnation	973	60	55.4	65.4	n.a.		n.a.	292.0	n.a.	(Estephane et al., 2015)
1Ni2Co/ZSM5					59.9	69.6	6.1		n.a.	237.0		
2Ni1Co/ZSM5					61.8	69.6	19.3		n.a.	284.0		

Table 2.2 Continued

Catalyst	Co (wt%)	Method	T (K)	GHSV (L g _{cat} ⁻¹ h ⁻¹)	Conversion (%)		D _d (%)	H ₂ yield (%)	C _d (%)	SA (m ² g ⁻¹)	Pore Diameter (nm)	Ref.
					CH ₄	CO ₂						
Co/Al ₂ O ₃	2	Controlled adsorption	973	22 000 ^a	52.0	53.2	21.9	n.a.	n.a.	88.0	14.7	Ewbank et al. (2014)
		Dry impregnation			31.6	30.7	37.4			84.0	16.0	
Co/SBA-15 Ru-Co/SBA-15	12	Two-solvents impregnation	1063	12.1	44.0 82.0	n.a. 71.0	n.a. n.a.	n.a.	n.a.	589.0 629.0	40.0 39.0	K. Jabbour, El Hassan, Casale, Estephane, and El Zakhem (2014)
Co/CeO ₂ Co-Ni/CeO ₂	7.5 3.75	Surfactant assisted co-precipitation	1023	30	86.0 83.5	n.a.	2.5 0.8	n.a.	30	67 105	n.a.	Luisetto, Tuti, and Di Bartolomeo (2012)
Co/ZrO ₂ Co-La/ZrO ₂ Co-K/ZrO ₂ Co-Mn/ZrO ₂ Co-Ce/ZrO ₂ Co-Mg/ZrO ₂	5	Sequential impregnation	923	60	36.5	47.5	39.9	30.8	4.0	22.0	n.a.	(Özkara-Aydınoğlu & Aksoylu, 2010)
27.2					43.7	0.0	20.8	0.2	27.0			
6.8					13.4	53.1	1.1	2.0	n.a.			
22.3					33.1	19.2	14.0	0.8	n.a.			
48.9					61.1	3.7	46.0	2.6	n.a.			
0					0	100	0	2.0	n.a.			
Co/SrCO ₃	7	Oxalate co-precipitation	1023	100	24.8	18.8	25.3	n.a.	42 ^b	n.a.	n.a.	Omata et al. (2004)
Co/SiO ₂ Co/MgO-SiO ₂	5	Incipient wetness impregnation	873	n.a.	41.0 42.3	64.5 65.3	60.5 65.3	n.a.	0.4 0.3	185 178	n.a.	Bouarab et al. (2004)

n.a. = not available, C_d = Amount of carbon deposited.

^aGas hourly space velocity (GHSV) in (h⁻¹)

^bcarbon deposition in mg g_{cat}⁻¹

Deactivation degree, D_d (%) = [1 - (Final CH₄ conversion / Initial CH₄ conversion)] × 100.

The introduction of second active metal as catalyst promoter is also considered as a promising approach in addressing low performance of Co catalysts since it is probably able to significantly increase the oxygen mobility, enhance metal dispersion, and reduce the acidity of the catalyst (S. Y. Foo, C. K. Cheng, T. H. Nguyen, & A. A. Adesina, 2011b). In fact, the catalyst deactivation could be prevented owing to the improvement in catalyst carbon resistance (Foo et al., 2011b). Ibrahim, Fakeeha, and Al-Fatesh (2014) evaluated the effect of Sr-promoter loading (0-1.5wt%) towards the catalytic performance of Co/Al₂O₃ in CO₂-CH₄ reforming. The author attained the highest hydrogen selectivity (50.9%) and hydrogen yield (77.9%) with Sr-promoter loading of 0.5wt.%, attributed to the highest surface area and the least carbon formation (5.1wt%). Yet, Taherian et al. (2017a) noticed a contrary result of reforming activity after introducing Sm₂O₃ as promoter on Co/SBA-15 with CH₄ conversion attained being lower than 25%. The authors clarified that this negative effect is not resulting from promoter addition, but because of the oxidation of Co to inactive phase and sintering of Co particles at high temperatures.

Aside from all the aforementioned efforts, it has been reported that the combination of Co with other metals to form bimetallic catalysts could alter the catalyst attributes, thus it is capable of enhancing the catalytic performance. According to Takanabe, Nagaoka, Nariai, and Aika (2005), a combination of Co-Ni to form bimetallic catalysts is capable of improving reforming activity, especially CH activation on the metallic surface, and also avoiding the undesirable metal oxidation. In literature, the combination of cobalt and nickel supported on various types of support for CO₂-CH₄ reforming received attention attributed to the formation of Co-Ni alloy (Siang et al., 2018; Xin, Cui, Cheng, & Zhou, 2018). Indeed, there are some studies reported that the bimetallic Co-Ni catalyst managed to exhibit superior reforming activity in CO₂-CH₄ reforming as compared to the monometallic Co-based catalysts. Ay and Üner (2015) proved that the formation of bimetallic Co catalyst with Ni exhibited higher activity as well as better stability and high carbon resistance as compared to monometallic Co-based catalyst owing to better active metal dispersion and strong metal-support interaction.

In summary, the lower catalytic performance exhibited by Co-based catalysts could be effectively tackled by choosing appropriate supports and promoters with excellent properties such as high surface area, great oxygen storage mobility, and strong

alkaline attributes. In fact, the structural changes resulting from different preparation techniques should be considered due to its vital role in affecting the catalytic CO₂-CH₄ reforming performance.

2.5.4 Mesoporous Support

As mentioned before, the selection of basic supports also important in CO₂-CH₄ reforming since it could provide thermal stability to active metals and could suppress the deposition of carbon (Bradford & Vannice, 1999). Among the metal oxide supports, CeO₂, CeO₂-ZrO₂, YSZ, MgO, and TiO₂ supports were utilized extensively due to their good redox properties and oxygen mobility (Abasaheed et al., 2015; Hassani Rad et al., 2016; Kambolis, Matralis, Trovarelli, & Papadopoulou, 2010). In fact, there are several authors reported that the employment of CeO₂ as the catalyst support in CO₂-CH₄ reforming improved metal dispersion and resisted sintering. This improvement in catalytic activity was attributed to strong metal-support interaction and high oxygen storage capacity (Djinović, Batista, & Pintar, 2012; Löfberg, Guerrero-Caballero, Kane, Rubbens, & Jalowiecki-Duhamel, 2017; Xie et al., 2018).

Apart from that, several effective techniques including the modification of the physical structure or chemical properties catalyst support and increasing the pore size of catalysts also were applied to suppress coking. Thus, these extensive approaches led to the employment of mesoporous materials as support in catalytic fields such as SBA-15 and MCM-41. Recently, mesoporous alumina (MA) obtained a lot of attention in reforming activity due to its large specific surface areas, controllable pore sizes, and high thermal stability (H. Ma et al., 2016; Leilei Xu et al., 2017). A lot of efforts have been carried out to extending the synthesis of mesoporous silica materials to MA. However, the common procedure for the synthesis of ordered mesoporous silica could not be implemented for the preparation of MA, due to the fast hydrolysis and condensation rates of aluminum alkoxides, resulting in the development of disordered alumina. In literature, the typical approach that had been employed for MA synthesis routes are; (1) surfactant-free pathway, (2) hard template pathway, and (3) soft template pathway.

2.5.4.1 Surfactant-Free Pathway

The surfactant-free pathway which is known as solvent-deficient synthesis is the technique for preparing MA without the employment of a template. This technique was carried out by mixing an aluminum salt (e.g., aluminum nitrate, chloride, alkoxide, etc.) with a base (e.g., ammonium bicarbonate) to initiate the reaction before calcining the intermediate at high temperatures (B. Huang, Bartholomew, Smith, & Woodfield, 2013; Sepehri, Rezaei, Garbarino, & Busca, 2016a). B. Huang et al. (2013) carried out the surfactant-free pathway for preparing MA using aluminum nitrate ($\text{Al}(\text{NO}_3)_3 \cdot 9\text{H}_2\text{O}$), aluminum chloride ($\text{AlCl}_3 \cdot 6\text{H}_2\text{O}$), aluminum isopropoxide ($\text{Al}(\text{OCH}(\text{CH}_3)_2)_3$), and aluminum sec-butoxide ($\text{Al}(\text{OCH}(\text{CH}_3)\text{CH}_2\text{CH}_3)_3$) as a solid metal salt while ammonium bicarbonate (NH_4HCO_3) as solid base. The authors found that the MA prepared using aluminum alkoxides exhibited large pore sizes (approximately 18 nm) and large pore volumes ($1.7 \text{ cm}^3 \text{ g}^{-1}$) as compared to the MA synthesised with aluminum inorganic salts. Indeed, the authors further explained that MA produced from aluminum alkoxides possessed high resistance against sintering and good thermal stability. The authors illustrated the self-templating mechanism in the surfactant-free pathway as seen in Figure 2.9. During the synthesis, the oxide group from alcohol will attach and cover boehmite's surface while the alky chains stretch away from boehmite's surface and working as a surfactant. The hydrogen bonding between boehmite's surface and oxide groups would lessen the free energy of the crystallite with low dimensions. Thus, the boehmite crystallites tend to enlarge in two dimensions and condense into larger γ -alumina crystallites of similar shape after H_2O is eliminated via the following calcination.

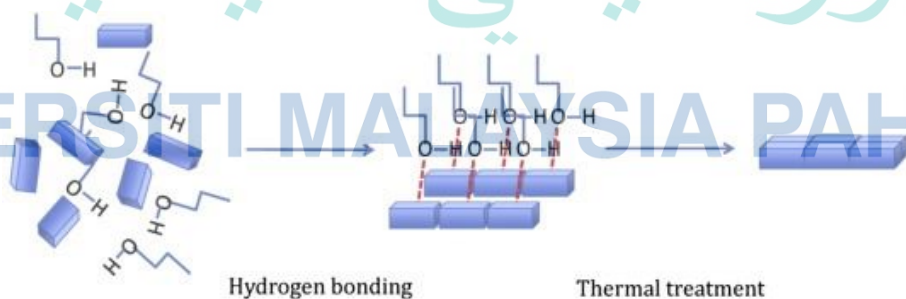


Figure 2.9 Schematic illustration of the self-templating mechanism.

Source : B. Huang et al. (2013)

Though the procedure for this pathway is simple, the mesoporous alumina generated are usually restricted to discrete surface areas and pore sizes, as opposed to template-assisted methods that accommodate a continuum of micelle structures and therefore mesostructures. This allows template-assisted synthesis methods to generate mesoporous alumina with high involvement in size-selective catalysis, in contrast to the template free, solvent deficient method (B. Huang et al., 2013).

2.5.4.2 Hard Template Pathway

Generally, the hard template pathway for MA involves the impregnation of a pre-made exoskeleton with carbon-based materials; CMK-3 (Q. Liu, Wang, Xu, et al., 2008), CMK-8 (Haffer, Weinberger, & Tiemann, 2012), FDU-15 (Z. Wu, Li, Feng, Webley, & Zhao, 2010), and MOF-5 (Derakhshani, Hashamzadeh, & Amini, 2018) since carbon materials could provide the possibility of crystallization at high temperature under an inert atmosphere as well as easy removal by burning out of the carbon template under air (Z. Wu et al., 2010). In fact, these carbon materials effectively guard the mesostructures of alumina from collapsing during the crystallization of MA framework walls via stepwise calcination (Derakhshani et al., 2018).

The steps for the preparation of MA using MOF-5 was illustrated by Derakhshani et al. (2018) in their recent work as seen in Figure 2.10. In that template preparation, the authors initially prepared metal-organic framework-5 synthesized at room temperature (RT-MOF-5) before forming porous carbon MOF via pyrolyzing technique. Then, the MOF exoskeleton is etched away with nitric acid before introduced with the aluminum source (aluminum tri-sec-butoxide). The removal of carbon endoskeleton for this work required three-stage heat treatment before the aluminum is calcined to achieve the desired MA phase. The authors reported that synthesised MA possessed BET surface area about $320 \text{ m}^2 \text{ g}^{-1}$, pore volume of $0.85 \text{ m}^3 \text{ g}^{-1}$, and narrow pore size distribution with an average value of 2.5 nm (Derakhshani et al., 2018).

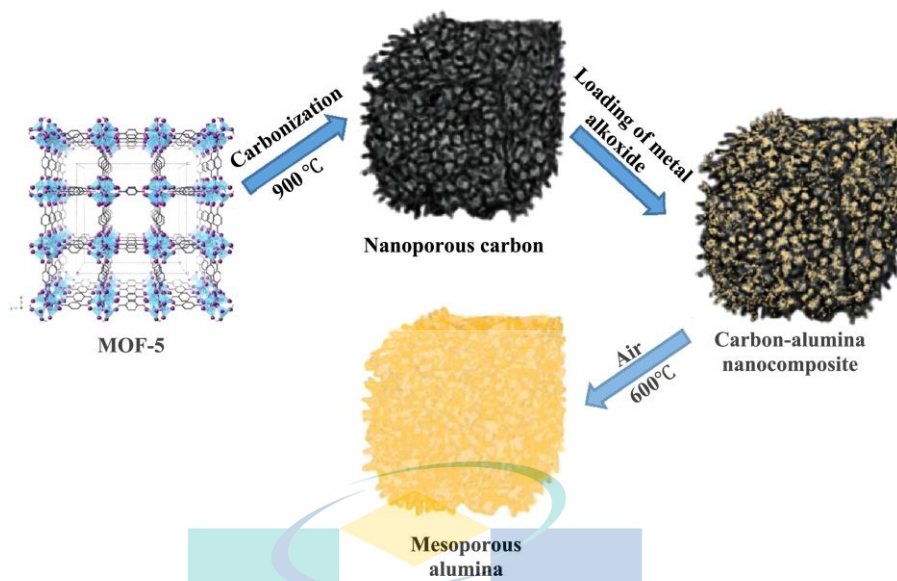


Figure 2.10 Steps for the preparation of mesoporous crystalline γ -alumina using MOF-5.
Source : Derakhshani et al. (2018)

However, despite this MA success preparation from various types of carbon templates, time-consuming and numerous complex steps are the real disadvantages of these approaches. For example, in the case of CMK-3, CMK-8, and FDU-15, these steps include the preparation of mesoporous silica, loading of sucrose solution and carbonization inside mesoporous silica, and then washing off the silica matrix using hydrofluoric acid or sodium hydroxide solution.

2.5.4.3 Soft Template Pathway

The soft template pathway has gained great interests as its easily accessible and reproducible in fabricating MA through a facile sol-gel process, as compared to the surfactant-free and hard template pathway (Yuan et al., 2008). In addition, this method can bypass the complex and time-consuming process of the hard template pathway and also realize the modulation of pore size continuously, better than the surfactant-free pathway. In this process, the hydrolysis behaviour of aluminum precursors is very complicated and is easily affected by the synthetic conditions such as acid, water, and crystallization temperature, leading to the need of rather strict control of the conditions and consequently differed structural properties of the obtained MA (Bleta, Alphonse, Pin, Gressier, & Menu, 2012). Understanding the effect of synthetic conditions on MA synthesis would enable the control of the mesoporosity features of MA.

In detail, the soft template synthesis pathway fundamentally relies on the use of an amphiphilic surfactant that acts as a structure-directing agent. The surfactant forms micelles in solution whereby the hydrophilic ends exist in contact with the solvent molecules, and the hydrophobic ends meet at the micelle center (Bleta et al., 2012). The added aluminum source such as aluminum isopropoxide will surround the outer surface of the micelle structure. After evaporation, the micelle groups condense together while the aluminum packs tighter against the micelle groups (Ghosh & Naskar, 2014). The template is removed via calcination before alumina was subsequently calcined to the desired phase transition.

There are three types of soft templates used for the synthesis of MA, classified as anionic, cationic, and non-ionic, depending on the charge of the amphiphilic component of the surfactant. Anionic template hydrolyses into an amphiphilic anion, and a cation (generally an alkaline metal or a quaternary ammonium ion). Some common examples include sodium dodecylbenzene sulphonate and long-chain carboxylic acids (often with sodium) (Pal & Bhaumik, 2013). The anionic template-assisted method is restricted to obtain MA with an ordered pore size smaller than 3.5 nm, which limits its applicability in catalysis.

In contrast, cationic template hydrolyses into a hydrophilic cation and an anion (often halide type). The templates in this class mostly belong to nitrogenous compounds such as amine salts and quaternary ammoniums, with one or more long-chain alkyl groups. Some common examples include quaternary ammonium salt C16TMABr (CTAB) and N-Dodecyl Pyridium chloride (Pal & Bhaumik, 2013). Contreras et al. (2015) successfully synthesized MA through this approach using $\text{Al}_2(\text{SO}_4)_3$, $(\text{NH}_4)\text{OH}$, and the cationic surfactant cetyl-trimethyl ammonium bromide (CTAB) or $(\text{CH}_3(\text{CH}_2)_{15}(\text{CH}_3)_3\text{NBr})$. The authors also investigate the effect of CTAB concentration on MA properties and noticed that the preparation using the lowest concentration of CTAB improved the thermal stability of MA.

Non-ionic templates are amphiphilic surfactants, which do not dissociate in solution in the same way as anionic and cationic templates. The most used non-ionic surfactants are composed of hydrophilic ethylene oxide chains and hydrophobic propylene oxide chains. A range of di-block copolymers (Tergitol, Igepal, and Triton) and tri-block copolymers (Pluronic P-123, F-127, L-64, and F-108) have been adopted as

the SDAs (Ghosh & Naskar, 2014). In this approach, when tri-block copolymer such as P-123 was added into the boehmite in acidic conditions, the hydrophilic polyethylene oxide (PEO) head groups of the surfactant can weakly interact with the surface hydroxyl groups of boehmite through hydrogen bonding while the hydrophobic polypropylene oxide (PPO) chains head away from the surface ((W. Wu, Wan, Chen, Zhu, & Zhang, 2015). Indeed, with P-123 assistance, the pre-formed boehmite nano crystallites work as the “building blocks” to form the mesostructures containing loosely stacked boehmite particles, resulting in MA structure with large pore sizes and pore volume. Recently, W. Yang, Li, Tian, Liu, and Liao (2020) managed to prepared MA through the non-ionic template using P-123 as a template, aluminum isopropoxide as an aluminum precursor and HNO₃ as an acid solution. The authors attained MA with larger surface area which also consists of ordered mesoporous structure.

Fulvio, Brosey, and Jaroniec (2010) proposed the mechanism for the synthesis of MA using the non-ionic template (block copolymer) as displayed in Figure 2.11; (1) dispersion of boehmite powder in acidic aqueous solution, (2) interaction of block copolymer with species formed during boehmite dispersion, (3) formation of polymer-alumina mesostructured composite, and (4) removal of polymer from for obtaining MA material. Indeed, the authors verified that the formation of MA in the presence of a triblock copolymer resulted in MA with large mesopores, large pore volume, high surface area, high crystallinity, greater acidity, and better thermal stability than the MA sample generated with soft template and without polymer template. In different works, Ray, You, Ahn, and Ahn (2007) compared the MA synthesis technique using anionic, cationic, and non-ionic surfactants with Al-tri-sec-butoxide and Al³⁺ in an organic solvent as aluminum precursors. The authors found that both cationic and non-ionic surfactants employment produced highly thermal stable MA while anionic surfactants resulted in a moderately stable MA phase. Indeed, several findings in literature stated that the presence of non-ionic surfactants as structure directing agents in MA synthesis led to excellent textural properties and high thermal stability (W. Wu, Wan, Zhu, & Zhang, 2016; W. Yang et al., 2020). Besides, Q. Liu, Wang, Wang, et al. (2008) strengthened that this enhancement could improve active site dispersion as well as increase the diffusion efficiency and mass transfer of reactant molecules when MA is employed as catalyst supports.

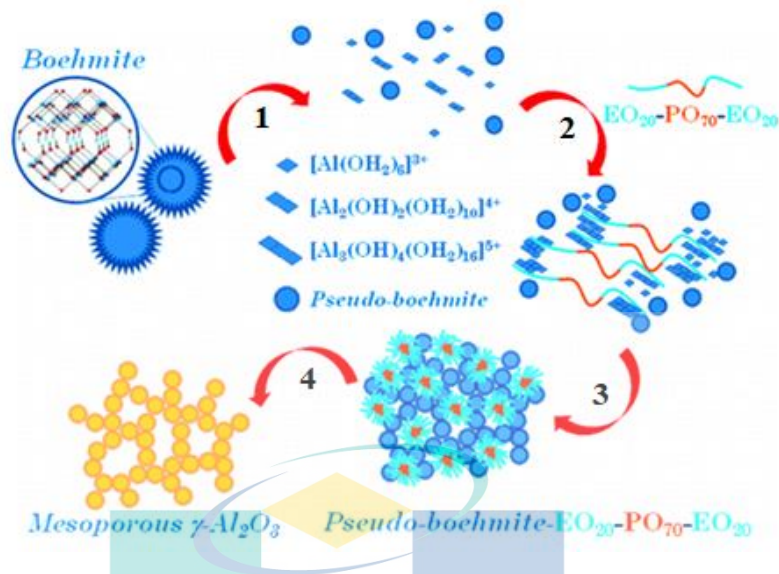


Figure 2.11 The mechanism for the formation of MA from boehmite using block copolymer.

Source : Fulvio et al. (2010)

Table 2.3 summarizes the previous application of MA as support in CO₂-CH₄ reforming. Xu et al. conducted several studies related to the combination of Ni-based catalysts with MA support in CO₂-CH₄ reforming. The authors initially investigated the catalytic properties and activity of ordered mesoporous NiO-Al₂O₃ composite oxides synthesized via an improved evaporation induced self-assembly (EISA) technique (Leilei Xu, Song, & Chou, 2011). High and stable catalytic activity (cf. Table 2.3) was attained in that work, owing to the higher number of “accessible” active Ni resulting from excellent Ni dispersion. Indeed, the confinement of active metal by mesoporous framework further inhibited Ni particles from sintering under severe reduction and reaction conditions. Similar findings had been achieved by the authors in the different experimental works related to MA employment (Leilei Xu et al., 2017; Leilei Xu, Zhao, Song, & Chou, 2012).

Different synthesis approach had been conducted by H. Arbag, Yasyerli, Yasyerli, Dogu, and Dogu (2013) in the preparation of MA. The authors examined the catalytic properties and performances of Ni supported over MA synthesised via sol-gel (SGA) and hydrothermal (MA) techniques in CO₂-CH₄ reforming. SGA possessed slightly lower surface area (cf. Table 2.3) as compared to MA resulted from the different morphology structure. The authors found that MA exhibited ordered mesopores structure while SGA consisted of pores with long range order (collection of alumina micro-grains). Reforming

activities revealed that Ni@SGA exhibited superior catalytic performance as compared with Ni@MA even though higher coke formation was recorded with this material (cf. Table 2.3). The authors also justified that this distinction was linked with the higher Lewis acidity of the SGA as compared to MA, and owing to better dispersion of Ni in MA.

Apart from that, the addition of active metal during MA synthesis had been carried out by several researchers to enhance catalyst attributes and performance (Tao et al., 2013; N. Wang et al., 2014). Fang et al. (2015) improvised the common evaporation induced self-assembly (EISA) method for preparing MA by introducing Ni precursor solution. Results revealed that the reforming activity and coke-resistance for this catalyst were significantly improved compared with the impregnation technique (cf. Table 2.3) accredited to the higher dispersion of smaller Ni⁰ active during the reduction of EISA catalyst. Indeed, the authors illustrated the comparison of coke formation on both types of catalysts as seen in Figure 2.12. The large Ni particles commonly formed after reduction on Ni/Al₂O₃-IMP which might aggregate during the high temperature reaction. Then, CH₄ molecules will dissociate around these large particles, and form a huge amount of carbon deposited. The carbon will encapsulate the Ni sites, hence, lowers the activity. On the other hand, on Ni-Al₂O₃-EISA, the ordered mesopores restrict the aggregation of the Ni particles even at high temperature, accredited to the stronger Ni-Al₂O₃ interaction. Thus, carbon that could encapsulate active Ni sites will be suppressed, resulting in higher activity.

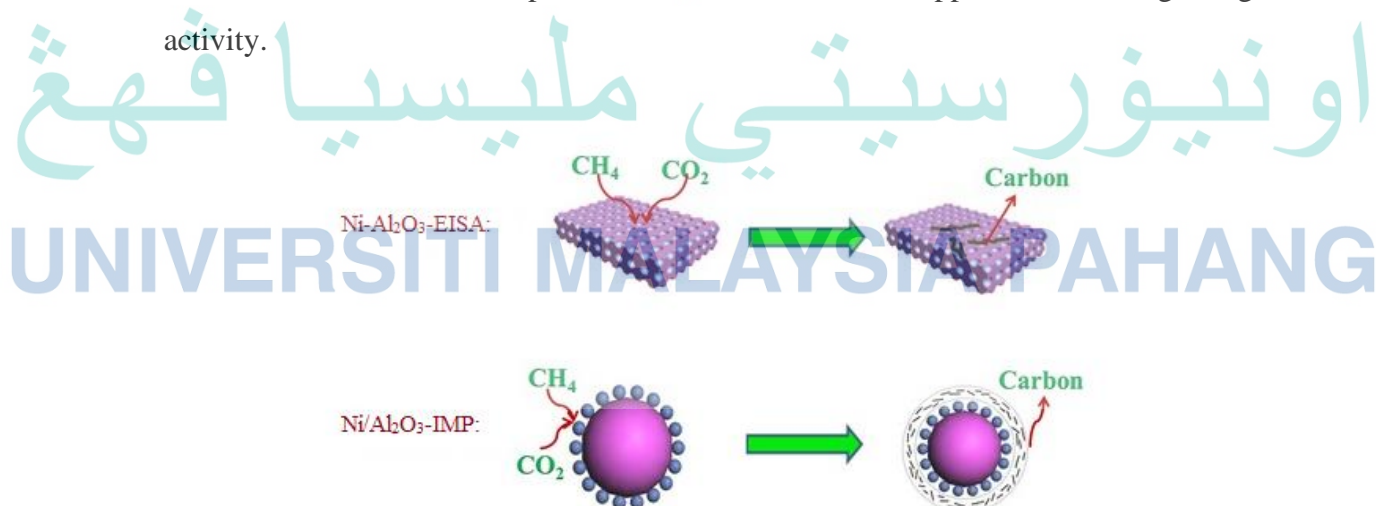


Figure 2.12 Schematic coke formation for CO₂-CH₄ reforming on the catalysts synthesised via EISA and impregnation (IMP).

Source : Fang et al. (2015)

Table 2.3 Bibliographic listing of CO₂-CH₄ reforming with mesoporous alumina support.

Catalyst	Method	T (K)	GHSV (L g _{cat} ⁻¹ h ⁻¹)	CH ₄ /CO ₂ ratio	Conversions (%)		H ₂ /CO ratio	Yield (%)		D _d (%)	Carbon formation	Surface area (m ² g ⁻¹)	Refs.
					CH ₄	CO ₂		H ₂	CO				
C5N5 N10	Sol- gel	1023	24.0	1:1	81.7-79.6	85.2-83.7	0.89-0.88	n.a.	2.57	n.a.	227.0	X. Huang et al. (2017)	
					81.4-77.7	84.4-81.8	0.89-0.87						
		773-1073	15.0	1:1	30.6-94.7	27.6-95.2	0.42-0.98	n.a.					
					33.9-95.3	31.2-96.0	0.40-1.01						
OMA-CoNi OMA-CoNiMg OMA-CoNiCa	EISA	1023	7.5-45.0	1:1	90.8-75.9	90.0-85.9	0.91-0.90	n.a.	212.0	Leilei Xu et al. (2017)			
					91.8-78.6	96.5-90.9	0.91-0.90						
		973	15.0	1:1	92.5-81.3	95.6-89.8	0.91-0.93	n.a.	3.61				
					77.5-74.7	82.9-81.7	0.83-0.81						
Ni-Al ₂ O ₃	EISA	1073	n.a.	1:1	80.0-78.7	86.8-84.3	0.86-0.87	n.a.	1.63	n.a.	188.0	Fang et al. (2015)	
					82.5-80.5	87.7-85.1	0.87-0.86						
Ni/Al ₂ O ₃	Impregnation	823-1073	n.a.	1:1	92.4-87.8	90.2-88.6	n.a.	44.6	n.a.	56.0			
					71.5-39.6	81.8-54.0							
NiAl NiCeAl	One-pot EISA	973	n.a.	1:1	21.9-83.6	24.6-79.3	0.68-0.98	n.a.	22.7	n.a.	173.0	N. Wang et al. (2014)	
					29.9-95.3	30.6-90.3	0.70-0.99						
					55.0-42.5	81.2-67.6	n.a.						
MA	EISA										266.0		
						n.a.					256.9		
Ni/MA	Incipient wetness impregnation	973	n.a.	1:1	60.3-56.9	75.7-72.8	0.89-0.88	n.a.	5.64	n.a.	219.0	Tao et al. (2013)	
NiMA	EISA				61.4-60.4	77.2-76.1	0.95-0.93		1.63		305.1		

Table 2.3 Continued

Catalyst	Method	T (K)	GHSV (L g _{cat} ⁻¹ h ⁻¹)	CH ₄ /CO ₂ ratio	Conversions (%)		H ₂ /CO ratio	Yield (%)		D _d (%)	Carbon formation	Surface area (m ² g ⁻¹)	Refs.
					CH ₄	CO ₂		H ₂	CO				
SGA	Sol-gel											191.5	
MA	Hydrothermal					n.a.						215.6	
Ni@SGA					34.9-37.6	49.2-46.3				-7.73	>80.0	159.3	
Mg@Ni@SGA					36.3-32.6	51.2-44.9				10.2	n.a.	152.5	H. Arbag et
W@Ni@SGA	Impregnation	873	36	1:1	28.0-28.7	44.2-44.5				-2.50	n.a.	199.5	al. (2013)
Ni@MA					24.9-24.7	38.8-40.0				0.80	<20.0	156.6	
Ni-MA	One-pot hydrothermal				35.6-30.9	47.5-42.1				13.2	n.a.	228.6	
OMA	EISA					n.a.						225.0	
Ni/OMA	Incipient wetness impregnation	873-1073	15.0	1:1	20.8-93.8	20.4-91.9	0.58-0.86			n.a.		212.2-157.9	Leilei Xu et al. (2012)
Ni/γ-Al ₂ O ₃	Wet impregnation				70.1-40.1	79.8-51.8	0.59			42.8		117.0	Newnham, Mantri, Amin, Tardio, and Bhargava (2012)
Ni-MAI	Coprecipitation	1073	52.0	1:1	62.4-51.0	74.8-65.9	0.78		n.a.		n.a.	315.0	
Ni/MA		773-1023			5.8-89.8	8.6-86.2							
Ni/MgMA	EISA	1023	n.a.	1:1	7.1-91.9	10.9-87.8			n.a.			177.0	Shen et al. (2011)
		1023			88.8-79.1					10.9	n.a.	169.0	
		923-1073			92.1-64.8					29.6	n.a.		
OM-NiAl	EISA	973	15.0	1:1	62.8-95.6	65.2-93.4	0.78-0.87			n.a.			
		973			77.2-76.9	80.7-79.0	0.84-0.82		n.a.	0.39	n.a.	188.8	Leilei Xu et al. (2011)
		1023	15.0-60.6		91.5-71.5	91.4-77.1	0.86-0.82			n.a.			

n.a. = not available, Deactivation degree, $D_d(\%) = [1 - (\text{Final CH}_4 \text{ conversion} / \text{Initial CH}_4 \text{ conversion})] \times 100$

2.5.5 Catalyst Promoter

The introduction of second active metal as catalyst promoter is a very promising approach in reforming reaction since it could significantly increase the oxygen mobility, enhance metal dispersion and reduce the acidity of catalyst (Foo et al., 2011b). This improvement could lead to the enhancement in catalytic activity and stability. In fact, the catalyst deactivation could be prevented owing to the improvement of carbon resistance (Foo, 2012). Rare earth metal oxides from lanthanide groups such as cerium, lanthanum, yttrium, and samarium gained considerable attention in catalytic reforming. The previous investigation on the impact of these promoter employment toward catalytic performance will be explained in the subsequent subsections.

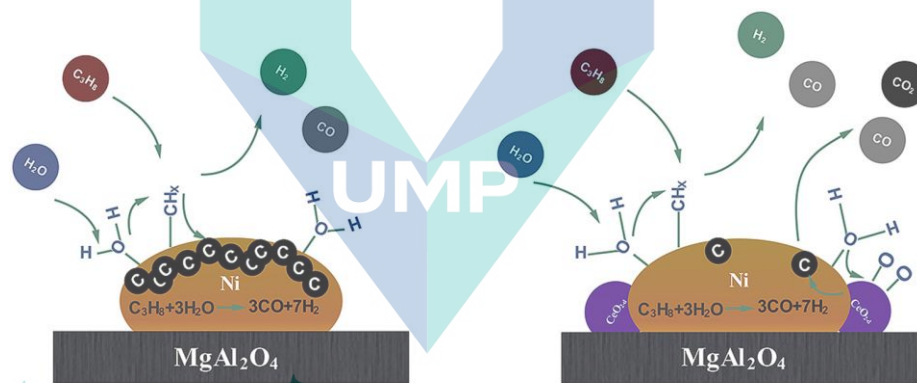
2.5.5.1 Cerium

One of the common promoters employed in CO₂-CH₄ reforming is cerium (Ce), owing to its superior attributes such as great Ce⁴⁺/Ce³⁺ reduction-oxidation potential which leads to the storage and the release of a large amount of oxygen, hence, greatly influence the catalytic performance (Tang, Xu, & Fan, 2014). According to le Saché et al. (2018), this attribute assists the removal of carbon deposited on the catalyst surface via promoting the oxidation and/or gasification of the carbon deposited. Movasati, Alavi, and Mazloom (2017) investigated the impact of Ce promoter incorporation over Ni/ZnAl₂O₄ catalysts prepared via co-precipitation technique. Results revealed that the incorporation of Ce promoter improved the particle dispersion and strengthened the Ni-support interaction which led to high catalytic activity along with lower carbon deposited. The authors also agreed that the strong Ce-Ni interaction through Ce-Ni solid solution formation as well as the “spacer” effect initiated by Ce incorporation suppressed the agglomeration of Ni during calcination. However, the authors noticed that the presence of excess Ce promoter (>7wt%) resulted in the aggregation of CeO₂ on the catalyst surface.

The positive impact of Ce promoter incorporation towards catalytic performance, stability, and carbon suppression was also experienced by Khajenoori, Rezaei, and Meshkani (2014) during the evaluation of Ni/ MgO catalyst in CO₂-CH₄ reforming. The authors also explained that the great carbon suppression after Ce addition accredited to high oxygen storage capacity owned by CeO₂. The CO₂-TPD analysis attained by Tang

et al. (2014) revealed that the addition of Ce promoter increased the number of peak for Lewis basic site. Therefore, the authors inferred that the addition of Ce promoter (>5wt%) increased the basic strength over the catalyst surface, thereby promoting the adsorption of CO₂ and the carbon resistance.

Cerium also was widely employed in other catalytic fields due to its great attributes (Bacariza et al., 2018; X. Yang, Da, Yu, & Wang, 2016). Azizzadeh Fard, Arvaneh, Alavi, Bazayari, and Valaei (2019) illustrated the formation of carbon on Ce-promoted Ni/MgAl₂O₄ and unpromoted catalyst during steam reforming process as seen in Figure 2.13. The authors explained that the incorporation of Ce promoter allows oxygen atoms to flow freely on the surface of Ni/MgAl₂O₄ catalyst on which accumulated carbon as an oxygen acceptor utilizes oxygen, thus gasifying into CO and CO₂. Indeed, the appearance of Ce improves the Ni dispersion and inhibits Ni sintering, thus minimizing the accumulation of carbon on Ni/MgAl₂O₄ surface.



Loading of the Ce promoter in Ni/MgAl₂O₄ catalyst introduces a low amount of coke deposition on the catalyst surface due to not forming a solid solution and fast carbon gasification.

Figure 2.13 Illustration represents the effect of Ce promoter addition.

Source : Azizzadeh Fard et al. (2019)

2.5.5.2 Lanthanum

Aside from cerium, the rare earth oxide lanthanum (La) also has received a compelling reputation as a catalyst promoter accredited to its strong Lewis basicity that enhanced the ability of the catalyst to chemisorb CO₂ and thus, reduced carbon formation through Boudouard reaction. Dahdah et al. (2017) examined the impact of La incorporation over Ni_xMg_{6-x}Al₂ catalysts in CO₂-CH₄ reforming. The authors stated that

the employment of La strengthened Ni oxide interaction inside the solid matrix leading to better dispersion and accessible active sites. As a result, the catalytic performance was significantly enhanced and stable within 14 h on stream. Besides, the authors also noticed that La_2O_3 played a crucial role in providing the additional basic sites for adsorbing larger quantities of CO_2 and thus eliminating the carbon deposited. This finding also has been experienced by several researchers resulting from the incorporation of La promoter during the evaluation of catalyst for CO_2 - CH_4 reforming (Abou Rached et al., 2018; H. Liu et al., 2016).

Apart from the abovementioned properties, the La promoter is also capable of suppressing carbon deposited attributed to the benefit of lanthanum oxycarbonate ($\text{La}_2\text{O}_2\text{CO}_3$) formation. This intermediate compound formed from the reaction between La_2O_3 and CO_2 will supply oxygen that can further react with the deposited carbon (Verykios, 2003). H. Liu, Hadjltaief, Benzina, Gálvez, and Da Costa (2019) reached the similar conclusion after noticed the improvement in catalytic stability and the decrement in the amount of carbon deposited with the incorporation of La-promoter in their works. In another study, Tran et al. (2020) proved the appearance of lanthanum oxycarbonate with the employment of La promoter after detected doublet peaks of La $3d_{3/2}$ and La $3d_{5/2}$ at a binding energy of 851.9 eV and 835.1 eV, respectively. Indeed, the transitional phase between La_2O_3 and $\text{La}_2\text{O}_2\text{CO}_3$ with the presence of CO_2 was elucidated by the authors as seen in Figure 2.14.

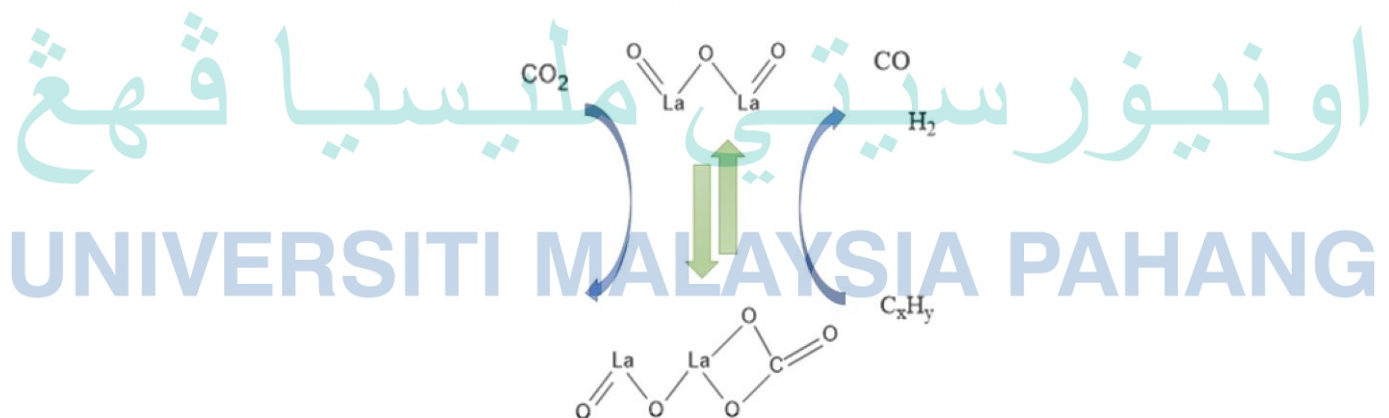


Figure 2.14 La_2O_3 redox cycle for surface carbon removal during CO_2 - CH_4 reforming.

Source : Tran et al. (2020)

In different reforming works, Shafiqah et al. (2019) and Bahari et al. (2016) reported that the catalytic activity was improved and achieved optimum performance at

3wt% La loading before drop beyond this value. Both authors inferred that the decrement of reforming activity beyond 3wt% La owes to the limited active metal dispersion in high promoter loading.

2.5.5.3 Yttrium

Yttrium also had been considered as a promising dopant in reforming since a lot of positive feedback had been reported in the literature linked with this metal oxide employment (Daneshmand-Jahromi, Rahimpour, Meshksar, & Hafizi, 2017). However, there are fewer literature reports regarding yttrium employment as a catalyst promoter in CO₂-CH₄ reforming. Świrk et al. (2019) evaluated the effect of yttrium promoter loading (4, 8, and 12 wt%) over Ni/KIT-6 catalyst synthesised by incipient impregnation. In this work, the authors noticed the improvement in Ni dispersion and catalyst reducibility with yttrium addition event though the Ni crystallite size was increased. Indeed, superior performance was obtained for the catalyst consisting 8wt% of yttrium. J. F. Li, Xia, Au, and Liu (2014) also investigated the influence of Y₂O₃ promoter loading (0-9wt%) on catalytic activity of Ni/SBA-15. The author explained that the improvement in reforming activity and carbon suppression is accredited to the reduction of catalyst surface acidity, enhancement of active metal dispersion, and improvement of oxygen vacancies. But in this work, the superior performance along with low carbon deposited was obtained for catalyst consisting 9wt% of yttrium, owing to the highest in surface area as well as in Ni⁰ dispersion. The author also explained that the formation of graphitic layers was greatly suppressed at 9wt% yttrium loading since the process of carbon deposition and gasification reaches equilibrium (cf. Figure 2.15)

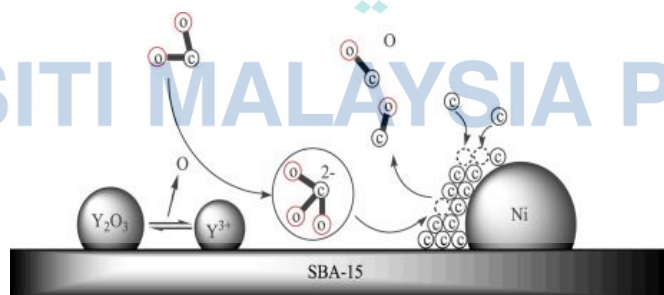


Figure 2.15 Scheme of carbon deposition and carbon removal over Ni-based catalysts.

Source : J. F. Li et al. (2014)

2.5.5.4 Samarium

In literature, Samarium has the least number of applications as a promoter in CO₂-CH₄ reforming as compared to cerium, lanthanum, and yttrium, despite being also classified as one of the rare-earth and lanthanide elements. Taherian, Yousefpour, Tajally, and Khoshandam (2017c) initiated the employment of Sm as a promoter for Ni/SBA-15 for CO₂-CH₄ reforming application. In that work, the authors reported that the incorporation of Sm₂O₃ promoter into the Ni/SBA-15 catalyst considerably improved catalytic performance and exhibited stable catalytic performance for 12 h reaction as compared to unpromoted catalyst. In addition, the authors explained that stable catalytic activity was attained due to the formation of tip type nanotube carbon, induced by Sm addition (cf. Figure 2.16). According to Djinović, Osojnik Črnivec, Erjavec, and Pintar (2012), the tip type nanotube carbon typically leads to weakened coke coverage on Ni active sites. As a result, Ni active sites are still in contact with the gas flow and are not deactivated.

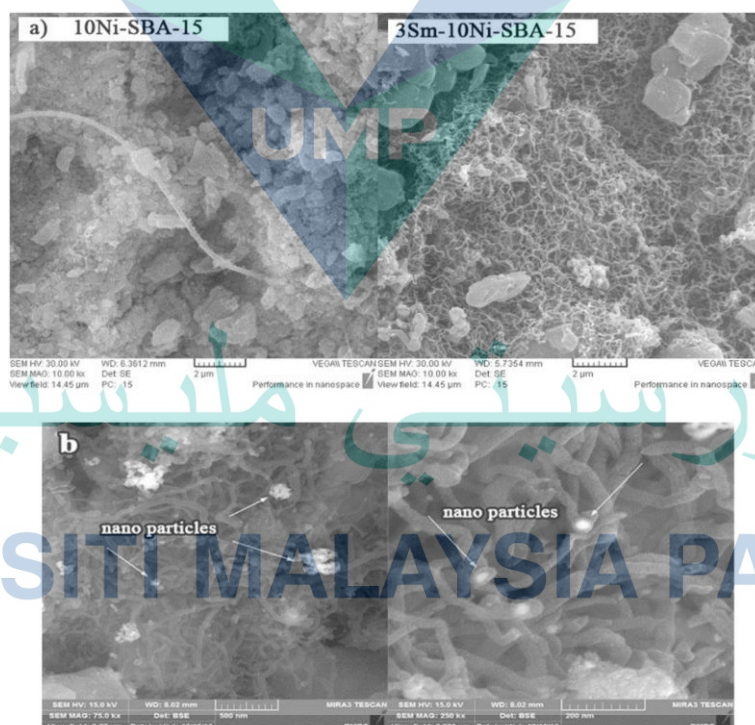


Figure 2.16 a) SEM images of 10Ni-SBA-15 and 3Sm-10Ni-SBA-15 catalysts and b) FESEM images of the 3Sm-10Ni-SBA-15 catalyst after 12 h of the reaction.

Source : Taherian et al. (2017c)

In another work, the authors compared the effect of Sm promoter addition over Ni and Co/SBA-15 synthesised via a two-solvent impregnation technique (Taherian et

al., 2017a). Prior to CO₂-CH₄ reforming, the authors investigated the effect of Sm promoter loading (0.5, 1, and 1.5wt%) and selected 1% wt of Sm as the best values owing to the smallest NiO and Co₃O₄ particles size and the highest dispersion. Reforming evaluation revealed that Sm significantly improved Ni/SBA-15 performance accredited to the smaller NiO particles sizes and excellent active NiO dispersion. However, a contradictory performance was experienced by the authors after incorporating Sm promoter over Co/SBA-15 due to the Co oxidation to the inactive phase and sintering of Co particles.

2.6 Catalyst Deactivation

Catalyst deactivation is the loss of catalytic activity or selectivity with time-on-stream. The deactivation process of catalysts could be occurred simultaneously with the main reaction because of its chemical and physical nature (Foo, 2012). Although the deactivation of catalysts is inevitable, this process could be decelerated and some of its effects might be avoided (Bartholomew, 2001). According to Argyle and Bartholomew (2015), the deactivation mechanisms of solid catalysts can be divided into six categories. Table 2.4 provides a summary of the major mechanisms for catalyst deactivation. The deactivation of catalysts resulted from fouling and sintering are further described in detail in the following sections since both mechanisms are the most common and relevant factors causing catalytic deactivation in CO₂-CH₄ reforming.

Table 2.4 Mechanisms of catalyst deactivation

Mechanism	Type	Description
Poisoning	Chemical	Strong chemisorption of species on catalytic sites resulting in blocked sites
Fouling	Mechanical	Physical deposition of species from fluid phase onto the surface and pores of catalyst
Thermal degradation (Sintering)	Thermal	Thermally induced loss of catalytic surface area, support area and active phase-support reactions
Vapor formation	Chemical	Reaction of gas with catalyst phase to produce volatile compounds
Vapor–solid and solid–solid reactions	Chemical	Reaction of vapor, support, or promoter with catalytic phase to produce inactive phases
Attrition/crushing	Mechanical	Loss of catalytic material due to abrasion and the loss of internal surface area due to mechanical-induced crushing of catalyst particles

Source: Argyle and Bartholomew (2015)

2.6.1 Fouling Phenomena

According to Bartholomew (2001), fouling is the physical deposition of residues (referred to as coke or carbon) onto the catalyst surface resulting in catalytic loss. Commonly, side reactions that occur during catalytic reactions especially involving hydrocarbons reactions may lead to coke formation (Forzatti & Lietti, 1999). Coke deposition physically covers the active surface of catalysts and may result in the disintegration of catalyst particles, loss of adsorption sites for reactants, and plugging of the reactor voids. Rostrup-Nielsen (1997) reported that carbon or coke species could be divided into three different kinds; encapsulated carbon (formed by slow polymerization of C_nH_m on Ni surface at temperatures lower than 773 K), filamentous or whisker-like carbon (produced by the diffusion of C into Ni crystals, detachment of Ni from the support and growth of whiskers with Ni on top) and pyrolytic-type carbon (generated by cracking of C_nH_m species at a temperature above 873 K). Basically, the formation of carbon could be minimized to a certain limit by using an appropriate combination of reaction conditions with an optimal catalyst composition (Bartholomew, 2001; Foo, 2012). Thus, thermodynamic analysis was carried out before the reaction for determining optimum reaction conditions.

In the case of CO_2 - CH_4 reforming, fouling, or well known as coking, has become the main criterion in designing of catalyst. According to the thermodynamic equilibrium plots of CO_2 - CH_4 reforming from literature (cf. Figure 2.17), the maximum amount of carbon deposited is mostly generated in the temperature range of 557-700 °C, via the decomposition of methane (>557 °C) and Boudouard reaction (<700 °C). A detailed explanation about both side reactions are discussed in thermodynamic study (Subchapter 4.3). Arora and Prasad (2016) reported that the appropriate reaction temperature for minimizing carbon formation is within 916-1300 K under atmospheric pressure conditions.

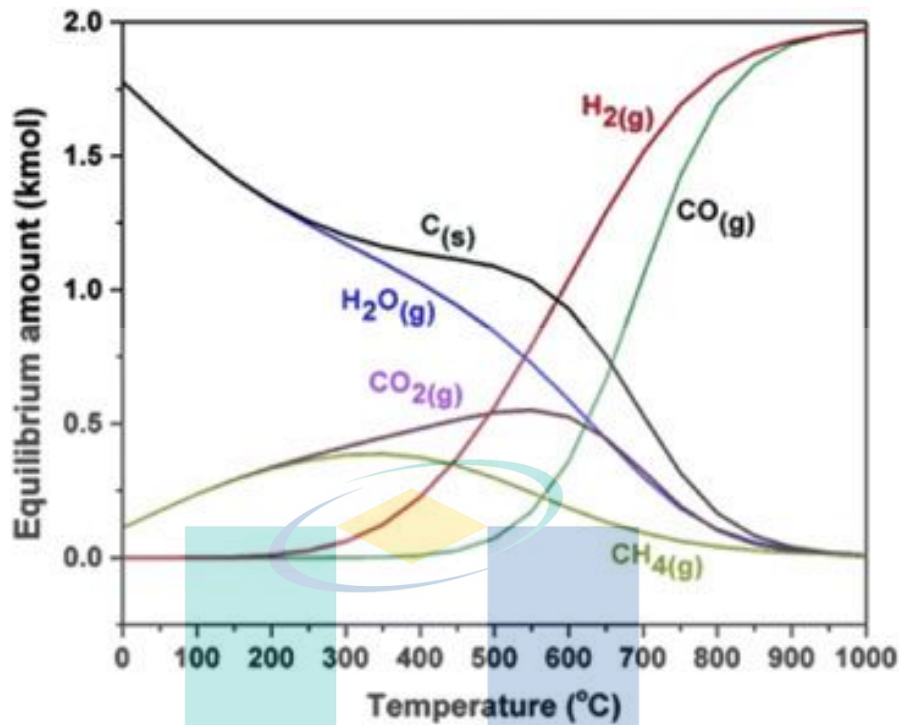


Figure 2.17 Thermodynamic equilibrium profiles for $\text{CO}_2\text{-CH}_4$ reforming at pressure of 1 atm, temperature range from 0 to 1000 °C and at CO_2/CH_4 feed ratio = 1

Source : Abasaed et al. (2015)

The carbon deposited during $\text{CO}_2\text{-CH}_4$ reforming are existing in different types, structures and attributes. Some types of carbon deposited could lower the catalyst activity by blocking the active sites, and some are not since they might be easily eliminated through gasification. The deposition of carbon on the catalyst surface which covers accessible active metal sites and block pore structure of support was illustrated by Argyle and Bartholomew (2015) as depicted in Figure 2.18. Arora and Prasad (2016) also elucidated the mechanism of different types of carbon deposited on catalyst surface during $\text{CO}_2\text{-CH}_4$ reforming as seen in Figure 2.19 along with the details of carbon formed in Table 2.5. Initially, the dissociation of CO and CH_4 on catalyst surface resulted in the formation of adsorbed atomic carbon, C_α . From these points, the C_α will further react to generate polymeric amorphous films, C_β which will be utilized to form C_γ , C_ν , and C_c based on the temperature changes (Argyle & Bartholomew, 2015; Arora & Prasad, 2016).

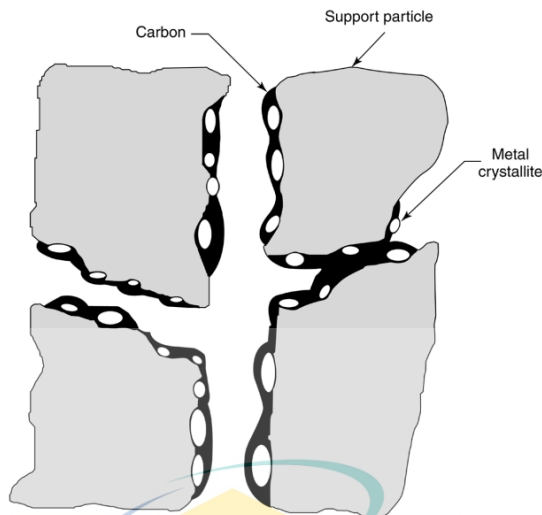


Figure 2.18 The deposition of carbon resulted in encapsulation of active metal sites and pore plugging of a supported metal catalyst.

Source : Argyle and Bartholomew (2015)

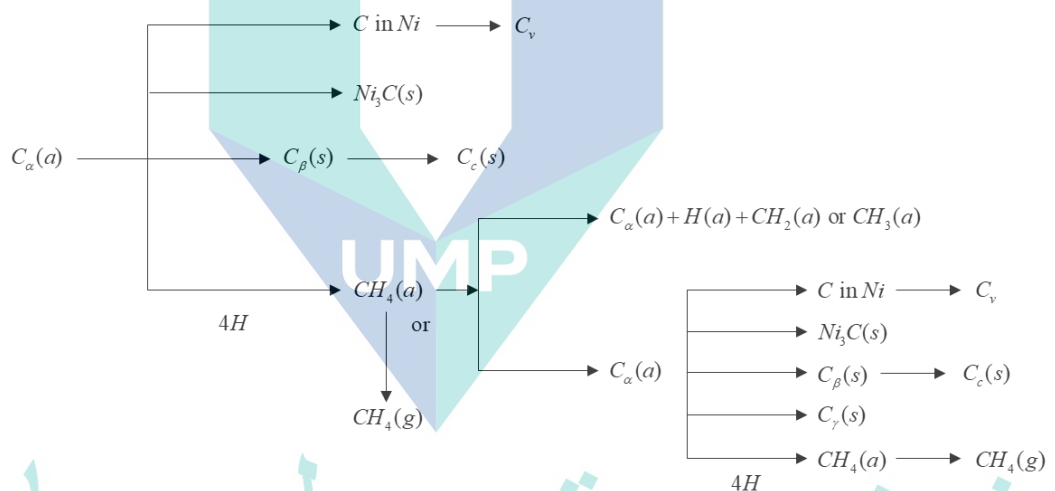


Figure 2.19 The mechanism of carbon formation in CO_2 - CH_4 reforming.

Source : Arora and Prasad (2016)

Table 2.5 Details of carbon formed in CO_2 - CH_4 reforming.

Types of carbon	Designation	Formation temperature (K)
Adsorbed. atomic carbon (surface carbide)	C_α	473-673
Polymers, amorphous films	C_β	523-773
Ni carbide (bulk)	C_γ	423-523
Vermicular filaments/ whiskers	C_v	573-1273
Graphite (crystalline) platelets film	C_c	773-823

Source :Arora and Prasad (2016)

The authors also claimed that the carbon types that could encapsulate the active metal site on catalyst surface during CO₂-CH₄ reforming are C_β at reforming temperature less than 573-673 K and C_c at temperature above 923 K (Arora & Prasad, 2016). On the other hand, the accumulation of carbidic carbon on catalyst surface may lead to the deactivation of active metal sites and thus could affect the catalytic performance in CO₂-CH₄ reforming.

2.6.2 Sintering Phenomena

Bartholomew (2001) reported that the loss of active surface area due to crystallite growth of the catalytic phase and the loss of support area due to support or pore collapse is identified as the sintering of catalyst. According to the literature, the mechanism of sintering was divided into two categories (cf. Fig. Figure 2.20); i) atomic migration, the migration of metal atom from crystallite to another crystallite through either surface or gas phase by eliminating small crystallites and then combining with the larger ones; ii) crystallite migration, the migration of the crystallites over the surface, followed by collision and combination of two crystallites (Bartholomew, 2001; Lassi, 2003).

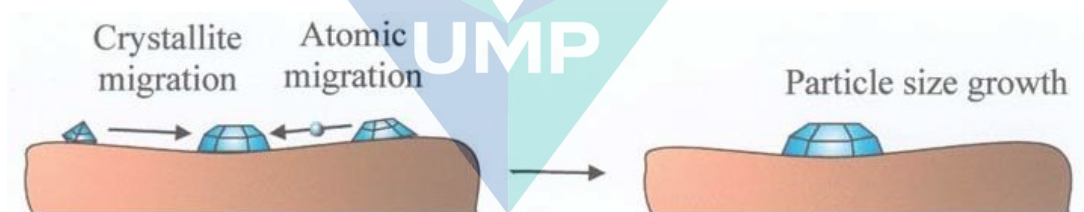


Figure 2.20 The illustration of atomic migration and crystallite migration models.

Source : Lassi (2003)

Typically, the sintering of catalyst might happen at all stages in the life cycle of catalyst such as calcination, reduction, reaction, and regeneration. According to Foo (2012), the prolonged exposure of the catalyst to high temperatures is the main cause of sintering. In fact, sintering commonly occurs at a high reaction temperature about >773 K and could be enhanced by the presence of water vapor (Bartholomew, 2001). Thus, the sintering effect could be minimized or avoided by selecting a suitable temperature for reaction. Moulijn, van Diepen, and Kapteijn (2001) suggested that reaction temperature should following the Hüttig and Tamman temperatures which T did not exceed 0.3 to 0.5 times of the melting point of catalyst. Apart from that, the sintering of catalyst also could

be reduced by the presence of strong metal-support interaction (Foo, 2012). The effective suppression of sintering had been proved in a lot of previous works. Rahbar Shamskar et al. (2017) reported that the successful suppression of Ni sintering was attained after incorporating Ce and La promoters over Ni/Al₂O₃ catalysts during CO₂-CH₄ reforming. A similar improvement was observed by Ning et al. (2019) during the addition of Ce-promoter on Pt-M/ZSM-22 catalyst. The author also explained that the strong bond of Pt-O-Ce created after Ce-addition is responsible for this high sintering resistance. Hence, appropriate promoters that may increase the stability of catalyst support should be selected for minimizing the sintering of catalyst.

Apart from fouling and sintering issues, the deactivation of Co-based catalysts (monometallic case) could be initiated by the Co oxidation (Budiman et al., 2012; Nagaoka, Takanabe, & Aika, 2003; Takanabe et al., 2005). Thus, the optimization of the Co loading in the catalyst was regarded as the solution for minimizing this occurrence since it will affect the catalytic performance. Ruckenstein and Wang (2002) examined the relationship between Co loading (2, 6, 9, 12, and 20wt.%) with the carbon deposition and catalytic deactivation. The Co loading about 6, 9, and 12wt.% recorded great conversion of CH₄ at a reaction temperature of 900°C, which is above 90%. In addition, the authors noticed that catalyst with high Co loadings (>12 wt.%) was deactivated due to high coke deposition since the rate of carbon formation via CH₄ cracking is superior to CO₂ activation. On the other hand, at low contents (about 2wt.%), the rate of oxygen species generation from CO₂ activation is too fast to oxidize the generated carbon, thus causing the generated oxygen species to oxidize the Co-active sites and form inactive spinel such as Co₂AlO₄ and/or CoAl₂O₄. The detailed correlation between carbon deposition and deactivation as a function of Co loading was illustrated by the authors and is depicted in Figure 2.21

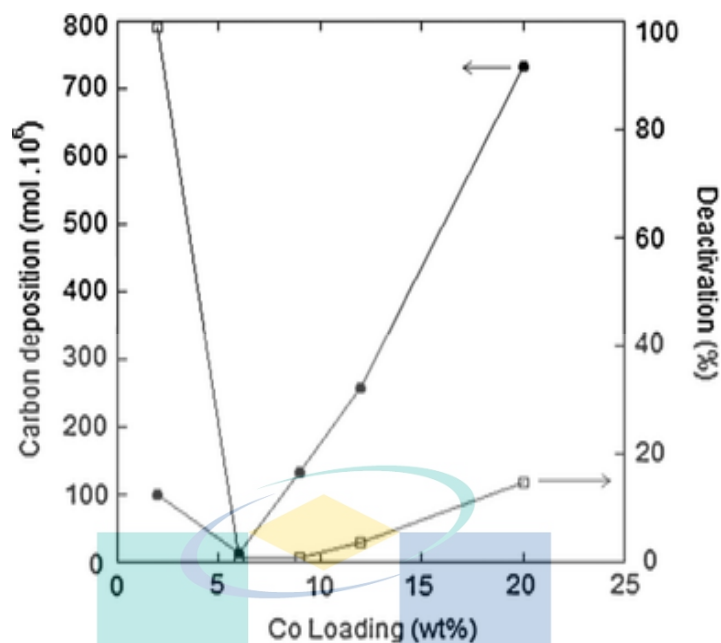


Figure 2.21 The correlation between carbon deposition and deactivation as a function of Co loading.

Source : Ruckenstein and Wang (2002)

On the other hand, for bimetallic Co catalysts, the main factor that could influence the occurrence of Co-Ni deactivation is the Co:Ni ratio. In previous work related to CO₂-CH₄ reforming, San-José-Alonso, Juan-Juan, Illán-Gómez, and Román-Martínez (2009) noticed that the probability for deactivation occurring during the employment of Co-Ni is generally low for the catalyst with higher amount of cobalt (Co:Ni = 8:1). Whilst, a significant deactivation was experienced for bimetallic Ni-Co with excess amount of Ni (Co:Ni = 1:8), as revealed in Fig. 6. In fact, the author observed the significant amount of carbon deposited on the bimetallic with a higher amount of cobalt after 6 h reaction as compared to Ni-Co catalyst (Co:Ni = 1:8), which is almost similar to the amount of carbon deposited recorded by Co monometallic catalyst. From this work, the authors clarified that bimetallic Co-Ni catalysts with the highest Co loading, are the most active and stable for CO₂-CH₄ reforming. Moreover, the generated carbon on this catalyst is non-deactivating carbon, which is not affecting the activity of the catalyst. However, this result contradicted with the finding attained by Nagaoka, Takanabe, and Aika (2004) which showed that there is a significant amount of carbon deposited with the rise in Ni loading in Co-Ni bimetallic catalyst.

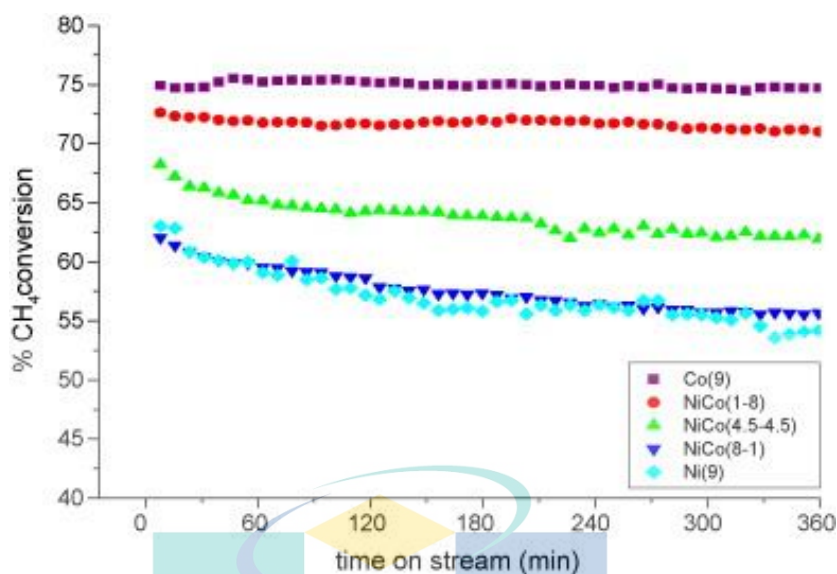


Figure 2.22 CH₄ conversion versus time on stream for different Co:Ni ratio.

Source : San-José-Alonso et al. (2009)

2.7 Research Gaps

Based on the literature review, the following knowledge gaps have been identified:

- i. Preparation of MA support using the SAHA approach and combined with Co incipient impregnation has not been studied for CO₂-CH₄ reforming.
- ii. The catalytic performance of the Co/MA catalyst has not been reported in the literature for CO₂-CH₄ reforming.
- iii. The influence of lanthanide promoters such as La₂O₃, Sm₃O₄, Y₂O₃, and CeO₂ on Co/MA catalysts towards CO₂-CH₄ reforming performance has not been reported in the previous study.

2.8 Concluding Remarks

The outcome obtained from this chapter is that syngas was considered as a potential energy for fossil fuel replacement. Among all synthesis routes aforementioned in this chapter, CO₂-CH₄ reforming appears as the promising approach for syngas production since it converted two major greenhouse gas, CO₂ and CH₄, into a desired H₂/CO ratio for the FTS or downstream processing. The effect of the operating condition such as pressure, temperature, and feed composition on CO₂-CH₄ reforming activity and carbon formation was reviewed since all these parameters play a crucial role in optimizing catalytic activity. Besides, many attempts have been conducted in designing

the best catalyst which could provide high performance as well as suppress carbon deposition. In the catalyst review part, Ni-based catalysts are frequently used in dry reforming reaction because of their cost-effectively and high availability. However, Ni-based catalyst can be deteriorated due to deposited carbon and sintering, which is a severe problem in the CO₂-CH₄ reforming reaction. Therefore, Co is suggested as a prospective active site for catalyst to replace Ni owing to its excellent stability and carbon resistance. Apart from that, a lot of efforts such as the employment of mesoporous support and rare-earth promoters have been implemented in previous studies to improve catalytic performance. The use of mesoporous support capable of improving the dispersion and increasing the accessibility to active sites, attributed to its large specific surface areas, controllable pore sizes, and high thermal stability. In fact, the confinement effect of mesoporous support could inhibit the metal sintering and hence resist carbon deposition. MA was selected since the employment of this support in CO₂-CH₄ reforming is less as compared to SBA-15 though both materials possessed almost similar advantages. Based upon the literature aforementioned before, the employment of lanthanide metals as the promoter was found to be able to enhance catalytic performance and stability due to the basic property and active metal-support interaction. Besides, greater oxygen capacity possessed by those metals is capable of eliminating the deposited carbon generated through the reforming reaction. Thus, in this work, La, Ce, Y, and Sm were selected as promoter candidates for the Co/MA catalyst. Based on the current state of reforming research, this work will establish the first study with a combination of rare-earth promoters (La, Ce, Y, and Sm) and Co/MA catalyst for syngas generation by CO₂-CH₄ reforming. For Co metal loading, the 10 wt% value was selected since higher value could lead to deactivation while lower value will affect the catalytic performance.

UNIVERSITI MALAYSIA PAHANG

CHAPTER 3

METHODOLOGY

3.1 Introduction

This chapter describes the detailed information on all chemicals, gases, and equipment involved in the synthesis, characterization, and evaluation of catalysts for CO₂-CH₄ reforming including their purity value and supplier's information. The comprehensive procedures for preparing catalysts, characterizing, and conducting reforming reactions are also explained in detail. The preliminary experiments including blank tests and the measurement of mass and heat transport limitations for determining suitable reaction conditions for catalytic tests are also reviewed in this chapter.

3.2 Materials and Equipment

3.2.1 Chemical and Gases

The purified chemicals used in this study are listed in Table 3.1 with detailed purity and application. Aluminum isopropoxide or known as aluminum triisopropylate Al[OCH(CH₃)₂]₃ and Pluronic P123: EO₂₀PO₇₀EO₂₀ used in the support preparation were purchased from Sigma-Aldrich (Kuala Lumpur, Malaysia). In addition, metal nitrates employed as metallic and promoter precursors during catalyst synthesis were also supplied by Sigma-Aldrich (Kuala Lumpur, Malaysia). The synthesis of support and catalysts throughout this work consumed absolute ethanol sourced from VWR Chemicals.

Table 3.1 List of used chemicals

Chemical	Formula	Purity/ Concentration (%)	Application
Aluminum isopropoxide	Al[OCH(CH ₃) ₂] ₃	≥98	Aluminum precursor
Poly(ethylene glycol)-block poly(propylene glycol)-block-poly(ethylene glycol)/Pluronic P123	EO ₂₀ PO ₇₀ EO ₂₀	PEG, 30 wt.	Support preparation
Hydrochloric acid	HCL	37 wt.	Support preparation
Cobalt (II) nitrate hexahydrate	Co(NO ₃) ₂ ·6H ₂ O	99.9	Metallic precursor
Cerium (III) nitrate hexahydrate	Ce(NO ₃) ₃ ·6H ₂ O	99.9	Promoter precursor
Lanthanum (III) nitrate hexahydrate	La(NO ₃) ₃ ·6H ₂ O	99.9	Promoter precursor
Yttrium (III) nitrate hexahydrate	Y(NO ₃) ₃ ·6H ₂ O	99.9	Promoter precursor
Samarium (III) nitrate hexahydrate	Sm(NO ₃) ₃ ·6H ₂ O	99.9	Promoter precursor
Ethanol	C ₂ H ₅ OH	99.9	Support and catalysts preparation
Drierite	CaSO ₄	98.9	Moisture removal

Table 3.2 provides the list of gases utilized in this study together with their purities and the applications. All cylinder gases listed in Table 3.2 were purchased from Air Products (Singapore).

Table 3.2 List of consumed gases

Gas	Formula	Purity (%)	Application
Carbon dioxide	CO ₂	99.5	Reactant
Methane	CH ₄	99.5	Reactant
Hydrogen	H ₂	99.9	Catalyst reduction
Nitrogen	N ₂	99.9	Diluent for CO ₂ -CH ₄ reforming reaction and carrier gas for H ₂ -chemisorption
Helium	He	99.9	Carrier gas for GC

3.2.2 Equipment

The list of equipment operated during support and catalysts synthesis is given in Table 3.3 with the specified of brands, models, and the applications of equipment.

Table 3.3 List of equipment used for the synthesis of support and catalysts

Equipment	Brand	Purpose
Labtech multiposition stirrer and magnetic stirrer	LabTech	Heating/stirring systems for support synthesis
Carbolite furnace	Carbolite Gero	Support and catalyst calcination
Electronic balance	Mettler Toledo	Balancing support, catalysts and chemicals
Oven	Memmert Germany UFB-500	Drying equipment for support and catalysts
Rotatory evaporator	BÜCHI Rotavapor R-200	Stirring equipment for catalysts preparation

3.3 Catalyst Preparation

3.3.1 Mesoporous Alumina

In literature, the synthesis of mesoporous alumina (MA) via self-assembly technique resulted in the hexagonal symmetry, well-developed mesoporosity, relatively high BET surface area, large pore widths, and crystalline pore walls (Morris, Fulvio, & Jaroniec, 2008) while that of via hydrothermal approach resulted in highly ordered mesoporous alumina with extremely high thermal and hydrothermal stability (X. Wang et al., 2013). Thus, the combination of both methods, known as self-assembly hydrothermal approach (SAHA) could offer the possibility to synthesize thermally stable MA with controlled morphological, textural and structural properties. In this technique, 8 g of (EO)₂₀(PO)₇₀(EO)₂₀ triblock copolymer (Pluronic P123) was dissolved in 160 mL of anhydrous ethanol at room temperature. Then, 12.8 mL of hydrochloric acid (HCl) and 16.32 g of aluminum isopropoxide (C₉H₂₁O₃Al) were added into the above solution with vigorous stirring for about 30 min at 313 K. Thereafter, the resulting mixture was transferred into an inner Teflon-lined container and heated for 24 h at 373 K. Afterwards, the mixture was placed into a 333 K drying oven to undergo the solvent evaporation before being air calcined at 1073 K with a heating rate of 1 K min⁻¹ for 5 h. The details of amount required along with calculation for support are provided in APPENDIX A.

3.3.2 Unpromoted Catalysts

The unpromoted catalyst was produced through the incipient wetness impregnation (IWI) method. In catalyst preparation, 10wt.% of Co was employed as the amount of metallic used in the catalyst since this value exhibited a steady catalytic performance, as reported in previous studies (Fayaz et al., 2016). 4.94 g of $\text{Co}(\text{NO}_3)_2 \cdot 6\text{H}_2\text{O}$ were completely dissolved in 5.82 mL of anhydrous ethanol before being mixed with calcined MA support and stirred in a rotary evaporator at a temperature of 333 K for 2 h in vacuum conditions. The employment of anhydrous ethanol as the solvent during the impregnation step is for improve the dispersion as well as suppress the agglomeration of cobalt particles on the surface of MA support. Then, the resulting solid was dried overnight at 383 K in an oven and further air calcined in the furnace at 873 K for 5 h with a heating rate of 1 K min^{-1} . The details of calculation for all catalyst preparation is provided in APPENDIX A.

3.3.3 Promoted Catalyst

The sequential incipient wetness impregnation (SIWI) approach was employed in this study for producing lanthanide promoted catalysts with excellent dispersion quality of Co active site (Cao, Mirjalili, Wheeler, Xie, & Jang, 2015). 10wt.% of Co was initially utilized as the amount of metallic over the MA via the IWI method as aforementioned in the 10%Co/MA catalyst preparation. The promoter loading about 3wt.% was applied for the amount of promoter owing to the excellent catalytic performance as well as a lower rate of carbon deposition (Fayaz et al., 2016; Siew et al., 2015). As an example, for 3%Ce-10%Co/MA synthesis, 0.93 g of $\text{Ce}(\text{NO}_3)_3$ precursor solution were initially dissolved in 1.67 mL anhydrous ethanol. Then, the resulting solution was mixed and stirred with calcined 10%Co/MA in a vacuum condition of the rotary evaporator at a temperature of about 333 K for 2 h. Afterward, the solid mixture was treated with an oven-drying process for overnight at 383 K before being calcined in the furnace at 873 K for 5 h with a heating rate of 1 K min^{-1} . A similar procedure was repeated by replacing the $\text{Ce}(\text{NO}_3)_3$ precursor solution with $\text{La}(\text{NO}_3)_3$, $\text{Sm}(\text{NO}_3)_3$ and $\text{Y}(\text{NO}_3)_3$ precursor solutions for synthesizing 3%La-10%Co/MA, 3%Sm-10%Co/MA, and 3%Y-10%Co/MA, respectively. The complete procedure for MA support, unpromoted, and promoted catalysts preparation is illustrated in flowchart Figure 3.1 below.

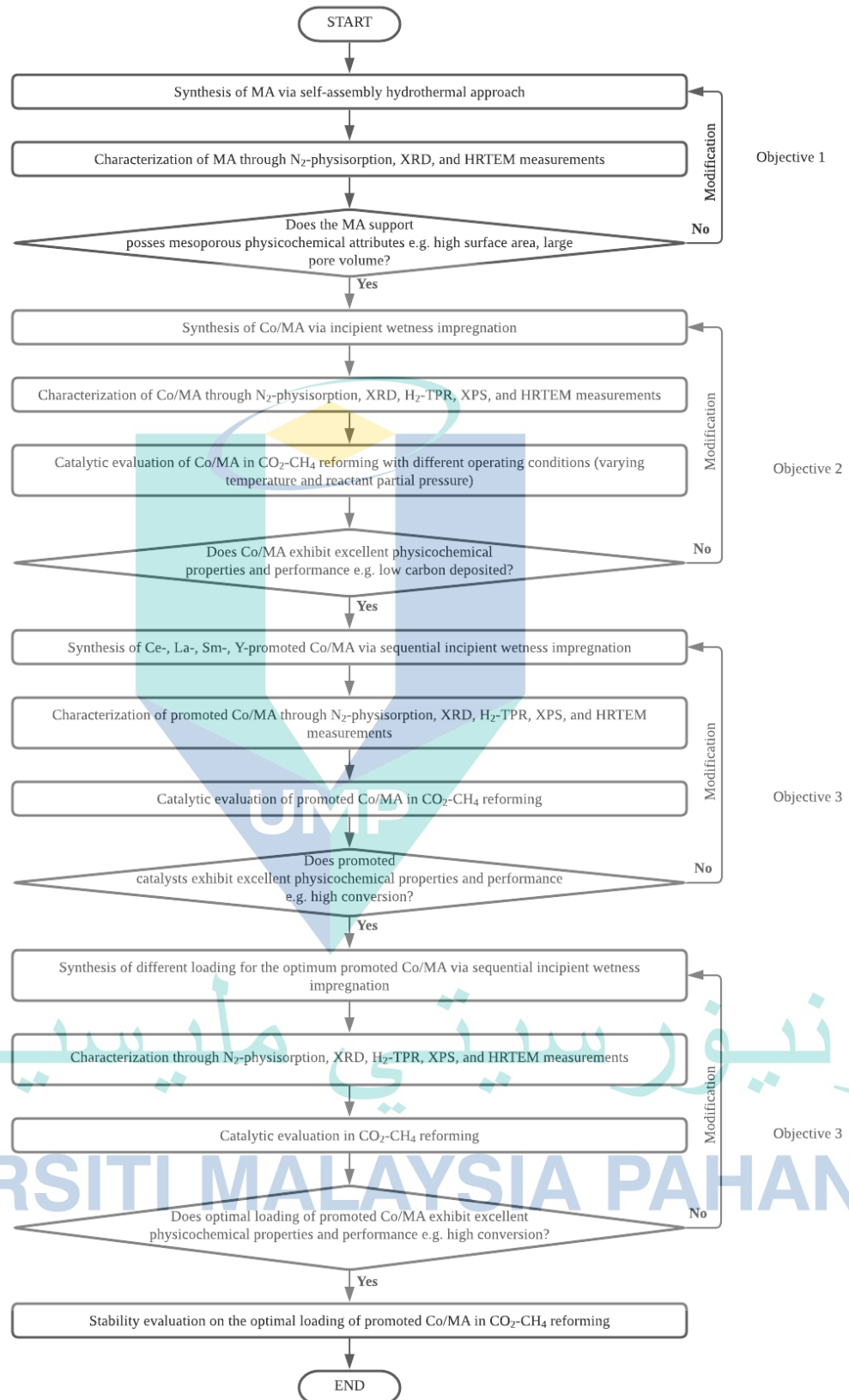


Figure 3.1 Overall flowchart of this study.

3.4 Catalyst Characterization

3.4.1 Textural Measurement

In this work, N₂ physisorption analysis for calcined MA support, promoted and unpromoted catalysts was carried out using a Micromeritics ASAP-2020 automated system for obtaining surface area, pore volume, and pore size distribution. The measurement is divided into two systems which are degasser and analyzer. Prior to the measurement, about 0.1-0.2 g of sample was first degassed at a temperature of 573 K for 1 h to completely remove all residual moisture and surface contamination in the sample followed by N₂ adsorption at 77 K. From N₂ adsorption-desorption isotherm, the specific surface area was calculated using multi-point Brunauer-Emmett-Teller (BET) technique while the average pore size distributions were estimated according to the analysis of Barrett-Joyner-Halendar (BJH).

3.4.2 X-ray Diffraction

X-ray diffraction (XRD) analysis was conducted to identify the crystalline structure and phases that exist in all calcined and spent catalysts. Rigaku Miniflex II system equipped with Cu monochromatic anode as a radiation source ($\lambda = 1.5418 \text{ \AA}$, 30 kV and 15 mA) was utilized to perform XRD analysis. In addition, XRD patterns were analyzed at 2θ within 3° to 80° using scan speed and step size of 1° min^{-1} and 0.02° , respectively. In this study, the X-ray diffractograms obtained from the analysis were further interpreted using a Match! Version 2.3.3 software while databased from Joint Committee on Powder Diffraction Standards (JCPDS) was used as the reference. The mean crystallite size of catalysts also was determined based on the XRD results by using the Scherrer equation as expressed in Eq. (3.1) (Patterson, 1939).

$$d(\text{nm}) = \frac{0.94\lambda}{B \times \cos \theta} \quad (3.1)$$

where β = full width at half maximum of peaks (FWHM) in radian, λ = wavelength of XRD radiation (nm), and θ = Bragg angle in radian.

3.4.3 Temperature-programmed Reduction

H₂ temperature-programmed reduction (H₂-TPR) measurement was conducted on a Micromeritics AutoChem II-2920 chemisorption unit for evaluating the reducibility of promoted and unpromoted Co-based catalysts. In this work, 0.1 g of catalyst sample was initially treated under a He gas flow (50 ml min⁻¹) for 30 min at 373 K to eliminate any moisture and volatile compounds. Then, the sample was exposed to 50 ml min⁻¹ of gas mixture (10% H₂/Ar) from 373 to 1173 K with a heating rate of 10 K min⁻¹ for undergoing H₂ reduction process. Before the cool down process, the reduction temperature was maintained at 1173 K for 30 min in order to complete the reduction process. TCD detector was used to determine the hydrogen consumption while the amount of hydrogen uptake in the reduction process was estimated by integrating H₂-TPR profiles.

3.4.4 X-ray Photoelectron Spectroscopy

X-ray photoelectron spectroscopy (XPS) measurement was carried out to study the elemental composition and chemical state within spent Co-based catalysts. XPS analysis was conducted in a JEOL JPS-9200 spectrometer equipped with a monochromatic Al K α X-ray source (300 W). The multi-channel detector with analyzer pass energy of 10 eV and energy resolution less than 0.65 eV was used to measure the binding energies. In this work, the narrow spectra obtained from XPS measurement was interpreted using CasaXPS Version 2.3.16 and calibrated using the peak energy of adventitious carbon at 284.5 eV.

3.4.5 Scanning Electron Microscopy

The morphology, element content, and atomic mapping of spent catalyst surfaces were determined in this study using scanning electron microscopy (SEM) analysis coupled with energy dispersive X-ray (EDX). For SEM, spent catalysts were analyzed on a Carl Zeiss AG - EVO® 50 Series instrument controlled by a SmartSEM software whilst EDX analysis on a Hitachi Tabletop Microscope TM3030Plus unit. Prior to the SEM test, samples were coated with platinum in BAL-TEC SCD 005 Sputter Coater for 70 s to decrease the electron charge on the catalyst surface and increase the sharpness of SEM image.

3.4.6 High-Resolution Transmission Electron Microscopy

High-resolution transmission electron microscopy (HRTEM) analysis was conducted using an EM-002B TEM instrument with a voltage of 200 kV to identify the particle and/or grain size, size distribution, and morphology of catalyst. Before analysis, the catalyst was suspended in ethanol and placed onto a Cu-microgrid.

3.4.7 Temperature-programmed Oxidation

Temperature-programmed oxidation (TPO) analysis is a common method for measuring the nature of carbonaceous species accumulated on the spent catalyst surface. This analysis was performed after the reaction on the spent catalyst using a TGA Q500 (TA Instruments). For complete removal of moisture and volatile compounds, a sample was initially preheated at 373 K with a 10 K min⁻¹ heating rate for 30 min in the flow of N₂ at 100 ml min⁻¹. Then, the temperature was raised to 1023 K with different heating rates of 10, 15, and 20 K min⁻¹ in the gas mixture of 1O₂:4N₂ (100 ml min⁻¹) for 30 min and kept isothermally and subsequently the sample was cooled down at room temperature in the same gas mixture. The obtained results show the weight changes versus temperature.

3.5 Experimental Set-up

The detailed schematic diagram for CO₂-CH₄ reforming is illustrated in Figure 3.2. A stainless-steel tube fixed-bed reactor (with O.D. = 9.7 mm and I.D. = 7.9 mm) was placed vertically in a split tubular furnace at 1 atm and temperature of 923-1073 K. About 0.1 g_{cat} of catalyst with a mean particle size of 140-250 μm mounted by quartz wool in the middle of quartz reactor and gas hourly space velocity, GHSV of 36 L g_{cat}⁻¹ h⁻¹ was used for each reaction to minimize the transport-disguised kinetics. Before conducting CO₂-CH₄ reforming run, the catalyst was reduced in situ in 60 ml min⁻¹ of 50% H₂/N₂ mixture at 1023 K for 2 h with a heating rate of 5 K min⁻¹. The gas mixture flow rates consisting of CH₄, CO₂, and N₂ were precisely controlled by Alicat mass flow controllers. In addition, N₂ gas also acts as a tie component for material balance purposes and warranting the total flow rate of 60 ml min⁻¹. In order to investigate the effect of feed ratio on CO₂-CH₄ reforming performance, one reactant (CO₂ or CH₄) was kept constant at partial pressure, *P* of 20 kPa whilst *P* of the other reactant was varied from 10 to 40 kPa.

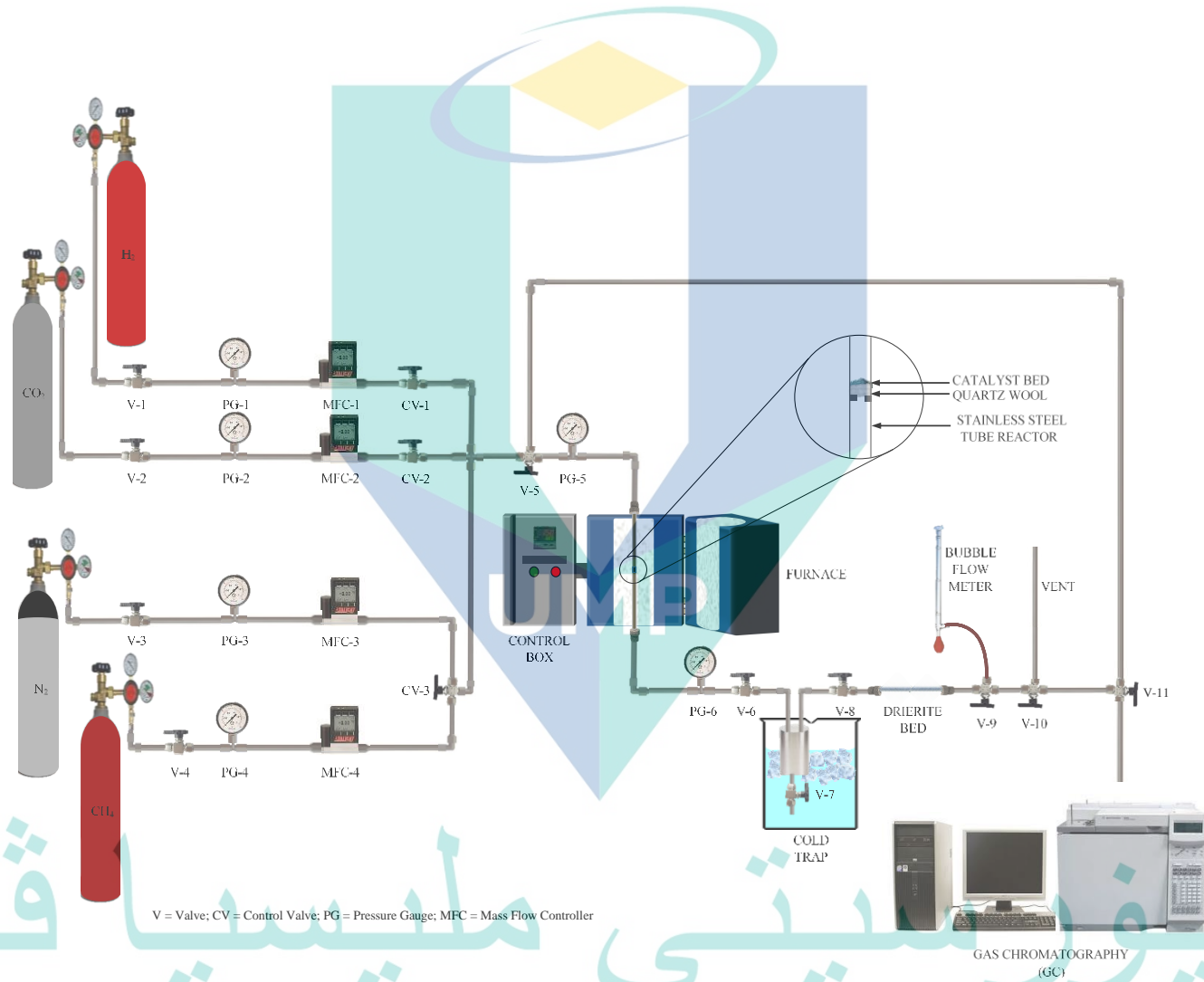


Figure 3.2 Experimental set-up for CO₂-CH₄ reforming reaction.

3.6 Gaseous Product Analysis

In this work, the gaseous product analysis was determined in Agilent 6890 Series gas chromatograph equipped with a thermal conductivity detector and capillary column, HP-MOLSIV (30.0 m × 530 μm × 40.0 μm). The column was operated at 353 K with Helium as a carrier gas, while the oven temperature was maintained at 393 K. For the gas chromatography calibration, the standard gas with known composition was injected five times to achieve calibration curves. In addition, the average value for each component was compared with the reference standard gas data as provided in Table 3.4.

Table 3.4 Standard gas data.

Compound	Composition (%)	Retention time (min)
CO ₂	19.98	10.07
H ₂	25.06	5.39
CH ₄	5.07	7.24
CO	24.89	13.73

3.7 Mass Flow Controller Calibration

The mass flow controllers (MFC) employed in this research were initially calibrated with the relevant gases fed to the CO₂-CH₄ reforming system (CO₂, CH₄ and N₂). Basically, the calibration tests were conducted by measuring for at least 5 points and the calibration procedure yielded linear plots of signal versus actual flow rate. The detailed calibration graphs for each MFC were plotted in APPENDIX C.

3.8 Reaction Metrics

The calculation formulas for both CH₄ and CO₂ conversions can be estimated using Eqs. (3.2) and (3.3), respectively.

$$CH_4 \text{ Conversion (\%)} = \frac{\dot{n}_{CH_4}^{in} - \dot{n}_{CH_4}^{out}}{\dot{n}_{CH_4}^{in}} \times 100 \quad (3.2)$$

$$CO_2 \text{ Conversion (\%)} = \frac{\dot{n}_{CO_2}^{in} - \dot{n}_{CO_2}^{out}}{\dot{n}_{CO_2}^{in}} \times 100 \quad (3.3)$$

where \dot{n}^{in} is the initial molar flow rate of the reactant fed in the system while \dot{n}^{out} is the final molar flow rate of the reactant in the effluents.

Since there was no recycling of product stream from the reactor, the reaction rates ($-r$), production rates (r), gaseous product yield, and H_2/CO ratio of this reaction may be calculated by using formulas in Eqs. (3.4)-(3.10):

$$-r_{CH_4} (\text{mol g}^{-1}\text{s}^{-1}) = \frac{\dot{n}_{CH_4}^{in} - \dot{n}_{CH_4}^{out}}{W_{cat.}} \quad (3.4)$$

$$-r_{CO_2} (\text{mol g}^{-1}\text{s}^{-1}) = \frac{\dot{n}_{CO_2}^{in} - \dot{n}_{CO_2}^{out}}{W_{cat.}} \quad (3.5)$$

$$r_{H_2} (\text{mol g}^{-1}\text{s}^{-1}) = \frac{\dot{n}_{H_2}^{out}}{W_{cat.}} \quad (3.6)$$

$$r_{CO} (\text{mol g}^{-1}\text{s}^{-1}) = \frac{\dot{n}_{CO}^{out}}{W_{cat.}} \quad (3.7)$$

$$H_2 \text{ Yield}(\%) = \frac{\dot{n}_{H_2}^{out}}{2\dot{n}_{CH_4}^{in}} \times 100 \quad (3.8)$$

$$CO \text{ Yield} (\%) = \frac{\dot{n}_{CO}^{out}}{\dot{n}_{CH_4}^{in} + \dot{n}_{CO_2}^{in}} \times 100 \quad (3.9)$$

$$H_2/CO \text{ Ratio} = \frac{\dot{n}_{H_2}^{out}}{\dot{n}_{CO}^{out}} \quad (3.10)$$

Where $w_{cat.}$ is the weight of catalyst consumed during reaction (g_{cat})

3.9 Preliminary Experiments

3.9.1 Blank Test

The blank test for CO₂-CH₄ reforming was conducted in an unfilled stainless-steel reactor at a temperature of 1023 K, stoichiometric condition, and under atmospheric pressure for 8 h. GC analysis detected the presence of H₂ and CO from the effluent gas streams implying that the occurrence of CH₄ decomposition and carbon gasification at the aforementioned operating condition. However, the blank test revealed relatively low conversion of CH₄ and CO₂ at below 1% and 5.2%, respectively as compared to both conversions achieved from CO₂-CH₄ reforming with the presence of a catalyst (as discussed in Chapters 6). The positive role of Co metallic sites in CO₂-CH₄ reforming was proven by a higher catalytic activity of Co/MA catalyst ($X_{CH_4} = 70.9\%$ and $X_{CO_2} = 71.7\%$) than the MA support only ($X_{CH_4} = 6.6\%$ and $X_{CO_2} = 23.5\%$). Thus, the improvement in catalytic activity for CO₂-CH₄ reforming over Co-based catalysts in this work was credited to the physicochemical attributes and efficient participation of used catalysts.

3.9.2 Thermodynamic Consideration

Thermodynamic analysis is worthy of effectively determining all the possibilities as well as the limitations of side reactions during CO₂-CH₄ reforming. In fact, it also can be used to efficiently optimize the yield of products while minimizing the formation of carbon. The changes in the standard Gibbs free energy (ΔG) for CO₂-CH₄ reforming and side reactions as a function of temperature are plotted in Figure 3.3, whilst the complete results of thermodynamic analysis attained from ChemEq Version 1.0 software are summarized in Table 3.5. According to the principles of thermodynamic, the reaction is spontaneous when the value of ΔG is negative.

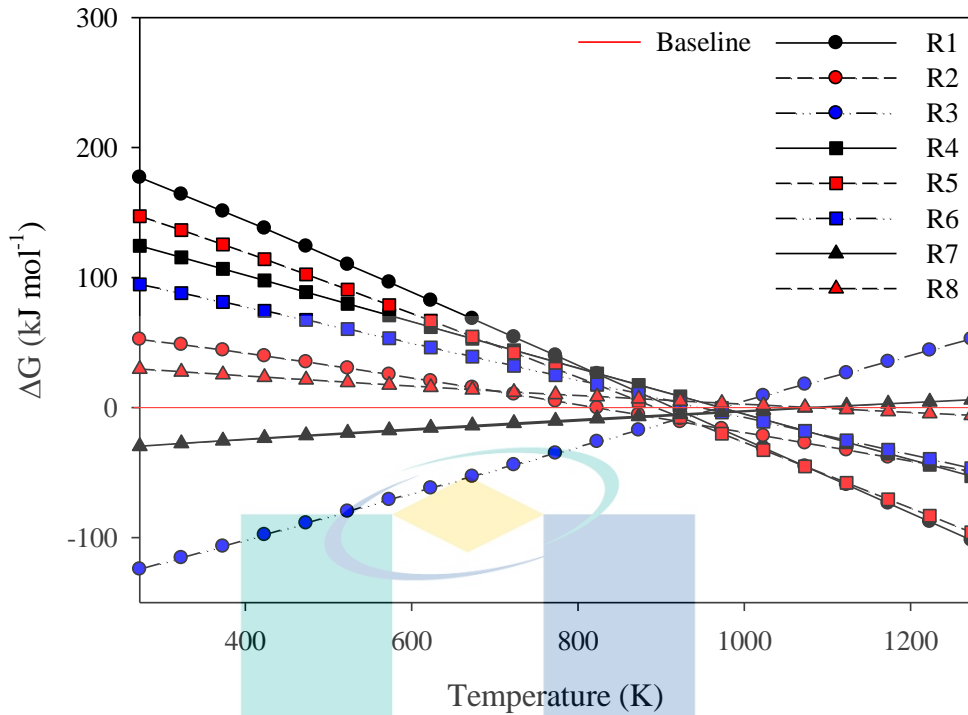


Figure 3.3 Effect of operating temperature on the variation of the Gibbs free energy for main and side reactions in $\text{CO}_2\text{-CH}_4$ reforming.

Source: ChemEq Version 1.0

Thermodynamic study on $\text{CO}_2\text{-CH}_4$ reforming reaction showed that main reaction (R1) could be completely operated at reaction temperature above 914 K. As seen in Table 3.5 the formation of carbon can occur at a significant rate due to methane decomposition (R2) and Boudouard (R3) at an operating temperature between 833 and 959 K. Therefore, $\text{CO}_2\text{-CH}_4$ reforming reaction was favorable to be conducted above 973 K to minimize the coke formation, and in turn, can avoid catalyst deactivation and reactor clogging. Indeed, the carbonaceous deposit could also be simultaneously gasified by CO_2 reactant due to the existence of reverse Boudouard reaction (R4) at temperature above 959 K. This condition is in good agreement with other studies of $\text{CO}_2\text{-CH}_4$ reforming (Omoregbe et al., 2017). Apart from carbon formation, the H_2/CO ratio in the product stream also could be varied since it is affected by the instantaneous occurrence of RWGS reaction (R8) at a temperature greater than 1275 K. At this point, the production of water from the RWGS reaction could further initiate methane steam reforming (R5) and carbon gasification by steam (R6) since both reactions will certainly occur at temperatures above 907 and 960 K, respectively.

Table 3.5 Summary of thermodynamic findings for CO₂-CH₄ reforming.

Reaction no.	Reaction	ΔG (kJ mol ⁻¹)	Required temperatures for reaction feasibility (K)
R1	CO ₂ -CH ₄ reforming $CH_4 + CO_2 \rightarrow 2CO + 2H_2$	256.05 - 0.28T	>914
R2	Methane decomposition $CH_4 \rightarrow C + 2H_2$	83.39 - 0.10T	>833
R3	Boudouard $2CO \rightarrow C + CO_2$	0.18T - 172.66	<959
R4	Reverse Boudouard $C + CO_2 \rightarrow 2CO$	-0.18T + 172.66	>959
R5	Methane steam reforming $CH_4 + H_2O \rightarrow CO + 3H_2$	217.79 - 0.24T	>907
R6	Carbon gasification by steam $C + H_2O \rightarrow CO + H_2$	-0.14T + 134.42	>960
R7	Water gas shift $CO + H_2O \rightarrow CO_2 + H_2$	0.03T - 38.26	<1275
R8	Reverse water gas shift $CO_2 + H_2 \rightarrow CO + H_2O$	-0.03T + 38.26	>1275

Source: Pakhare and Spivey (2014)

3.9.3 Elimination of Transport Intrusions

According to Fogler (2006), there are seven steps involved in the interaction between reactants and catalyst for the heterogeneous catalytic system. These steps are given as:

1. The mass transfer of reactants from the bulk fluid to the external surface of the catalyst.
2. The transport of gaseous reactants by diffusion process through the pores into the particle.
3. The adsorption of reactants onto the internal catalyst surface.
4. Reaction on the internal surface of the catalyst.
5. Desorption of products from the surface.
6. Transport of products through the pores to the external surface of the catalyst.
7. Mass transfer of products from the external surface to the bulk fluid.

In the interaction process, the chemical reaction kinetics was represented by steps 3, 4, and 5. While steps 1 and 7 indicate the external transport processes, steps 2 and 6 are associated with internal transport processes. The system for CO₂-CH₄ reforming must be operated as far away from the transport-limited zones to minimize the effect of mass

and heat transfer intrusions in reaction kinetics data. Four major transport resistances were considered and eliminated from CO₂-CH₄ reforming system. The properties for the reforming system together with parameters to calculate the values of the transport resistances are provided in Table 3.6. The detailed calculations involved are presented in APPENDIX B.

Table 3.6 Properties used in the calculation of transport resistances

Parameter	Value	Source
A	$4.90 \times 10^{-5} \text{ m}^2$	Reactor tube property
C_{Ab}	$4.09 \times 10^{-5} \text{ mol cm}^{-3}$	Experimental condition
C_{p-CH_4}	$4.60 \times 10^3 \text{ J kg}^{-1} \text{ K}^{-1}$	Perry and Green (2008)
C_{p-CO_2}	$1.24 \times 10^3 \text{ J kg}^{-1} \text{ K}^{-1}$	Perry and Green (2008)
C_{p-N_2}	$1.17 \times 10^3 \text{ J kg}^{-1} \text{ K}^{-1}$	Perry and Green (2008)
h_w	$30 \text{ J m}^{-1} \text{ s}^{-1} \text{ K}^{-1}$	Perry and Green (2008)
R	$8.314 \text{ J mol}^{-1} \text{ K}^{-1}$	Perry and Green (2008)
λ_{CH_4}	$0.17 \text{ J m}^{-1} \text{ s}^{-1} \text{ K}^{-1}$	Perry and Green (2008)
λ_{CO_2}	$0.07 \text{ J m}^{-1} \text{ s}^{-1} \text{ K}^{-1}$	Perry and Green (2008)
λ_{N_2}	$0.07 \text{ J m}^{-1} \text{ s}^{-1} \text{ K}^{-1}$	Perry and Green (2008)
λ_m	$7.89 \text{ J m}^{-1} \text{ s}^{-1} \text{ K}^{-1}$	Perry and Green (2008)
μ_{CH_4}	$2.84 \times 10^{-5} \text{ kg m}^{-1} \text{ s}^{-1}$	Perry and Green (2008)
μ_{CO_2}	$4.06 \times 10^{-5} \text{ kg m}^{-1} \text{ s}^{-1}$	Perry and Green (2008)
μ_{N_2}	$4.21 \times 10^{-5} \text{ kg m}^{-1} \text{ s}^{-1}$	Perry and Green (2008)
D_{eff}	$1.41 \times 10^{-5} \text{ m}^2 \text{ s}^{-1}$	Calculation
D_g	$1.36 \times 10^{-4} \text{ m}^2 \text{ s}^{-1}$	Calculation
d_p	$1.95 \times 10^{-4} \text{ m}$	Experimental condition
d_t	$7.90 \times 10^{-3} \text{ m}$	Reactor tube property
E_A	$27.56 \text{ kJ mol}^{-1}$	Experimental condition
$-\Delta H_r$	$297.58 \text{ kJ mol}^{-1}$	Experimental condition
$-r_{exp}$	$6.88 \times 10^{-5} \text{ mol g}_{cat}^{-1} \text{ s}^{-1}$	Experimental condition
R_p	$9.75 \times 10^{-5} \text{ m}$	Experimental condition
T	1023 K	Experimental condition
V	60 mL min^{-1}	Experimental condition
ε	0.8	Adhikari, Fernando, and Haryanto (2007)
ρ_c	3.35 g cm^{-3}	Experimental condition
ρ_b	0.67 g cm^{-3}	$(1 - \varepsilon)\rho_c$

Table 3.6 Continued

Parameter	Value	Source
ρ_g	0.435 kg m ⁻³	Calculation
σ_c	0.8	Fogler (2006)
$\tilde{\tau}$	3.0	Fogler (2006)
ω_p	0.4	Fogler (2006)
n	0.88	Experimental condition

3.9.3.1 External Mass Transfer

The film layer between the bulk fluid and the external catalyst surface may create the external mass transfer resistance. Thus, the value calculated must satisfy the Mears criterion (cf. Eq. (3.11)) to neglect the effect of external mass transfer resistance (Mears, 1971).

$$\frac{(-r_{\text{exp}})\rho_b R_p n}{k_c C_{Ab}} < 0.15 \quad (3.11)$$

where

$(-r_{\text{exp}})$ = rate of reaction (mol g_{cat}⁻¹ s⁻¹) (the highest reaction rate obtained from experimental data was used for calculation)

ρ_b = bulk density of catalyst bed (g cm³)

R_p = catalyst particle radius (m)

n = reaction order

C_{Ab} = bulk gas-phase concentration of CH₄ (mol cm⁻³)

k_c = mass transfer coefficient (cm s⁻¹)

The mass transfer coefficient, k_c can be determined from Eq. (3.12) (Dwivedi & Upadhyay, 1977).

$$k_c = \frac{j_D U}{Sc^{1/3}} \quad (3.12)$$

where

j_D = Colburn's mass transfer factor

U = superficial gas velocity (m s⁻¹)

Sc = Schmidt number

The value of Mears criterion in Eq. (3.11) was obtained about $1.92 \times 10^{-4} \ll 0.15$, indicating the negligible external mass transfer resistance for this CO₂-CH₄ reforming system.

3.9.3.2 Internal Mass Transfer

The internal mass transport resistance generally occurs during the diffusion of reactants and products through the pores of the catalyst. The internal mass transfer is considered to be negligible if Weisz-Prater criterion (Fogler, 2006) given in Eq. (3.13) is satisfied.

$$\frac{(-r_{\text{exp}}) \rho_c R_p^2}{D_{\text{eff}} C_{As}} < 1 \quad (3.13)$$

where

- ρ_c = density of catalyst pellet (g cm⁻³)
 C_{As} = concentration of CH₄ on the catalyst surface (mol cm⁻³)
 D_{eff} = effective diffusivity of CO₂ in a mixture of N₂ and CH₄ (m² s⁻¹)

The concentration of CH₄ on the catalyst surface (C_{Ab}) is considered to be equal to the concentration of CH₄ in the bulk gas-phase (C_{As}) since the external mass transport resistance was found to be negligible. The effective diffusivity (D_{eff}) can be estimated from Eq. (3.14).

$$D_{\text{eff}} = \frac{D_g \omega_p \sigma_c}{\tilde{\tau}} \quad (3.14)$$

where

- D_g = diffusivity of CO₂ in a mixture of N₂ and CH₄ (m² s⁻¹)
 ω_p = catalyst pellet porosity
 σ_c = construction factor
 $\tilde{\tau}$ = tortuosity

The value for the left-hand side of Eq. (3.13) was about 4.43×10^{-3} extremely less than unity, suggesting that the internal mass transfer resistance may be neglected in the system.

3.9.3.3 External Heat Transfer

Fogler (2006) reported that the external heat transport resistance in a reactor may be insignificant if Mears criterion as seen in Eq. (3.15) is fulfilled.

$$\frac{|(-\Delta H_r)|(-r_{\text{exp}})\rho_b R_p E_A}{hRT_b^2} < 0.15 \quad (3.15)$$

where

$-\Delta H_r$ = heat of reaction for CO₂-CH₄ reforming (J mol⁻¹)

E_A = activation energy (J mol⁻¹)

h = heat transfer coefficient between gas mixture and catalyst (J m⁻² s⁻¹ K⁻¹)

R = ideal gas constant (J mol⁻¹ K⁻¹)

T_b = reactant gas bulk temperature (K)

The heat transfer coefficient (h) may be achieved from the correlation between j -factor of heat and mass transfer given by the Colburn-Chilton analogy in Eq. (3.16) (Perry & Green, 2008).

$$j_D = j_H = \frac{h \text{Pr}^{2/3}}{C_{pg} \rho_g U} \quad (3.16)$$

where

j_H = j -factor for heat transfer ($j_H = j_D$)

C_{pg} = specific heat capacity of feed gas mixture (J kg⁻¹ K⁻¹)

Pr = Prandtl number

ρ_g = density of the gas mixture (kg m⁻³)

U = superficial gas velocity (m s⁻¹)

After substituting the suitable values in both equations, the left-hand side of Eq. (3.15) obtained as $1.33 \times 10^{-5} \ll 0.15$. Hence, the external heat transport resistance is considered to be negligible for the CO₂-CH₄ reforming system.

3.9.3.4 Internal Heat Transfer

The internal heat transfer resistance is considered to be negligible if the experimental conditions and reaction rate data for CO₂-CH₄ reforming follow the Anderson criterion as provided in Eq. (3.17) (Anderson, 1963).

$$\frac{|(-\Delta H_r)|(-r_{\text{exp}})\rho_b R_p^2 E_A}{\lambda_p R T_s^2} < 0.75 \quad (3.17)$$

where

$$\begin{aligned} \lambda_p &= \text{thermal conductivity of catalyst pellet (J m}^{-2} \text{ s}^{-1} \text{ K}^{-1}) \\ T_s &= \text{reactant gas bulk temperature} \end{aligned}$$

The gas phase bulk temperature (T_b) was considered to be equal to the catalyst surface temperature (T_s) since the external heat transfer was found to be negligible. The thermal conductivity of catalyst pellet (λ_p) was determined from the thermal conductivity of the catalyst material (λ_m) using the correlation provided in Eq. (3.18) (R. Wilhelm, Johnson, Wynkoop, & Collier, 1948).

$$\log(\lambda_p \times 10^5) = 0.859 + 3.12 \left(\frac{\lambda_m}{\omega_p} \right) \quad (3.18)$$

where

$$\lambda_m = \text{thermal conductivity of the catalyst material (J m}^{-1} \text{ s}^{-1} \text{ K}^{-1})$$

Therefore, the value for the left-hand side of Eq. (3.17) was calculated to be around 7.74×10^{-29} , suggesting the negligibility of internal heat transfer resistance.

3.9.3.5 Wall and Radial Heat Dispersion Effects

According to Dixon (1997), the wall heat transfer effects can be considered to be negligible if the ratio of reactor tube diameter (d_t) to the catalyst particle diameter (d_p) is greater than 4. For CO₂-CH₄ reforming system, the d_t/d_p was about 40.5, satisfying the criteria for negligible wall effects. However, a high ratio of d_t/d_p may contribute to radial heat transfer effects. Thus, the Mears' criterion (Mears, 1971) shown in Eq. (3.19) was used to determine the insignificant effects of the radial heat transfer.

$$(3.19) \quad \left(\frac{E_a}{RT_w} \right) \left(\frac{(-\Delta H_r)(-r_{\text{exp}})\rho_b R_p^2 [(1-\varepsilon)/(1-b)]}{4\lambda_p T_w} \right) \left(\frac{1}{8} + \frac{B_p}{Bi_w R_t} \right) < 0.05$$

where

- $T_w = T_b$ = tube wall temperature (K)
- ε = void fraction in the catalyst bed
- b = inert solids fraction of the catalyst bed
- R_t = radius of reactor tube (m)

while, the wall Biot number (Bi_w) can be estimated from Eq. (3.20).

$$Bi_w = \frac{h_w d_p}{\lambda_p} \quad (3.20)$$

where

- h_w = heat transfer coefficient of reactor tube wall ($\text{J m}^{-2} \text{s}^{-1} \text{K}^{-1}$)
- d_p = catalyst particle diameter (m)
- λ_p = thermal conductivity of catalyst pellet ($\text{J m}^{-2} \text{s}^{-1} \text{K}^{-1}$)

The left-hand side of Eq. (4.9) was calculated to be 1.05×10^{-8} . Therefore, the reactor system is able to meet Mears' criterion for the negligible radial heat dispersion effects.

3.10 Concluding Remarks

The combination of self-assembly and hydrothermal could offer the possibility to synthesize thermally stable MA with controlled morphological, textural and structural properties. 10wt.% of Co was employed as the amount of metallic used in the catalyst since this value exhibited a steady catalytic performance, as reported in previous studies. The promoter loading about 3wt.% was applied for the amount of promoter owing to the excellent catalytic performance as well as a lower rate of carbon deposition. The sequential incipient wetness impregnation approach was employed in this study for producing lanthanide promoted catalysts with excellent dispersion quality of Co active site. Several characterizations were performed on fresh and spent catalysts or determining the textural and physicochemical properties catalysts which could be related with the catalytic performances. Based on the thermodynamic study, CO₂-CH₄ reforming reaction was favourable to be conducted above 973 K to minimize the coke formation, and in turn, can avoid catalyst deactivation. Therefore, the operating temperature in the range of 923-1023 K was applied for evaluating the catalyst performance. The blank test analysis proved the positive role of Co metallic sites in CO₂-CH₄ with the improvement of CH₄ and CO₂ conversion about 90.7% and 67.2%, respectively, as compared with results using MA support only. Besides, the mass and heat transport limitations were pre-determined in this chapter using the different calculations of transport resistance. The total flow rate of 60 ml min⁻¹ at various reaction temperatures (923-1023 K) and reactant partial pressure (10-40 kPa) was applied. In the present study, the Mears criterion was negligible for both external and internal mass-heat transfer resistance as well as radial heat dispersion influence. Thus, the operating values were evaluated in the CO₂-CH₄ reforming reaction for the following chapters.

CHAPTER 4

RESULTS AND DISCUSSIONS

4.1 Introduction

This chapter discusses the results attained from the MA support and Co/MA characterizations as well as its performance during the evaluation in CO₂-CH₄ reforming. In addition, the results obtained in this study were compared with previous studies related to the employment of MA support and Co-based catalysts during CO₂-CH₄ reforming. Co/MA catalysts was further evaluated under the influence of reaction temperature (923-1023 K) and reactant partial pressure (10-40 kPa) for 8 h with GHSV about 36 L g_{cat}⁻¹ h⁻¹.

4.2 Evaluation of Co/MA Catalyst for CO₂-CH₄ Reforming

This subtopic discusses the results attained from the MA support and Co/MA characterizations as well as its performance during the evaluation in CO₂-CH₄ reforming. In addition, the results obtained in this study were compared with previous studies related to the employment of MA support and Co-based catalysts during CO₂-CH₄ reforming. Co/MA catalysts was further evaluated under the influence of reaction temperature (923-1023 K) and reactant partial pressure (10-40 kPa) for 8 h with GHSV about 36 L g_{cat}⁻¹ h⁻¹.

4.2.1 Catalyst Characterization

4.2.1.1 Physisorption Measurement

The adsorption isotherms and pore size distribution profile of MA support and 10%Co/MA catalyst are illustrated in Figure 4.1. It is noteworthy that both support and catalyst displayed a typical type-IV isotherm with a hysteresis loop of H1 shaped, confirming the formation of mesoporous structure based on IUPAC classification. In addition, the steepness of the capillary condensation step observed at P/P_0 in the range between 0.65-0.85 indicated that mesoporous was uniformly distributed, in agreement

with the study reported by Karam Jabbour, Massiani, Davidson, Casale, and El Hassan (2017) and N. Wang et al. (2014) for Ni-Mg(Ca)-Al₂O₃ and NiCeAl catalysts, respectively.

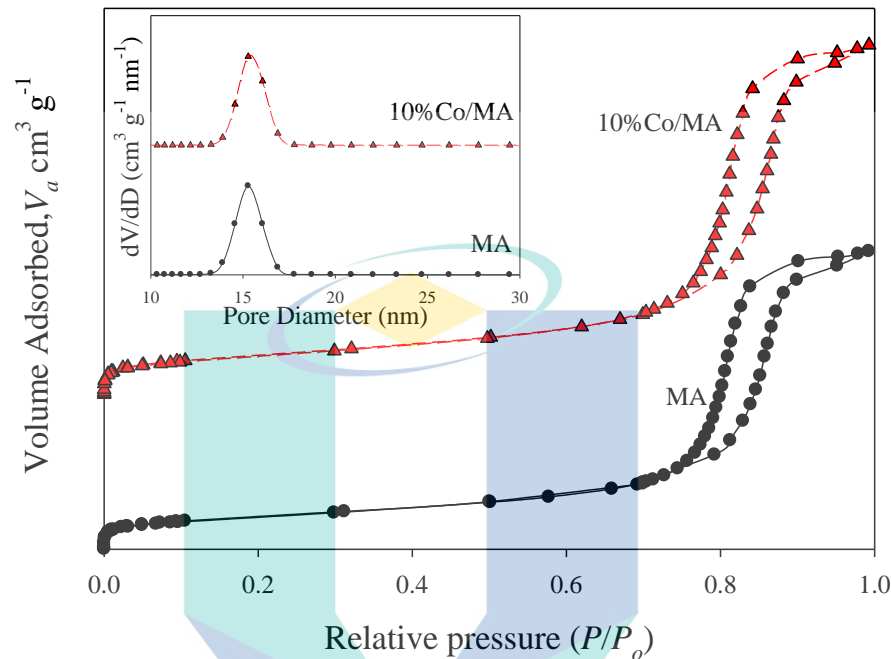


Figure 4.1 The physisorption isotherms and pore size distribution profile of MA support and 10%Co/MA catalyst

4.2.1.2 X-ray Diffraction Analysis

Figure 4.2 illustrates the XRD profiles of MA support and 10%Co/MA in the range of 10°-80°. XRD profile of fresh 10%Co/MA catalyst exhibited the (111), (311), (222), (400), and (440) reflections of cubic γ -Al₂O₃ at 2θ of 19.45°, 32.30°, 36.99°, 45.69°, and 67.20° (JCPDS card No. 04-0858), respectively (Qian et al., 2019). Besides, the reflections associated with the lattice planes of (220), (311), (400), (511), and (440) Co₃O₄ (JCPDS card No. 74-2120) was detected at 2θ about 31.45°, 37.10°, 44.79°, and 55.66°, respectively (Qian et al., 2019; Z. Wang, Jiang, & Shangguan, 2007). Furthermore, the reflections associated with the (511) and (440) of CoAl₂O₄ spinel (JCPDS card No. 82-2246) was observed at angle $2\theta = 59.51^\circ$ and 65.38° , respectively, indicating that the intense Co-MA interaction (J. F. Li et al., 2014; P. Li et al., 2011). The mean crystallite size of Co₃O₄ (220) 12.9 nm was recorded for 10%Co/MA. It is noted that the calculated mean crystallite size of Co₃O₄ was lower than the pore diameter of the MA support obtained in N₂-physisorption analysis, implying that most Co₃O₄ particles were held inside the pores structure of the MA support.

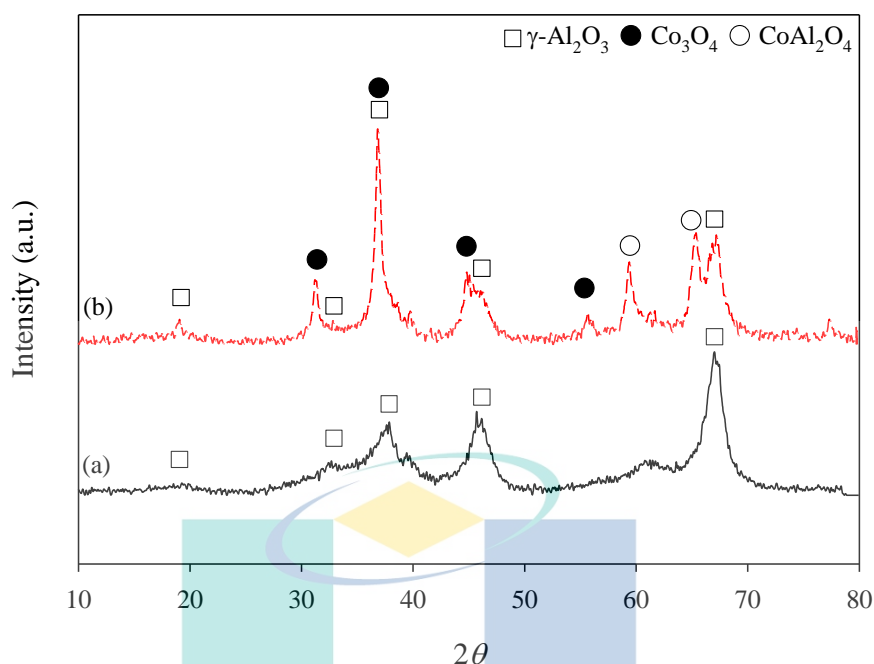


Figure 4.2 XRD patterns of (a) MA support and (b) 10%Co/MA catalyst.

4.2.1.3 Temperature Programmed Reduction

The deconvolution of TPR curve for 10%Co/MA catalyst displayed in Figure 4.3 revealed three distinct peaks in the temperature range of 774.7-899.9 K, signifying the reduction of different kinds of cobalt phases. The low reduction peak (P1) centered at 674.7 K was associated with the reduction of $\text{Co}_3\text{O}_4 \rightarrow \text{CoO}$ (as expressed in Eq.(4.1)) while reduction peak (P2) observed at 778.8 K was corresponded to the subsequent reduction of CoO to Co^0 (cf. Eq.(4.2)) (Hull & Trawczyński, 2014; K. Jabbour et al., 2014). The high reduction peak (P3) detected at a temperature of about 899.9 K was assigned to CoAl_2O_4 reduction (see Eq.(4.3)) which typically formed because of the intense interaction between MA support and Co particles (Cooper et al., 2008; Hull & Trawczyński, 2014). Additionally, high calcination temperature was responsible for generating spinel CoAl_2O_4 since this condition could enhance the migration of Co^{2+} ions inside the MA support lattice and settle in the tetrahedral positions of spinel (Papageridis et al., 2016). This finding is tallied with the TPR results stated by K. Jabbour et al. (2014) and Fayaz et al. (2016) with Co/SBA-15 and Co/ Al_2O_3 catalysts employment, respectively. In their study, three reduction peaks were also appeared in the range 588-1005 K, indicating the reduction of $\text{Co}_3\text{O}_4 \rightarrow \text{CoO}$, $\text{CoO} \rightarrow \text{Co}$, and spinel Co_2SiO_4 or spinel $\text{CoAl}_2\text{O}_4 \rightarrow \text{Co}$.

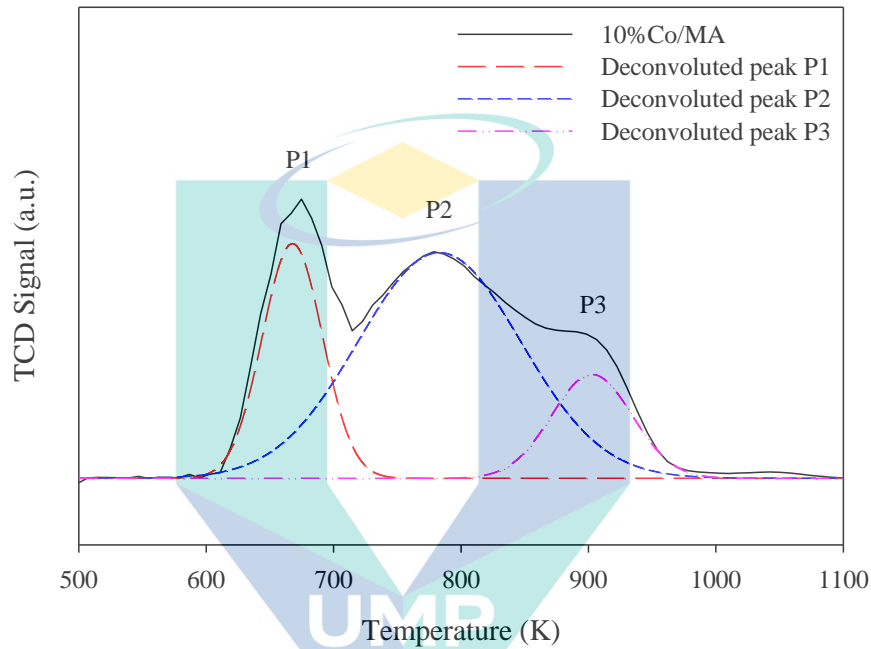
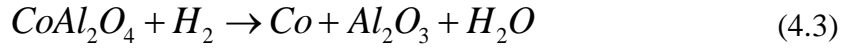
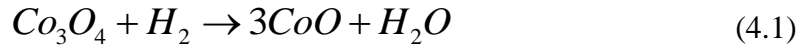
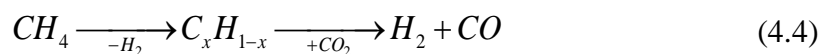


Figure 4.3 H₂-TPR profile of 10%Co/MA catalyst.

4.2.2 CO₂-CH₄ Reforming Analysis

4.2.2.1 Influence of CO₂ and CH₄ Partial Pressure

The dependences of CH₄ and CO₂ conversions with CO₂ partial pressure, P_{CO_2} in CO₂-CH₄ reforming, are pictured in Figure 4.4. Regardless of reaction temperature, it should be noted that CH₄ conversion was improved non-linearly by up to 42.8%, with increasing P_{CO_2} from 10 kPa to 40 kPa, while P_{CH_4} was maintained at 20 kPa (Figure 4.4 (a)). This behaviour was linked to the improved gasification rate of carbonaceous deposits that were typically generated from methane dissociation, as expressed in Eq. (4.4) (Foo et al., 2011b).



where C_xH_{1-x} represents the deposited carbon while the value of x is ≤ 1 .

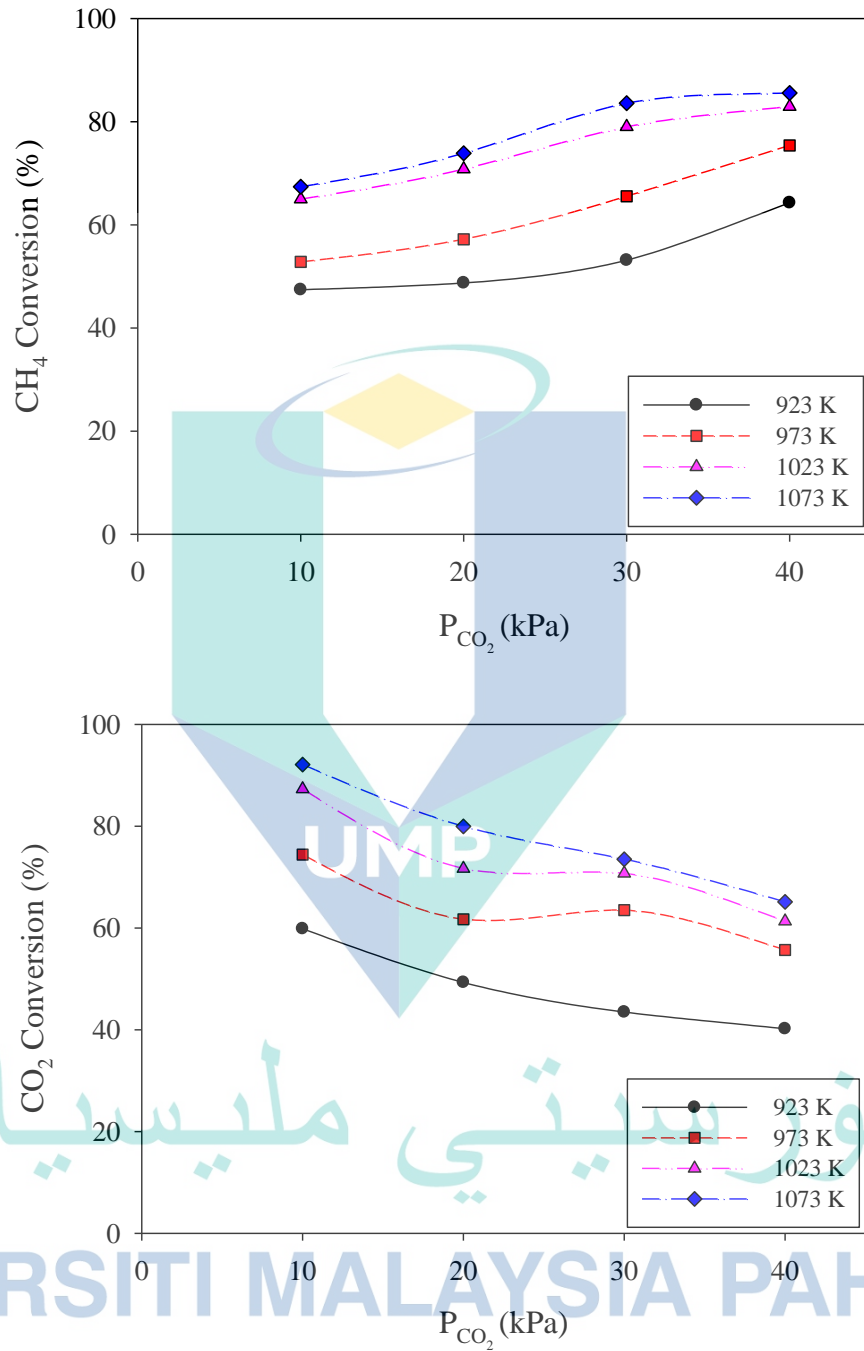


Figure 4.4 Influence of P_{CO_2} on (a) CH₄ conversion and (b) CO₂ conversion for 10%Co/MA catalyst at $P_{CH_4} = 20$ kPa and $T = 923-1023$ K.

Apart from that, Donazzi, Beretta, Groppi, and Forzatti (2008) also justified that the increment in CH₄ conversion with rising P_{CO_2} was probably associated with the simultaneous occurrence of methane steam reforming which resulted from the growing H₂O formation via RWGS in CO-rich feedstock (Eq. (4.5)). In contrast, the decline of CO₂ conversion has been experienced during the rise of P_{CO_2} from 10 kPa-40 kPa (Figure 4.4(b)). This observation was ascribed to the deficient amount of CH₄ for consuming the CO₂-rich feedstock, and was in agreement with those previously reported by Nikoo and Amin (2011). Besides, Omoregbe et al. (2017) explained that the presence of surplus CO₂ during CO₂-CH₄ reforming system could increase the probability for active metallic particles to oxidize (Eq. (4.6)), resulting in a decreased CO₂ adsorption.



Figure 4.5 reveals the H₂/CO ratio as a function of P_{CO_2} . Clearly, the H₂/CO ratio was declined by up to 72.4% with the growth P_{CO_2} from 10 kPa to 40 kPa and obtained a value of less than the stoichiometric ratio of unity. This performance resulted from the high consumption of H₂ in the system for generating CO via the concomitant occurrence of RWGS. In addition, the enhancement of the CO₂ gasification rate (Eq. (4.7)) during the CO₂-CH₄ reforming also influenced the decrease in the H₂/CO ratio. This result seemed to be well in agreement with the previous evaluation carried out by Omoregbe et al. (2017) and Ayodele, Khan, and Cheng (2015) over Ni/SBA-15 and Co/CeO₂ catalysts, respectively.



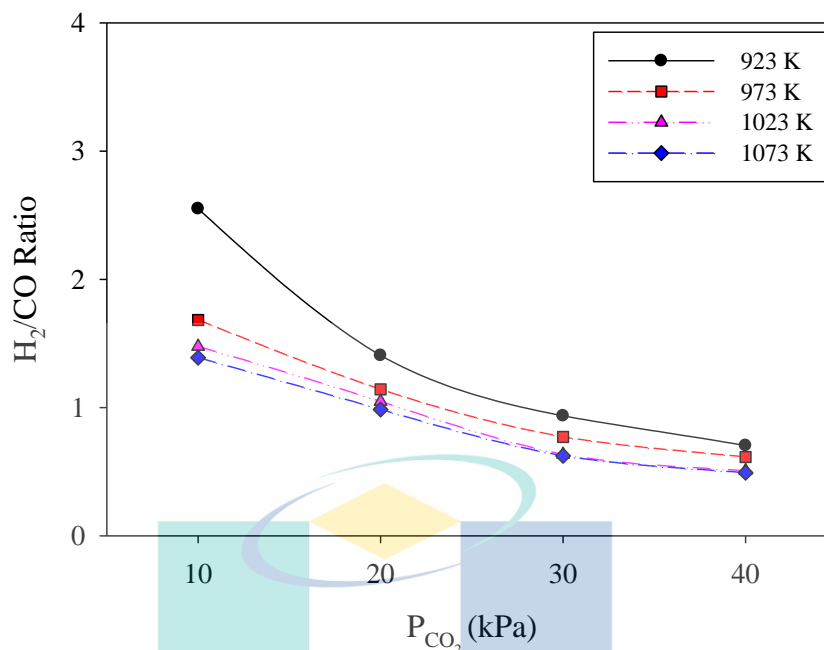


Figure 4.5 Influence of P_{CO_2} on $H_2:CO$ ratio for 10%Co/MA catalyst at $P_{CH_4} = 20$ kPa and $T = 923-1023$ K.

The reactant conversions and product ratio profiles for 10%Co/MA catalyst as functions of CH_4 partial pressure, P_{CH_4} are presented in Figure 4.6 to Figure 4.8. Observably, the conversion of CH_4 was gradually decreased by up to 41.3% with the rise of P_{CH_4} from 10 kPa to 40 kPa, regardless of the reaction temperature (Figure 4.6). This trend was exhibited due to the growth of deposited carbon since direct CH_4 cracking was facilitated by the surplus CH_4 feedstock. In addition, Ayodele et al. (2015) explained that the increment in the formation rate of deposited carbon led to the blocking of active sites on catalyst surface; hence, resulted in the decline-trend plots of CH_4 conversion. This outcome was in accordance with previous findings by Omoregbe et al. (2017) who observed a decrement in CH_4 conversion with increased P_{CH_4} .

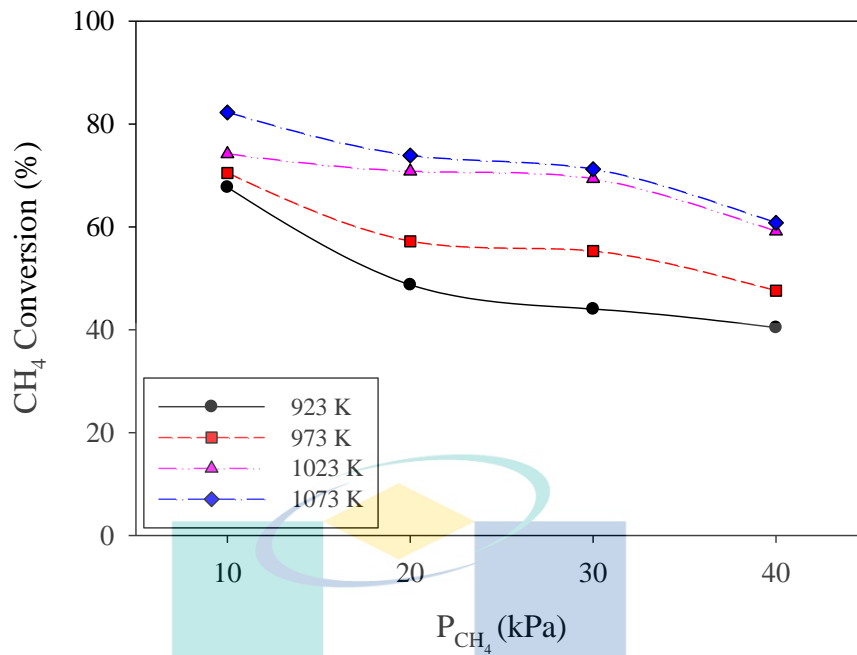


Figure 4.6 Effect of P_{CH_4} on CH_4 conversion for 10%Co/MA catalyst at $P_{CO_2} = 20$ kPa and $T = 923$ - 1023 K.

On the other hand, CO_2 conversion was slightly improved with the growth of P_{CH_4} from 10 kPa to 40 kPa which corresponded to the enhancement in CO_2 - CH_4 reforming (Figure 4.7). Nikoo and Amin (2011) justified that this performance was attributed to the coexistence of CH_4 dissociation, which generated H_2 and C during the gas phase reaction. Therefore, H_2 and C were further reacted with CO_2 in RWGS and CO_2 gasification, respectively. This improvement was also noticed by Ayodele et al. (2015) in a reforming work over ceria supported cobalt catalyst. According to Naeem, Alfatesh, Khan, Abasaed, and Fakeeha (2013), the increment of P_{CH_4} also resulted in greater CH_4 adsorption on catalyst surface; consequently, increased the consumption of CO_2 . Figure 4.8 displays the plot for the H_2/CO ratio as a function of change in P_{CH_4} . Apparently, H_2/CO ratio value raised greater than 1 along with P_{CH_4} increment from 10 kPa to 40 kPa, regardless of the operating temperature. This achieved trend indicated that more H_2 was generated as compared to CO via CH_4 cracking during CO_2 - CH_4 reforming.

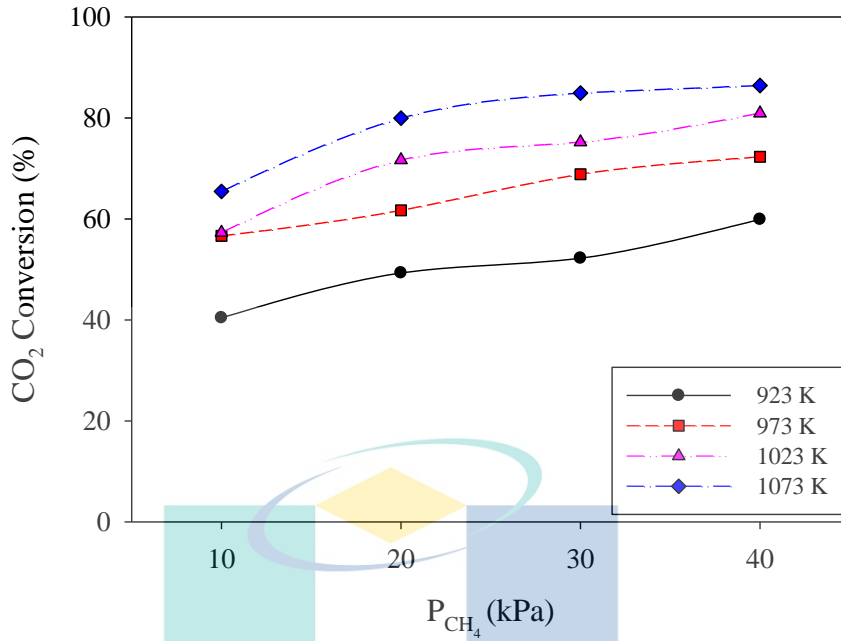


Figure 4.7 Effect of P_{CH_4} on CO₂ conversion and (c) H₂:CO ratio for 10%Co/MA catalyst at $P_{CO_2} = 20$ kPa and T = 923-1023 K.

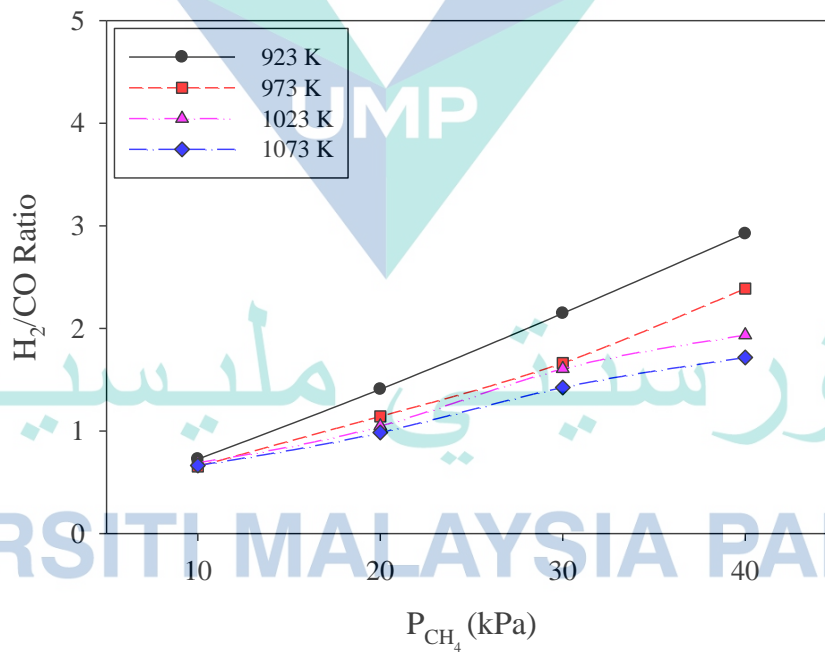
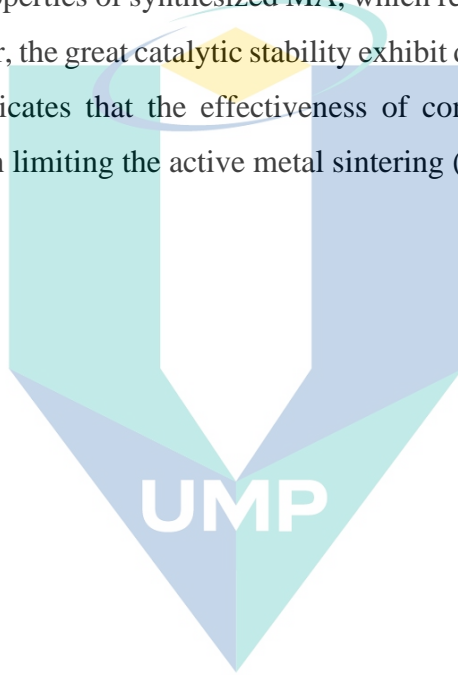


Figure 4.8 Effect of P_{CH_4} on H₂:CO ratio for 10%Co/MA catalyst at $P_{CO_2} = 20$ kPa and T = 923-1023 K.

The catalytic performance of 10%Co/MA at 1023 K and $P_{CH_4} = P_{CO_2} = 20$ kPa was summarized in Table 4.1. The CO₂-CH₄ reforming test over MA support has recorded extremely low conversions of CH₄ (6.6%) and CO₂ (23.5%), suggesting that the Co metallic sites are crucial in the CO₂-CH₄ reforming. In comparison with other catalysts listed in Table 4.1, 10%Co/MA demonstrated comparable catalytic activity ($X_{CH_4} = 70.9\%$, $X_{CO_2} = 71.7\%$) with degree of deactivation at about 4.2% after 8 h CO₂-CH₄ reforming. A good catalytic performance of 10%Co/MA was related to the interesting textural properties of synthesized MA, which resulted in a well distribution of Co particles. Moreover, the great catalytic stability exhibit during the CO₂-CH₄ reforming reaction probably indicates that the effectiveness of confinement effect provided by mesoporous support in limiting the active metal sintering (Leilei Xu et al., 2013).



اونيورسيتي مليسيا قهغ

UNIVERSITI MALAYSIA PAHANG

Table 4.1 Summary of the catalytic performance of catalysts for CO₂-CH₄ reforming

Catalysts	Method ^a	Textural properties					Operating parameters					Catalytic Performance ^f				Ref.	
		S_{BET} (m ² g ⁻¹)	V_p (cm ³ g ⁻¹)	D_p (nm)	Fresh d_{Co}^b (nm)	Spent d_{Co}^c (nm)	T (K)	GHSV (Lg _{cat} ⁻¹ h ⁻¹)	Feed ratio	TOS (h)	X_{CH_4} (%)	X_{CO_2} (%)	D_d^e (%)	H ₂ /CO ratio	E_a (kJmol ⁻¹)		C_d (%)
MA	SAHA	243.1	0.85	15.3	-	-	1023	36	1.0	8	6.6	23.5	35.6	0.11	-	-	This study
10%Co/MA	IWI	203.9	0.70	15.3	12.9 ^c	13.7	1023	36	1.0	8	70.9	71.7	4.2	1.05	28.88	24.6	
Non-mesoporous support																	
20%Co/La ₂ O ₃	IMP	16.45	0.03	1.2	-	-	1023	30000 ^d	1.0	-	49.0	59.9	-	-	96.1	-	(Ayodele, Khan, Lam, et al., 2016)
5%Co-15%Ni/Al ₂ O ₃		110.8	0.50	17.9	174	-							0.95	56.4	-	(S. Y. Foo, C. K. Cheng, T.-H. Nguyen, & A. A. Adesina, 2011a)	
2.5%Ce-5%Co-15%Ni/Al ₂ O ₃	SWI	110.7	0.45	16.4	154	-	1023	20000 ^d	1.0	-	-	-	-	54.5	-	(Pichas, Pomonis, Petrakis, & Ladavos, 2010)	
LaSrNiO ₄	So-CNR	-	-	-	-	-	673	-	1.0	48	11.6	14.0	0	41.2	4.7	(Sierra Gallego, Batiot-Dupeyrat, Barrault, & Mondragón, 2008)	
Ni/La ₂ O ₃	SCM	-	-	-	-	-	973	120	1.0	100	84.2	86.3	0	68.0	-		
Mesoporous alumina support																	
OMA		225.0	0.54	9.5	-	-	-	-	-	-	-	-	-	-	-	-	(Leilei Xu et al., 2012)
OMA-5%Co5%Ni	EISA	212.0	0.48	11.0	11.8	11.2	973	15	1.0	100	77.6	78.9	3.9	0.83	-	8.0	(Leilei Xu et al., 2017)
OMA	EISA	310.0	0.95	-	-	-	1023	-	1.0	100	-	-	-	-	-	-	(Q. Ma et al., 2016)
6%Ni/OMA	IWI	287.0	0.61	-	-	-	1023	-	1.0	100	78.0	86.0	4.2	1.02	-	15.2	
10%Ni-Al ₂ O ₃		253.0	0.55	5.9	9.1	22.9	1023	24	1.0	150	81.5	84.4	4.6	-	-	33.6	(X. Huang et al., 2017)
5%Co5%Ni-Al ₂ O ₃	SG	227.0	0.51	6.2	11.6	12.6	1023	24	1.0	150	81.7	85.2	2.6	-	-	27.1	
MA	EISA	256.9	0.83	10.1	-	-	-	-	-	-	-	-	-	-	-	-	(Tao et al., 2013)
5%NiMA	EISA	305.1	0.76	6.9	-	-	973	-	1.0	24	61.3	77.1	1.6	0.95	-	6.0	
MA	EISA	295.0	0.78	8.3	-	-	-	-	-	-	-	-	-	-	-	-	(Aw et al., 2016)
CoW/MACeZr	WI	220.0	0.49	13.5	-	-	1023	-	1.0	20	61.0	64.0	59.0	0.35	-	4.7	

Table 4.1 Continued

Catalysts	Method ^a	Textural properties					Operating parameters				Catalytic Performance ^f				Ref.		
		S_{BET} (m ² g ⁻¹)	V_p (cm ³ g ⁻¹)	D_p (nm)	Fresh d_{Co}^b (nm)	Spent d_{Co}^c (nm)	T (K)	GHSV (Lg _{cat} ⁻¹ h ⁻¹)	Feed ratio	TOS (h)	X_{CH_4} (%)	X_{CO_2} (%)	D_d^e (%)	H ₂ /CO ratio		E_a (kJmol ⁻¹)	C_d (%)
MA	H	207.0	0.56	10	-	-	-	-	-	-	-	-	-	-	-	-	(Huseyin Arbag, 2018)
5%Ni/MA	IMP	150	0.55	13.0	-	-	1023	36	1.0	4	77.5	87.4	0.5	-	-	-	

^aSelf-assembly hydrothermal-assisted (SAHA), incipient wetness impregnation (IWI), impregnation method (IMP), wetness impregnation (WI), sequential wetness impregnation (SWI), so-called nitrate route (So-CNR), self-combustion method (SCM), evaporation-induced self-assembly (EISA), sol-gel (SG), hydrothermal (H)

^bCrystallite size was calculated based on XRD measurement via Scherrer formula.

^cCrystallite size was measured using TEM.

^dGHSV (Gas hourly space velocity) unit is h⁻¹.

^eDegree of catalyst deactivation, D_d (%) = [1 - (Final conversion of CH₄/ Initial conversion of CH₄)] × 100%.

^fValue of reactant conversions and H₂/CO ratio for previous studies were obtained at 1 h time-on-stream.



UMP

اونيور سيڤي مليسيا قهغ

UNIVERSITI MALAYSIA PAHANG

4.2.3 Post-Reaction Characterizations

4.2.3.1 X-ray Diffraction Analysis

For comparison purposes, the XRD profiles of spent 10%Co/MA was illustrated in Figure 4.9 along with XRD profiles of fresh 10%Co/MA (10%Co/MA-F). In comparison with 10%Co/MA-F catalyst, all XRD profiles of spent 10%Co/MA catalysts revealed the presence of (002) graphite carbon at a diffraction angle of 26.38° (JCPDS card No. 75-0444), regardless of reforming temperature (Maia, Assaf, & Assaf, 2014). Three peaks related to γ - Al_2O_3 phase ($2\theta = 36.99^\circ$, 45.69° , and 67.20°) and Co_3O_4 phase ($2\theta = 31.45^\circ$, 37.10° , 44.79°) remained noticeable on spent catalyst while one peak of CoAl_2O_4 spinel was detected at 2θ of 65.38° . Notably, the Co metallic phases do not appear on all spent catalysts which may indicate the re-oxidation of active Co^0 by CO_2 during 8 h CO_2 - CH_4 reforming (X. Zhang et al., 2018).

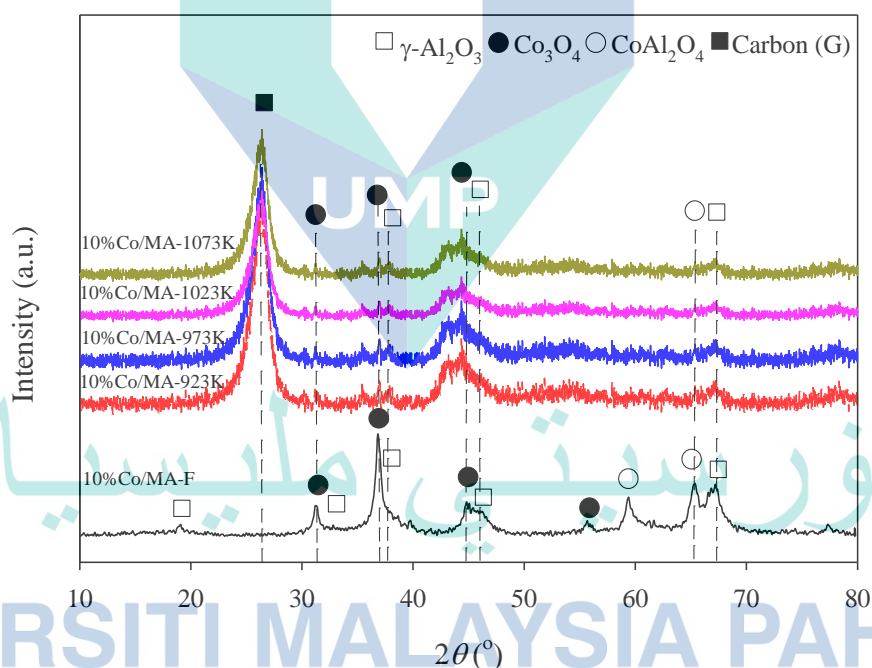


Figure 4.9 XRD patterns of 10%Co/MA-F and spent 10%Co/MA after 8 h CO_2 - CH_4 reforming at temperature of 923-1073 K and $P_{\text{CO}_2} = P_{\text{CH}_4} = 20$ kPa.

4.2.3.2 Temperature-Programmed Oxidation

The TPO result for spent 10%Co/MA catalyst is depicted in Figure 4.10. Notably, the broad peak for derivative weight profile of spent 10%Co/MA catalyst appeared at above 629 K corresponded to the deposition of two distinct forms of carbonaceous

species (Figure 4.10(a)). The first oxidation peak (O_I) was observed at temperature of about 753K-796.3 K, which belonged to the oxidation of amorphous carbon, mainly generated though CH_4 cracking at the early stage during CO_2 - CH_4 reforming (Ji, Tang, Zeng, Lin, & Tan, 2001). Otherwise, the second oxidation peak (O_{II}) detected at temperature of above 809.2 K, which was appointed as the oxidation of graphitic carbon (Leilei Xu et al., 2011). Apart from that, it was evident that the percentage of coke accumulated estimated from TPO weight loss analysis (Figure 4.10(b)) was slightly lessened from 32.3% to 24.6% with the rise in temperature from 923 K to 1073 K. This trend was experienced accredited to the augmentation of reverse Boudouard reaction during CO_2 - CH_4 reforming. Comparing the degree of catalyst deactivation (D_d) and coke accumulated percentage (C_d) for 10%Co/MA with previous findings (see Table 4.1), both values were slightly lower and comparable with other values due to the confinement effect of MA support which protecting Co metals from sintering; hence, minimizing the deactivation of 10%Co/MA catalyst during 8 h of CO_2 - CH_4 reforming.

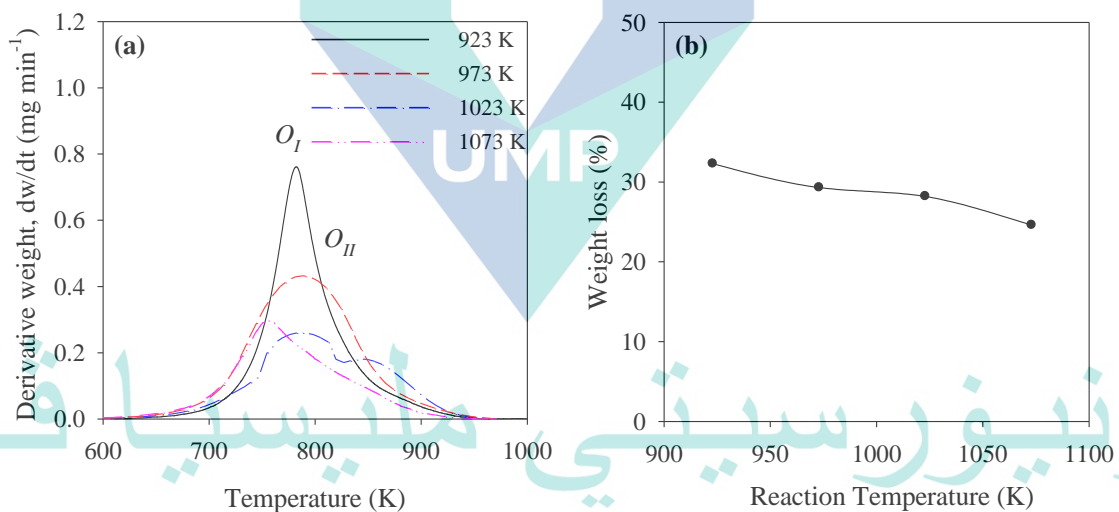


Figure 4.10 (a) Derivative weight profiles and (b) weight loss profile of spent 10% Co/MA catalyst attained from TPO after 8 h CO_2 - CH_4 reforming at temperature of 923-1073 K and $P_{\text{CH}_4} = P_{\text{CO}_2} = 20$ kPa.

4.2.3.3 High Resolution Transmission Electron Microscopy

HRTEM image and particle size distribution of fresh and spent 10%Co/MA are revealed in Figure 4.11. The HRTEM image of 10%Co/MA-F showed the presence of Co particles lied between 6-22 nm, with majority of particles at approximately 12.9 nm. Meanwhile, the HRTEM image of spent 10%Co/MA showed the presence of Co particles

(size about 13.7 nm) with traces of filamentous-type carbon (CNF) on the MA support. The existences of CNF on MA were in accordance with the finding described by Ji et al. (2001) during the CO₂-CH₄ reforming over Co-based catalysts. It was worth noting that the crystallites size of Co particles was slightly influenced by the sintering effect due to an increment in the particle size distribution of the catalyst (Figure 4.29(a) and (b)). However, the increment in the particle size of 10%Co/MA was lower than other reported catalysts listed in Table 4.1, indicating the superior sintering resistance of the synthesized 10%Co/MA. Leilei Xu et al. (2011) also experienced the slight increment of Ni particles size after CO₂-CH₄ reforming reaction. They justified that this slight suppression on metal sintering was resulted from mesoporous alumina capability in confining those active metal particles, thus assisted in the improvement of catalytic activity and stability.

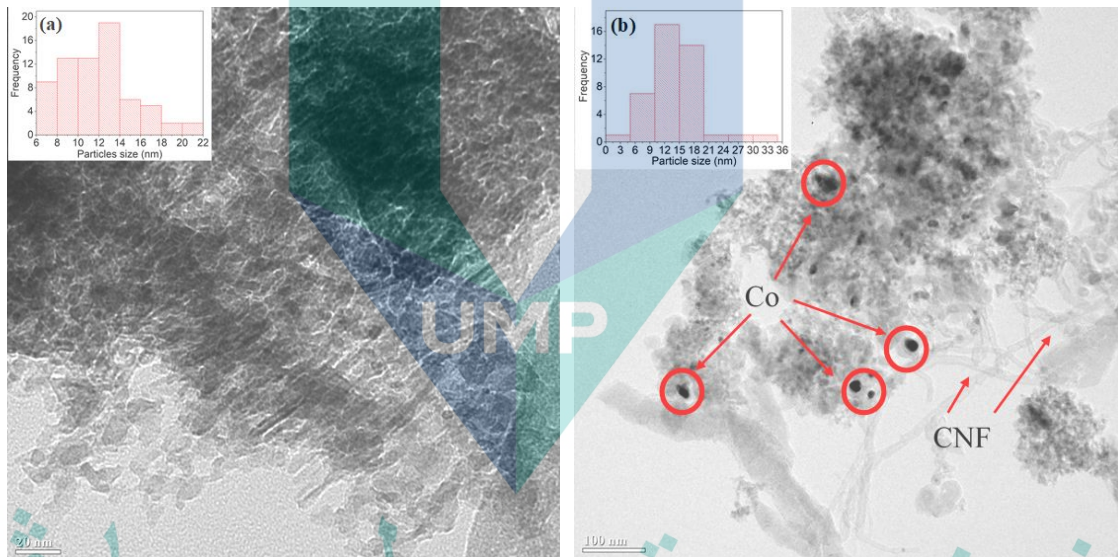


Figure 4.11 TEM image and particle size distribution of (a) 10%Co/MA-F and (b) spent 10%Co/MA catalyst after 8 h CO₂-CH₄ reforming at temperature of 1023 K and $P_{CH_4} = P_{CO_2} = 20$ kPa.

4.3 Effect of Lanthanides Promoters on Co/MA Catalyst for CO₂-CH₄ Reforming

This subchapter studies the effect of lanthanides promoter; Ce, La, Sm and Y addition (3wt%) towards physicochemical properties of 10%Co/MA as well as its catalytic performance in CO₂-CH₄ reforming (at T= 1023 K, CH₄/CO₂ =1 and 1 atm). The changes on catalyst physicochemical properties were determined via XRD, TPR, HRTEM, XPS, and TPO analysis and thoroughly discussed in this chapter. The correlation between these properties with CO₂-CH₄ reforming activity is elucidated through this chapter, and the best catalyst combination will be screened out for further evaluation.

4.3.1 Catalyst Characterizations

4.3.1.1 X-ray Diffraction Measurement

Figure 4.12 illustrates the diffraction spectra of all fresh catalysts as well as the support. All diffraction spectra of calcined catalysts displayed γ -Al₂O₃ phase reflection at $2\theta = 19.4^\circ, 32.3^\circ, 36.9^\circ, 45.6^\circ$ and 67.2° (JCPDS card No. 04-0858), was matched with the diffraction spectrum of MA support (Yin et al., 2013). For promoted and unpromoted catalysts, the reflection lines corresponding to crystalline Co₃O₄ were visibly detected at 2θ angles of $31.4^\circ, 37.1^\circ, 44.7^\circ$ and 55.6° (JCPDS card No. 74-2120) (Xiuhua Wang et al., 2016). However, the diffraction lines for La₂O₃ ($2\theta = 27.8^\circ, 30.0^\circ, 46.2^\circ, 52.1^\circ$ and 55.4° , JCPDS card No. 65-3185), CeO₂ ($2\theta = 28.5^\circ, 33.1^\circ$ and 56.3° , JCPDS card No. 34-0394), Sm₂O₃ ($2\theta = 28.3^\circ, 32.7^\circ$ and 46.8° , JCPDS card No. 42-1461) and Y₂O₃ ($2\theta = 29.1^\circ, 33.7^\circ, 48.5^\circ$, and 57.6° , JCPDS card No. 41-1105) did not appear on La-, Ce-, Sm- and Y-promoted catalysts respectively, implying that the promoter particles were finely dispersed outside the detection limit of XRD (De la Luz, Prades, Beltrán, & Cordoncillo, 2013; Ibrahim et al., 2016; Rabiah Nizah et al., 2014; R. Yang, Xing, Lv, Shi, & Tsubaki, 2010). It is noteworthy that the promoted and unpromoted catalysts exhibited the characteristic peaks of CoAl₂O₄ spinel (JCPDS card No. 82-2246) at $2\theta = 59.5^\circ$ and 65.3° as illustrated in Figure 4.12, signifying intense Co-MA interaction (Z. Wang et al., 2007).

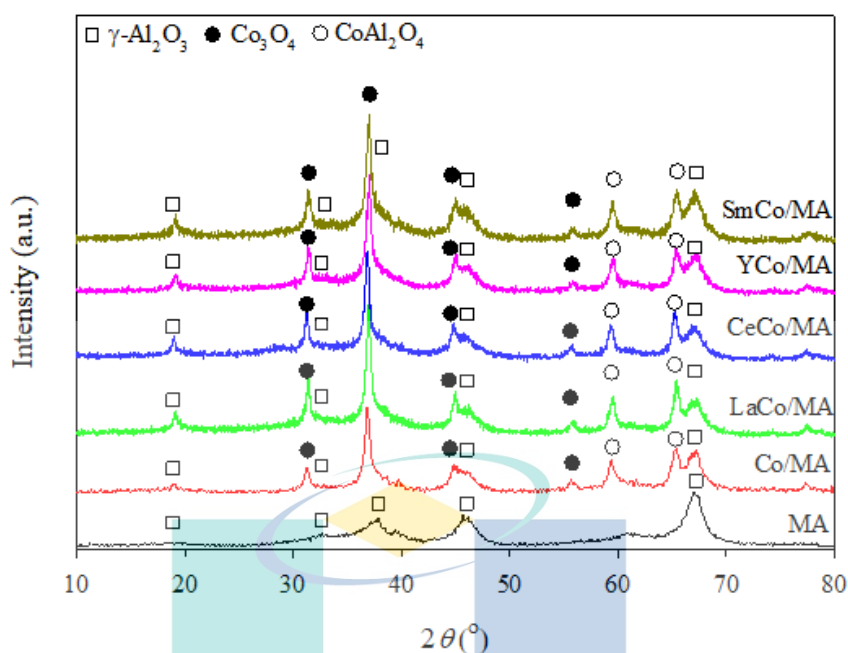


Figure 4.12 X-ray diffractograms of MA support, Co/MA and promoted Co/MA catalysts.

The values of Co_3O_4 crystallite size were obtained using Scherrer formula on XRD peak at $2\theta = 31.4^\circ$ and recorded in Table 4.2. Co_3O_4 crystallite size for 10%Co/MA catalysts were attained about 12.87 nm. After the incorporation of promoters, crystallite size value was slightly reduced in the order; Co/MA (12.87 nm) > CeCo/MA (12.83 nm) > LaCo/MA (12.76 nm) > SmCo/MA (12.70 nm) > YCo/MA (12.66 nm) owing to the enhancement of Co_3O_4 dispersion with the assistance of promoter (Omogrebe et al., 2016; Świrk et al., 2019; Taherian et al., 2017c). Indeed, Movasati et al. (2017) and Lihao Xu, Mi, and Su (2011) experienced a similar trend on crystallite size of Ni after introducing Ce promoter on Ni/ZnAl₂O₄ and La promoter on Ni/ γ -Al₂O₃, respectively. They concluded that promoter incorporation improved metal support interaction through “spacer” effect, sequentially assisting in the suppression of particle agglomeration on catalyst surface.

4.3.1.2 Textural Properties

Table 4.2 tabulates the physicochemical attributes of the synthesized support and catalysts such as BET surface area, pore volume, and pore diameter. The BET surface area and pore volume were lessened in the following order; MA support > Co/MA > LaCo/MA > CeCo/MA > SmCo/MA > YCo/MA, which might be accredited to Co metal oxide appearance on both surface and pore structure of the MA support. It is interesting

to notice that the addition of Co onto MA support slightly increased MA pore diameter implying the occurrence of Co agglomeration in the pore, leading to a slight expansion of the pore. However, the introduction of promoter eliminated this phenomenon, indicating the well dispersion of Co particle on both pore and surface of support. For the effect of promotor, significant changes observed with the addition of Sm and Y, as compared to La and Ce, might be a result of the high number of Co particles entering MA pore structure due to the small particle size of Co. This assumption can be proven by H₂-TPR (Figure 4.13), whereby the reduction temperature of Co particles was higher for SmCo/MA and YCo/MA as compared with LaCo/MA and CeCo/MA.

Table 4.2 Textural properties of promoted and unpromoted catalysts.

Catalyst	BET surface area (m ² g ⁻¹)	Average pore Volume (cm ³ g ⁻¹)	Average pore diameter (nm)	Average Co ₃ O ₄ particle size (nm)		Deactivation degree, <i>D_d</i> (%) ^c
				Fresh ^a	Spent ^b	
MA	243.05	0.85	15.3	-	-	-
Co/MA	203.89	0.70	15.4	12.87	13.60	4.21
YCo/MA	155.81	0.52	14.8	12.66	11.04	0.57
CeCo/MA	164.63	0.58	15.2	12.83	12.52	0.84
LaCo/MA	169.25	0.63	15.0	12.76	12.39	0.95
SmCo/MA	159.14	0.52	14.8	12.70	11.93	2.04

^aAverage crystallite size was determined using XRD.

^bAverage crystallite size of spent catalysts after 8 h reaction was measured using HRTEM.

^cDegree of catalyst deactivation, D_d (%) = [1 - (Final conversion of CH₄/ Initial conversion of CH₄)] × 100%.

4.3.1.3 Temperature-Programmed Reduction

Figure 4.13 illustrates H₂-TPR profiles for Co/MA and promoted Co/MA catalysts. By comparing with TPR profiles of Co/MA, the incorporation of La or Ce promoter over 10%Co/MA catalyst shifted all reduction peaks towards lessened reduction temperature (below 753.3 K) than that of 10%Co/MA catalyst. With the redox properties owned by La and Ce promoters, the amount of surface oxygen mobility on the support was improved and resulted in lowering the reduction ability of Co (B. Li, Xu, & Zhang, 2013). Indeed, the decrease in Co reduction temperature might be due to the role of La and Ce promoters in restraining Co ions from migrating into MA structure and lowering the Co-Al₂O₃ interaction (Pardo-Tarifa, Cabrera, Sanchez-Dominguez, & Boutonnet, 2017). A similar trend was noted by Natesakhawat, Oktar, and Ozkan (2005), whereby Ni reduction peak was shifted to lower temperature after they implemented Ce

or La promoter over Ni/Al₂O₃ catalyst via the sol-gel approach. They also justified that this finding was due to a weak Ni-Al₂O₃ interaction when La or Ce promoter was present.

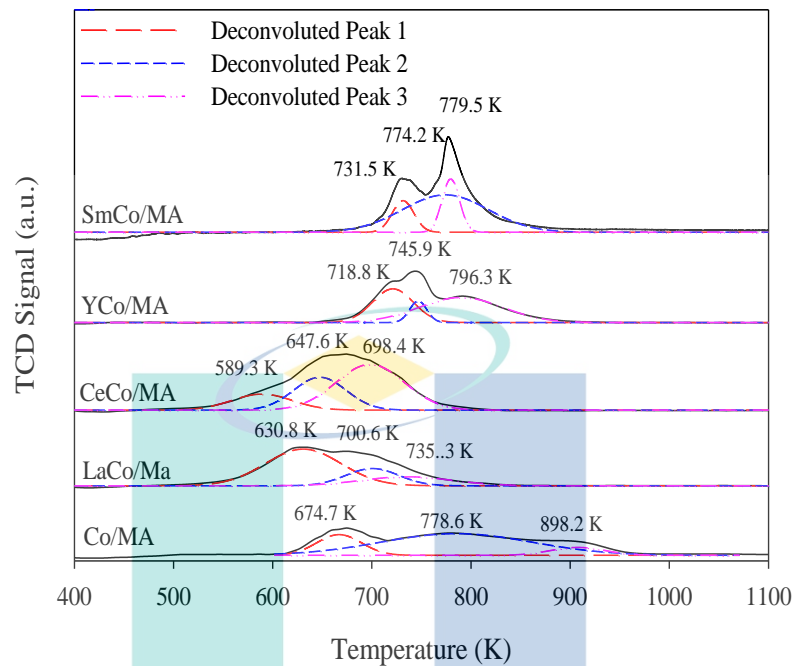


Figure 4.13 H₂ temperature-programmed reduction of promoted and unpromoted Co-based catalysts.

In contrast, TPR profiles for Y and Sm-promoted catalysts revealed that the reduction peak of Co₃O₄ shifted toward the elevated temperature region (within 718.8-796.3 K) suggesting that the inclusion of Y and Sm promoters enhanced Co-MA interaction, hence lessening the reducibility of the 10%Co/MA catalyst (Zhu et al., 2011). This finding concurred with the results obtained by Świrk et al. (2019) during the employment of Y with Ni/KIT-6, for which the increment in reduction temperature of NiO was observed during TPR analysis. Apart from that, the enhancement in Co-MA interaction of SmCo/MA and YCo/MA catalysts can be clarified by the smaller crystal size of Co particles of these catalysts compared to other catalysts as listed in Table 4.2. With this smaller size, Co particles could easily enter the pore structure of MA and form strong metal-support interaction.

4.3.2 CO₂-CH₄ Reforming Analysis

The catalytic activity of the promoted and unpromoted catalysts on 8 h stream at 1023 K with stoichiometric feed ratio ($\text{CH}_4/\text{CO}_2 = 1$) is summarized in Figure 4.14 to Figure 4.16. Irrespective of the catalyst employed, superior value of CO₂ conversion than that of CH₄ conversion could be signified by the RWGS ($\text{CO}_2 + \text{H}_2 \leftrightarrow \text{CO} + \text{H}_2\text{O}$) that always accompanied CO₂-CH₄ reforming process. This trend was previously explored by Xin et al. (2018) and Xiang et al. (2016) during the evaluation of MDR using Ni-Co/SBA-15 and Ni/Si-MCeZr catalysts, respectively. As appeared in Figure 4.14 and Figure 4.15, the values of CH₄ and CO₂ conversion were significantly improved after adoption of La, Ce, Y and Sm promoters, probably due to fine Co₃O₄ dispersion, greater oxygen vacancies, and the redox abilities of these promoters. Indeed, both conversion values were increased in the order of YCo/MA (CH₄ Conv. = 85.4%, CO₂ Conv. = 90.7%) > LaCo/MA (CH₄ Conv. = 84.8%, CO₂ Conv. = 89.6%) > CeCo/MA (CH₄ Conv. = 82.4%, CO₂ Conv. = 88.6%) > SmCo/MA (CH₄ Conv. = 79.9%, CO₂ Conv. = 83.8%) > Co/MA (CH₄ Conv. = 71.3%, CO₂ Conv. = 73.5%) within 8 h of CO₂-CH₄ reforming. The improvement in catalytic activity of Co/MA catalyst by promoter (La, Ce, Y and Sm) addition concurred with the previous findings in the literature (De la Luz et al., 2013; Ibrahim et al., 2016; Z. Wang et al., 2007; R. Yang et al., 2010).

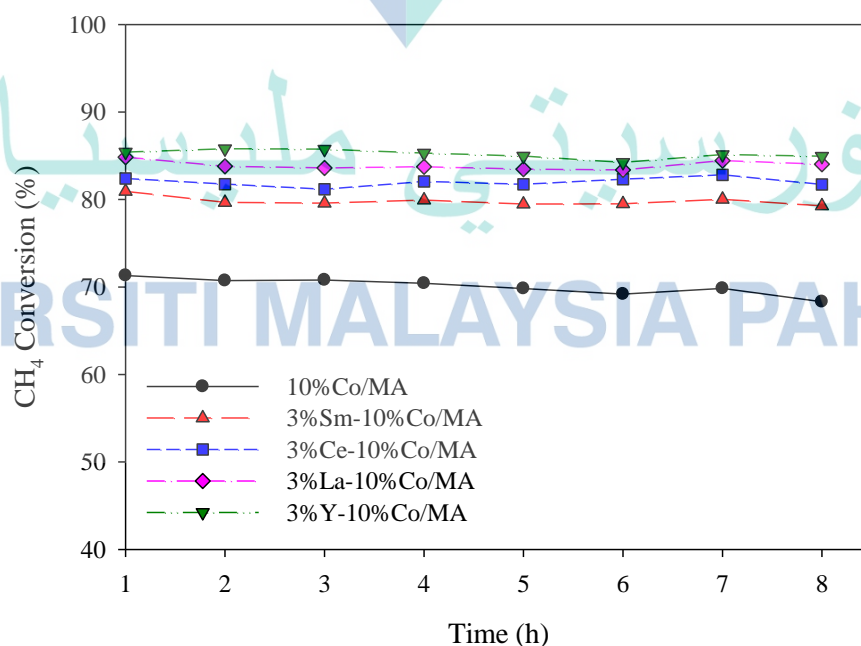


Figure 4.14 CH₄ conversion of promoted and unpromoted catalysts as a function of time.

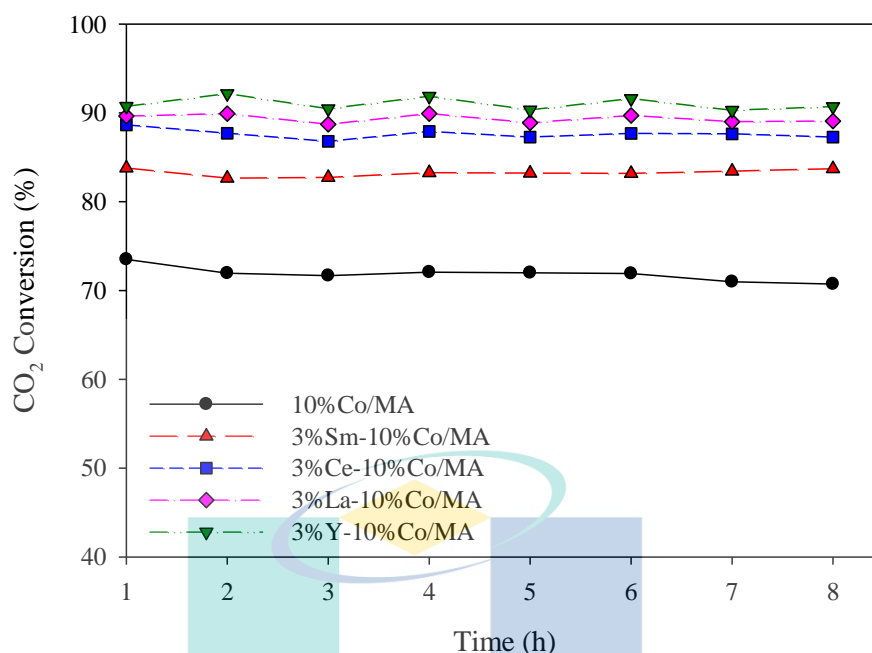


Figure 4.15 CO₂ conversion of promoted and unpromoted catalysts as a function of time

In order to assess the catalytic stability, percentage for the degree of catalyst deactivation in CO₂-CH₄ reforming was computed based on the decrement in CH₄ conversion after 8 h of CO₂-CH₄ reforming (Table 4.2). Notably, the degree of catalyst deactivation measured for each catalyst was minimized in the order: Co/MA (4.21%) < SmCo/MA (2.04%) < LaCo/MA (0.95%) < CeCo/MA (0.84%) < YCo/MA (0.57%), which correlated with the redox properties of these promoters. Pizzolitto et al. (2018) investigated the redox ability of Ce and La towards Ni-based catalysts for syngas generation. They strongly disagreed that the redox abilities of both metals not only improved catalyst stability, but it also effectively assisted in enhancing carbon gasification, thus preserving the catalyst from deactivation.

Apart from that, there are a few studies that described that La₂O₃, Y₂O₃, and Sm₂O₃ can simply react with CO₂ for producing an oxycarbonate species that is favorable for the carbon removal process. Oemar, Hidajat, and Kawi (2011) reported that yttrium oxycarbonate, Y₂O₂CO₃ generated between CO₂ and Y₂O₃ reaction was further utilized for the oxidation of surface carbon on PdO-NiO, hence promoting catalyst stability. A similar reasoning was attained by H. Liu et al. (2016) and Osazuwa, Khan, Lam, Assabumrungrat, and Cheng (2018) during the employment of La and Sm, respectively, for which the La₂O₂CO₃ or Sm₂O₂CO₃ intermediate compound was generated for minimizing the carbon deposit.

The (H_2/CO) ratio profiles as a function of reaction time during CO_2-CH_4 reforming at 1023 K are presented in Figure 4.16. According to these results, H_2/CO ratio of unpromoted catalyst exhibited inferior values (within 0.78-0.86) to the stoichiometric values of 1 as a consequence of the accrual in CO generation via RWGS. However, the addition of promoter slightly increased value of H_2/CO ratio close to 1, signifying that the incorporation of these metals (Ce, La, Y and Sm) could lessen the rate of RWGS. A similar inference has been stated by Chen et al. (2017), for which the H_2/CO ratio grew near to stoichiometric values when La was incorporated over Ni/SiO₂ catalyst for CO_2-CH_4 reforming. In terms of stability for H_2/CO ratio with time, 10%Co/MA exhibited a declining trend while 3%Y-10%Co/MA possessed almost a stable trend during 8 h of reforming, probably linked to the coke resistant ability of the catalyst.

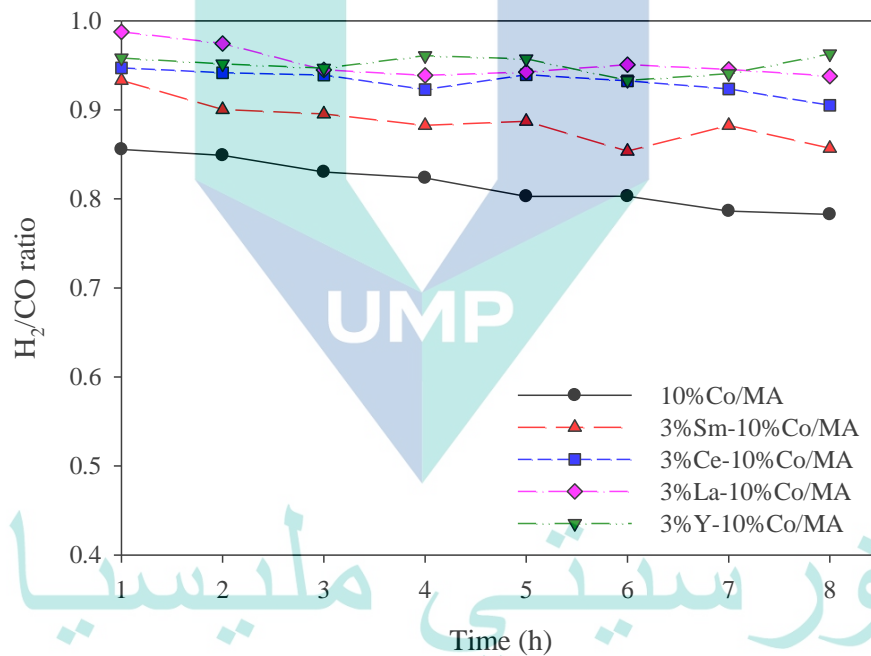


Figure 4.16 H_2/CO ratio of promoted and unpromoted catalysts as a function of time.

Figure 4.17 displays the overall catalytic performances of promoted and unpromoted catalyst during CO_2-CH_4 reforming. In terms of product yields, it was found that YCo/MA catalyst recorded optimum H_2 and CO yield values of about 64.0% and 66.5%, respectively, compared to Ce-, La-, Sm-promoted and unpromoted catalysts. As seen in Figure 4.17, both yield values were slightly improved in similar order as mentioned for the effect of promoter on reactant conversions ($Y > La > Ce > Sm > unpromoted$). This further proved that this promoter incorporation played a positive role in catalytic activity, crediting to their abilities in improving active metal distribution and

suppressing carbon accumulation. Besides, H₂ yield exhibited by all catalysts in this work was slightly lower than CO yield, corroborating the concomitant of RWGS during CO₂-CH₄ reforming. The superior value of CO₂ yield than H₂ yield is in agreement to a previous work carried out by Al-Fatesh, Fakeeha, and Abasaed (2011) where the authors examined the effect of Zr, Ce, and Ca incorporation toward Ni supported by γ -Al₂O₃ in CO₂-CH₄ reforming. Based on the overall catalytic performances of promoted and unpromoted catalysts plotted in Figure 4.17, the employment of Y promoter on Co/MA effectively improved the catalytic performance of Co/MA better than Ce, La, and Sm due to the smaller particle size, intense Co-MA interaction, well Co dispersion, and redox properties. Indeed, the high capacity for releasing/storing oxygen and its capability to form intermediate yttrium oxycarbonate compound proved its beneficial influence on carbon gasification since it exhibited the lowest carbon deposit and deactivation rate.

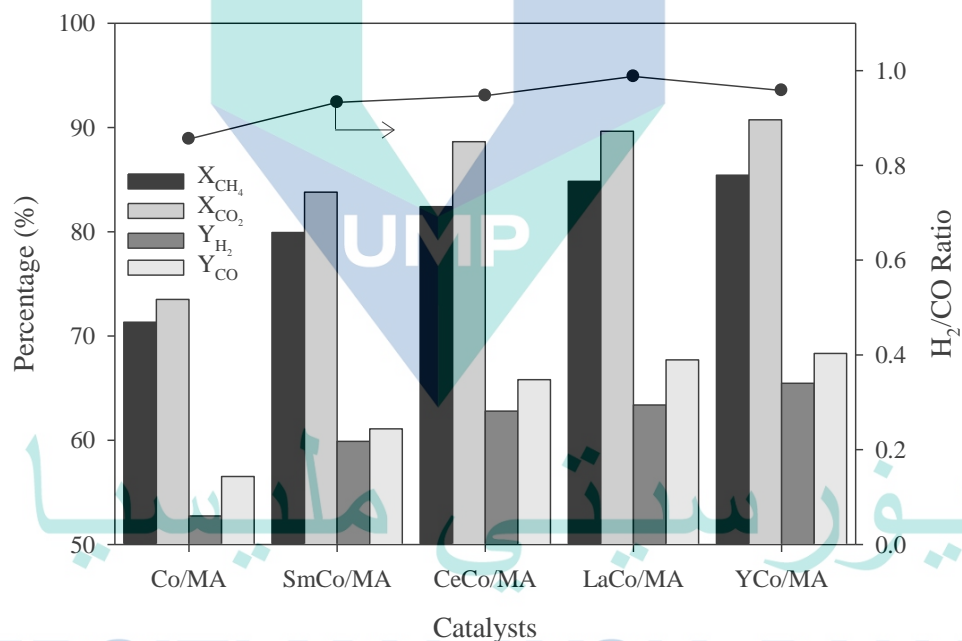


Figure 4.17 Catalytic performance comparison for all catalysts at steady state condition.

4.3.3 Post-Reaction Characterizations

4.3.3.1 X-ray Diffraction Analysis

The results of XRD diffraction peaks for all utilized catalysts after 8 h of CO₂-CH₄ reforming are revealed in Figure 4.18. It is shown that all the spent catalysts possessed an X-ray reflection of graphite carbon at value 2θ of 26.38° (JCPDS card No.

75-0444) (Y.-F. Wang, Tsai, Chang, & Kuo, 2010). Interestingly, the strength for X-ray reflection of graphite for promoted catalysts as depicted in Figure 4.18 was slightly lessened with the addition of Ce, La, Sm, and Y promoter compared with the unpromoted catalyst, which was attributed to the high storage capacity of oxygen for these metals, resulting in better carbon resistance. Taufiq-Yap, Sudarno, Rashid, and Zainal (2013) reported a similar observation for CeO₂-SiO₂ supported nickel catalyst, credited to the high capacity of Ce in storing/releasing oxygen. The decline of graphite peak intensity in the order of Co/MA > LaCo/MA > CeCo/MA > SmCo/MA > YCo/MA, indicated the superior role of Y promoter in carbon suppression. Additionally, X-ray reflection lines recorded at $2\theta = 31.45^\circ$, 37.10° , and 44.79° corresponded to Co₃O₄ phases (JCPDS card No. 74-2120), which indicated the re-oxidation of active Co⁰ by CO₂ during 8 h CO₂-CH₄ reforming (X. Zhang et al., 2018). Compared to Figure 4.12, a low intensity peak of spinel CoAl₂O₄ was observed at $2\theta = 65.38^\circ$ (JCPDS card No. 82-2246) on all spent catalysts (Zhao & Li, 2015).

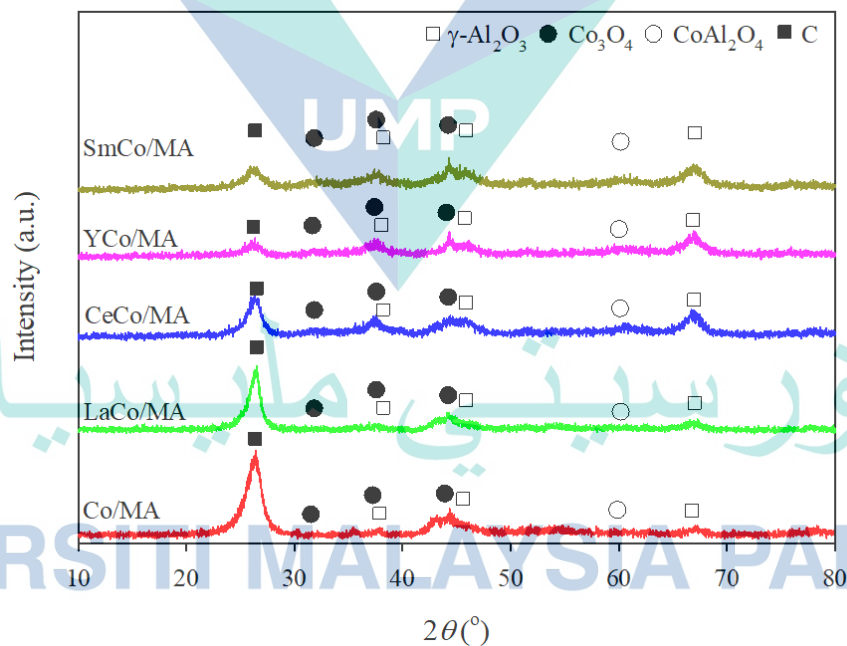


Figure 4.18 XRD patterns of spent Co/MA and promoted Co/MA catalysts after 8 h CO₂-CH₄ at T = 1023 K, GHSV = 36000 mL g_{cat}⁻¹ h⁻¹, and CO₂:CH₄:N₂ = 1:1:3.1.

4.3.3.2 X-ray Photoelectron Spectroscopy

XPS analysis was operated for determining the oxidation state as well as the surface atomic composition of spent promoted and unpromoted catalysts. Figure 4.19 depicts the spectra acquired from XPS measurement, whilst the values of corresponding binding energy (BE) are listed in Table 4.3. Co 2p spectra for all spent catalysts were fitted with Gaussian deconvolution, as appeared in Figure 4.19(a). Notably, there are four deconvoluted peaks observed at BE at about 778.6 eV, 780.3-780.8 eV, 781.0-781.1 eV, and 784.9 eV, which were ascribed to Co^0 , CoAl_2O_4 , Co_3O_4 , and a shake-up satellite for Co 2p_{3/2} region, respectively (Álvarez-Docio, Reinosa, Del Campo, & Fernández, 2019; Ao et al., 2018; Paksoy et al., 2015). On the other hand, a similar number of peaks was detected under the Co 2p_{1/2} section at 793.5-793.4 eV, 795.3-795.5 eV, 796.6-796.9 eV, and 803.1-803.2 eV which belonged to metallic Co, Co_3O_4 , spinel CoAl_2O_4 , and satellite for Co 2p_{1/2} region, respectively (Álvarez-Docio et al., 2019; Ao et al., 2018; Paksoy et al., 2015). Certainly, the detection of those Co species was also consistent with the XRD findings (Figure 4.18). As seen in Figure 4.19(a), Co 2p_{1/2} peak associated with metallic Co at BE about 793.5 eV for Co/MA catalysts was not detected, probably due to the low dispersion of Co on MA support.

In order to investigate the influence of promoter addition toward Co dispersion over MA support, the Co/Al atomic ratios by XPS were estimated and summarized in Table 4.3. The Co/Al atomic ratios were improved in the order of Co/MA (0.17%) > SmCo/MA (0.26%) > CeCo/MA (0.34%) > LaCo/MA (0.54%) > YCo/MA (2.67%), suggesting the improvement in Co dispersion with the addition of promoter. The improvement in the metal/Al atomic ratio with promoter employment was also reported by Meng, Li, Liu, Cui, and Zheng (2015) for Ce-promoter over Ni/Al₂O₃ catalyst, indicating a positive impact of promoter in improving the dispersion of metal particles. The largest Co/Al atomic ratios of YCo/MA clarified the smaller particle size and strong Co-MA interaction owned by YCo/MA catalyst as discussed in BET and TPR findings, which resulted in superior performances of YCo/MA catalyst within 8 h of CO₂-CH₄ reforming compared to other catalysts.

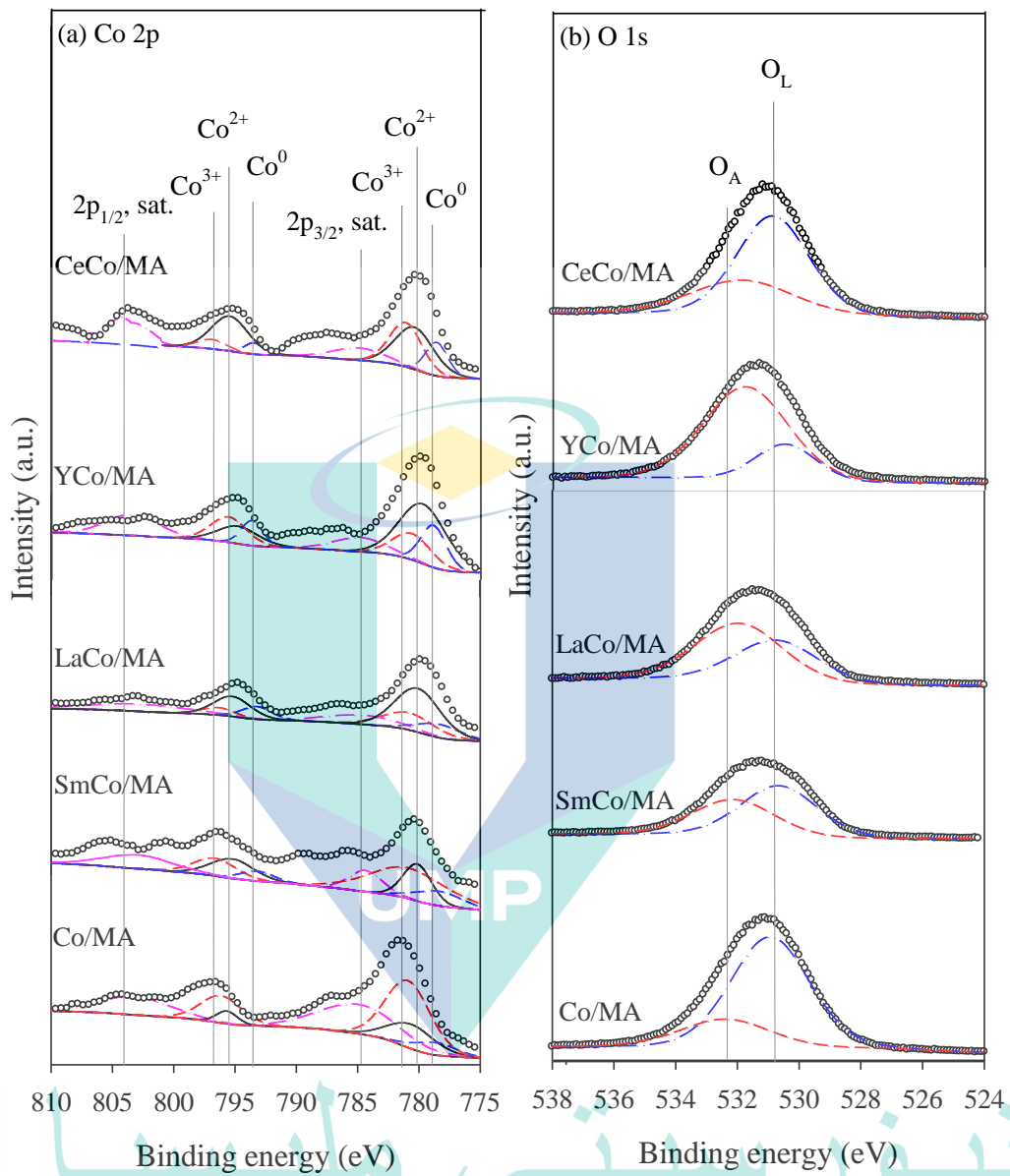


Figure 4.19(a) Co 2p and (b) O 1s XPS spectra of used promoted and unpromoted catalysts after 8 h CO_2 - CH_4 reforming at $T = 1023$ K, $GHSV = 36000$ mL $g_{cat}^{-1} h^{-1}$ and $CO_2:CH_4:N_2 = 1:1:3.1$.

Table 4.3 Binding energies, atomic ratios and oxygen vacancies values obtained from the XPS analysis of all spent catalysts.

Catalyst	Binding energy (eV)				Atomic ratio Co/Al	O _v (%)
	Co 2p _{3/2}	Co 2p _{1/2}	C 1s	O 1s		
Co/MA	778.6	795.5	284.6	530.8	0.17	24.4
	780.8					
	781.1					
	784.9					
YCo/MA	778.6	793.5	284.6	530.5	2.67	78.1
	780.8					
	781.1					
	784.9					
CeCo/MA	778.6	795.4	284.6	530.6	0.34	34.8
	780.4					
	781.0					
	784.9					
LaCo/MA	778.6	793.5	284.6	530.7	0.54	29.8
	780.5					
	781.1					
	784.9					
SmCo/MA	778.6	793.5	284.6	530.8	0.26	22.6
	780.3					
	781.1					
	784.9					

The deconvolution of O 1s spectra as exposed in Figure 4.19(b) discovered two main peaks at BE about 530.5-530.8 eV and 532.0-532.4 eV linked to lattice oxygen (O_L) which was associated with Al_2O_3 and Co_3O_4 and surface adsorbed oxygen (O_A) respectively (N. Wang, K. Shen, et al., 2013). Based on previous literature, the number of oxygen vacancies (O_V) can be estimated based on the ratio of peak integrated areas for O_L and O_A ($O_V(\%) = (A_{O_A} / (A_{O_A} + A_{O_L})) \times 100(\%)$) (J. Zhang, Li, Wang, Zhang, & He, 2015). As summarized in Table 4.3, YCo/MA catalyst possessed the highest O_V of 78.1% followed by CeCo/MA, LaCo/MA, SmCo/MA, and Co/MA. The highest oxygen vacancies of YCo/MA catalyst may enrich carbon gasification since oxygen vacancies were able to act as an active site for activating CO_2 during CO_2-CH_4 reforming. This advantage further clarified the steady catalytic performance and low deactivation rate exhibited by YCo/MA compared to its counterparts.

As revealed in Figure 4.20, the C 1s spectra of all promoted catalysts have two deconvoluted peaks which were attributed to two different carbon species generated via Boudouard or CH_4 decomposition. The fitted curve located at binding energy of about

284.6 eV belonged to graphitic carbon (ordered and nonreactive), whereas the deconvoluted peak centered about 285.3 eV belonged to amorphous carbon (less ordered and reactive) (Dang et al., 2017). The deposition of both of these carbon structures identified through XPS was consistent to results obtained in TPO. Remarkably, the C 1s spectra for all promoted catalysts showed smaller peaks compared to the unpromoted catalyst, further confirming that effectiveness of coke resistance ability exhibited by Ce, La, Sm and Y promoters.

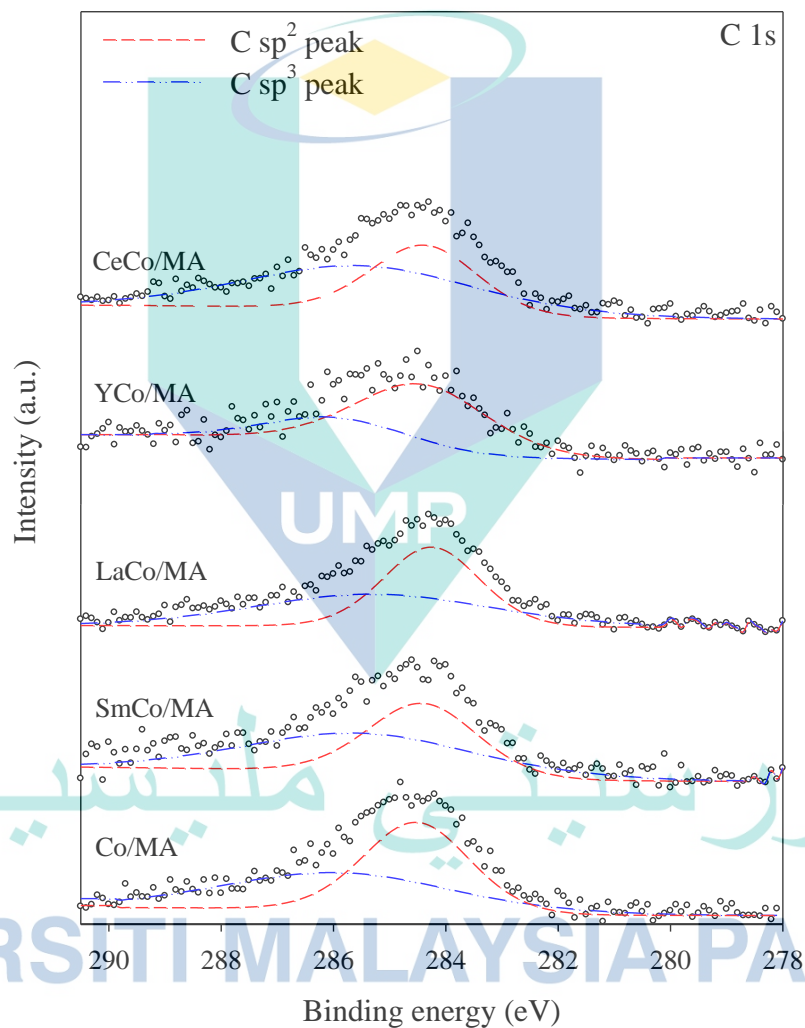


Figure 4.20 C 1s XPS spectra of used promoted and unpromoted catalysts after 8 h CO₂-CH₄ reforming at T = 1023 K, GHSV = 36000 mL g_{cat}⁻¹ h⁻¹ and CO₂:CH₄:N₂ = 1:1:3.1.

4.3.3.3 Temperature-Programmed Oxidation

The total amount of coke formed within 8 h CO₂-CH₄ reforming was estimated through TPO analyses and both derivative weight and weight loss profiles are displayed in Figure 4.21. As can be seen, two discrete peaks eluting between the temperature range of 600-950 K in derivative weight profile symbolized the oxidation of carbon which had two different bonding configurations. The low-temperature peak (P1) located within the range of 700-800 K was related to the elimination of non-crystalline amorphous carbon which was highly reactive toward oxygen (Swatsitang, Phokha, Hunpratub, & Maensiri, 2016). The other peak (P2) observed at high oxidation temperature (> 800 K) was appointed to the removal of crystalline graphitic carbon (Swatsitang et al., 2016). Based on the CO₂-CH₄ reforming literature, both carbon species were typically accumulated on the catalyst surface through side reaction either via Boudouard ($2CO \rightarrow CO_2 + C(s)$) or CH₄ cracking ($CH_4 \rightarrow 2H_2 + C(s)$) (Khajenoori, Rezaei, & Meshkani, 2015). Remarkably, the incorporation of promoters significantly lessened the intensity for graphitic peak, supporting the previous observation in XRD results of employed catalysts (Figure 4.18).

Apart from that, the percentage of weight loss was lowered with promoter addition in the order of 10%Co/MA (28.21%) > 3%Sm-10%Co/MA (26.95%) > 3%La-10%Co/MA (19.49%) > 3%Ce-10%Co/MA (17.35%) > 3%Y-10%Co/MA (7.02%). This result inferred that the incorporation of promoters efficiently suppressed carbon deposited on the catalyst surface due to their multi-advantages, namely, high oxygen vacancies, strong basic attributes and excellent redox properties (X. Huang et al., 2016; Rabiah Nizah et al., 2014; Taherian et al., 2017c). Besides, the formation of intermediate oxycarbonate compound (Y₂O₂CO₃, La₂O₂CO₃, and Sm₂O₂CO₃) aforementioned in the reaction part also proved the high carbon-resistance abilities of those promoted catalysts. Interestingly, the trend of the percentage of weight loss was almost similar to the trend for crystallite size, with YCo/MA recording better values for both trends. Xin et al. (2018) inferred that the increment in crystallite size could promote the rate of carbon deposition. Thus, this statement further verified the lower amount of carbon deposited by YCo/MA compared to other catalysts after 8 h CO₂-CH₄ reforming. However, that statement is not in agreement with the addition of Sm-promoter since it exhibited the second highest carbon deposit, although it had a small crystallite size compared to Ce and La-promoted

catalysts. This phenomenon could be due to the acidic attributes resulted from the combination between Co and Sm, as previously reported by Taherian et al. (2017a) during the employment of Sm over Co/SBA-15 for CO₂-CH₄ reforming. In fact, they also observed lower catalytic performances in CO₂-CH₄ reforming after introducing Sm-promoter on Co/SBA-15 compared to Ni/SBA-15, consistent with this work's 3%Sm-10%Co/MA performance.

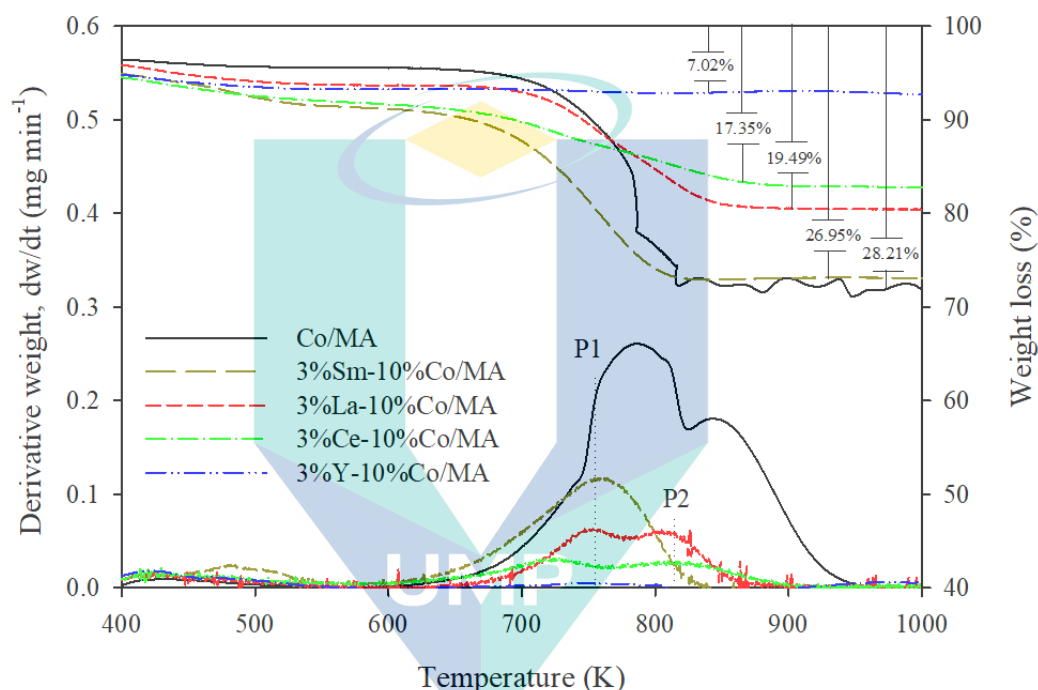


Figure 4.21 TPO profiles and weight loss of the spent catalysts after 8 h CO₂-CH₄ reforming at T = 1023 K, GHSV = 36000 mL g_{cat}⁻¹ h⁻¹ and CO₂:CH₄:N₂ = 1:1:3.1.

4.3.3.4 High Resolution Transmission Electron Microscopy

The morphologies of MA support and all spent catalysts for CO₂-CH₄ reforming obtained from HRTEM analysis are revealed in Figure 4.22. On these images, Co particles exist as dark dots while MA support can be detected in grey depended on the different of electronic density. For HRTEM image of spent 10%Co/MA (cf. Figure 4.22(b)), some agglomerations of Co metal particles (yellow circle) were observed over the MA support, resulting in large Co particle size (around 13.6 nm). However, it can be noted that Co particle size was slightly lessened in Figure 4.22(c)-(f) with less agglomeration, suggesting that the addition of those promoters led to fine and narrow size distributions of Co particles over MA support within 11.0-12.5 nm (cf. Table 4.2). Apparently, the crystallite size of Co₃O₄ from catalysts was reduced with the trend of Co/MA

> CeCo/MA > LaCo/MA > SmCo/MA > YCo/MA, which directly related to the strength of Co-MA interaction as reviewed in TPR. Hence, strong Co-MA interaction belonging to YCo/MA revealed its superior sintering resistibility compared to other catalysts.

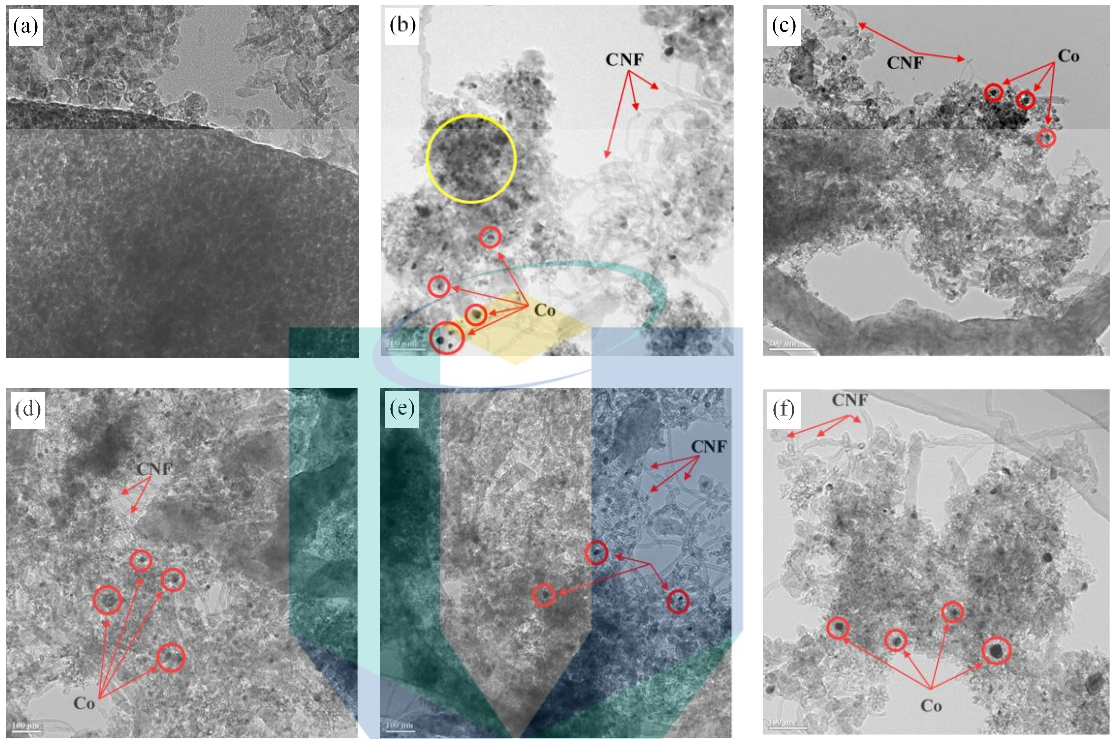


Figure 4.22 HRTEM images of (a) MA support, spent (b) Co/MA, (c) LaCo/MA, (d) CeCo/MA, (e) YCo/MA and (f) SmCo/MA catalysts after 8 h of CO₂-CH₄ reforming at T = 1023 K, GHSV = 36000 mL g_{cat}⁻¹ h⁻¹ and CO₂:CH₄:N₂ = 1:1:3.1.

Apart from that, it is apparent that carbon nanofilaments (CNF) were inevitably generated on all spent catalysts as seen in Figure 4.22(b)-(f). Previously, it was reported that a CNF consists of a hollow inner channel inside, which could be easily gasified with CO₂ and not cause any negative consequence on catalytic activity (Rabiah Nizah et al., 2014). Indeed, this type of carbon could relocate the active metal on the top of filament, thus maintaining the accessible contact with gas flow and hindering the deactivation of catalyst (Djinović, Osojnik Črnivec, et al., 2012). R. Yang et al. (2010) also reported that spent 10%Ni/3%CeO₂-3%LaO₃-γ-Al₂O₃ possessed a huge amount of CNF compared to its counterpart. Thus, the authors inferred that the addition of La₂O₃ and CeO₂ was able to stimulate the formation of CNF. The appearance of CNF type was also noted by J. F. Li et al. (2014) during the evaluation of SBA-15 supported on Y-NiO catalyst .

4.4 Impact of Yttrium Promoter Loading on Co/MA Catalyst for CO₂-CH₄ Reforming

In previous subchapter, YCo/MA catalyst possessed superior catalytic performance as compared to other catalysts at stoichiometric feed composition and reaction temperature of 1023 K. Therefore, in this work, a series of different weight percentage of yttrium (1, 2, 3 and 5wt.%) loaded to 10%Co/MA catalysts were prepared, and their structures were characterized using several techniques. In addition, the influence of yttrium loading towards the CO₂-CH₄ reforming performance was evaluated and interpreted through this work. Furthermore, the optimal yttrium promoter loading for 10%Co/MA catalyst in terms of catalytic performance will be further conducted in the longevity tests for a duration of 72 h at stoichiometric condition for evaluating their catalytic stability.

4.4.1 Catalyst Characterizations

4.4.1.1 Textural Characteristics

The textural characteristic of prepared MA support, unpromoted and Y₂O₃-promoted catalysts in terms of average BET surface area are listed in Table 4.4. As can be noticed from the table, the successive 10wt.% Co incorporation led to an inevitable decline in the average BET surface area for MA support from 243 m² g⁻¹ to 204 m² g⁻¹. This observation was ascribed to the partial blockage of support pores by Co oxide clusters (Martínez, López, Marquez, & Díaz, 2003; G. Zhang et al., 2014). The decrement trend was continued with the adoption of 1-2wt.% Y₂O₃ promoter on 10%Co/MA catalysts since some pore structures of MA support were blocked by both Co and Y₂O₃ particles. In fact, both amounts were not enough to assist the dispersion of Co particles on the Co/MA surface. However, the increment in surface area was recorded with the rising of promoter loading beyond 2wt.% Y₂O₃, suggesting that a positive impact in particles dispersion has effectively worked. Both trends recorded through this analysis were also attained by J. F. Li et al. (2014) when the authors incorporated about 3, 6, and 9wt.% of Y₂O₃ promoter over NiO/SBA-15.

Table 4.4 Textural properties of MA support $\delta\%$ Y-10%Ni/MA ($\delta = 0$ -5wt%) catalyst.

Catalyst	Average BET surface area ($\text{m}^2 \text{g}^{-1}$)	Average Co_3O_4 particle size (nm)
MA support	243	-
10%Co/MA	204	12.9
1%Y-10%Co/MA	143	12.8
2%Y-10%Co/MA	144	12.7
3%Y-10%Co/MA	156	12.7
5%Y-10%Co/MA	160	12.8

^a Determined by XRD at 2θ of 31.45° .

4.4.1.2 X-ray Diffraction Analysis

The XRD spectra attained for calcined MA support and $\delta\%$ Y-10%Co/MA ($\delta = 0, 1, 2, 3, \text{ and } 5\text{wt.}\%$) samples are presented in Figure 4.23. As pictured in Figure 4.23(b)-(f), all the calcined catalysts possessed the peak of $\gamma\text{-Al}_2\text{O}_3$ phase at value 2θ at about $19.45^\circ, 32.30^\circ, 36.99^\circ, 45.69^\circ$ and 67.20° (JCPDS card No. 04-0858) tallied with XRD spectra of calcined MA support (cf. Figure 4.23(a)) (Braga, Essayem, & Valentini, 2017; Yin et al., 2013). The crystalline diffraction peaks for (220), (311), (400), (511), and (440) planes of Co_3O_4 were clearly observed in Figure 4.23(b)-(f) at angle 2θ about $31.45^\circ, 37.10^\circ, 44.79^\circ$ and 55.66° (JCPDS card No. 74-2120), respectively [34, 35]. Additionally, 2θ value centred at 59.51° and 65.38° as shown in Figure 4.23(b)-(f) belonged to the CoAl_2O_4 spinel (JCPDS card No. 82-2246), which corresponded to the (511) and (440) reflections (P. Li et al., 2011; Z. Wang et al., 2007). The existence of spinel CoAl_2O_4 species on the surface of all calcined catalysts was possibly because of the intense Co-MA interaction. A slight increment in the intensities of these peaks with an increase in Y_2O_3 loadings signified the increment in strength of Co-MA interaction upon the rising of Y_2O_3 loadings. Regardless of promoter loading (0-5wt%), the characteristic peak belonging to Y_2O_3 cubic phase (JCPDS card No. 41-1105) was not detected for all promoted catalysts (cf. Figure 4.23(c) to Figure 4.23(f)) because of the fine dispersion of Co_3O_4 particles on MA support (Joshi, Dwivedi, & Rai, 2014). Scherrer formula was applied for estimating the mean crystallite size of Co_3O_4 .

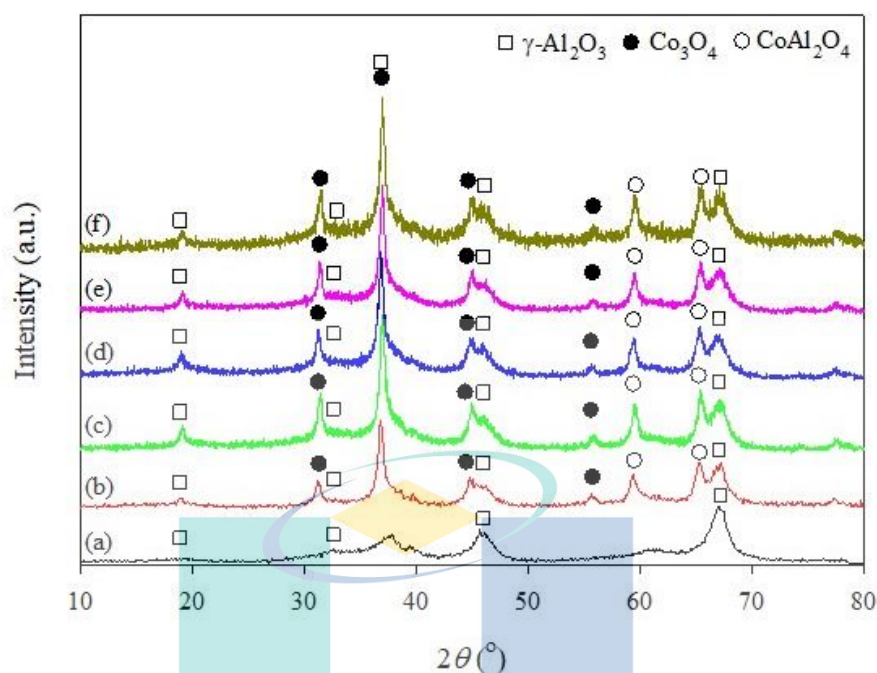


Figure 4.23 XRD patterns of (a) MA support, (b) 10%Co/MA, (c) 1%Y-10%Co/MA, (d) 2%Y-10%Co/MA, (e) 3%Y-10%Co/MA and (f) 5%Y-10%Co/MA.

As seen in Table 4.4, the reduction in the average particle size of Co_3O_4 was discerned with the increase in Y_2O_3 loading from 0-3wt.%. This was due to the role of Y_2O_3 promoter acting as a capping agent to prevent the agglomeration of cobalt particles during the calcination process (J.-Y. Park et al., 2011). Indeed, it is a positive indication that the employment of Y_2O_3 as a promoter could improve the dispersion quality of Co particles on MA support. However, those values were slightly higher with the Y_2O_3 loading of 5wt.%, probably because of the high diffusion competition among the Y_2O_3 promoter and Co_3O_4 . An excess amount of Y_2O_3 may reside on the surface of MA support, hence contributing to metal agglomeration.

4.4.1.3 Temperature Programmed Reduction

The results of TPR profiles deconvolution for as-prepared 10%Co/MA catalysts with 0, 1, 2, 3, and 5wt.% of Y_2O_3 loading are displayed in Figure 4.24. In previous findings, G. B. Sun, Hidajat, Wu, and Kawi (2008) and Passos, Oliveira, Mattos, and Noronha (2006) found that the pure Y_2O_3 can only be partially reduced within 733-1073 K due to the consumption of surface oxygen with hydrogen. However, no reduction peak related to Y_2O_3 was detected in this study, probably due to the low concentration of Y_2O_3 or overlapping with Co reduction peaks, in accordance with the TPR findings stated by

J. F. Li et al. (2014) and Bellido and Assaf (2009). As seen in Figure 4.24(a)-(e), regardless of catalysts, three deconvoluted reduction peaks were detected at the temperature range of 674.7-1011.8 K due to the reduction of different types of cobalt particles in the catalyst. The reduction peak detected in the temperature range from 674.7-724.4 K for all reduced catalysts signified the metal oxide reduction; $\text{Co}_3\text{O}_4 \rightarrow \text{CoO}$ and $\text{CoO} \rightarrow \text{Co}^0$ with different strengths of Co-MA interaction. Meanwhile, the reduction peaks located at temperature above 850 K corresponded to the reduction of cobalt aluminate (CoAl_2O_4) to metallic Co with strong metal-support interaction (Cooper et al., 2008; Hull & Trawczyński, 2014).

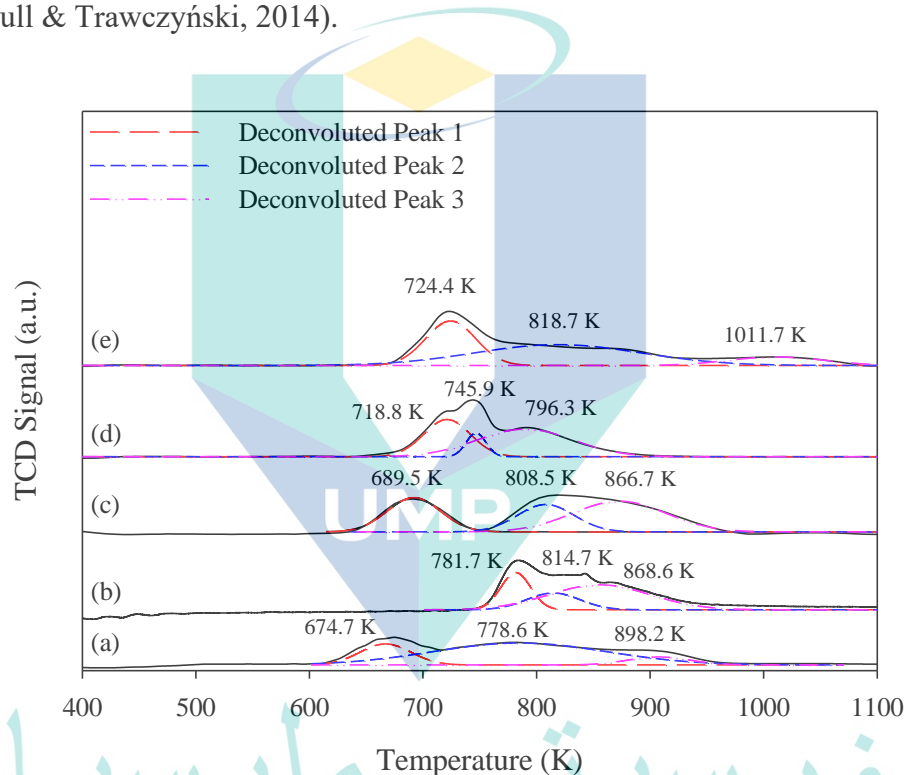


Figure 4.24 H_2 temperature-programmed reduction of (a) 10%Co/MA, (b) 1%Y-10%Co/MA, (c) 2%Y-10%Co/MA, (d) 3%Y-10%Co/MA and (e) 5%Y-10%Co/MA.

As shown in Figure 4.24, the first reduction peak at 674.7 K in 10%Co/MA catalyst was slightly increased after the incorporation of Y_2O_3 , suggesting the enhancement in the interaction between both Co and MA support. These results also clearly justified the smaller crystal size of Co particles obtained in the XRD results (cf. Figure 4.23). Apart from the rise in Co-MA interaction, the increment in reduction temperature and appearance of high reduction temperature peak for 5% Y_2O_3 loading at a temperature above 850 K could also indicate that some of the Co particles on Co/MA were inevitably covered by the Y_2O_3 rich environment, thus demanding higher temperature to be reduced. The slight increment noticed on some reduction peaks after

the incorporation of the promoter which was linked to the strength of metal-support interaction and size particles was coherent with the previous works (J. F. Li et al., 2014).

4.4.2 Reaction Analysis

The relationships between reactant conversion and Y_2O_3 promoter loadings during CO_2 - CH_4 reforming ($T = 1023$ K and CH_4/CO_2 molar ratio = 1:1) are shown in Fig. 3. Regardless of promoter loading, the value of CO_2 conversion (Figure 4.25(B)) is greater than CH_4 (Figure 4.25 (A)), inferring the involvement of RWGS. Additionally, it was apparent that the conversion profiles for both CH_4 and CO_2 were slightly improved and achieved optimum values at about 85.8% and 90.5% respectively upon the increase of Y_2O_3 loading from 0 to 3wt.%. This positive impact could be clarified by the improvement of Co metal dispersion on the catalyst surface with the addition of Y_2O_3 . As previously stated in the average particle size discussion, the spacing effect initiated by the Y_2O_3 promoter was responsible for minimizing the agglomeration of Co particles, hence providing more exposed active Co sites for the reaction. In literature, Santos, Madeira, and Passos (2010) also found out that the incorporation of Y_2O_3 as catalyst promoter on $Ni/\alpha-Al_2O_3$ efficiently segregated Ni active metals on the catalyst surface, hence enhancing the dispersion rate of active metal particles.

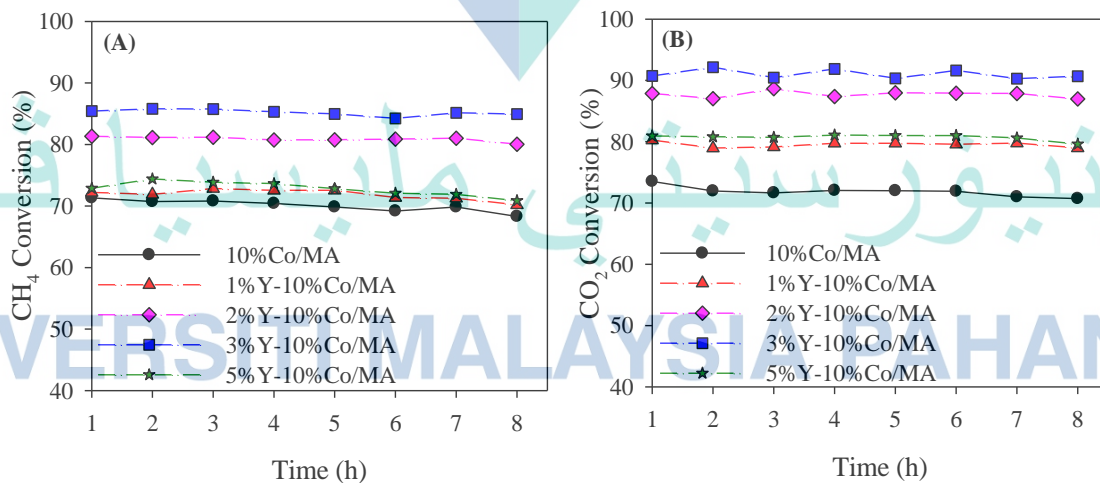


Figure 4.25 Effect of yttrium loading on (A) CH_4 and (B) CO_2 conversions during CO_2 - CH_4 reforming at 1023 K and molar ratio of $CH_4/CO_2 = 1:1$ for 8 h time-on-stream.

Besides, the improvement in catalytic activity was possible due to the efficient removal of surface carbon related to the remarkable oxygen storage/release capability of Y_2O_3 but this is inconsistent with the trend observed by Świrk et al. (2018) and Atribak, Bueno-López, and García-García (2009) with Y_2O_3 promoter incorporation. In another study, J. F. Li et al. (2014) evaluated the influence of Y_2O_3 loading over SBA-15 supported Ni in CO_2 - CH_4 reforming. The author observed the enhancement of catalytic performances with low carbon deposition rate alongside the increment of Y_2O_3 loading. However, in our case, those values experienced a slight drop with Y_2O_3 loading beyond 3wt.%, probably due to the competitive diffusion of Y_2O_3 and Co_3O_4 particles in high Y_2O_3 loading, resulting in the decrement of Co dispersion. Thus, the slight increment in Co_3O_4 crystallite size was noticed for 5wt.% Y_2O_3 (cf. Table 4.4). Besides, this behaviour can also be explained with the inevitable closure of some Co active sites by Y_2O_3 particles during the impregnation step. Therefore, reduction peaks in TPR analysis (cf. Figure 4.24) exhibited a slight change towards higher temperatures which explained that Co particles covered by Y_2O_3 particles were not easy to be reduced.

The catalytic stability of prepared catalysts for CO_2 - CH_4 reforming was evaluated by calculating the degree of catalyst deactivation (D_d). It was evident that the degree of catalyst deactivation decreased in the order; 10%Co/MA (4.2%) > 1%Y-10%Co/MA (2.8%) > 5%Y-10%Co/MA (2.7%) > 2%Y-10%Co/MA (1.6%) > 3%Y-10%Co/MA (0.6%). Apparently, the addition of the Y_2O_3 promoter efficiently minimized the degree of catalyst deactivation. Several studies reported that this trend was directly attributed to the redox properties of Y_2O_3 which efficiently assisted the carbon removal process and retained the active metal-free from carbon formation (Amin, Putla, Bee Abd Hamid, & Bhargava, 2015; Younis, Malaibari, Ahmad, & Ahmed, 2018). As clearly pointed out by Y. Wang et al. (2014), Y_2O_3 and CO_2 easily reacted to form an intermediate yttrium oxycarbonate, $Y_2O_2CO_3$ which is highly reactive towards surface carbon species, hence preserving the active metal sites (cf. Eqs. (4.8) and (4.9)). Thus, this evolution could clearly explain the stable catalytic activity with 8 h time on stream (cf. Fig. 3).



Figure 4.26 displays the influence of Y_2O_3 loading on the syngas ratio. The same trend was also observed with the increment of Y_2O_3 loading from 0-5wt.%. Again, this result can also be clarified from the dispersion efficiency of Co metal on support surfaces. Typically, CO_2-CH_4 reforming generates a syngas ratio of 1.0. However, the syngas ratio between 0.83 to 0.95 was obtained in this study over the unpromoted and Y_2O_3 -promoted catalysts based on the RWGS reaction (Singh et al., 2018).

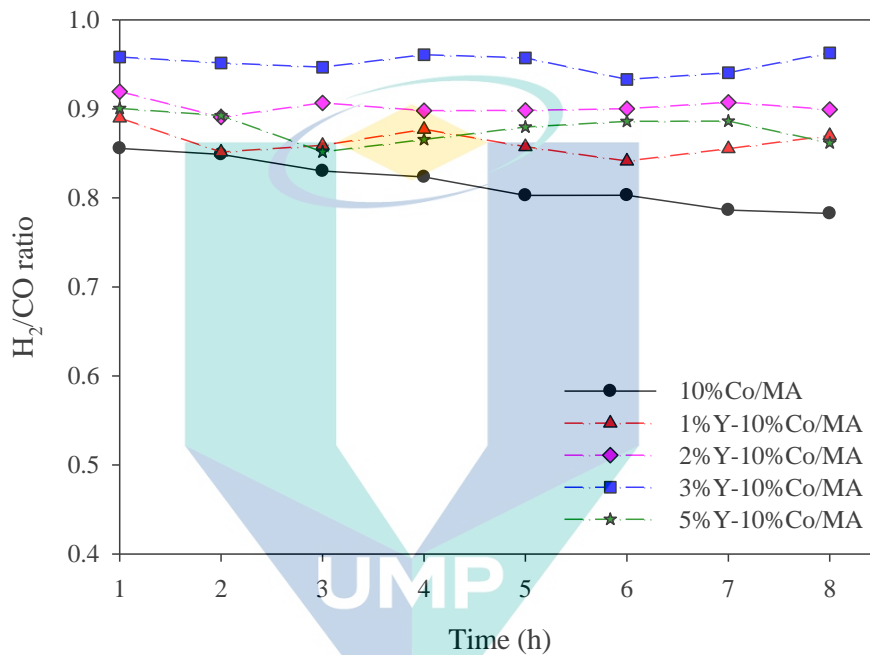


Figure 4.26 Effect of yttrium loadings on H_2/CO ratio during CO_2-CH_4 reforming at 1023 K and molar ratio of $CH_4/CO_2 = 1:1$ for 8 h time-on-stream.

The yield of H_2 and CO which improved up to 46.9% and 23.8% in this order with increasing Y_2O_3 loading from 0 to 3wt.% (cf. Figure 4.27) proved the clear correlation between active metal dispersion and catalytic performance as aforementioned for the improvement in reactant conversion. Afterwards, as loading of the Y_2O_3 promoter rose beyond 3wt.%, the small decline of both product yields was noticed and achieved about 53.5% and 59.3%, respectively. This point strengthened the idea that the high promoter loading of Y_2O_3 certainly covered Co active sites and lowered the surface concentration of Co. Apart from that, the yield of CO was always greater than H_2 yield for all catalysts indicating that H_2 generated from the main reaction was continuously consumed by the RWGS reaction.

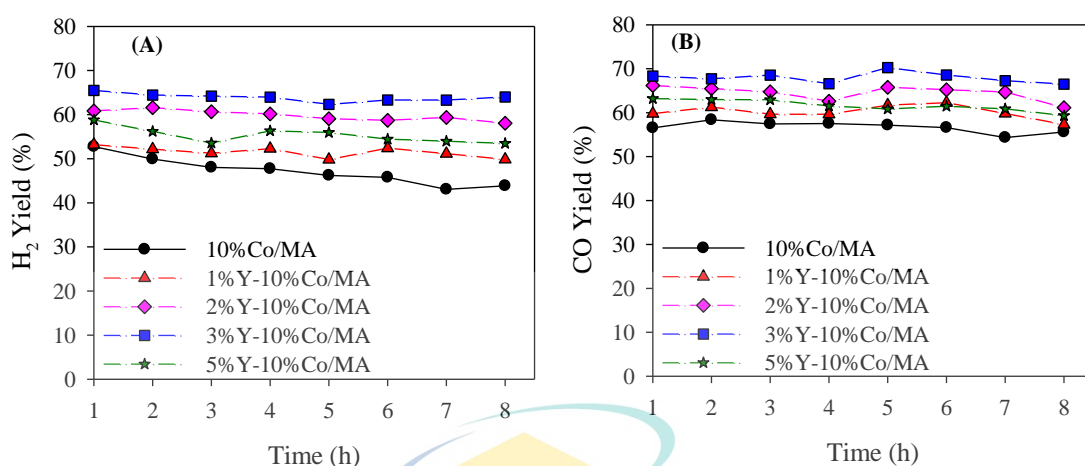


Figure 4.27 Effect of yttrium loading on (A) H₂ and (B) CO yields during CO₂-CH₄ reforming at 1023 K and molar ratio of CH₄/CO₂ = 1:1 for 8 h time-on-stream.

4.4.3 Post-Reaction Characterizations

4.4.3.1 X-ray Diffraction Measurement

The diffractograms of the used Y₂O₃-promoted and unpromoted catalysts after 8 h of CO₂-CH₄ reforming are illustrated in Fig. 6. The strong diffraction lines corresponding to graphite carbon phases (002) was noticed at angle 2θ of 26.38° (JCPDS card No. 75-0444) on the surface of all used catalysts. According to the XRD patterns, the reduction in the intensity of graphitic phase reflection observed with the increment of Y₂O₃ promoter loading might be due to the improvement in oxygen mobility facilitating carbon gasification (J. F. Li et al., 2014). CoAl₂O₄ spinel reflection was detected at 2θ of 65.38° (JCPDS card No. 82-2246). Additionally, all the XRD profiles of spent catalysts exhibited a low intense diffraction peak of metallic Co (200) at 2θ of 51.50° (JCPDS card No. 15-0806) and three characteristic peaks for Co₃O₄ at angle 2θ of 31.45°, 37.10° and 44.79° (JCPDS card No. 74-2120). This is an indication that most Co active metals were re-oxidised with CO₂ oxidising agent under the reforming reaction whilst some of these metals remained in the reduced form since a passivating layer of carbon successfully covered them, hence preventing the re-oxidation process (Estephane et al., 2015).

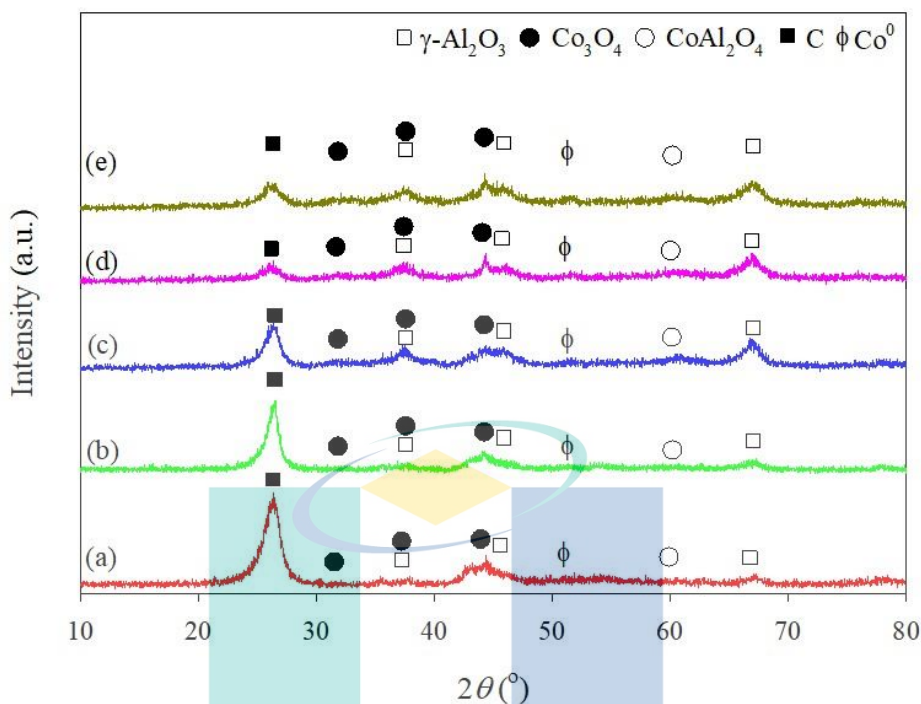


Figure 4.28 X-ray diffractograms of spent (a) 10%Co/MA, (b) 1%Y-10%Co/MA, (c) 2%Y-10%Co/MA, (d) 3%Y-10%Co/MA and (e) 5%Y-10%Co/MA.

4.4.3.2 High Resolution Transmission Electron Microscopy

The high-resolution TEM images of calcined MA support and all spent catalysts are presented in Figure 4.29. The black dots found in all the TEM images of spent catalysts represent the metallic Co particles on the MA support conforming to the reduction of Co_3O_4 , CoO and spinel CoAl_2O_4 as has been previously discussed in TPR analysis. As noticed in Figure 4.29(b)-(f), the Co particle size was slightly decreased with the addition of Y_2O_3 promoter, implying that the agglomeration of the Co particles on catalyst surface was effectively suppressed. This finding is supported by the decrement in Co_3O_4 crystallite size with the increase in Y_2O_3 loading from 0-3wt.%, as aforementioned. At the same time, CNF was obviously formed over the surface of spent catalysts. In literature, the introduction of Y_2O_3 promoters would stimulate the formation of reactive filamentous carbon, which can be easily removed compared to graphitic carbon (Younis et al., 2018). Hence, this explained the stable catalytic activity of promoted catalysts within 8 h on stream. Apparently, the coke deposited on spent catalysts seemed to decrease in the trend of 10%Co/MA > 1%Y-10%Co/MA > 2%Y-10%Co/MA > 5%Y-10%Co/MA > 3%Y-10%Co/MA, which could be directly linked to the oxygen vacancies of catalysts. The lowest coke formation on 3%Y-10%Co/MA also

proved the excellent activity with a lower deactivation rate as discussed in the previous reaction part.

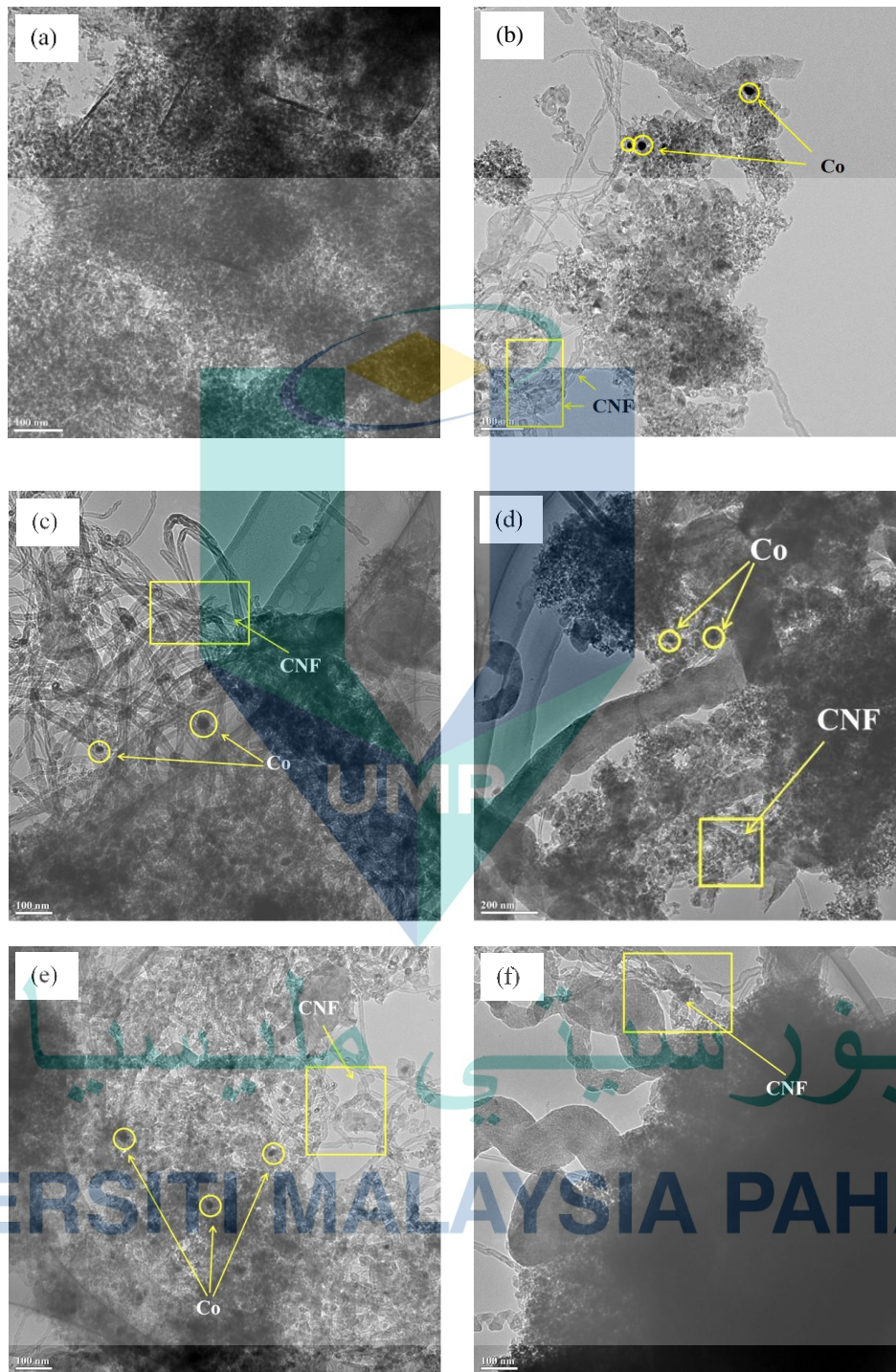


Figure 4.29 HRTEM images of (a) MA support, spent (b) 10%Co/MA, (c) 1%Y-10%Co/MA, (d) 2%Y-10%Co/MA, (e) 3%Y-10%Co/MA and (f) 5%Y-10%Co/MA.

4.4.3.3 Temperature Programmed Oxidation

The influences of Y_2O_3 loading on derivative weight profiles and percentage weight loss of 10%Co/MA catalysts are shown in Figure 4.30. Apparently, there are two characteristic peaks observed for derivative weight profiles which represented two types of carbon with distinct oxidation reactivity. The first peak at a temperature of 700-800 K was appointed to the removal of amorphous carbon while the second peak located at temperature above 850 K belonged to the gasification of crystalline carbon (graphite) (Paksoy et al., 2015). In this regard, it has been reported in the literature that undesirable amorphous and graphitic carbons were inevitably generated through CO disproportionation and CH_4 decomposition, respectively during CO_2 - CH_4 reforming (Khajenoori et al., 2015).

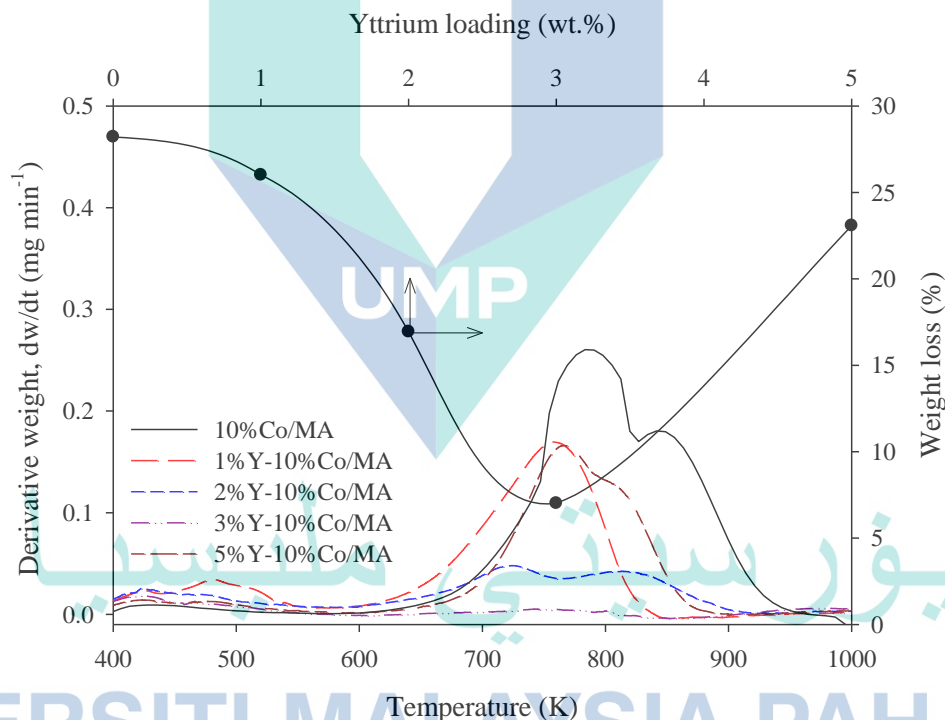


Figure 4.30 TPO profiles and weight loss of the spent catalysts after 8 h CO_2 - CH_4 reforming reaction at 1023 K, $GHSV = 36000 \text{ cm}^3 \text{ g}_{\text{cat}}^{-1} \text{ h}^{-1}$ and $CH_4: CO_2 = 1:1$.

Interestingly, the derivative weight profiles displayed a reduction in the area and intensity of the carbon peak with the addition of Y_2O_3 promoter from 1-5wt.% compared to that of an unpromoted catalyst. This observation was accredited to the improvement of Co metal dispersion and carbon resistance with yttrium incorporation into Co/MA catalyst (J. F. Li et al., 2014; Świrk et al., 2018). Besides, the significant decline in intensity of graphitic carbon peak in accordance with the XRD results of spent catalysts

is displayed in Figure 4.28. According to J. F. Li et al. (2014), active amorphous carbon is mostly generated on the surface of catalysts that have been modified with Y_2O_3 promoter compared to graphitic carbon during CO_2-CH_4 reforming. The percentage of weight loss as seen in Figure 4.30 also shows a declining trend in an order of 10%Co/MA (28.21%) > 1%Y-10%Co/MA (26.0%) > 5%Y-10%Co/MA (23.08%) > 2%Y-10%Co/MA (16.94%) > 3%Y-10%Co/MA (7.0%). This trend clearly explained the excellent activity, selectivity, and stability of 3wt.% Y_2O_3 promotion on 10%Co/MA catalyst compared to the 0, 1, 2, and 5wt.% Y_2O_3 .

4.4.3.4 X-ray Photoelectron Spectroscopy

The XPS data on all spent catalysts are listed in Table 4.5 while Co 2p, C 1s, and O 1s spectra for those catalysts are displayed in Figure 4.31 to Figure 4.33.

Table 4.5 Binding energies, atomic ratios, and oxygen vacancies values obtained from the XPS analysis of all spent catalysts.

Catalyst	Binding energy (eV)							Atomic ratio Co/Al	O _v (%)
	Co 2p _{3/2}	Co 2p _{1/2}	C 1s	O 1s	Al 2p	Y 3d _{3/2}	Y 3d _{5/2}		
10% Co/MA	778.6	795.5	284.6	530.8	74.0	-	-	0.17	24.4
	780.8	796.9							
	781.1	803.2							
	784.9	803.2							
1%Y-10% Co/MA	778.6	793.5	284.6	530.8	73.8	156.5	158.6	0.26	42.6
	780.8	795.5							
	781.1	796.9							
	784.9	803.2							
2%Y-10% Co/MA	778.6	793.5	284.6	530.8	73.8	156.5	158.6	0.54	41.4
	780.8	795.5							
	781.1	796.9							
	784.9	803.2							
3%Y-10% Co/MA	778.6	793.5	284.6	530.8	73.8	156.5	158.6	2.67	78.1
	780.8	795.3							
	781.1	796.9							
	784.9	803.2							
5%Y-10% Co/MA	778.6	793.5	284.6	530.8	73.8	156.5	158.6	0.56	32.9
	780.8	795.5							
	781.1	796.9							
	784.9	803.2							

Regardless of catalysts, the recorded Al 2p binding energy within 73.8-74.0 eV (as listed in Table 4.5) belonged to alumina support (Kourtelesis, Panagiotopoulou, Ladas, & Verykios, 2015; Rahemi, Haghghi, Babaluo, & Fallah Jafari, 2014). For promoted catalysts, the detected binding energies of Y 3d_{5/2} and Y 3d_{3/2} doublet peaks at about 156.5 eV and 158.6 eV respectively corroborated the existence of Y₂O₃ compound. Indeed, the appearance of Y 3d doublet peaks was also noticed in the previously reported results with the employment of yttrium oxide (Durand et al., 2004; Kim & Kim, 2001).

The image of the Co 2p spectrum (Figure 4.31) exhibited two major peaks that corresponded to Co 2p_{1/2} (left part) and Co 2p_{3/2} (right part) spin-orbit peaks. The Gaussian deconvolution of Co 2p_{3/2} broad peak of all catalysts revealed four discrete peaks with binding energy at about 778.6 eV, 780.8 eV, 781.1 eV, and 784.9 eV, denoting to the characteristics of Co⁰, CoAl₂O₄, Co₃O₄, and a shake-up satellite, respectively. Meanwhile, for Co 2p_{1/2} region, there were also four deconvoluted peaks located at binding energy of 793.5 eV (Co⁰), 794.6 eV (Co₃O₄), 795.6 eV (CoAl₂O₄) and 803.7 eV (satellite). These XPS results were consistent with the previous data provided in the literature (Álvarez-Docio et al., 2019; Ao et al., 2018; Paksoy et al., 2015). In addition, the appearance of Co⁰, CoAl₂O₄, Co₃O₄ phases in XPS results was consistent with the result aforementioned in XRD analysis of spent catalysts. Apart from Co 2p binding energy, the atomic ratio of Co/Al summarized in Table 4.5 significantly increased after the incorporation of Y₂O₃ promoter (1-3wt.%), implying the improvement of cobalt particles dispersion. Moreover, a similar trend was described by Meng et al. (2015) after the successful introduction of Ce promoter to Ni/Al₂O₃ catalyst during CO methanation. However, this value was reduced for the catalysts with Y₂O₃ loading of 5wt.%, which may be due to the covering of Co particles in the yttrium-rich content. This finding strongly verified the reason for the improvement in reforming activity upon the increase of Y₂O₃ loading from 0 to 3wt.% and the declining trend with 5wt.% (cf. Figure 4.25- Figure 4.27).

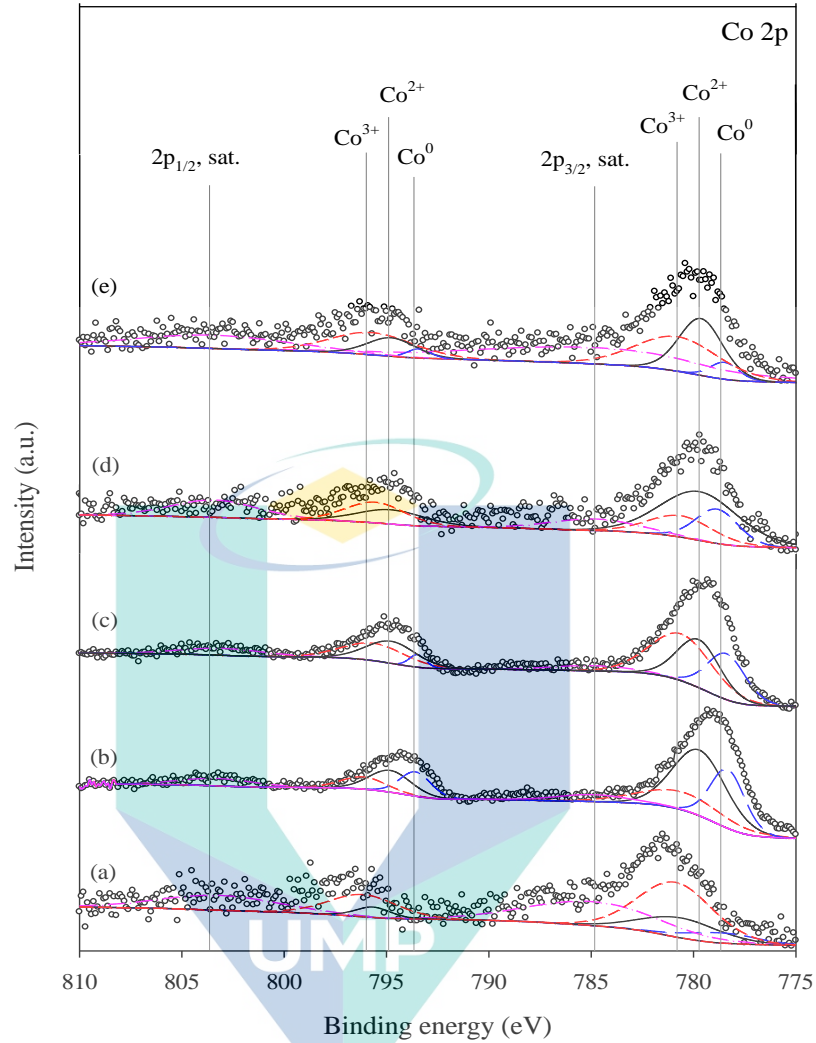


Figure 4.31 XPS Co 2p spectra of the spent (a) 10%Co/MA, (b) 1%Y-10%Co/MA, (c) 2%Y-10%Co/MA, (d) 3%Y-10%Co/MA and (e) 5%Y-10%Co/MA catalysts after 8 h CO₂-CH₄ reforming reaction at 1023 K, GHSV = 36000 cm³ g_{cat}⁻¹ h⁻¹ and CH₄: CO₂ = 1:1.

The O 1s photoelectron spectra of spent catalysts consisting of two deconvoluted peaks (O_L and O_A) are revealed in Figure 4.32. The peak (O_L) detected at low binding energy about 530.3-530.8 eV belonged to surface lattice oxygen from the copresence of Co₃O₄ and Al₂O₃ phases (N. Wang, K. Shen, et al., 2013). The second peak (O_A) detected at binding energy in the range of 532.0 to 532.4 eV signified the existence of surface adsorbed oxygen atoms (N. Wang, K. Shen, et al., 2013; Xiao Wang et al., 2017). In addition, the binding energy of both peaks were slightly decreased with the addition of Y₂O₃ promoter, probably because of the increment of the amount of oxygen contributed from Y₂O₃. Lu, Wang, Chen, Huang, and Li (2017) also noted similar trends during the introduction of CeO₂ to Co₃O₄ compound. In order to compute the amount of oxygen

vacancies (O_v) in catalysts, formula aforementioned in subchapter 6.4.2 was employed by referring to the integrated peak areas of surface lattice oxygen (O_L) and surface adsorbed oxygen (O_A). As listed in Table 4.5, the amounts of oxygen vacancies were significantly improved up to 78.1% with the incorporation of yttrium promoter compared to 10%Co/MA (24.4%). This enhancement further explained the low deposition of carbon as measured by TPO analysis (cf. Figure 4.30). Indeed, this greater oxygen vacancies estimated from this calculation further supported the enhancement in the degree of catalyst deactivation as previously discussed in the evaluation of catalytic CO_2 - CH_4 reforming part.

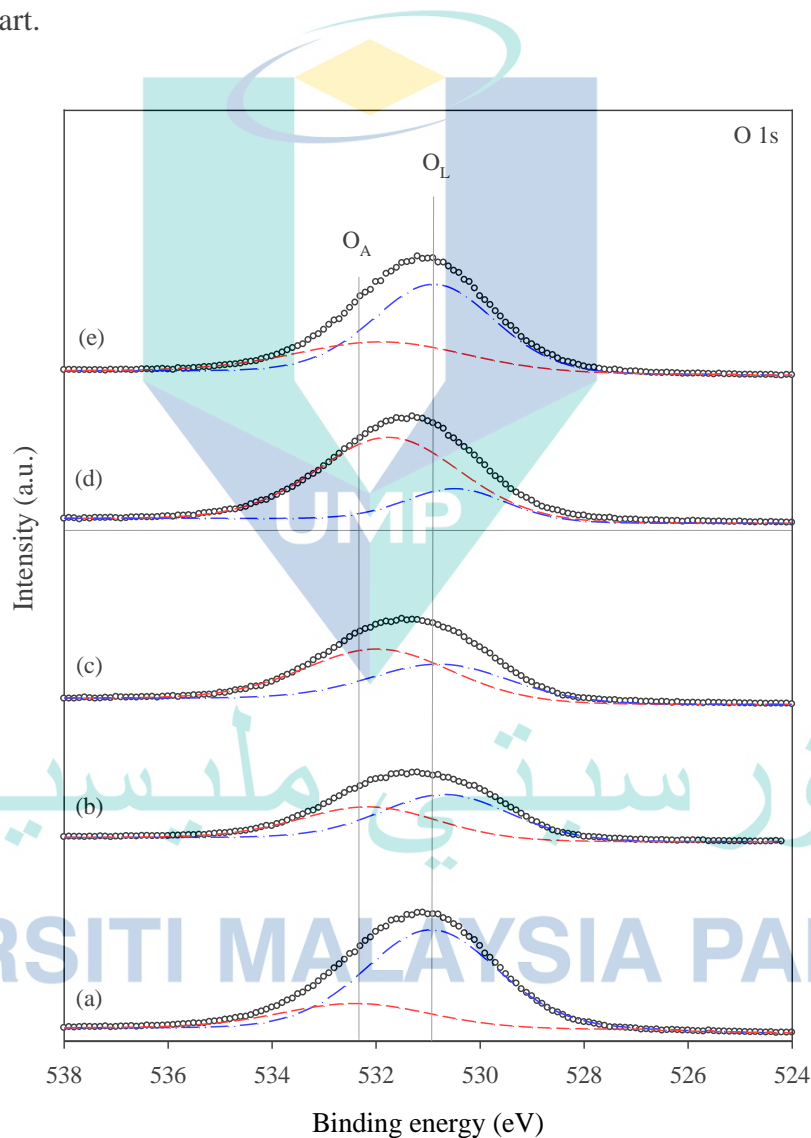


Figure 4.32 XPS O 1s spectra of the spent (a) 10%Co/MA, (b) 1%Y-10%Co/MA, (c) 2%Y-10%Co/MA, (d) 3%Y-10%Co/MA and (e) 5%Y-10%Co/MA catalysts after 8 h CO_2 - CH_4 reforming reaction at 1023 K, $GHSV = 36000 \text{ cm}^3 \text{ g}_{\text{cat}}^{-1} \text{ h}^{-1}$ and $CH_4:CO_2 = 1:1$.

Figure 4.33 presents the high-resolution of the C 1s spectrum with two fitted curves centred at 284.6 eV and 285.3 eV, corresponded to the formation of the C=C double bond (graphene) and C-C single bond (amorphous) in this order (Campos Roldán et al., 2016; Dang et al., 2017; Y.-H. Wang, Wang, Li, Zhu, & Xu, 2005). In fact, this finding was consistent with our previous study in TPO results. As seen in Figure 4.33, 3%Y-10%Co/MA catalysts possessed the lowest intensity of both carbon peaks compared to other catalysts, probably due to the greater oxygen vacancies (about 78.1%) which effectively assisted in carbon gasification.

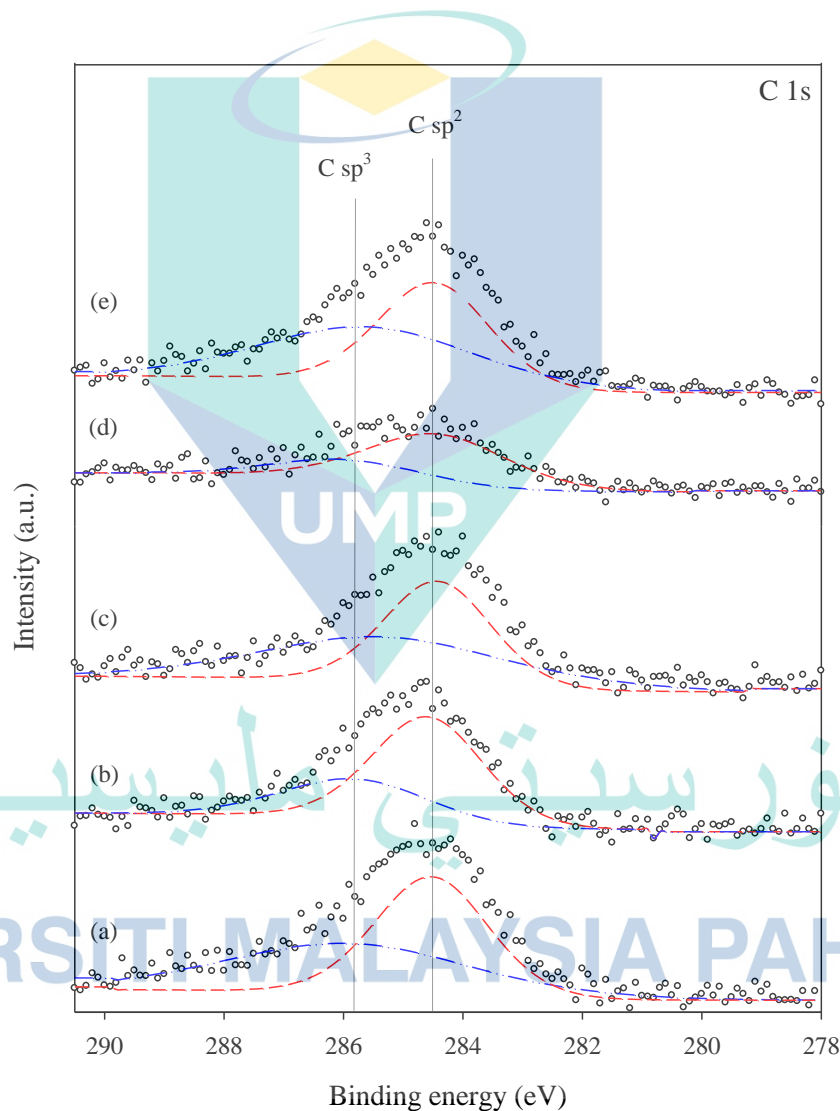


Figure 4.33 XPS C 1s spectra of the spent (a) 10%Co/MA, (b) 1%Y-10%Co/MA, (c) 2%Y-10%Co/MA, (d) 3%Y-10%Co/MA and (e) 5%Y-10%Co/MA catalysts after 8 h CO₂-CH₄ reforming reaction at 1023 K, GHSV = 36000 cm³ g_{cat}⁻¹ h⁻¹ and CH₄: CO₂ = 1:1.

The impact by varying the amounts of Y_2O_3 promoter loading (0-5wt%) towards catalyst properties and CO_2 - CH_4 reforming performances was elucidated in Figure 4.34. As shown, the positive impact of the Y_2O_3 promoter addition was evidenced through this work. After the incorporation of Y_2O_3 promoter on Co/MA, the agglomeration on Co/MA was effectively controlled and the crystallite size of Co was reduced. Indeed, this phenomenon indicated that the dispersion of Co on MA support was significantly improved, in agreement with the increasing of Co/Al atomic ratio estimated through XPS analysis. This improvement resulted in the significant enhancement of catalytic reforming, especially recorded by 3wt.% Y_2O_3 promoter loading, credited by the smallest crystallite size (12.66 nm) and the highest Co/Al ratio (2.67%) of 3%Y-10%Co/MA, compared to other prepared catalysts. Moreover, the highest oxygen vacancies held by 3wt.% Y_2O_3 promoter loading (78.1%) effectively resisted the carbon formation during 8 h reforming activity as it recorded the lowest deactivation rate (0.6%) and carbon deposit (7.0%). However, there is a limit in the increasing amount of Y_2O_3 promoter loading whereby 5wt.% Y_2O_3 exhibited a decline in reforming activity as well as an increase in the formation of carbon. This condition could be explained by the obstruction of the Y_2O_3 promoter as the excess amount of these particles may cover the Co active sites.

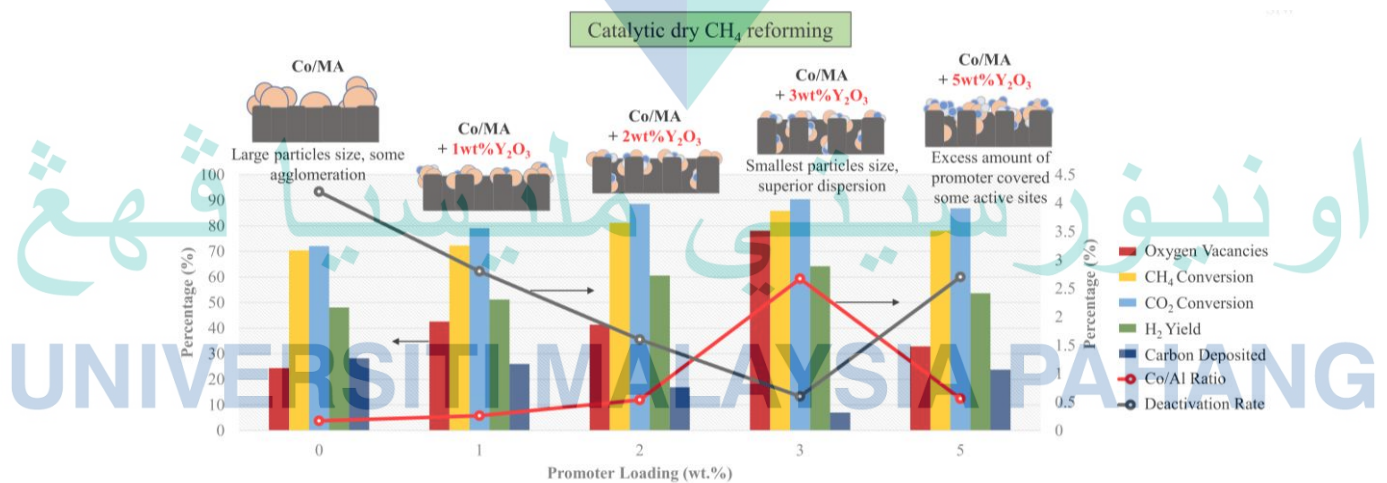


Figure 4.34 Summary on the relationship between promoter loading with catalyst properties and catalytic performances in CO_2 - CH_4 reforming.

4.4.4 Longevity Test

Since Y-dopant with 3wt.% was the optimal loading Y-promoted 10%Co/MA catalyst in CO₂-CH₄ reforming activity (conversion and yield), thus the longevity tests were further conducted over 72 h at stoichiometric condition (CH₄/CO₂ = 1:1) and 1023 K in order to evaluate their catalytic stability. The time-on-stream profiles for reactant conversions and product yields of 3%Y-10%Co/MA during the longevity test is shown in Figure 4.35. It was noticed that reactant conversions appeared to be stable with time-on-stream at beyond 8 h on-stream and recorded low deactivation rate about 3.48% within 72 h as compared with the longevity tests conducted by Ma et al. (2016), Huang et al. (2017), and Xu et al. (2017) using 6%Ni/OMA (15.2%), 5%Co-5%Ni-Al₂O₃ (27.1%), and OMA-5%Co5%Ni (8.0) catalysts, respectively. This observation clearly proved that the redox properties of Y₂O₃ effectively assisted the carbon removal process and persevered the Co active metal sites for a long duration. As can be clearly seen in Figure 4.35, the CO₂ conversion was always greater than CH₄ confirming the predominance of RWGS reaction. For the product yields, both time-on-stream profiles exhibited a slight decreased trend after 72 h.

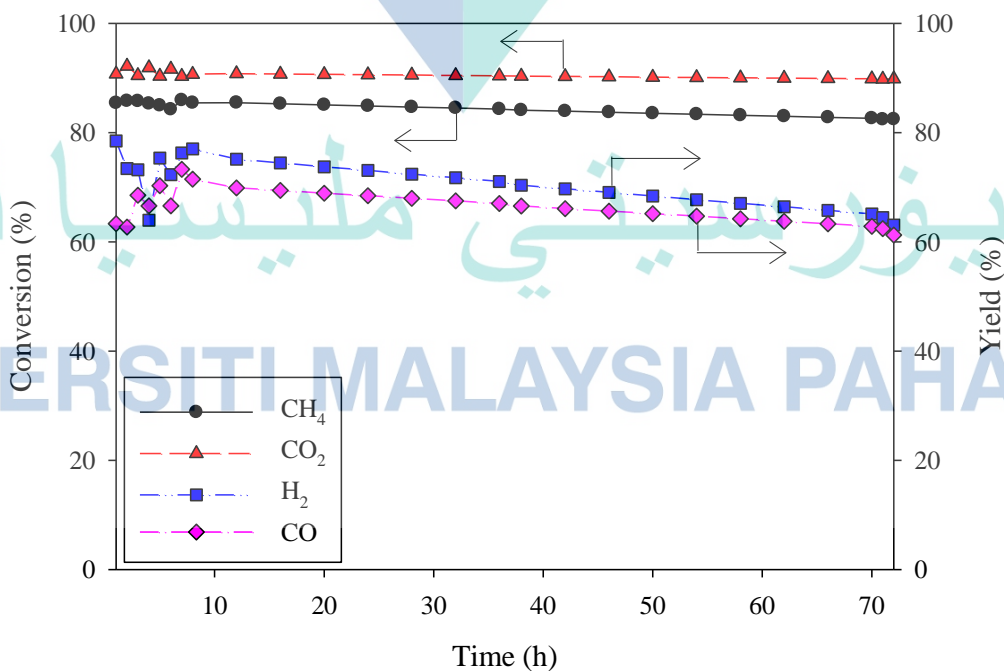


Figure 4.35 Time-on-stream profile for reactant conversions and product yields attained from longevity test of 3%Y-10%Co/MA at 1023 K and molar ratio of CH₄/CO₂ = 1:1.

4.5 Concluding Remarks

MA support has been successfully generated using the self-assembly hydrothermal approach (SAHA) whilst 10%Co/MA catalysts via incipient wetness impregnation technique. The effect of operating condition has been thoroughly examined and substantially discussed in this chapter. XRD analyses recorded the appearance of spinel CoAl_2O_4 on 10%Co/MA surface credited to the strong Co-MA interaction. The catalytic activity evaluation exhibited that the increment of CO_2 partial pressure of from 10-40 kPa resulted in a positive consequence on CH_4 conversion, but declining CO_2 conversion. The increment of CH_4 partial pressure from 10-40 kPa, CH_4 conversion declined by up to 41.3% while the CO_2 conversion improved significantly. The excellent catalytic performance for 10%Co/MA in CO_2 - CH_4 reforming was credited to intense Co-MA interaction and fine Co particle dispersion. The confinement effect by MA support effectively reduced the degree of deactivation (4.2%) and amount of coke accumulated on the catalyst surface as compared to the previous studies. The reforming condition for CO_2 - CH_4 reforming at 1023 K and $P_{\text{CH}_4} = P_{\text{CO}_2} = 20$ kPa was selected as the optimum condition due to great catalytic activity ($X_{\text{CH}_4} = 70.9\%$, $X_{\text{CO}_2} = 71.7\%$, $D_d = 4.2\%$) along with low carbon deposited.

Notably, the addition of all those promoters improved the particle dispersion on MA support, then successively suppressed the agglomeration of Co particles onto the surface or pore of MA support. In fact, the effectiveness in Co dispersion was the key to controlling the Co particle size, which is significant for affecting the Co-MA interaction. It is no doubt that the smaller particle size and stronger Co-MA interaction of YCo/MA catalysts as acquired via XRD and TPR analysis, respectively, provided high catalytic performance in CO_2 - CH_4 reforming with excellent sintering resistibility. The weak Co-MA interaction resulted from Ce and La promoter addition (as revealed in H_2 -TPR analysis) managed to lower the reducibility of Co/MA catalyst since these promoters effectively restrained Co ions from migrating into MA structure. However, this attributed to lowering the performance of both Ce- and La-promoted Co/MA as compared to YCo/MA. Although SmCo/MA catalyst also had smaller crystallite size and stronger Co-MA interaction as compared to Ce- and La-promoted catalysts, this catalyst still exhibited the lower catalytic activity as compared to all promoters since Co and Sm combination resulted in the increment in acid properties of SmCo/MA catalyst. The great oxygen

storage capacity proved through XPS measurements and the ability to form intermediate dioxycarbonate compounds ($\text{La}_2\text{O}_2\text{CO}_3$, $\text{Y}_2\text{O}_2\text{CO}_3$, and $\text{Sm}_2\text{O}_2\text{CO}_3$) owned by these promoters efficiently assisted in suppressing carbon formation generated via both Boudouard and CH_4 cracking. Thus, the lower deactivation rate and the amount of carbon deposited (via TPO analysis) were attained by all promoted catalysts, especially Y/CoMA catalyst as compared to Co/MA catalyst. Definitively, regardless of all mentioned attributes, all the promoted catalysts still provided positive effects toward the CO_2 - CH_4 reforming activity as well as in terms of carbon deposition as compared to Co/MA catalyst. In catalytic evaluation, both conversions and yield values were improved in the order of YCo/MA (CH_4 Conv. = 85.4%, CO_2 Conv. = 90.7%, H_2 Yield = 65.5%, CO Yield = 68.3%) > LaCo/MA (CH_4 Conv. = 84.8%, CO_2 Conv. = 89.6%, H_2 Yield = 63.4%, CO Yield = 67.7%) > CeCo/MA (CH_4 Conv. = 82.4%, CO_2 Conv. = 88.6%, H_2 Yield = 62.8%, CO Yield = 65.8%) > SmCo/MA (CH_4 Conv. = 79.9%, CO_2 Conv. = 83.8%, H_2 Yield = 59.9%, CO Yield = 61.1%) > Co/MA (CH_4 Conv. = 71.3%, CO_2 Conv. = 73.5%, H_2 Yield = 52.7%, CO Yield = 56.5%).

The influence of Y_2O_3 promoter loadings (0, 1, 2, 3, and 5wt.%) over Co/MA catalysts was conducted under CO_2 - CH_4 reforming conditions at $T = 1023$ K and CH_4/CO_2 molar ratio = 1:1. In the performance evaluation, the catalytic activities were increased in the order of 10%Co/MA > 1%Y-10%Co/MA > 5%Y-10%Co/MA > 2%Y-10%Co/MA > 3%Y-10%Co/MA, consistent with the trend for Co/Al ratio which is linked with Co dispersion. The decline in catalytic activity for Y_2O_3 loadings beyond 3wt% Y_2O_3 was due to the blocked Co active sites by the high amount of Y_2O_3 particles. The 3%Y-10%Co/MA catalyst recorded the lowest amount of carbon deposit (7.0%) in TPO analysis due to a large amount of oxygen vacancies (as verified through XPS analysis), thereby supporting its excellent performances in CO_2 - CH_4 reforming. In fact, the longevity test conducted on the optimal catalyst (3wt% Y_2O_3) revealed the stable catalytic performance of the catalyst with a low deactivation rate within 72 h reaction.

CHAPTER 5

CONCLUSIONS AND RECOMMENDATIONS

5.1 Conclusions

The objectives of this research have been achieved to a large extent and the outcomes for CO₂-CH₄ reforming evaluation over promoted (La, Ce, Y, Sm) and unpromoted Co/MA catalysts may be summarized as;

- i) Objective 1: To synthesize the mesoporous alumina support, promoted and unpromoted Co/MA catalysts, and to determine their physicochemical properties using various characterization techniques.

MA support, promoted, and unpromoted Co/MA catalysts were successfully synthesized and characterized in this work. Both support and catalyst displayed a typical type-IV isotherm with a hysteresis loop of H1 shaped, confirming the formation of mesoporous structure. The mean crystallite size of Co₃O₄ was lower than the pore diameter of the MA support implying that most Co₃O₄ particles were held inside the pores structure of the MA support. Three reduction peaks detected in TPR represented the reduction of Co₃O₄ to CoO, CoO to Co, and spinel CoAl₂O₄ to Co. The slight increment of Co size after reaction indicated that metal sintering was slightly suppressed owing to the confinement effect of MA.

- ii) Objective 2: To evaluate the catalytic performance of as-synthesized catalysts for CO₂-CH₄ reforming at various operation conditions.

The employment of MA support prepared efficiently lowered the degree of deactivation (4.2%) and reduced the amount of coke accumulated during 8 h CO₂-CH₄ reforming as compared to conventional alumina accredited to their confinement effect which assisted in suppressing Co from metal sintering. Indeed, great catalytic activity ($X_{CH_4} = 70.9\%$, $X_{CO_2} = 71.7\%$) in CO₂-CH₄

reforming was linked with the well distributed Co particles on MA support. The influence of operating conditions capable of optimizing the catalytic performance of CO₂-CH₄ reforming. It was evident that the reaction partial pressure managed to influence the catalytic activity. The increment of CO₂ partial pressure from 10-40 kPa resulted in a positive consequence on CH₄ conversion (improved up to 42.8%) but reduced the CO₂ conversion. On the other hand, the rising of CH₄ partial pressure from 10-40 kPa caused CH₄ conversion to decline by up to 41.3% but raising the CO₂ conversion.

- iii) To investigate the effects of promoter types and loadings on the physiochemical properties of catalyst and catalytic performance during CO₂-CH₄ reforming.

In this work, the addition of promoters capable of enhancing the particle dispersion of Co particles on MA support along with suppressing the agglomeration of Co particles. The low deactivation rate and less amount of carbon deposited recorded for promoted catalysts compared to Co/MA catalyst accredited to the great oxygen storage capacity and ability to form intermediate dioxycarbonate compounds (La₂O₂CO₃, Y₂O₂CO₃, and Sm₂O₂CO₃). According to analysis conducted, the smaller particle size and stronger Co-MA interaction of YCo/MA catalysts provided high catalytic performance in CO₂-CH₄ reforming with excellent sintering resistibility compared to other promoted catalysts. The negative impact exhibited by Co and Sm combination in reforming activity was linked with the increment in acid properties. Apart from that, during the investigation on effect Y₂O₃ promoter loading (0, 1, 2, 3 and 5wt.%) towards CO₂-CH₄ reforming, the catalytic activities were increased in the order of 10%Co/MA > 1%Y-10%Co/MA > 5%Y-10%Co/MA > 2%Y-10%Co/MA > 3%Y-10Co/MA, attributed to the improvement in Co dispersion on MA support. Co/MA catalyst with 3wt.% Y promoter loading recorded the lowest amount of carbon deposit (7.0%) due to a large amount of oxygen vacancies, thereby supporting its superior performances in CO₂-CH₄ reforming. Longevity test proved that the optimal catalyst (3wt% Y₂O₃) owned stable catalytic performance of the catalyst with a low deactivation rate (3.48%) within 72 h reaction.

5.2 Recommendations

Based on the above outcomes of CO₂-CH₄ reforming project, the following suggestions may be recommended for the future work;

- i) This project applied only SIWI and IWI techniques during the preparation of promoted and unpromoted catalysts respectively. Since the performance of the catalyst in reforming activities strongly depends on the catalytic properties such as BET surface area and metal dispersion, different techniques preparation should be considered such as sol-gel and precipitation methods.
- ii) Power-law and 7 Langmuir-Hinshelwood rate expressions of the best catalyst should be performed in this work for determining the best mechanism that could be expressed of CO₂-CH₄ reforming. Indeed, further studies could be conducted for determining the intermediate and formed species during CO₂-CH₄ reforming via in-situ diffuse reflectance Fourier Transformation (DRIFT) spectroscopy and pulse-rate surface analysis (PSRA).
- iii) Since the yttrium promoter with 3wt.% loading exhibited superior performance and catalytic stability, the regeneration test of this optimum catalyst could be considered in the future work in order to assess this catalyst regeneration capability.

اونيورسيتي ملايسيا قهغ

UNIVERSITI MALAYSIA PAHANG

REFERENCES

- Abas, N., Kalair, A., & Khan, N. (2015). Review of fossil fuels and future energy technologies. *Futures*, 69, 31-49.
doi:<https://doi.org/10.1016/j.futures.2015.03.003>
- Abasaheed, A. E., Al-Fatesh, A. S., Naeem, M. A., Ibrahim, A. A., & Fakeeha, A. H. (2015). Catalytic performance of CeO₂ and ZrO₂ supported Co catalysts for hydrogen production via dry reforming of methane. *International Journal of Hydrogen Energy*, 40(21), 6818-6826.
doi:<https://doi.org/10.1016/j.ijhydene.2015.03.152>
- Abdul Mujeebu, M. (2016). Hydrogen and syngas production by superadiabatic combustion – A review. *Applied Energy*, 173, 210-224.
doi:<https://doi.org/10.1016/j.apenergy.2016.04.018>
- Abdullah, B., Abd Ghani, N. A., & Vo, D.-V. N. (2017). Recent advances in dry reforming of methane over Ni-based catalysts. *Journal of Cleaner Production*, 162, 170-185. doi:<https://doi.org/10.1016/j.jclepro.2017.05.176>
- Abou Rached, J., Cesario, M. R., Estephane, J., Tidahy, H. L., Gennequin, C., Aouad, S., . . . Abi-Aad, E. (2018). Effects of cerium and lanthanum on Ni-based catalysts for CO₂ reforming of toluene. *Journal of Environmental Chemical Engineering*, 6(4), 4743-4754. doi:<https://doi.org/10.1016/j.jece.2018.06.054>
- Adhikari, S., Fernando, S., & Haryanto, A. (2007). Production of hydrogen by steam reforming of glycerin over alumina-supported metal catalysts. *Catalysis Today*, 129(3), 355-364. doi:<https://doi.org/10.1016/j.cattod.2006.09.038>
- Adris, A. M., Pruden, B. B., Lim, C. J., & Grace, J. R. (1996). On the reported attempts to radically improve the performance of the steam methane reforming reactor. *The Canadian Journal of Chemical Engineering*, 74(2), 177-186.
doi:10.1002/cjce.5450740202
- Al-Fatesh, A. S. A., Fakeeha, A. H., & Abasaheed, A. E. (2011). Effects of Selected Promoters on Ni/Y-Al₂O₃ Catalyst Performance in Methane Dry Reforming. *Chinese Journal of Catalysis*, 32(9), 1604-1609.
doi:[https://doi.org/10.1016/S1872-2067\(10\)60267-7](https://doi.org/10.1016/S1872-2067(10)60267-7)
- Álvarez-Docio, C. M., Reinoso, J. J., Del Campo, A., & Fernández, J. F. (2019). Investigation of thermal stability of 2D and 3D CoAl₂O₄ particles in core-shell nanostructures by Raman spectroscopy. *Journal of Alloys and Compounds*, 779, 244-254. doi:<https://doi.org/10.1016/j.jallcom.2018.11.263>
- Amin, M. H., Putla, S., Bee Abd Hamid, S., & Bhargava, S. K. (2015). Understanding the role of lanthanide promoters on the structure–activity of nanosized Ni/γ-Al₂O₃ catalysts in carbon dioxide reforming of methane. *Applied Catalysis A: General*, 492, 160-168. doi:<https://doi.org/10.1016/j.apcata.2014.12.038>
- Anderson, J. (1963). A criterion for isothermal behaviour of a catalyst pellet. *Chemical Engineering Science*, 18, 147-148.

- Angeli, S. D., Monteleone, G., Giaconia, A., & Lemonidou, A. A. (2014). State-of-the-art catalysts for CH₄ steam reforming at low temperature. *International Journal of Hydrogen Energy*, 39(5), 1979-1997.
doi:<https://doi.org/10.1016/j.ijhydene.2013.12.001>
- Anil, C., Modak, J. M., & Madras, G. (2020). Syngas production via CO₂ reforming of methane over noble metal (Ru, Pt, and Pd) doped LaAlO₃ perovskite catalyst. *Molecular Catalysis*, 484, 110805.
doi:<https://doi.org/10.1016/j.mcat.2020.110805>
- Ao, K., Li, D., Yao, Y., Lv, P., Cai, Y., & Wei, Q. (2018). Fe-doped Co₉S₈ nanosheets on carbon fiber cloth as pH-universal freestanding electrocatalysts for efficient hydrogen evolution. *Electrochimica Acta*, 264, 157-165.
doi:<https://doi.org/10.1016/j.electacta.2018.01.080>
- Arbag, H. (2018). Effect of impregnation sequence of Mg on performance of mesoporous alumina supported Ni catalyst in dry reforming of methane. *International Journal of Hydrogen Energy*, 43(13), 6561-6574.
doi:<https://doi.org/10.1016/j.ijhydene.2018.02.063>
- Arbag, H., Yasyerli, S., Yasyerli, N., Dogu, T., & Dogu, G. (2013). Coke Minimization in Dry Reforming of Methane by Ni Based Mesoporous Alumina Catalysts Synthesized Following Different Routes: Effects of W and Mg. *Topics in Catalysis*, 56(18), 1695-1707. doi:10.1007/s11244-013-0105-3
- Argyle, M. D., & Bartholomew, C. H. (2015). Heterogeneous Catalyst Deactivation and Regeneration: A Review. *Catalysts*, 5(1), 145-269.
- Arora, S., & Prasad, R. (2016). An overview on dry reforming of methane: strategies to reduce carbonaceous deactivation of catalysts. *RSC Advances*, 6(110), 108668-108688. doi:10.1039/C6RA20450C
- Atribak, I., Bueno-López, A., & García-García, A. (2009). Role of yttrium loading in the physico-chemical properties and soot combustion activity of ceria-zirconia catalysts. *Journal of Molecular Catalysis A: Chemical*, 300(1), 103-110.
doi:<https://doi.org/10.1016/j.molcata.2008.10.043>
- Aw, M. S., Dražić, G., Djinović, P., & Pintar, A. (2016). Transition metal pairs on ceria-promoted, ordered mesoporous alumina as catalysts for the CO₂ reforming reaction of methane. *Catalysis Science & Technology*, 6(11), 3797-3805.
doi:10.1039/C5CY02082D
- Ay, H., & Üner, D. (2015). Dry reforming of methane over CeO₂ supported Ni, Co and Ni-Co catalysts. *Applied Catalysis B: Environmental*, 179, 128-138.
doi:<https://doi.org/10.1016/j.apcatb.2015.05.013>
- Ayodele, B. V., Khan, M. R., & Cheng, C. K. (2015). Syngas production from CO₂ reforming of methane over ceria supported cobalt catalyst: Effects of reactants partial pressure. *Journal of Natural Gas Science and Engineering*, 27, 1016-1023.

doi:<https://doi.org/10.1016/j.jngse.2015.09.049>

Ayodele, B. V., Khan, M. R., & Cheng, C. K. (2016). Catalytic performance of ceria-supported cobalt catalyst for CO-rich hydrogen production from dry reforming of methane. *International Journal of Hydrogen Energy*, *41*(1), 198-207. doi:<https://doi.org/10.1016/j.ijhydene.2015.10.049>

Ayodele, B. V., Khan, M. R., Lam, S. S., & Cheng, C. K. (2016). Production of CO-rich hydrogen from methane dry reforming over lanthania-supported cobalt catalyst: Kinetic and mechanistic studies. *International Journal of Hydrogen Energy*, *41*(8), 4603-4615. doi:<https://doi.org/10.1016/j.ijhydene.2016.01.091>

Azizzadeh Fard, A., Arvaneh, R., Alavi, S. M., Bazyari, A., & Valaei, A. (2019). Propane steam reforming over promoted Ni-Ce/MgAl₂O₄ catalysts: Effects of Ce promoter on the catalyst performance using developed CCD model. *International Journal of Hydrogen Energy*, *44*(39), 21607-21622. doi:<https://doi.org/10.1016/j.ijhydene.2019.06.100>

Bacariza, M. C., Biset-Peiró, M., Graça, I., Guilera, J., Morante, J., Lopes, J. M., . . . Henriques, C. (2018). DBD plasma-assisted CO₂ methanation using zeolite-based catalysts: Structure composition-reactivity approach and effect of Ce as promoter. *Journal of CO₂ Utilization*, *26*, 202-211. doi:<https://doi.org/10.1016/j.jcou.2018.05.013>

Bahari, M. B., Goo, B. C., Pham, T. L. M., Siang, T. J., Danh, H. T., Ainirazali, N., & Vo, D.-V. N. (2016). Hydrogen-rich Syngas Production from Ethanol Dry Reforming on La-doped Ni/Al₂O₃ Catalysts: Effect of Promoter Loading. *Procedia Engineering*, *148*, 654-661. doi:<https://doi.org/10.1016/j.proeng.2016.06.531>

Bartholomew, C. H. (2001). Mechanisms of catalyst deactivation. *Applied Catalysis A: General*, *212*(1), 17-60. doi:[https://doi.org/10.1016/S0926-860X\(00\)00843-7](https://doi.org/10.1016/S0926-860X(00)00843-7)

Bellido, J. D. A., & Assaf, E. M. (2009). Effect of the Y₂O₃-ZrO₂ support composition on nickel catalyst evaluated in dry reforming of methane. *Applied Catalysis A: General*, *352*(1), 179-187. doi:<https://doi.org/10.1016/j.apcata.2008.10.002>

Bleta, R., Alphonse, P., Pin, L., Gressier, M., & Menu, M.-J. (2012). An efficient route to aqueous phase synthesis of nanocrystalline γ -Al₂O₃ with high porosity: From stable boehmite colloids to large pore mesoporous alumina. *Journal of Colloid and Interface Science*, *367*(1), 120-128. doi:<https://doi.org/10.1016/j.jcis.2011.08.087>

Bouarab, R., Akdim, O., Auroux, A., Cherifi, O., & Mirodatos, C. (2004). Effect of MgO additive on catalytic properties of Co/SiO₂ in the dry reforming of methane. *Applied Catalysis A: General*, *264*(2), 161-168. doi:<https://doi.org/10.1016/j.apcata.2003.12.039>

Bradford, M. C. J., & Vannice, M. A. (1999). CO₂ Reforming of CH₄. *Catalysis Reviews*, *41*(1), 1-42. doi:10.1081/CR-100101948

- Braga, T. P., Essayem, N., & Valentini, A. (2017). Correlation between the basicity of Cu–M_xO_y–Al₂O₃ (M = Ba, Mg, K or La) oxide and the catalytic performance in the glycerol conversion from adsorption microcalorimetry characterization. *Journal of Thermal Analysis and Calorimetry*, 129(1), 65-74. doi:10.1007/s10973-017-6145-3
- Budiman, A. W., Song, S.-H., Chang, T.-S., Shin, C.-H., & Choi, M.-J. (2012). Dry Reforming of Methane Over Cobalt Catalysts: A Literature Review of Catalyst Development. *Catalysis Surveys from Asia*, 16(4), 183-197. doi:10.1007/s10563-012-9143-2
- Campos Roldán, C., Ramos-Sanchez, G., Gonzalez-Huerta, R., vargas-garcia, j. r., Balbuena, P., & Alonso-Vante, N. (2016). Influence of sp³-sp² Carbon Nano-Domains on Metal/Support Interaction, Catalyst Durability and Catalytic Activity for the Oxygen Reduction Reaction. *ACS Applied Materials & Interfaces*, 8. doi:10.1021/acsami.6b06886
- Cao, X., Mirjalili, A., Wheeler, J., Xie, W., & Jang, B. W. L. (2015). Investigation of the preparation methodologies of Pd-Cu single atom alloy catalysts for selective hydrogenation of acetylene. *Frontiers of Chemical Science and Engineering*, 9(4), 442-449. doi:10.1007/s11705-015-1547-x
- Capodaglio, A. G., & Bolognesi, S. (2019). 2 - Ecofuel feedstocks and their prospects. In K. Azad (Ed.), *Advances in Eco-Fuels for a Sustainable Environment* (pp. 15-51): Woodhead Publishing.
- Chen, C., Wang, X., Zhang, L., Zou, X., Ding, W., & Lu, X. (2017). Synthesis of mesoporous Ni–La₂O₃/SiO₂ by ploy(ethylene glycol)-assisted sol-gel route as highly efficient catalysts for dry reforming of methane with a H₂/CO ratio of unity. *Catalysis Communications*, 94, 38-41. doi:https://doi.org/10.1016/j.catcom.2017.02.018
- Chong, C. C., Bukhari, S. N., Cheng, Y. W., Setiabudi, H. D., Jalil, A. A., & Phalakornkule, C. (2019). Robust Ni/Dendritic fibrous SBA-15 (Ni/DFSBA-15) for methane dry reforming: Effect of Ni loadings. *Applied Catalysis A: General*, 584, 117174. doi:https://doi.org/10.1016/j.apcata.2019.117174
- Cimino, S., Lisi, L., & Mancino, G. (2017). Effect of phosphorous addition to Rh-supported catalysts for the dry reforming of methane. *International Journal of Hydrogen Energy*, 42(37), 23587-23598. doi:https://doi.org/10.1016/j.ijhydene.2017.04.264
- Contreras, J. L., Gómez, G., Zeifert, B., Salmones, J., Vázquez, T., Fuentes, G. A., . . . Nuño, L. (2015). Synthesis of Pt/Al₂O₃ catalyst using mesoporous alumina prepared with a cationic surfactant. *Catalysis Today*, 250, 72-86. doi:https://doi.org/10.1016/j.cattod.2014.10.010
- Cooper, C. G., Nguyen, T.-H., Lee, Y.-J., Hardiman, K. M., Safinski, T., Lucien, F. P., & Adesina, A. A. (2008). Alumina-supported cobalt-molybdenum catalyst for

slurry phase Fischer–Tropsch synthesis. *Catalysis Today*, 131(1), 255-261.
doi:<https://doi.org/10.1016/j.cattod.2007.10.056>

da Fonseca, R. O., Rabelo-Neto, R. C., Simões, R. C. C., Mattos, L. V., & Noronha, F. B. (2020). Pt supported on doped CeO₂/Al₂O₃ as catalyst for dry reforming of methane. *International Journal of Hydrogen Energy*, 45(8), 5182-5191.
doi:<https://doi.org/10.1016/j.ijhydene.2019.09.207>

da Rosa, A. (2013). Chapter 10 - Hydrogen Production. In A. da Rosa (Ed.), *Fundamentals of Renewable Energy Processes (Third Edition)* (pp. 371-428). Boston: Academic Press.

Dahdah, E., Abou Rached, J., Aouad, S., Gennequin, C., Tidahy, H. L., Estephane, J., Abi Aad, E. (2017). CO₂ reforming of methane over Ni_xMg_{6-x}Al₂ catalysts: Effect of lanthanum doping on catalytic activity and stability. *International Journal of Hydrogen Energy*, 42(17), 12808-12817.
doi:<https://doi.org/10.1016/j.ijhydene.2017.01.197>

Daneshmand-Jahromi, S., Rahimpour, M. R., Meshksar, M., & Hafizi, A. (2017). Hydrogen production from cyclic chemical looping steam methane reforming over yttrium promoted Ni/SBA-16 oxygen carrier. *Catalysts*, 7(10), 286.

Dang, M. N., Ung, T. D. T., Phan, H. N., Truong, Q. D., Bui, T. H., Phan, M. N., Tran, P. D. (2017). A novel method for preparation of molybdenum disulfide/graphene composite. *Materials Letters*, 194, 145-148.
doi:10.1016/j.matlet.2017.02.018

de Caprariis, B., de Filippis, P., Palma, V., Petrullo, A., Ricca, A., Ruocco, C., & Scarsella, M. (2016). Rh, Ru and Pt ternary perovskites type oxides BaZr_(1-x)Me_xO₃ for methane dry reforming. *Applied Catalysis A: General*, 517, 47-55. doi:<https://doi.org/10.1016/j.apcata.2016.02.029>

De la Luz, V., Prades, M., Beltrán, H., & Cordoncillo, E. (2013). Environmental-friendly yellow pigment based on Tb and M (M=Ca or Ba) co-doped Y₂O₃. *Journal of the European Ceramic Society*, 33(15), 3359-3368.
doi:<https://doi.org/10.1016/j.jeurceramsoc.2013.05.021>

Dedov, A. G., Loktev, A. S., Komissarenko, D. A., Mazo, G. N., Shlyakhtin, O. A., Parkhomenko, K. V., Moiseev, I. I. (2015). Partial oxidation of methane to produce syngas over a neodymium–calcium cobaltate-based catalyst. *Applied Catalysis A: General*, 489, 140-146.
doi:<https://doi.org/10.1016/j.apcata.2014.10.027>

Delgado Dobladez, J. A., Águeda Maté, V. I., Torrellas, S. Á., Larriba, M., & Brea, P. (2020). Efficient recovery of syngas from dry methane reforming product by a dual pressure swing adsorption process. *International Journal of Hydrogen Energy*. doi:<https://doi.org/10.1016/j.ijhydene.2020.02.153>

Derakhshani, M., Hashamzadeh, A., & Amini, M. M. (2018). Novel synthesis of mesoporous crystalline γ -alumina by replication of MOF-5-derived nanoporous

carbon template. *Ceramics International*, 44(14), 17102-17106.
doi:<https://doi.org/10.1016/j.ceramint.2018.06.161>

Di Giuliano, A., & Gallucci, K. (2018). Sorption enhanced steam methane reforming based on nickel and calcium looping: a review. *Chemical Engineering and Processing - Process Intensification*, 130, 240-252.
doi:<https://doi.org/10.1016/j.cep.2018.06.021>

Dixon, A. G. (1997). Heat Transfer in Fixed Beds at Very Low (<4) Tube-to-Particle Diameter Ratio. *Industrial & Engineering Chemistry Research*, 36(8), 3053-3064. doi:10.1021/ie9605950

Djinović, P., Batista, J., & Pintar, A. (2012). Efficient catalytic abatement of greenhouse gases: Methane reforming with CO₂ using a novel and thermally stable Rh–CeO₂ catalyst. *International Journal of Hydrogen Energy*, 37(3), 2699-2707.
doi:<https://doi.org/10.1016/j.ijhydene.2011.10.107>

Djinović, P., Osojnik Črnivec, I. G., Erjavec, B., & Pintar, A. (2012). Influence of active metal loading and oxygen mobility on coke-free dry reforming of Ni–Co bimetallic catalysts. *Applied Catalysis B: Environmental*, 125, 259-270.
doi:<https://doi.org/10.1016/j.apcatb.2012.05.049>

Donazzi, A., Beretta, A., Groppi, G., & Forzatti, P. (2008). Catalytic partial oxidation of methane over a 4% Rh/ α -Al₂O₃ catalyst Part II: Role of CO₂ reforming. *Journal of Catalysis*, 255(2), 259-268. doi:<https://doi.org/10.1016/j.jcat.2008.02.010>

Dou, J., Zhang, R., Hao, X., Bao, Z., Wu, T., Wang, B., & Yu, F. (2019). Sandwiched SiO₂@Ni@ZrO₂ as a coke resistant nanocatalyst for dry reforming of methane. *Applied Catalysis B: Environmental*, 254, 612-623.
doi:<https://doi.org/10.1016/j.apcatb.2019.05.021>

Drif, A., Bion, N., Brahmi, R., Ojala, S., Pirault-Roy, L., Turpeinen, E., . . . Epron, F. (2015). Study of the dry reforming of methane and ethanol using Rh catalysts supported on doped alumina. *Applied Catalysis A: General*, 504, 576-584.
doi:<https://doi.org/10.1016/j.apcata.2015.02.019>

Durand, C., Vallée, C., Loup, V., Salicio, O., Dubourdieu, C., Blonkowski, S., . . . Joubert, O. (2004). Metal-Insulator-Metal capacitors using Y₂O₃ dielectric grown by pulsed-injection plasma enhanced metalorganic chemical vapor deposition. *Journal of Vacuum Science & Technology A*, 22, 655-660.
doi:10.1116/1.1722633

Dwivedi, P. N., & Upadhyay, S. N. (1977). Particle-Fluid Mass Transfer in Fixed and Fluidized Beds. *Industrial & Engineering Chemistry Process Design and Development*, 16(2), 157-165. doi:10.1021/i260062a001

El Hassan, N., Kaydouh, M. N., Geagea, H., El Zein, H., Jabbour, K., Casale, S., . . . Massiani, P. (2016). Low temperature dry reforming of methane on rhodium and cobalt based catalysts: Active phase stabilization by confinement in mesoporous

SBA-15. *Applied Catalysis A: General*, 520, 114-121. doi:https://doi.org/10.1016/j.apcata.2016.04.014

- Estephane, J., Aouad, S., Hany, S., El Khoury, B., Gennequin, C., El Zakhem, H., . . .
Abi Aad, E. (2015). CO₂ reforming of methane over Ni–Co/ZSM5 catalysts.
Aging and carbon deposition study. *International Journal of Hydrogen Energy*,
40(30), 9201-9208. doi:https://doi.org/10.1016/j.ijhydene.2015.05.147
- Ewbank, J. L., Kovarik, L., Kenvin, C. C., & Sievers, C. (2014). Effect of preparation
methods on the performance of Co/Al₂O₃ catalysts for dry reforming of methane.
Green Chemistry, 16(2), 885-896. doi:10.1039/C3GC41782D
- Fang, X., Peng, C., Peng, H., Liu, W., Xu, X., Wang, X., . . . Zhou, W. (2015). Methane
Dry Reforming over Coke-Resistant Mesoporous Ni-Al₂O₃ Catalysts Prepared by
Evaporation-Induced Self-Assembly Method. *ChemCatChem*, 7(22), 3753-3762.
doi:10.1002/cctc.201500538
- Fayaz, F., Danh, H. T., Nguyen-Huy, C., Vu, K. B., Abdullah, B., & Vo, D.-V. N. (2016).
Promotional effect of Ce-dopant on Al₂O₃-supported Co catalysts for syngas
production via CO₂ reforming of ethanol. *Procedia Engineering*, 148, 646-653.
- Figen, H. E., & Baykara, S. Z. (2015). Hydrogen production by partial oxidation of
methane over Co based, Ni and Ru monolithic catalysts. *International Journal of
Hydrogen Energy*, 40(24), 7439-7451.
doi:https://doi.org/10.1016/j.ijhydene.2015.02.109
- Fogler, H. S. (2006). *Elements of chemical reaction engineering* (4th ed.). Upper Saddle
River, NJ: Prentice Hall PTR.
- Foo, S. Y. (2012). *Oxidative dry reforming of methane over alumina-supported Co-Ni
catalyst systems*. (Ph.D), The University of New South Wales, Australia.
- Foo, S. Y., Cheng, C. K., Nguyen, T.-H., & Adesina, A. A. (2011a). Kinetic study of
methane CO₂ reforming on Co–Ni/Al₂O₃ and Ce–Co–Ni/Al₂O₃ catalysts.
Catalysis Today, 164(1), 221-226.
doi:https://doi.org/10.1016/j.cattod.2010.10.092
- Foo, S. Y., Cheng, C. K., Nguyen, T. H., & Adesina, A. A. (2011b). Evaluation of
lanthanide-group promoters on Co-Ni/Al₂O₃ catalysts for CH₄ dry reforming.
Journal of Molecular Catalysis A: Chemical, 344(1-2), 28-36.
doi:10.1016/j.molcata.2011.04.018
- Forzatti, P., & Lietti, L. (1999). Catalyst deactivation. *Catalysis Today*, 52(2), 165-181.
doi:https://doi.org/10.1016/S0920-5861(99)00074-7
- Fulvio, P. F., Brosey, R. I., & Jaroniec, M. (2010). Synthesis of Mesoporous Alumina
from Boehmite in the Presence of Triblock Copolymer. *ACS Applied Materials
& Interfaces*, 2(2), 588-593. doi:10.1021/am9009023

- Ghosh, S., & Naskar, M. K. (2014). Understanding the Role of Triblock Copolymers for the Synthesis of Mesoporous Alumina, and Its Adsorption Efficiency for Congo Red. *Journal of the American Ceramic Society*, 97(1), 100-106. doi:10.1111/jace.12663
- Ginsburg, J. M., Piña, J., El Solh, T., & de Lasa, H. I. (2005). Coke Formation over a Nickel Catalyst under Methane Dry Reforming Conditions: Thermodynamic and Kinetic Models. *Industrial & Engineering Chemistry Research*, 44(14), 4846-4854. doi:10.1021/ie0496333
- Haffer, S., Weinberger, C., & Tiemann, M. (2012). Mesoporous Al₂O₃ by Nanocasting: Relationship between Crystallinity and Mesoscopic Order. *European Journal of Inorganic Chemistry*, 2012(20), 3283-3288. doi:10.1002/ejic.201200131
- Hassani Rad, S. J., Haghghi, M., Alizadeh Eslami, A., Rahmani, F., & Rahemi, N. (2016). Sol-gel vs. impregnation preparation of MgO and CeO₂ doped Ni/Al₂O₃ nanocatalysts used in dry reforming of methane: Effect of process conditions, synthesis method and support composition. *International Journal of Hydrogen Energy*, 41(11), 5335-5350. doi:https://doi.org/10.1016/j.ijhydene.2016.02.002
- Hernández, S., Amin Farkhondehfal, M., Sastre, F., Makkee, M., Saracco, G., & Russo, N. (2017). Syngas production from electrochemical reduction of CO₂: current status and prospective implementation. *Green Chemistry*, 19(10), 2326-2346. doi:10.1039/C7GC00398F
- Hou, Z., Chen, P., Fang, H., Zheng, X., & Yashima, T. (2006). Production of synthesis gas via methane reforming with CO₂ on noble metals and small amount of noble-(Rh-) promoted Ni catalysts. *International Journal of Hydrogen Energy*, 31(5), 555-561. doi:https://doi.org/10.1016/j.ijhydene.2005.06.010
- Huang, B., Bartholomew, C. H., Smith, S. J., & Woodfield, B. F. (2013). Facile solvent-deficient synthesis of mesoporous γ -alumina with controlled pore structures. *Microporous and Mesoporous Materials*, 165, 70-78. doi:https://doi.org/10.1016/j.micromeso.2012.07.052
- Huang, X., Ji, C., Wang, C., Xiao, F., Zhao, N., Sun, N., . . . Sun, Y. (2017). Ordered mesoporous CoO-NiO-Al₂O₃ bimetallic catalysts with dual confinement effects for CO₂ reforming of CH₄. *Catalysis Today*, 281, 241-249. doi:https://doi.org/10.1016/j.cattod.2016.02.064
- Huang, X., Xue, G., Wang, C., Zhao, N., Sun, N., Wei, W., & Sun, Y. (2016). Highly stable mesoporous NiO-Y₂O₃-Al₂O₃ catalysts for CO₂ reforming of methane: effect of Ni embedding and Y₂O₃ promotion. *Catalysis Science & Technology*, 6(2), 449-459. doi:10.1039/C5CY01171J
- Hull, S., & Trawczyński, J. (2014). Steam reforming of ethanol on zinc containing catalysts with spinel structure. *International Journal of Hydrogen Energy*, 39(9), 4259-4265. doi:https://doi.org/10.1016/j.ijhydene.2013.12.184

- Ibrahim, A. A., Fakeeha, A. H., & Al-Fatesh, A. S. (2014). Enhancing hydrogen production by dry reforming process with strontium promoter. *International Journal of Hydrogen Energy*, 39(4), 1680-1687. doi:https://doi.org/10.1016/j.ijhydene.2013.11.050
- Ibrahim, A. A., Umar, A., Kumar, R., Kim, S. H., Bumajdad, A., & Baskoutas, S. (2016). Sm₂O₃-doped ZnO beech fern hierarchical structures for nitroaniline chemical sensor. *Ceramics International*, 42(15), 16505-16511. doi:https://doi.org/10.1016/j.ceramint.2016.07.061
- Iglesias, I., Baronetti, G., Alemany, L., & Mariño, F. (2019). Insight into Ni/Ce_{1-x}Zr_xO_{2-δ} support interplay for enhanced methane steam reforming. *International Journal of Hydrogen Energy*, 44(7), 3668-3680. doi:https://doi.org/10.1016/j.ijhydene.2018.12.112
- Iglesias, I. D., Baronetti, G., & Mariño, F. (2017). Nickel-based doped ceria-supported catalysts for steam reforming of methane at mild conditions. *Energy Sources, Part A: Recovery, Utilization, and Environmental Effects*, 39(2), 129-133. doi:10.1080/15567036.2016.1214639
- Ismagilov, I. Z., Matus, E. V., Nefedova, D. V., Kuznetsov, V. V., Yashnik, S. A., Kerzhentsev, M. A., & Ismagilov, Z. R. (2015). Effect of support modification on the physicochemical properties of a NiPd/Al₂O₃ catalyst for the autothermal reforming of methane. *Kinetics and Catalysis*, 56(3), 394-402. doi:10.1134/S0023158415030064
- Iulianelli, A., Liguori, S., Wilcox, J., & Basile, A. (2016). Advances on methane steam reforming to produce hydrogen through membrane reactors technology: A review. *Catalysis Reviews*, 58(1), 1-35. doi:10.1080/01614940.2015.1099882
- Jabbour, K., El Hassan, N., Casale, S., Estephane, J., & El Zakhem, H. (2014). Promotional effect of Ru on the activity and stability of Co/SBA-15 catalysts in dry reforming of methane. *International Journal of Hydrogen Energy*, 39(15), 7780-7787. doi:https://doi.org/10.1016/j.ijhydene.2014.03.040
- Jabbour, K., Massiani, P., Davidson, A., Casale, S., & El Hassan, N. (2017). Ordered mesoporous "one-pot" synthesized Ni-Mg(Ca)-Al₂O₃ as effective and remarkably stable catalysts for combined steam and dry reforming of methane (CSDRM). *Applied Catalysis B: Environmental*, 201, 527-542. doi:https://doi.org/10.1016/j.apcatb.2016.08.009
- Ji, L., Tang, S., Zeng, H. C., Lin, J., & Tan, K. L. (2001). CO₂ reforming of methane to synthesis gas over sol-gel-made Co/γ-Al₂O₃ catalysts from organometallic precursors. *Applied Catalysis A: General*, 207(1), 247-255. doi:https://doi.org/10.1016/S0926-860X(00)00659-1
- Johnsson, F., Kjärstad, J., & Rootzén, J. (2019). The threat to climate change mitigation posed by the abundance of fossil fuels. *Climate Policy*, 19(2), 258-274. doi:10.1080/14693062.2018.1483885

- Joshi, C., Dwivedi, A., & Rai, S. B. (2014). Structural morphology, upconversion luminescence and optical thermometric sensing behavior of $Y_2O_3:Er^{3+}/Yb^{3+}$ nano-crystalline phosphor. *Spectrochimica Acta Part A: Molecular and Biomolecular Spectroscopy*, 129, 451-456. doi:https://doi.org/10.1016/j.saa.2014.03.048
- Kambolis, A., Matralis, H., Trovarelli, A., & Papadopoulou, C. (2010). Ni/CeO₂-ZrO₂ catalysts for the dry reforming of methane. *Applied Catalysis A: General*, 377(1), 16-26. doi:https://doi.org/10.1016/j.apcata.2010.01.013
- Khajenoori, M., Rezaei, M., & Meshkani, F. (2014). Characterization of CeO₂ Promoter of a Nanocrystalline Ni/MgO Catalyst in Dry Reforming of Methane. *Chemical Engineering & Technology*, 37(6), 957-963. doi:10.1002/ceat.201300503
- Khajenoori, M., Rezaei, M., & Meshkani, F. (2015). Dry reforming over CeO₂-promoted Ni/MgO nano-catalyst: Effect of Ni loading and CH₄/CO₂ molar ratio. *Journal of Industrial and Engineering Chemistry*, 21, 717-722. doi:https://doi.org/10.1016/j.jiec.2014.03.043
- Kim, Y.-C., & Kim, C.-I. (2001). Etching mechanism of Y₂O₃ thin films in high density Cl₂/Ar plasma. *Journal of Vacuum Science & Technology A*, 19(5), 2676-2679. doi:10.1116/1.1399316
- Koh, A. C. W., Chen, L., Kee Leong, W., Johnson, B. F. G., Khimyak, T., & Lin, J. (2007). Hydrogen or synthesis gas production via the partial oxidation of methane over supported nickel-cobalt catalysts. *International Journal of Hydrogen Energy*, 32(6), 725-730. doi:https://doi.org/10.1016/j.ijhydene.2006.08.002
- Kourtelesis, M., Panagiotopoulou, P., Ladas, S., & Verykios, X. E. (2015). Influence of the Support on the Reaction Network of Ethanol Steam Reforming at Low Temperatures Over Pt Catalysts. *Topics in Catalysis*, 58(18), 1202-1217. doi:10.1007/s11244-015-0485-7
- Lassi, U. (2003). *Deactivation Correlations of Pd/Rh Three-way Catalysts Designed for Euro IV Emission Limits.*, University of Oulu,
- le Saché, E., Santos, J. L., Smith, T. J., Centeno, M. A., Arellano-Garcia, H., Odriozola, J. A., & Reina, T. R. (2018). Multicomponent Ni-CeO₂ nanocatalysts for syngas production from CO₂/CH₄ mixtures. *Journal of CO₂ Utilization*, 25, 68-78. doi:https://doi.org/10.1016/j.jcou.2018.03.012
- Li, B., Xu, X., & Zhang, S. (2013). Synthesis gas production in the combined CO₂ reforming with partial oxidation of methane over Ce-promoted Ni/SiO₂ catalysts. *International Journal of Hydrogen Energy*, 38(2), 890-900. doi:https://doi.org/10.1016/j.ijhydene.2012.10.103
- Li, J. F., Xia, C., Au, C. T., & Liu, B. S. (2014). Y₂O₃-promoted NiO/SBA-15 catalysts highly active for CO₂/CH₄ reforming. *International Journal of Hydrogen Energy*, 39(21), 10927-10940. doi:https://doi.org/10.1016/j.ijhydene.2014.05.021

- Li, P., He, C., Cheng, J., Ma, C. Y., Dou, B. J., & Hao, Z. P. (2011). Catalytic oxidation of toluene over Pd/Co₃AlO catalysts derived from hydrotalcite-like compounds: Effects of preparation methods. *Applied Catalysis B: Environmental*, *101*(3), 570-579. doi:<https://doi.org/10.1016/j.apcatb.2010.10.030>
- Li, S., & Gong, J. (2014). Strategies for improving the performance and stability of Ni-based catalysts for reforming reactions. *Chemical Society Reviews*, *43*(21), 7245-7256. doi:10.1039/C4CS00223G
- Li, X., Li, D., Tian, H., Zeng, L., Zhao, Z.-J., & Gong, J. (2017). Dry reforming of methane over Ni/La₂O₃ nanorod catalysts with stabilized Ni nanoparticles. *Applied Catalysis B: Environmental*, *202*, 683-694. doi:<https://doi.org/10.1016/j.apcatb.2016.09.071>
- Liander, H. (1929). The utilisation of natural gases for the ammonia process. *Transactions of the Faraday Society*, *25*(0), 462-472. doi:10.1039/TF9292500462
- Liu, H., Hadjltaief, H. B., Benzina, M., Gálvez, M. E., & Da Costa, P. (2019). Natural clay based nickel catalysts for dry reforming of methane: On the effect of support promotion (La, Al, Mn). *International Journal of Hydrogen Energy*, *44*(1), 246-255. doi:<https://doi.org/10.1016/j.ijhydene.2018.03.004>
- Liu, H., Wierzbicki, D., Debek, R., Motak, M., Grzybek, T., Da Costa, P., & Galvez, M. (2016). La-promoted Ni-hydrotalcite-derived catalysts for dry reforming of methane at low temperatures. *Fuel*, *182*, 8-16. doi:10.1016/j.fuel.2016.05.073
- Liu, Q., Wang, A., Wang, X., Gao, P., Wang, X., & Zhang, T. (2008). Synthesis, characterization and catalytic applications of mesoporous γ -alumina from boehmite sol. *Microporous and Mesoporous Materials*, *111*(1), 323-333. doi:<https://doi.org/10.1016/j.micromeso.2007.08.007>
- Liu, Q., Wang, A., Xu, J., Zhang, Y., Wang, X., & Zhang, T. (2008). Preparation of ordered mesoporous crystalline alumina replicated by mesoporous carbon. *Microporous and Mesoporous Materials*, *116*(1), 461-468. doi:<https://doi.org/10.1016/j.micromeso.2008.05.011>
- Löfberg, A., Guerrero-Caballero, J., Kane, T., Rubbens, A., & Jalowiecki-Duhamel, L. (2017). Ni/CeO₂ based catalysts as oxygen vectors for the chemical looping dry reforming of methane for syngas production. *Applied Catalysis B: Environmental*, *212*, 159-174. doi:<https://doi.org/10.1016/j.apcatb.2017.04.048>
- Lu, S., Wang, F., Chen, C., Huang, F., & Li, K. (2017). Catalytic oxidation of formaldehyde over CeO₂-Co₃O₄ catalysts. *Journal of Rare Earths*, *35*(9), 867-874. doi:[https://doi.org/10.1016/S1002-0721\(17\)60988-8](https://doi.org/10.1016/S1002-0721(17)60988-8)
- Luisetto, I., Tuti, S., Battocchio, C., Lo Mastro, S., & Sodo, A. (2015). Ni/CeO₂-Al₂O₃ catalysts for the dry reforming of methane: The effect of CeAlO₃ content and nickel crystallite size on catalytic activity and coke resistance. *Applied Catalysis A: General*, *500*, 12-22. doi:<https://doi.org/10.1016/j.apcata.2015.05.004>

- Luisetto, I., Tuti, S., & Di Bartolomeo, E. (2012). Co and Ni supported on CeO₂ as selective bimetallic catalyst for dry reforming of methane. *International Journal of Hydrogen Energy*, 37(21), 15992-15999. doi:<https://doi.org/10.1016/j.ijhydene.2012.08.006>
- Luneau, M., Gianotti, E., Guilhaume, N., Landrison, E., Meunier, F. C., Mirodatos, C., & Schuurman, Y. (2017). Experiments and Modeling of Methane Autothermal Reforming over Structured Ni–Rh-Based Si–SiC Foam Catalysts. *Industrial & Engineering Chemistry Research*, 56(45), 13165-13174. doi:10.1021/acs.iecr.7b01559
- Ma, H., Zeng, L., Tian, H., Li, D., Wang, X., Li, X., & Gong, J. (2016). Efficient hydrogen production from ethanol steam reforming over La-modified ordered mesoporous Ni-based catalysts. *Applied Catalysis B: Environmental*, 181, 321-331. doi:<https://doi.org/10.1016/j.apcatb.2015.08.019>
- Ma, Q., Sun, J., Gao, X., Zhang, J., Zhao, T., Yoneyama, Y., & Tsubaki, N. (2016). Ordered mesoporous alumina-supported bimetallic Pd–Ni catalysts for methane dry reforming reaction. *Catalysis Science & Technology*, 6(17), 6542-6550. doi:10.1039/C6CY00841K
- Maia, T. A., Assaf, J. M., & Assaf, E. M. (2014). Study of Co/CeO₂- γ -Al₂O₃ catalysts for steam and oxidative reforming of ethanol for hydrogen production. *Fuel Processing Technology*, 128, 134-145. doi:<https://doi.org/10.1016/j.fuproc.2014.07.009>
- Martínez, A. n., López, C., Marquez, F., & Díaz, I. (2003). Fischer-Tropsch synthesis of hydrocarbons over mesoporous Co/SBA-15 catalysts: The influence of metal loading, cobalt precursor, and promoters. *Journal of Catalysis*, 220, 486-499. doi:10.1016/S0021-9517(03)00289-6
- Martins, F., Felgueiras, C., Smitkova, M., & Caetano, N. (2019). Analysis of Fossil Fuel Energy Consumption and Environmental Impacts in European Countries. *Energies*, 12(6), 964.
- Mears, D. E. (1971). Tests for Transport Limitations in Experimental Catalytic Reactors. *Industrial & Engineering Chemistry Process Design and Development*, 10(4), 541-547. doi:10.1021/i260040a020
- Meng, F., Li, Z., Liu, J., Cui, X., & Zheng, H. (2015). Effect of promoter Ce on the structure and catalytic performance of Ni/Al₂O₃ catalyst for CO methanation in slurry-bed reactor. *Journal of Natural Gas Science and Engineering*, 23, 250-258. doi:<https://doi.org/10.1016/j.jngse.2015.01.041>
- Mirzaei, F., Rezaei, M., Meshkani, F., & Fattah, Z. (2015). Carbon dioxide reforming of methane for syngas production over Co–MgO mixed oxide nanocatalysts. *Journal of Industrial and Engineering Chemistry*, 21, 662-667. doi:<https://doi.org/10.1016/j.jiec.2014.03.034>

- Monteiro, W. F., Vieira, M. O., Calgaro, C. O., Perez-Lopez, O. W., & Ligabue, R. A. (2019). Dry reforming of methane using modified sodium and protonated titanate nanotube catalysts. *Fuel*, 253, 713-721. doi:https://doi.org/10.1016/j.fuel.2019.05.019
- Morris, S. M., Fulvio, P. F., & Jaroniec, M. (2008). Ordered Mesoporous Alumina-Supported Metal Oxides. *Journal of the American Chemical Society*, 130(45), 15210-15216. doi:10.1021/ja806429q
- Moulijn, J. A., van Diepen, A. E., & Kapteijn, F. (2001). Catalyst deactivation: is it predictable?: What to do? *Applied Catalysis A: General*, 212(1), 3-16. doi:https://doi.org/10.1016/S0926-860X(00)00842-5
- Moura-Nickel, C. D., Tachinski, C. G., Landers, R., De Noni, A., Virmond, E., Peterson, M., . . . José, H. J. (2019). Syngas production by dry reforming of methane using lyophilized nickel catalysts. *Chemical Engineering Science*, 205, 74-82. doi:https://doi.org/10.1016/j.ces.2019.04.035
- Movasati, A., Alavi, S. M., & Mazloom, G. (2017). CO₂ reforming of methane over Ni/ZnAl₂O₄ catalysts: Influence of Ce addition on activity and stability. *International Journal of Hydrogen Energy*, 42(26), 16436-16448. doi:https://doi.org/10.1016/j.ijhydene.2017.05.199
- Movasati, A., Alavi, S. M., & Mazloom, G. (2019). Dry reforming of methane over CeO₂-ZnAl₂O₄ supported Ni and Ni-Co nano-catalysts. *Fuel*, 236, 1254-1262. doi:https://doi.org/10.1016/j.fuel.2018.09.069
- Naeem, M., Alfatesh, A., Khan, W., Abasaeed, A., & Fakeeha, A. (2013). Syngas Production from Dry Reforming of Methane over Nano Ni Polyol Catalysts. *International Journal of Chemical Engineering and Applications*, 315-320. doi:10.7763/IJCEA.2013.V4.317
- Nagaoka, K., Takanabe, K., & Aika, K.-i. (2003). Influence of the reduction temperature on catalytic activity of Co/TiO₂ (anatase-type) for high pressure dry reforming of methane. *Applied Catalysis A: General*, 255(1), 13-21. doi:https://doi.org/10.1016/S0926-860X(03)00631-8
- Nagaoka, K., Takanabe, K., & Aika, K.-i. (2004). Modification of Co/TiO₂ for dry reforming of methane at 2MPa by Pt, Ru or Ni. *Applied Catalysis A: General*, 268(1), 151-158. doi:https://doi.org/10.1016/j.apcata.2004.03.029
- Natesakhawat, S., Oktar, O., & Ozkan, U. S. (2005). Effect of lanthanide promotion on catalytic performance of sol-gel Ni/Al₂O₃ catalysts in steam reforming of propane. *Journal of Molecular Catalysis A: Chemical*, 241(1), 133-146. doi:https://doi.org/10.1016/j.molcata.2005.07.017
- Nawfal, M., Gennequin, C., Labaki, M., Nsouli, B., Aboukaïs, A., & Abi-Aad, E. (2015). Hydrogen production by methane steam reforming over Ru supported on Ni-Mg-Al mixed oxides prepared via hydrotalcite route. *International Journal of*

- Newnham, J., Mantri, K., Amin, M. H., Tardio, J., & Bhargava, S. K. (2012). Highly stable and active Ni-mesoporous alumina catalysts for dry reforming of methane. *International Journal of Hydrogen Energy*, 37(2), 1454-1464.
doi:<https://doi.org/10.1016/j.ijhydene.2011.10.036>
- Nikoo, M. K., & Amin, N. A. S. (2011). Thermodynamic analysis of carbon dioxide reforming of methane in view of solid carbon formation. *Fuel Processing Technology*, 92(3), 678-691. doi:<https://doi.org/10.1016/j.fuproc.2010.11.027>
- Ning, Q., Zhang, H., He, Y., Chen, Z., Liu, S., & Ren, J. (2019). Suppression of platinum sintering on Pt-M/ZSM-22 (M = Ce, La, and Re) catalyst for n-dodecane isomerization. *New Journal of Chemistry*, 43(35), 13967-13978.
doi:10.1039/C9NJ03194D
- Nishimoto, H.-a., Nakagawa, K., Ikenaga, N.-o., Nishitani-Gamo, M., Ando, T., & Suzuki, T. (2004). Partial oxidation of methane to synthesis gas over oxidized diamond catalysts. *Applied Catalysis A: General*, 264(1), 65-72.
doi:<https://doi.org/10.1016/j.apcata.2003.12.029>
- Niu, J., Du, X., Ran, J., & Wang, R. (2016). Dry (CO₂) reforming of methane over Pt catalysts studied by DFT and kinetic modeling. *Applied Surface Science*, 376, 79-90. doi:<https://doi.org/10.1016/j.apsusc.2016.01.212>
- Oemar, U., Hidajat, K., & Kawi, S. (2011). Role of catalyst support over PdO-NiO catalysts on catalyst activity and stability for oxy-CO₂ reforming of methane. *Applied Catalysis A: General*, 402(1), 176-187.
doi:<https://doi.org/10.1016/j.apcata.2011.06.002>
- Ogden, J. M. (2001). *Review of small stationary reformers for hydrogen production*. Retrieved from Princeton, NJ
- Omata, K., Nukui, N., Hottai, T., Showa, Y., & Yamada, M. (2004). Strontium carbonate supported cobalt catalyst for dry reforming of methane under pressure. *Catalysis Communications*, 5(12), 755-758.
doi:<https://doi.org/10.1016/j.catcom.2004.09.012>
- Omogbe, O., Danh, H., Abidin, S., Setiabudi, H., Abdullah, B., Vu, K., & Vo, D.-V. (2016). Influence of Lanthanide Promoters on Ni/SBA-15 Catalysts for Syngas Production by Methane Dry Reforming. *Procedia Engineering*, 148, 1388-1395.
doi:10.1016/j.proeng.2016.06.556
- Omogbe, O., Danh, H. T., Nguyen-Huy, C., Setiabudi, H. D., Abidin, S. Z., Truong, Q. D., & Vo, D.-V. N. (2017). Syngas production from methane dry reforming over Ni/SBA-15 catalyst: Effect of operating parameters. *International Journal of Hydrogen Energy*, 42(16), 11283-11294.
doi:<https://doi.org/10.1016/j.ijhydene.2017.03.146>

- Osazuwa, O. U., Khan, M. R., Lam, S. S., Assabumrungrat, S., & Cheng, C. K. (2018). An assessment of the longevity of samarium cobalt trioxide perovskite catalyst during the conversion of greenhouse gases into syngas. *Journal of Cleaner Production*, 185, 576-587. doi:<https://doi.org/10.1016/j.jclepro.2018.03.060>
- Özkara-Aydinoğlu, Ş., & Aksoylu, A. E. (2010). Carbon dioxide reforming of methane over Co-X/ZrO₂ catalysts (X=La, Ce, Mn, Mg, K). *Catalysis Communications*, 11(15), 1165-1170. doi:<https://doi.org/10.1016/j.catcom.2010.07.001>
- Padban, N., & Becher, V. (2005). Clean hydrogen-rich synthesis gas: literature and state-of-the-art review. *Report No. CHRISGAS October*.
- Padi, S. P., Shelly, L., Komarala, E. P., Schweke, D., Hayun, S., & Rosen, B. A. (2020). Coke-free methane dry reforming over nano-sized NiO-CeO₂ solid solution after exsolution. *Catalysis Communications*, 138, 105951. doi:<https://doi.org/10.1016/j.catcom.2020.105951>
- Pakhare, D., & Spivey, J. (2014). A review of dry (CO₂) reforming of methane over noble metal catalysts. *Chemical Society Reviews*, 43(22), 7813-7837. doi:10.1039/C3CS60395D
- Paksoy, A. I., Caglayan, B. S., & Aksoylu, A. E. (2015). A study on characterization and methane dry reforming performance of Co-Ce/ZrO₂ catalyst. *Applied Catalysis B: Environmental*, 168-169, 164-174. doi:<https://doi.org/10.1016/j.apcatb.2014.12.038>
- Pal, N., & Bhaumik, A. (2013). Soft templating strategies for the synthesis of mesoporous materials: Inorganic, organic-inorganic hybrid and purely organic solids. *Advances in Colloid and Interface Science*, 189-190, 21-41. doi:<https://doi.org/10.1016/j.cis.2012.12.002>
- Palo, D. R., Dagle, R. A., & Holladay, J. D. (2007). Methanol Steam Reforming for Hydrogen Production. *Chemical Reviews*, 107(10), 3992-4021. doi:10.1021/cr050198b
- Papageridis, K. N., Siakavelas, G., Charisiou, N. D., Avraam, D. G., Tzounis, L., Kousi, K., & Goula, M. A. (2016). Comparative study of Ni, Co, Cu supported on γ -alumina catalysts for hydrogen production via the glycerol steam reforming reaction. *Fuel Processing Technology*, 152, 156-175. doi:<https://doi.org/10.1016/j.fuproc.2016.06.024>
- Pardo-Tarifa, F., Cabrera, S., Sanchez-Dominguez, M., & Boutonnet, M. (2017). Ce-promoted Co/Al₂O₃ catalysts for Fischer-Tropsch synthesis. *International Journal of Hydrogen Energy*, 42(15), 9754-9765. doi:<https://doi.org/10.1016/j.ijhydene.2017.01.056>
- Park, J.-H., Yeo, S., & Chang, T.-S. (2018). Effect of supports on the performance of Co-based catalysts in methane dry reforming. *Journal of CO₂ Utilization*, 26, 465-475. doi:<https://doi.org/10.1016/j.jcou.2018.06.002>

- Park, J.-Y., Lee, Y.-J., Karandikar, P. R., Jun, K.-W., Bae, J. W., & Ha, K.-S. (2011). Ru promoted cobalt catalyst on γ -Al₂O₃ support: Influence of pre-synthesized nanoparticles on Fischer–Tropsch reaction. *Journal of Molecular Catalysis A: Chemical*, 344(1), 153-160. doi:<https://doi.org/10.1016/j.molcata.2011.05.022>
- Passos, F. B., Oliveira, E. R., Mattos, L. V., & Noronhe, F. B. (2006). Effect of the support on the mechanism of partial oxidation of methane on platinum catalysts. *Catalysis Letters*, 110(3), 261-267. doi:10.1007/s10562-006-0119-6
- Patterson, A. (1939). The Scherrer formula for X-ray particle size determination. *Physical review*, 56(10), 978.
- Peng, W. X., Wang, L. S., Mirzaee, M., Ahmadi, H., Esfahani, M. J., & Fremaux, S. (2017). Hydrogen and syngas production by catalytic biomass gasification. *Energy Conversion and Management*, 135, 270-273. doi:<https://doi.org/10.1016/j.enconman.2016.12.056>
- Perry, R. H., & Green, D. W. (2008). *Perry's chemical engineers' handbook* (8th ed. / ed.). New York: McGraw-Hill.
- Peymani, M., Alavi, S. M., & Rezaei, M. (2016). Preparation of highly active and stable nanostructured Ni/CeO₂ catalysts for syngas production by partial oxidation of methane. *International Journal of Hydrogen Energy*, 41(15), 6316-6325. doi:<https://doi.org/10.1016/j.ijhydene.2016.03.033>
- Pichas, C., Pomonis, P., Petrakis, D., & Ladavos, A. (2010). Kinetic study of the catalytic dry reforming of CH₄ with CO₂ over La_{2-x}Sr_xNiO₄ perovskite-type oxides. *Applied Catalysis A: General*, 386(1), 116-123. doi:<https://doi.org/10.1016/j.apcata.2010.07.043>
- Pizzolitto, C., Menegazzo, F., Ghedini, E., Innocenti, G., Di Michele, A., Cruciani, G., . . . Signoretto, M. (2018). Increase of Ceria Redox Ability by Lanthanum Addition on Ni Based Catalysts for Hydrogen Production. *ACS Sustainable Chemistry & Engineering*, 6(11), 13867-13876. doi:10.1021/acssuschemeng.8b02103
- Qian, C., Guo, X., Zhang, W., Yang, H., Qian, Y., Xu, F., . . . Fan, T. (2019). Co₃O₄ nanoparticles on porous bio-carbon substrate as catalyst for oxygen reduction reaction. *Microporous and Mesoporous Materials*, 277, 45-51. doi:<https://doi.org/10.1016/j.micromeso.2018.10.020>
- Rabiah Nizah, M. F., Taufiq-Yap, Y. H., Rashid, U., Teo, S. H., Shajaratun Nur, Z. A., & Islam, A. (2014). Production of biodiesel from non-edible Jatropha curcas oil via transesterification using Bi₂O₃–La₂O₃ catalyst. *Energy Conversion and Management*, 88, 1257-1262. doi:<https://doi.org/10.1016/j.enconman.2014.02.072>
- Rahbar Shamskar, F., Meshkani, F., & Rezaei, M. (2017). Preparation and characterization of ultrasound-assisted co-precipitated nanocrystalline La-, Ce-, Zr –promoted Ni–Al₂O₃ catalysts for dry reforming reaction. *Journal of CO₂ Utilization*, 22, 124-134. doi:<https://doi.org/10.1016/j.jcou.2017.09.014>

- Rahemi, N., Haghghi, M., Babaluo, A. A., & Fallah Jafari, M. (2014). Syngas production via CO₂ reforming of methane over plasma assisted synthesized Ni-Co/Al₂O₃-ZrO₂ nanocatalysts with different Ni-loadings. *International Journal of Energy Research*, 38(6), 765-779. doi:10.1002/er.3084
- Ray, J. C., You, K.-S., Ahn, J.-W., & Ahn, W.-S. (2007). Mesoporous alumina (I): Comparison of synthesis schemes using anionic, cationic, and non-ionic surfactants. *Microporous and Mesoporous Materials*, 100(1), 183-190. doi:https://doi.org/10.1016/j.micromeso.2006.10.036
- Reitmeier, R. E., Atwood, K., Bennett, H., & Baugh, H. (1948). Production of Synthetic Gas - Reaction of Light Hydrocarbons with Steam and Carbon Dioxide. *Industrial & Engineering Chemistry*, 40(4), 620-626. doi:10.1021/ie50460a010
- Rostrup-Nielsen, J. R. (1997). Industrial relevance of coking. *Catalysis Today*, 37(3), 225-232. doi:https://doi.org/10.1016/S0920-5861(97)00016-3
- Ruckenstein, E., & Wang, H. Y. (2002). Carbon Deposition and Catalytic Deactivation during CO₂ Reforming of CH₄ over Co/ γ -Al₂O₃ Catalysts. *Journal of Catalysis*, 205(2), 289-293. doi:https://doi.org/10.1006/jcat.2001.3458
- San-José-Alonso, D., Juan-Juan, J., Illán-Gómez, M. J., & Román-Martínez, M. C. (2009). Ni, Co and bimetallic Ni-Co catalysts for the dry reforming of methane. *Applied Catalysis A: General*, 371(1), 54-59. doi:https://doi.org/10.1016/j.apcata.2009.09.026
- Santos, D. C. R. M., Madeira, L., & Passos, F. B. (2010). The effect of the addition of Y₂O₃ to Ni/ α -Al₂O₃ catalysts on the autothermal reforming of methane. *Catalysis Today*, 149(3), 401-406. doi:https://doi.org/10.1016/j.cattod.2009.06.015
- Sepehri, S., Rezaei, M., Garbarino, G., & Busca, G. (2016a). Facile synthesis of a mesoporous alumina and its application as a support of Ni-based autothermal reforming catalysts. *International Journal of Hydrogen Energy*, 41(5), 3456-3464. doi:https://doi.org/10.1016/j.ijhydene.2015.12.122
- Sepehri, S., Rezaei, M., Garbarino, G., & Busca, G. (2016b). Preparation and characterization of mesoporous nanocrystalline La-, Ce-, Zr-, Sr-containing NiAl₂O₃ methane autothermal reforming catalysts. *International Journal of Hydrogen Energy*, 41(21), 8855-8862. doi:https://doi.org/10.1016/j.ijhydene.2016.03.139
- Shafiqah, M.-N. N., Nguyen, T. D., Jun, L. N., Bahari, M. B., Phuong, P. T. T., Abdullah, B., & Vo, D.-V. N. (2019). Production of syngas from ethanol CO₂ reforming on La-doped Cu/Al₂O₃: Impact of promoter loading. *AIP Conference Proceedings*, 2124(1), 020011. doi:10.1063/1.5117071
- Shamsi, A., & Johnson, C. D. (2007). The Effect of Pressure on CO₂ Reforming of Methane and the Carbon Deposition Route Using Noble Metal Catalysts. In *Ultraclean Transportation Fuels* (Vol. 959, pp. 87-101): American Chemical Society.

- Shang, Z., Li, S., Li, L., Liu, G., & Liang, X. (2017). Highly active and stable alumina supported nickel nanoparticle catalysts for dry reforming of methane. *Applied Catalysis B: Environmental*, 201, 302-309. doi:https://doi.org/10.1016/j.apcatb.2016.08.019
- Shen, W., Momoi, H., Komatsubara, K., Saito, T., Yoshida, A., & Naito, S. (2011). Marked role of mesopores for the prevention of sintering and carbon deposition in dry reforming of methane over ordered mesoporous Ni–Mg–Al oxides. *Catalysis Today*, 171(1), 150-155. doi:https://doi.org/10.1016/j.cattod.2011.04.003
- Siang, T. J., Singh, S., Omoregbe, O., Bach, L. G., Phuc, N. H. H., & Vo, D.-V. N. (2018). Hydrogen production from CH₄ dry reforming over bimetallic Ni–Co/Al₂O₃ catalyst. *Journal of the Energy Institute*, 91(5), 683-694. doi:https://doi.org/10.1016/j.joei.2017.06.001
- Sierra Gallego, G., Batiot-Dupeyrat, C., Barrault, J., & Mondragón, F. (2008). Dual Active-Site Mechanism for Dry Methane Reforming over Ni/La₂O₃ Produced from LaNiO₃ Perovskite. *Industrial & Engineering Chemistry Research*, 47(23), 9272-9278. doi:10.1021/ie800281t
- Siew, K. W., Lee, H. C., Gim bun, J., Chin, S. Y., Khan, M. R., Taufiq-Yap, Y. H., & Cheng, C. K. (2015). Syngas production from glycerol-dry(CO₂) reforming over La-promoted Ni/Al₂O₃ catalyst. *Renewable Energy*, 74, 441-447. doi:https://doi.org/10.1016/j.renene.2014.08.048
- Singh, S., Bahari, M. B., Abdullah, B., Phuong, P. T. T., Truong, Q. D., Vo, D.-V. N., & Adesina, A. A. (2018). Bi-reforming of methane on Ni/SBA-15 catalyst for syngas production: Influence of feed composition. *International Journal of Hydrogen Energy*, 43(36), 17230-17243. doi:https://doi.org/10.1016/j.ijhydene.2018.07.136
- Singha, R. K., Shukla, A., Yadav, A., Sivakumar Konathala, L. N., & Bal, R. (2017). Effect of metal-support interaction on activity and stability of Ni-CeO₂ catalyst for partial oxidation of methane. *Applied Catalysis B: Environmental*, 202, 473-488. doi:https://doi.org/10.1016/j.apcatb.2016.09.060
- Singha, R. K., Yadav, A., Shukla, A., Kumar, M., & Bal, R. (2017). Low temperature dry reforming of methane over Pd-CeO₂ nanocatalyst. *Catalysis Communications*, 92, 19-22. doi:https://doi.org/10.1016/j.catcom.2016.12.019
- Souza, M. M. V. M., & Schmal, M. (2005). Autothermal reforming of methane over Pt/ZrO₂/Al₂O₃ catalysts. *Applied Catalysis A: General*, 281(1), 19-24. doi:https://doi.org/10.1016/j.apcata.2004.11.007
- Sun, G. B., Hidajat, K., Wu, X. S., & Kawi, S. (2008). A crucial role of surface oxygen mobility on nanocrystalline Y₂O₃ support for oxidative steam reforming of ethanol to hydrogen over Ni/Y₂O₃ catalysts. *Applied Catalysis B: Environmental*, 81(3), 303-312. doi:https://doi.org/10.1016/j.apcatb.2007.12.021

- Sun, Y., Zhang, G., Liu, J., Xu, Y., & Lv, Y. (2020). Production of syngas via CO₂ methane reforming process: Effect of cerium and calcium promoters on the performance of Ni-MSO catalysts. *International Journal of Hydrogen Energy*, 45(1), 640-649. doi:<https://doi.org/10.1016/j.ijhydene.2019.10.228>
- Swatsitang, E., Phokha, S., Hunpratub, S., & Maensiri, S. (2016). Modification of Ce valence states by Sm/Sr co-doping of CeO₂ nanoparticles for improved magneto-electrochemical properties. *Materials & Design*, 108, 27-33. doi:<https://doi.org/10.1016/j.matdes.2016.06.092>
- Świrk, K., Gálvez, M. E., Motak, M., Grzybek, T., Rønning, M., & Da Costa, P. (2018). Yttrium promoted Ni-based double-layered hydroxides for dry methane reforming. *Journal of CO₂ Utilization*, 27, 247-258. doi:<https://doi.org/10.1016/j.jcou.2018.08.004>
- Świrk, K., Gálvez, M. E., Motak, M., Grzybek, T., Rønning, M., & Da Costa, P. (2019). Syngas production from dry methane reforming over yttrium-promoted nickel-KIT-6 catalysts. *International Journal of Hydrogen Energy*, 44(1), 274-286. doi:<https://doi.org/10.1016/j.ijhydene.2018.02.164>
- Taherian, Z., Yousefpour, M., Tajally, M., & Khoshandam, B. (2017a). Catalytic performance of Samaria-promoted Ni and Co/SBA-15 catalysts for dry reforming of methane. *International Journal of Hydrogen Energy*, 42(39), 24811-24822. doi:<https://doi.org/10.1016/j.ijhydene.2017.08.080>
- Taherian, Z., Yousefpour, M., Tajally, M., & Khoshandam, B. (2017b). A comparative study of ZrO₂, Y₂O₃ and Sm₂O₃ promoted Ni/SBA-15 catalysts for evaluation of CO₂/methane reforming performance. *International Journal of Hydrogen Energy*, 42(26), 16408-16420. doi:<https://doi.org/10.1016/j.ijhydene.2017.05.095>
- Taherian, Z., Yousefpour, M., Tajally, M., & Khoshandam, B. (2017c). Promotional effect of samarium on the activity and stability of Ni-SBA-15 catalysts in dry reforming of methane. *Microporous and Mesoporous Materials*, 251, 9-18. doi:<https://doi.org/10.1016/j.micromeso.2017.05.027>
- Takanabe, K., Nagaoka, K., Nariai, K., & Aika, K.-i. (2005). Titania-supported cobalt and nickel bimetallic catalysts for carbon dioxide reforming of methane. *Journal of Catalysis*, 232(2), 268-275. doi:<https://doi.org/10.1016/j.jcat.2005.03.011>
- Tang, M., Xu, L., & Fan, M. (2014). Effect of Ce on 5 wt% Ni/ZSM-5 catalysts in the CO₂ reforming of CH₄ reaction. *International Journal of Hydrogen Energy*, 39(28), 15482-15496. doi:<https://doi.org/10.1016/j.ijhydene.2014.07.172>
- Tao, K., Shi, L., Ma, Q., wang, D., Zeng, C., Kong, C., . . . Tsubaki, N. (2013). Methane reforming with carbon dioxide over mesoporous nickel–alumina composite catalyst. *Chemical Engineering Journal*, 221, 25-31. doi:<https://doi.org/10.1016/j.cej.2013.01.073>

- Taufiq-Yap, Y. H., Sudarno, S., Rashid, U., & Zainal, Z. (2013). CeO₂-SiO₂ supported nickel catalysts for dry reforming of methane toward syngas production. *Applied Catalysis A: General*, 468, 359-369. doi:10.1016/j.apcata.2013.09.020
- Tran, N. T., Van Le, Q., Van Cuong, N., Nguyen, T. D., Huy Phuc, N. H., Phuong, P. T. T., . . . Vo, D.-V. N. (2020). La-doped cobalt supported on mesoporous alumina catalysts for improved methane dry reforming and coke mitigation. *Journal of the Energy Institute*, 93(4), 1571-1580. doi:https://doi.org/10.1016/j.joei.2020.01.019
- Tsoukalou, A., Imtiaz, Q., Kim, S. M., Abdala, P. M., Yoon, S., & Müller, C. R. (2016). Dry-reforming of methane over bimetallic Ni-M/La₂O₃ (M=Co, Fe): The effect of the rate of La₂O₂CO₃ formation and phase stability on the catalytic activity and stability. *Journal of Catalysis*, 343, 208-214. doi:https://doi.org/10.1016/j.jcat.2016.03.018
- Usman, M., Wan Daud, W. M. A., & Abbas, H. F. (2015). Dry reforming of methane: Influence of process parameters—A review. *Renewable and Sustainable Energy Reviews*, 45, 710-744. doi:https://doi.org/10.1016/j.rser.2015.02.026
- Verykios, X. E. (2003). Catalytic dry reforming of natural gas for the production of chemicals and hydrogen. *International Journal of Hydrogen Energy*, 28(10), 1045-1063. doi:https://doi.org/10.1016/S0360-3199(02)00215-X
- Vizcaíno, A. J., Lindo, M., Carrero, A., & Calles, J. A. (2012). Hydrogen production by steam reforming of ethanol using Ni catalysts based on ternary mixed oxides prepared by coprecipitation. *International Journal of Hydrogen Energy*, 37(2), 1985-1992. doi:https://doi.org/10.1016/j.ijhydene.2011.04.179
- Wang, N., Shen, K., Huang, L., Yu, X., Qian, W., & Chu, W. (2013). Facile Route for Synthesizing Ordered Mesoporous Ni-Ce-Al Oxide Materials and Their Catalytic Performance for Methane Dry Reforming to Hydrogen and Syngas. *ACS Catalysis*, 3(7), 1638-1651. doi:10.1021/cs4003113
- Wang, N., Xu, Z., Deng, J., Shen, K., Yu, X., Qian, W., . . . Wei, F. (2014). One-pot Synthesis of Ordered Mesoporous NiCeAl Oxide Catalysts and a Study of Their Performance in Methane Dry Reforming. *ChemCatChem*, 6(5), 1470-1480. doi:10.1002/cctc.201300720
- Wang, N., Yu, X., Wang, Y., Chu, W., & Liu, M. (2013). A comparison study on methane dry reforming with carbon dioxide over LaNiO₃ perovskite catalysts supported on mesoporous SBA-15, MCM-41 and silica carrier. *Catalysis Today*, 212, 98-107. doi:https://doi.org/10.1016/j.cattod.2012.07.022
- Wang, X., Cao, R., Zhang, S., Hou, P., Han, R., Shao, M., & Xu, X. (2017). Hierarchical flowerlike metal/metal oxide nanostructures derived from layered double hydroxides for catalysis and gas sensing. *Journal of Materials Chemistry A*, 5(45), 23999-24010. doi:10.1039/C7TA06809C

- Wang, X., Pan, D., Guo, M., He, M., Niu, P., & Li, R. (2013). Facile synthesis of highly ordered mesoporous alumina with high thermal and hydrothermal stability using zirconia as promoter. *Materials Letters*, 97, 27-30. doi:<https://doi.org/10.1016/j.matlet.2013.01.083>
- Wang, X., Xia, H., Wang, X., Gao, J., Shi, B., & Fang, Y. (2016). Facile synthesis ultrathin mesoporous Co_3O_4 nanosheets for high-energy asymmetric supercapacitor. *Journal of Alloys and Compounds*, 686, 969-975. doi:<https://doi.org/10.1016/j.jallcom.2016.06.156>
- Wang, Y.-F., Tsai, C.-H., Chang, W.-Y., & Kuo, Y.-M. (2010). Methane steam reforming for producing hydrogen in an atmospheric-pressure microwave plasma reactor. *International Journal of Hydrogen Energy*, 35(1), 135-140. doi:<https://doi.org/10.1016/j.ijhydene.2009.10.088>
- Wang, Y.-H., Wang, H., Li, Y., Zhu, Q.-M., & Xu, B.-Q. (2005). Performance of Ni/MgO-AN catalyst in high pressure CO_2 reforming of methane. *Topics in Catalysis*, 32(3), 109-116. doi:10.1007/s11244-005-2882-9
- Wang, Y., Wang, L., Gan, N., Lim, Z.-Y., Wu, C., Peng, J., & Wang, W. G. (2014). Evaluation of Ni/ $\text{Y}_2\text{O}_3/\text{Al}_2\text{O}_3$ catalysts for hydrogen production by autothermal reforming of methane. *International Journal of Hydrogen Energy*, 39(21), 10971-10979. doi:<https://doi.org/10.1016/j.ijhydene.2014.05.074>
- Wang, Z., Jiang, Z., & Shangguan, W. (2007). Simultaneous catalytic removal of NO_x and soot particulate over Co-Al mixed oxide catalysts derived from hydrotalcites. *Catalysis Communications*, 8(11), 1659-1664. doi:<https://doi.org/10.1016/j.catcom.2007.01.025>
- Whang, H. S., Choi, M. S., Lim, J., Kim, C., Heo, I., Chang, T.-S., & Lee, H. (2017). Enhanced activity and durability of Ru catalyst dispersed on zirconia for dry reforming of methane. *Catalysis Today*, 293-294, 122-128. doi:<https://doi.org/10.1016/j.cattod.2016.12.034>
- Wilhelm, D. J., Simbeck, D. R., Karp, A. D., & Dickenson, R. L. (2001). Syngas production for gas-to-liquids applications: technologies, issues and outlook. *Fuel Processing Technology*, 71(1), 139-148. doi:[https://doi.org/10.1016/S0378-3820\(01\)00140-0](https://doi.org/10.1016/S0378-3820(01)00140-0)
- Wilhelm, R., Johnson, W., Wynkoop, R., & Collier, D. (1948). Reaction rate, heat transfer, and temperature distribution in fixed-bed catalytic converters-solution by electrical network. *Chemical Engineering Progress*, 44(2), 105-116.
- Wisniewski, M., Boréave, A., & Gélin, P. (2005). Catalytic CO_2 reforming of methane over Ir/ $\text{Ce}_{0.9}\text{Gd}_{0.1}\text{O}_{2-x}$. *Catalysis Communications*, 6(9), 596-600. doi:<https://doi.org/10.1016/j.catcom.2005.05.008>
- Wu, W., Wan, Z., Chen, W., Zhu, M., & Zhang, D. (2015). Synthesis of mesoporous alumina with tunable structural properties. *Microporous and Mesoporous Materials*, 217, 12-20. doi:<https://doi.org/10.1016/j.micromeso.2015.06.002>

- Wu, W., Wan, Z., Zhu, M., & Zhang, D. (2016). A facile route to aqueous phase synthesis of mesoporous alumina with controllable structural properties. *Microporous and Mesoporous Materials*, 223, 203-212.
doi:<https://doi.org/10.1016/j.micromeso.2015.11.004>
- Wu, Z., Li, Q., Feng, D., Webley, P. A., & Zhao, D. (2010). Ordered Mesoporous Crystalline γ -Al₂O₃ with Variable Architecture and Porosity from a Single Hard Template. *Journal of the American Chemical Society*, 132(34), 12042-12050.
doi:[10.1021/ja104379a](https://doi.org/10.1021/ja104379a)
- Xiang, X., Zhao, H., Yang, J., Zhao, J., Yan, L., Song, H., & Chou, L. (2016). Nickel based mesoporous silica-ceria-zirconia composite for carbon dioxide reforming of methane. *Applied Catalysis A: General*, 520, 140-150.
doi:<https://doi.org/10.1016/j.apcata.2016.04.020>
- Xie, Z., Yan, B., Kattel, S., Lee, J. H., Yao, S., Wu, Q., . . . Chen, J. G. (2018). Dry reforming of methane over CeO₂-supported Pt-Co catalysts with enhanced activity. *Applied Catalysis B: Environmental*, 236, 280-293.
doi:<https://doi.org/10.1016/j.apcatb.2018.05.035>
- Xin, J., Cui, H., Cheng, Z., & Zhou, Z. (2018). Bimetallic Ni-Co/SBA-15 catalysts prepared by urea co-precipitation for dry reforming of methane. *Applied Catalysis A: General*, 554, 95-104. doi:<https://doi.org/10.1016/j.apcata.2018.01.033>
- Xu, L., Mi, W., & Su, Q. (2011). Hydrogen production through diesel steam reforming over rare-earth promoted Ni/ γ -Al₂O₃ catalysts. *Journal of Natural Gas Chemistry*, 20(3), 287-293. doi:[https://doi.org/10.1016/S1003-9953\(10\)60188-0](https://doi.org/10.1016/S1003-9953(10)60188-0)
- Xu, L., Song, H., & Chou, L. (2011). Carbon dioxide reforming of methane over ordered mesoporous NiO-Al₂O₃ composite oxides. *Catalysis Science & Technology*, 1(6), 1032-1042. doi:[10.1039/C1CY00129A](https://doi.org/10.1039/C1CY00129A)
- Xu, L., Song, H., & Chou, L. (2013). Ordered mesoporous MgO-Al₂O₃ composite oxides supported Ni based catalysts for CO₂ reforming of CH₄: Effects of basic modifier and mesopore structure. *International Journal of Hydrogen Energy*, 38(18), 7307-7325. doi:<https://doi.org/10.1016/j.ijhydene.2013.04.034>
- Xu, L., Wang, F., Chen, M., Fan, X., Yang, H., Nie, D., & Qi, L. (2017). Alkaline-promoted Co-Ni bimetal ordered mesoporous catalysts with enhanced coke-resistant performance toward CO₂ reforming of CH₄. *Journal of CO₂ Utilization*, 18, 1-14. doi:<https://doi.org/10.1016/j.jcou.2017.01.003>
- Xu, L., Zhao, H., Song, H., & Chou, L. (2012). Ordered mesoporous alumina supported nickel based catalysts for carbon dioxide reforming of methane. *International Journal of Hydrogen Energy*, 37(9), 7497-7511.
doi:<https://doi.org/10.1016/j.ijhydene.2012.01.105>
- Yan, Y., Zhang, Z., Zhang, L., Wang, X., Liu, K., & Yang, Z. (2015). Investigation of autothermal reforming of methane for hydrogen production in a spiral multi-

cylinder micro-reactor used for mobile fuel cell. *International Journal of Hydrogen Energy*, 40(4), 1886-1893.
doi:<https://doi.org/10.1016/j.ijhydene.2014.11.140>

Yang, L., & Ge, X. (2016). Chapter Three - Biogas and Syngas Upgrading. In Y. Li & X. Ge (Eds.), *Advances in Bioenergy* (Vol. 1, pp. 125-188): Elsevier.

Yang, R., Xing, C., Lv, C., Shi, L., & Tsubaki, N. (2010). Promotional effect of La_2O_3 and CeO_2 on $\text{Ni}/\gamma\text{-Al}_2\text{O}_3$ catalysts for CO_2 reforming of CH_4 . *Applied Catalysis A: General*, 385(1), 92-100. doi:<https://doi.org/10.1016/j.apcata.2010.06.050>

Yang, W., Li, C., Tian, S., Liu, L., & Liao, Q. (2020). Influence of synthesis variables of a sol-gel process on the properties of mesoporous alumina and their fluoride adsorption. *Materials Chemistry and Physics*, 242, 122499.
doi:<https://doi.org/10.1016/j.matchemphys.2019.122499>

Yang, X., Da, J., Yu, H., & Wang, H. (2016). Characterization and performance evaluation of Ni-based catalysts with Ce promoter for methane and hydrocarbons steam reforming process. *Fuel*, 179, 353-361.
doi:<https://doi.org/10.1016/j.fuel.2016.03.104>

Yin, M., He, S., Yu, Z., Wu, K., Wang, L., & Sun, C. (2013). Effect of alumina support on catalytic performance of Pt-Sn/ Al_2O_3 catalysts in one-step synthesis of N-phenylbenzylamine from aniline and benzyl alcohol. *Chinese Journal of Catalysis*, 34(8), 1534-1542. doi:[https://doi.org/10.1016/S1872-2067\(12\)60608-1](https://doi.org/10.1016/S1872-2067(12)60608-1)

Younis, M. N., Malaibari, Z. O., Ahmad, W., & Ahmed, S. (2018). Hydrogen Production through Steam Reforming of Diesel over Highly Efficient Promoted $\text{Ni}/\gamma\text{-Al}_2\text{O}_3$ Catalysts Containing Lanthanide Series (La, Ce, Eu, Pr, and Gd) Promoters. *Energy & Fuels*, 32(6), 7054-7065. doi:10.1021/acs.energyfuels.8b00890

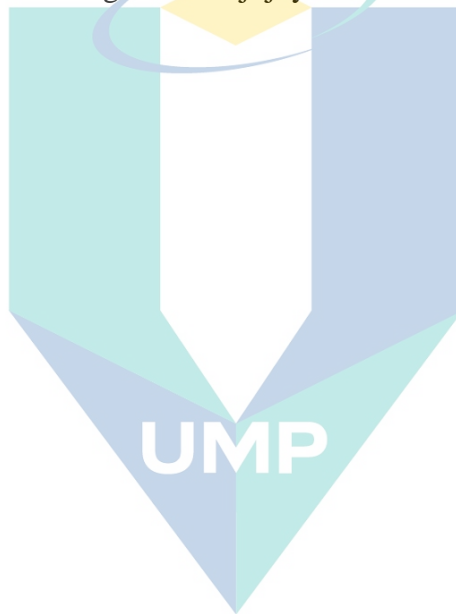
Yuan, Q., Yin, A.-X., Luo, C., Sun, L.-D., Zhang, Y.-W., Duan, W.-T., . . . Yan, C.-H. (2008). Facile Synthesis for Ordered Mesoporous γ -Aluminas with High Thermal Stability. *Journal of the American Chemical Society*, 130(11), 3465-3472.
doi:10.1021/ja0764308

Zhang, G., Su, A., Du, Y., Qu, J., & Xu, Y. (2014). Catalytic performance of activated carbon supported cobalt catalyst for CO_2 reforming of CH_4 . *Journal of Colloid and Interface Science*, 433, 149-155.
doi:<https://doi.org/10.1016/j.jcis.2014.06.038>

Zhang, J., Li, Y., Wang, L., Zhang, C., & He, H. (2015). Catalytic oxidation of formaldehyde over manganese oxides with different crystal structures. *Catalysis Science & Technology*, 5(4), 2305-2313. doi:10.1039/C4CY01461H

Zhang, L., Wang, X., Chen, C., Zou, X., Shang, X., Ding, W., & Lu, X. (2017). Investigation of mesoporous $\text{NiAl}_2\text{O}_4/\text{MO}_x$ (M= La, Ce, Ca, Mg)- $\gamma\text{-Al}_2\text{O}_3$ nanocomposites for dry reforming of methane. *RSC Advances*, 7(53), 33143-33154.

- Zhang, X., Junhui, Y., Jing, Y., Ting, C., Bei, X., Zhe, L., . . . Dannong, H. (2018). Excellent low-temperature catalytic performance of nanosheet Co-Mn oxides for total benzene oxidation. *Applied Catalysis A: General*, 566, 104-112. doi:<https://doi.org/10.1016/j.apcata.2018.05.039>
- Zhao, S., & Li, J. (2015). Silver–Cobalt Oxides Derived from Silver Nanoparticles Deposited on Layered Double Hydroxides for Methane Combustion. *ChemCatChem*, 7(13), 1966-1974. doi:10.1002/cctc.201500254
- Zhu, J., Peng, X., Yao, L., Shen, J., Tong, D., & Hu, C. (2011). The promoting effect of La, Mg, Co and Zn on the activity and stability of Ni/SiO₂ catalyst for CO₂ reforming of methane. *International Journal of Hydrogen Energy*, 36(12), 7094-7104. doi:<https://doi.org/10.1016/j.ijhydene.2011.02.133>



اونيورسيتي ملايسيا قهغ

UNIVERSITI MALAYSIA PAHANG

APPENDIX A
CALCULATIONS FOR SUPPORT AND CATALYST PREPARATION

A.1 MA Support Preparation

The mass components were calculated by considering the ratio of 16.32 g: 8 g: 12.8 ml: 160 ml corresponding to Al precursor: P123: HCl: Ethanol.

$$\frac{\text{mass of Al precursor}}{\text{molar mass of Al precursor}} = \frac{\text{mass of Alumina}}{\text{molar mass of Alumina}}$$

$$\frac{16.32 \text{ g}}{204.25 \text{ g mol}^{-1}} = \frac{\text{mass of Alumina}}{26.98 \text{ g mol}^{-1}}$$

Therefore, 16.32 g of Al precursor contains about 2.2 g of Alumina. In our work, the combination of 16.32 g: 8 g: 12.8 ml: 160 ml generates about 3 g of MA.

A.2 Catalysts Preparation

The list of catalysts for CO₂-CH₄ reforming is given below:

- i) 10%Co/MA
- ii) X% Y-10%Co/MA (X=1-5wt.%)
- iii) 3%M-10%Co/MA (M= Ce, La, Y, Sm)

Each catalyst was prepared about 10 g for catalyst characterization and CO₂-CH₄ reforming evaluation. The detailed estimation for the amount of chemicals employed to synthesize a representative catalyst is given below.

Preparation of 10 g of 10%Co/MA catalyst:

- i) 10%Co/MA contains 1 g of Co and 9 g of MA
The amount Co(NO₃)₂.6H₂O salt required to get 1 g of Co metal

$$= \frac{m_i \times M_i^{salt}}{M_i}$$

where m_i refers to mass of active metal, M_i is molecular weight of active metal, and M_i^{Salt} refers to molecular weight of the precursor of i metal.

ii) For 1 g of Co, amount of $\text{Co}(\text{NO}_3)_2 \cdot 6\text{H}_2\text{O}$ needed

$$= \frac{1 \text{ g} \times 291.03 \text{ g mol}^{-1}}{58.93 \text{ g mol}^{-1}}$$

$$= 4.94 \text{ g of } \text{Co}(\text{NO}_3)_2 \cdot 6\text{H}_2\text{O}$$

iii) Amount of water in metal salt, m_w

$$= \frac{m_i^{\text{salt}} \times M_w}{M_i^{\text{salt}}}$$

where M_w is the molecular weight of water ($6 \times 18 \text{ g mol}^{-1}$)

= 1.83 g, which is 1.83 ml (density 1 g cm^{-3}) of water.

iv) From BET measurement, the average pore volume of MA = $0.85 \text{ cm}^3 \text{ g}^{-1}$

Since, 9 g of MA support was utilized to prepare 10 g of 10%Co/MA catalyst, the overall pore volume of the support, V_p

$$= \text{average pore volume} \times 9$$

$$= 0.85 \text{ cm}^3 \text{ g}^{-1} \times 9 \text{ g}$$

$$= 7.65 \text{ cm}^3$$

Thus, amount of water required for incipient wetness impregnation

= Overall pore volume of the support - water content in salt

$$= 7.65 \text{ ml} - 1.83 \text{ ml}$$

$$= 5.82 \text{ ml}$$

Preparation of 10 g of 3%Ce-10%Co/MA catalyst:

i) 3%Ce-10%Co/MA contains 0.3 g of Ce, 1 g of Co and 8.7 g of MA

For 1 g of Co, amount of $\text{Co}(\text{NO}_3)_2 \cdot 6\text{H}_2\text{O}$ needed

$$= \frac{1 \text{ g} \times 291.03 \text{ g mol}^{-1}}{58.93 \text{ g mol}^{-1}}$$

$$= 4.94 \text{ g of } \text{Co}(\text{NO}_3)_2 \cdot 6\text{H}_2\text{O}$$

For 0.3 g of Ce, amount of $\text{Ce}(\text{NO}_3)_3 \cdot 6\text{H}_2\text{O}$ needed

$$= \frac{0.3 \text{ g} \times 362.12 \text{ g mol}^{-1}}{140.12 \text{ g mol}^{-1}}$$

$$= 0.78 \text{ g of } \text{Ce}(\text{NO}_3)_3 \cdot 6\text{H}_2\text{O}$$

ii) Amount of water in $\text{Co}(\text{NO}_3)_2 \cdot 6\text{H}_2\text{O}$

$$= 1.83 \text{ ml}$$

Amount of water in $\text{Ce}(\text{NO}_3)_3 \cdot 6\text{H}_2\text{O}$

$$= \frac{0.78 \times (6 \times 18)}{362.12}$$

$$= 0.23 \text{ g, which is } 0.23 \text{ ml.}$$

- iii) From BET measurement, the average pore volume of MA = $0.85 \text{ cm}^3 \text{ g}^{-1}$
 Since, 8.7 g of MA support was utilized to prepare 10 g of 3Ce-10%Co/MA catalyst, the overall pore volume of the support, V_p
 = average pore volume \times 8.7
 = $0.85 \text{ cm}^3 \text{ g}^{-1} \times 8.7 \text{ g}$
 = 7.40 cm^3

Thus, amount of water required for incipient wetness impregnation
 = Overall pore volume of the support - water content in salt
 = $7.40 \text{ ml} - 1.83 \text{ ml} - 0.23 \text{ ml}$
 = 5.34 ml

The detailed description for other promoted catalysts is give in Table A.1.

Table A.1 Catalyst preparation amount

Catalyst	Mass of solid required (g)						Volume of ethanol (mL)
	MA	Co	Ce	La	Sm	Y	
10%Co/MA	9	4.94	-	-	-	-	5.82
3%Ce-10%Co/MA	8.7	4.94	0.78	-	-	-	5.34
3%La-10%Co/MA	8.7	4.94	-	0.94	-	-	5.34
3%Sm-10%Co/MA	8.7	4.94	-	-	0.89	-	5.35
1%Y-10%Co/MA	8.9	4.94	-	-	-	0.31	5.62
2%Y-10%Co/MA	8.8	4.94	-	-	-	0.62	5.41
3%Y-10%Co/MA	8.7	4.94	-	-	-	0.93	5.21
5%Y-10%Co/MA	8.5	4.94	-	-	-	1.55	4.79

APPENDIX B TRANSPORT RESISTANCE ESTIMATION

B.1 External Mass Transfer

The value calculated must be satisfied with the Mears criterion (cf. Eq. B.1) to neglect the effect of external mass transfer resistance.

$$\frac{(-r_{\text{exp}})\rho_b R_p n}{k_c C_{Ab}} < 0.15 \quad (\text{B.1})$$

where

$$(-r_{\text{exp}}) = 6.88 \times 10^{-5} \text{ mol g}_{\text{cat}}^{-1} \text{ s}^{-1}$$

$$\rho_b = 0.67 \text{ g cm}^{-3}$$

$$R_p = 9.75 \times 10^{-5} \text{ m}$$

$$n = 0.88$$

$$C_{Ab} = 4.09 \times 10^{-5} \text{ mol cm}^{-3}$$

The mass transfer coefficient, k_c can be determined from Eq. (B.2).

$$k_c = \frac{J_D U}{Sc^{\frac{2}{3}}} \quad (\text{B.2})$$

The Colburn's mass transfer factor (J_D), superficial gas velocity (U) and Schmidt number (Sc), have to determine for calculating the k_c .

In order to determine value for Colburn's mass transfer factor (J_D) and Schmidt number (Sc), the value of viscosity, diffusivity and Reynolds number (Re) have to be determined.

Viscosity of the gas mixture was calculated using Eqs. (B.3), (B.4) and (B.5):

$$\mu_g = \sum_i \frac{y_i \mu_i}{\sum_{j \neq i} y_j \phi_{ij}} \quad (\text{B.3})$$

$$\phi_{ji} = \left(\frac{\mu_j}{\mu_i} \right) \left(\frac{M_i}{M_j} \right) \phi_{ij} \quad (\text{B.4})$$

$$\phi_{ij} = \frac{\left[1 + \left(\frac{\mu_i}{\mu_j} \right)^{\frac{1}{2}} \left(\frac{M_j}{M_i} \right)^{\frac{1}{4}} \right]^2}{\left[8 \left(1 + \left(\frac{M_i}{M_j} \right) \right) \right]^{\frac{1}{2}}} \quad (\text{B.5})$$

where

$i, j = \text{N}_2, \text{CO}_2, \text{CH}_4$

$y =$ mole fraction of component gases ($\text{N}_2 = 0.605$, $\text{CO}_2 = 0.197$ and $\text{CH}_4 = 0.197$)

$M =$ molecular weight of component gases

($\text{N}_2 = 28.01 \text{ g mol}^{-1}$, $\text{CO}_2 = 44.01 \text{ g mol}^{-1}$ and $\text{CH}_4 = 16.04 \text{ g mol}^{-1}$)

$\mu =$ viscosity of component gases

($\text{N}_2 = 4.21 \times 10^{-5} \text{ kg m}^{-1} \text{ s}^{-1}$, $\text{CO}_2 = 4.06 \times 10^{-5} \text{ kg m}^{-1} \text{ s}^{-1}$ and $\text{CH}_4 = 2.84 \times 10^{-5} \text{ kg m}^{-1} \text{ s}^{-1}$)

Therefore, substituting the values for M and μ in Eqs. (B.4) and (B.5) to obtain the values for ϕ . Then substituting the values for ϕ and y in Eq. (B.3) to get $u_g = 4.01 \times 10^{-5} \text{ kg m}^{-1} \text{ s}^{-1}$

The superficial gas velocity was determined from:

$$U = \frac{V}{A} \quad (\text{B.6})$$

where

$V = 60 \text{ mL min}^{-1}$ (at 298 K)

$A = 4.90 \times 10^{-5} \text{ m}^2$

$$U = \frac{60 \text{ mL min}^{-1} \times 1 \text{ m}^3 \times 1 \text{ min} \times 973 \text{ K}}{4.90 \times 10^{-5} \text{ m}^2 \times 10^6 \text{ mL} \times 60 \text{ s} \times 298 \text{ K}} = 6.66 \times 10^{-2} \text{ m s}^{-1}$$

Therefore, Reynolds number (Re) can be estimated using Eq. (B.7):

$$\text{Re} = \frac{\rho_g U d_p}{\mu_g} \quad (\text{B.7})$$

$$\text{Re} = \frac{0.343 \text{ kg m}^{-3} \times 6.66 \times 10^{-2} \text{ m s}^{-1} \times 1.95 \times 10^{-4} \text{ m}}{4.01 \times 10^{-5} \text{ kg m}^{-1} \text{ s}^{-1}} = 0.111$$

The diffusivity of CO₂ in a mixture N₂ and CH₄ is given by:

$$D_g = \frac{1 - y_i}{\sum_j \frac{y_j}{D_{ij}}} \quad (\text{B.8})$$

$$D_{ij} = \frac{1 \times 10^{-3} T^{1.75} \sqrt{\frac{(M_i + M_j)}{M_i M_j}}}{P \left[\left(\sum \nu_i \right)^{\frac{1}{3}} + \left(\sum \nu_j \right)^{\frac{1}{3}} \right]^2} \quad (\text{B.9})$$

where

i = CO₂

j = N₂, CH₄

y = mole fraction of component gases (N₂ = 0.605, CO₂ = 0.197 and CH₄ = 0.197)

M = molecular weight of component gases (N₂ = 28.01 g mol⁻¹, CO₂ = 44.01 g mol⁻¹ and CH₄ = 16.04 g mol⁻¹)

P = standard pressure (1 atm)

T = reaction temperature (973 K)

ν = atomic diffusion volumes (N₂ = 17.9 cm³ mol, CO₂ = 26.9 cm³ mol and CH₄ = 24.4 cm³ mol)

$$D_g = \frac{1-0.197}{\sum \left(\frac{0.197}{1.12 \times 10^{-4} \text{ m}^2 \text{ s}^{-1}} + \frac{0.605}{1.46 \times 10^{-4} \text{ m}^2 \text{ s}^{-1}} \right)} = 1.36 \times 10^{-4} \text{ m}^2 \text{ s}^{-1}$$

The Schmidt number, Sc , may be calculated from:

$$Sc = \frac{\mu_g}{\rho_g D_g} \quad (\text{B.10})$$

$$Sc = \frac{4.01 \times 10^{-5} \text{ kg m}^{-1} \text{ s}^{-1}}{0.343 \text{ kg m}^3 \times 1.36 \times 10^{-4} \text{ m}^2 \text{ s}^{-1}} = 0.862$$

Since the Reynolds number, $Re < 350$, Colburn's mass transfer factor may be estimated using Eq. (B.11) (Dwivedi and Upadhyay, 1977).

$$J_D = \frac{1}{\varepsilon} \left[\left(\frac{0.765}{Re^{0.82}} \right) + \left(\frac{0.365}{Re^{0.386}} \right) \right] \quad (\text{B.11})$$

where $\varepsilon =$ void fraction (0.8)

$$J_D = \frac{1}{0.8} \left[\left(\frac{0.765}{0.111^{0.82}} \right) + \left(\frac{0.365}{0.111^{0.386}} \right) \right] = 6.86$$

Therefore, the value of k_c determined from Eq. (B.2):

$$k_c = \frac{6.86 \times 6.66 \times 10^{-2} \text{ m s}^{-1}}{0.862^{\frac{2}{3}}} = 50.48 \text{ cm s}^{-1}$$

Hence the value of Mears criterion in Eq. (B.1):

$$\frac{6.88 \times 10^{-5} \text{ mol g}_{\text{cat}}^{-1} \text{ s}^{-1} \times 0.67 \text{ g cm}^3 \times 9.75 \times 10^{-5} \text{ m} \times 0.88}{50.48 \text{ cm s}^{-1} \times 4.09 \times 10^{-5} \text{ mol cm}^3} = 1.92 \times 10^{-4}$$

The value of Mears criterion about $1.92 \times 10^{-4} \ll 0.15$ indicating the negligible external mass transfer resistance.

B.2 Internal Mass Transfer

The internal mass transfer is considered to be negligible if Weisz-Prater criterion given in Eq. (B.12) is satisfied.

$$\frac{(-r_{\text{exp}})\rho_c R_p^2}{D_{\text{eff}} C_{A_s}} < 1 \quad (\text{B.12})$$

where

$$\begin{aligned} \rho_c &= 3.35 \text{ g cm}^{-3} \\ C_{A_s} &= C_{A_b} = 4.09 \times 10^{-5} \text{ mol cm}^{-3} \\ R_p &= 9.75 \times 10^{-5} \text{ m} \end{aligned}$$

The effective diffusivity (D_{eff}) can be estimated from Eq. (B.13).

$$D_{\text{eff}} = \frac{D_g \omega_p \sigma_c}{\tilde{\tau}} \quad (\text{B.13})$$

$$\frac{1.36 \times 10^{-4} \text{ m}^2 \text{ s}^{-1} \times 0.4 \times 0.8}{3} = 1.45 \times 10^{-5} \text{ m}^2 \text{ s}^{-1}$$

$$\frac{(6.88 \times 10^{-5} \text{ mol g}_{\text{cat}}^{-1} \text{ s}^{-1}) \times 3.35 \text{ g cm}^{-3} \times 9.75 \times 10^{-3} \text{ cm}}{1.45 \times 10^{-5} \text{ m}^2 \text{ s}^{-1} \times 4.09 \times 10^{-5} \text{ mol cm}^{-3}} = 4.43 \times 10^{-3} < 1$$

Therefore, the value for internal mass transfer was about 4.43×10^{-3} suggesting that the internal mass transfer resistance may be neglected in system.

B.3 External Heat Transfer

The external heat transport resistance in a reactor may be insignificant if Mears criterion as seen in Eq. (B.14) is fulfilled.

$$\frac{|(-\Delta H_r)|(-r_{\text{exp}})\rho_b R_p E_A}{hRT_b^2} < 0.15 \quad (\text{B.14})$$

where

$$-\Delta H_r = 297.58 \times 10^3 \text{ J mol}^{-1}$$

$$E_A = 27.56 \times 10^3 \text{ J mol}^{-1}$$

$$R = 8.314 \text{ J mol}^{-1} \text{ K}^{-1}$$

$$T_b = 1023 \text{ K}$$

$$(-r_{\text{exp}}) = 6.88 \times 10^{-5} \text{ mol g}_{\text{cat}}^{-1} \text{ s}^{-1}$$

$$\rho_b = 0.67 \text{ g cm}^{-3}$$

$$R_p = 9.75 \times 10^{-5} \text{ m}$$

The heat transfer coefficient (h) may be determined using Colburn-Chilton analogy in Eq. (B.15)

$$j_D = j_H = \frac{h \text{Pr}^{2/3}}{C_{pg} \rho_g U} \quad (\text{B.15})$$

where

$$j_H = (j_H = j_D) 6.86$$

$$C_{pg} = 1.89 \times 10^3 \text{ J kg}^{-1} \text{ K}^{-1}$$

$$\text{Pr} = 0.96$$

$$\rho_g = 0.343 \text{ kg m}^{-3}$$

$$U = 6.66 \times 10^{-2} \text{ m s}^{-1}$$

The value of heat transfer coefficient (h) was obtained about $306.53 \text{ J m}^{-2} \text{ s}^{-1} \text{ K}^{-1}$. Hence, the external heat transport resistance in Eq. (B.14) was attained about $1.38 \times 10^{-5} < 0.15$, implying that external heat transfer may be neglected for $\text{CO}_2\text{-CH}_4$ reforming system.

B.4 Internal Heat Transfer

The internal heat transfer resistance is considered to be negligible if the experimental conditions and reaction rate data for $\text{CO}_2\text{-CH}_4$ reforming follow the Anderson criterion as provided in Eq. (B.16)

$$\frac{|(-\Delta H_r)|(-r_{\text{exp}})\rho_b R_p^2 E_A}{\lambda_p RT_s^2} < 0.75 \quad (\text{B.16})$$

where

$$(-r_{\text{exp}}) = 6.88 \times 10^{-5} \text{ mol g}_{\text{cat}}^{-1} \text{ s}^{-1}$$

$$\rho_b = 670 \text{ kg m}^{-3}$$

$$R_p = 9.75 \times 10^{-5} \text{ m}$$

$$-\Delta H_r = 297.58 \times 10^3 \text{ J mol}^{-1}$$

$$E_A = 27.56 \times 10^3 \text{ J mol}^{-1}$$

$$R = 8.314 \text{ J mol}^{-1} \text{ K}^{-1}$$

$$T_b = T_s = 1023 \text{ K (since external heat transport is negligible)}$$

The thermal conductivity of catalyst pellet (λ_p) was determined from the thermal conductivity of the catalyst material (λ_m) using the correlation provided in Eq. (B.17)

$$\log(\lambda_p \times 10^5) = 0.859 + 3.12 \left(\frac{\lambda_m}{\omega_p} \right) \quad (\text{B.17})$$

where

$$\lambda_m = 7.89 \text{ J m}^{-1} \text{ s}^{-1} \text{ K}^{-1}$$

The thermal conductivity of catalyst pellet (λ_p) obtained about $5.34 \times 10^{21} \text{ J m}^{-1} \text{ s}^{-1} \text{ K}^{-1}$. Therefore, the value for internal heat transfer resistance in Eq. (B.16) was achieved around $7.74 \times 10^{-29} < 0.15$, suggesting the negligibility of internal heat transfer resistance.

B.5 Wall and Radial Heat Dispersion Effects

For CO₂-CH₄ reforming system, the d_i/d_p was about 40.5, satisfying the criteria for negligible wall effects. However, a high ratio of d_i/d_p may contribute to radial heat transfer effects. Thus, Mears' criterion shown in Eq. (B.18) was used to determine the insignificant effects of the radial heat transfer.

$$\left(\frac{E_a}{RT_w} \right) \left(\frac{|\Delta H_r| (-r_{\text{exp}}) \rho_b R_p^2 [(1-\varepsilon)/(1-b)]}{4\lambda_p T_w} \right) \left(\frac{1}{8} + \frac{B_p}{Bi_w R_t} \right) < 0.05 \quad (\text{B.18})$$

where

$$T_w = T_b = 1023 \text{ K}$$

$$\begin{aligned}\varepsilon &= 0.8 \\ b &= 0 \\ R_t &= 3.95 \times 10^{-3} \text{ m}\end{aligned}$$

while, the wall Biot number (Bi_w) can be estimated from Eq. (B.19).

$$Bi_w = \frac{h_w d_p}{\lambda_p} \quad (\text{B.19})$$

where

$$\begin{aligned}h_w &= 25 \text{ J m}^{-2} \text{ s}^{-1} \text{ K}^{-1} \\ d_p &= 1.95 \times 10^{-4} \text{ m} \\ \lambda_p &= 5.34 \times 10^{21} \text{ J m}^{-2} \text{ s}^{-1} \text{ K}^{-1}\end{aligned}$$

The the wall Biot number (Bi_w) obtained about 9.13×10^{-25} . Thus, the left hand side of Eq. (4.9) was attained around 1.05×10^{-8} . Therefore, the reactor system is able to meet Mears' criterion for the negligible radial heat dispersion effects.

UMP

اونيورسيتي ملايسيا قهغ

UNIVERSITI MALAYSIA PAHANG

APPENDIX C CALIBRATION CURVES

C.1 Calibration Curve for Mass Flow Controller (MFC)

Equipment: mass flow controller (MFC), bubble flowmeter, stopwatch

Gases: N₂

i) MFC Model No: MFC104205

Gas used: CO₂

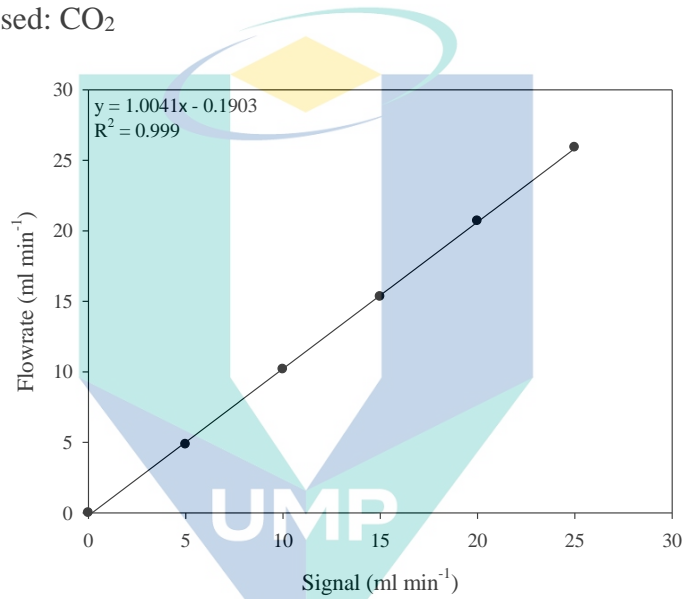


Figure D.2. The calibration curve of mass flow controller using CO₂ gas

ii) MFC Model No: MFC106433

Gas used: CO₂

اونيور سيطي مليسيا قهغ
UNIVERSITI MALAYSIA PAHANG

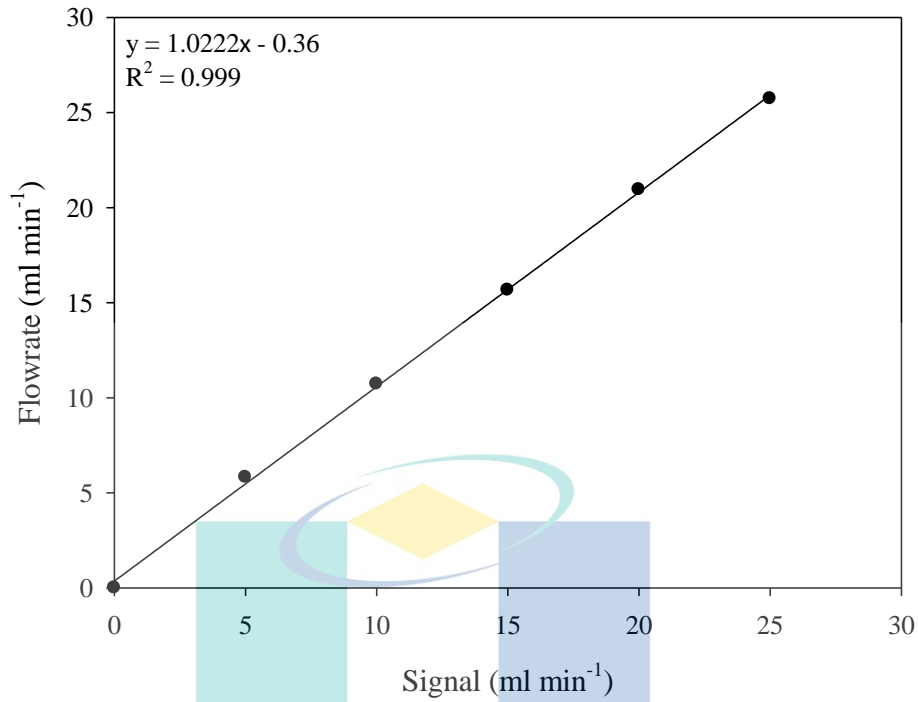


Figure D.3. The calibration curve of mass flow controller using N₂ gas

- i) MFC Model No: MFC106433
Gas used: CH₄

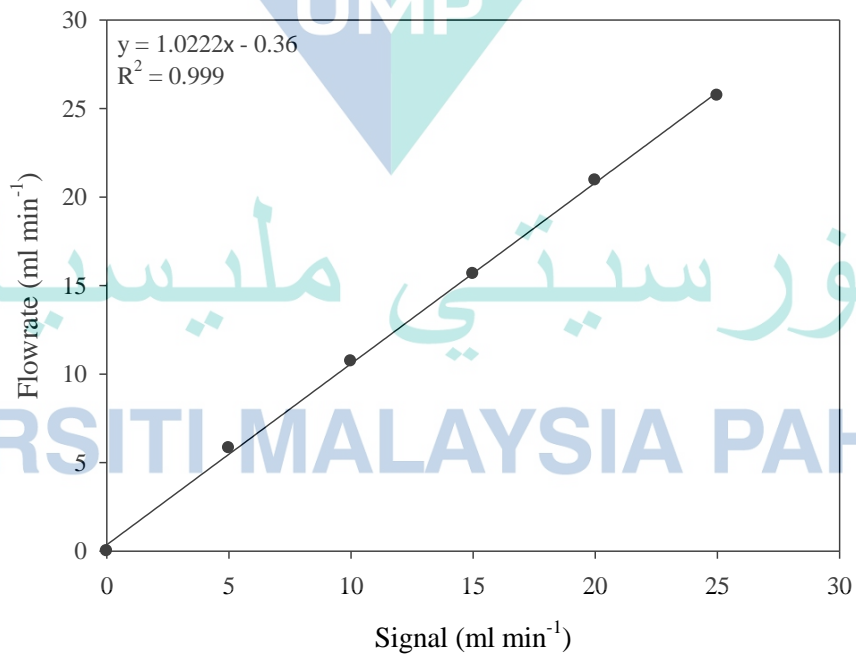


Figure D.3. The calibration curve of mass flow controller using N₂ gas

APPENDIX D
LIST OF PUBLICATIONS & CONFERENCE PROCEEDINGS

Journal

1. **M.B. Bahari**, H.D. Setiabudi, T. Nishino, N. Ayas, D.-V.N. Vo (2020), *Coke-resistant Y_2O_3 -promoted cobalt supported on mesoporous alumina for enhanced hydrogen production*, Journal of the Energy Institute, 94, 272-284.
2. **M.B. Bahari**, H.D. Setiabudi, T.D. Nguyen, P.T.T. Phuong, Q.D. Truong, A.A. Jalil, N. Ainirazali, D.-V. N. Vo (2020), *Insight into the influence of rare-earth promoter (CeO_2 , La_2O_3 , Y_2O_3 , and Sm_2O_3) addition toward methane dry reforming over Co/mesoporous alumina catalysts*, Chemical Engineering Science, 228, 115967.
3. **M.B. Bahari**, H.D. Setiabudi, T.D. Nguyen, A.A. Jalil, N. Ainirazali, D.-V.N. Vo (2020), *Hydrogen production via CO_2 - CH_4 reforming over cobalt-supported mesoporous alumina: A kinetic evaluation*, International Journal of Hydrogen Energy, In Press, Corrected Proof.
4. C.C. Chong, Y.W. Cheng, **M.B. Bahari**, L.P. Teh, S.Z. Abidin, H.D. Setiabudi (2020), *Development of nanosilica-based catalyst for syngas production via CO_2 reforming of CH_4 : A review*, International Journal of Hydrogen Energy, In Press, Corrected Proof.
5. F. Fayaz, L.G. Bach, **M.B. Bahari**, T.D. Nguyen, K.B. Vu, R. Kanthasamy, C. Samart, C. Nguyen-Huy, D.-V.N. Vo (2019), *Stability evaluation of ethanol dry reforming on Lanthania-doped cobalt-based catalysts for hydrogen-rich syngas generation*, International Journal of Energy Research, 43(1), 405-416.
6. L.N. Jun, **M.B. Bahari**, P.T.T. Phuong, N.H.H. Phuc, C. Samart, B. Abdullah, H.D. Setiabudi, D.-V.N. Vo (2018), *Ethylene glycol dry reforming for syngas generation on Ce-promoted Co/Al_2O_3 catalysts*, Applied Petrochemical Research, 8 (4), 253-261.

7. S. Singh, **M.B. Bahari**, B. Abdullah, P.T.T. Phuong, Q.D. Truong, D.-V.N. Vo, A.A. Adesina (2018), *Bi-reforming of methane on Ni/SBA-15 catalyst for syngas production: Influence of feed composition*, International Journal of Hydrogen Energy, 43(36), 17230-17243.

Proceeding

1. **M.B. Bahari**, H.D. Setiabudi, N. Ainirazali, D.-V.N. Vo (2020), *A Short Review on Bimetallic Co-based Catalysts for Carbon Dioxide Reforming of Methane*, Materials Today: Proceeding, submitted.
2. **M.B. Bahari**, S.N. Bukhari, L.N. Jun, H.D. Setiabudi (2020), *Development of Fibrous Mesoporous Silica for Catalytic Reaction: A Short Review*, Materials Today: Proceeding, submitted.
3. **M.B. Bahari**, T.D. Nguyen, S. Singh, T.J. Siang, M.-N.N. Shafiqah, L.N. Jun, P.T.T. Phuong, N. Ainirazali, D.-V.N. Vo (2019), *Catalytic performance of yttrium-doped Co/mesoporous alumina catalysts for methane dry reforming*, AIP Conference Proceedings, 2124 (1), 020018.
4. M.-N.N. Shafiqah, T.D. Nguyen, L.N. Jun, **M.B. Bahari**, P.T.T. Phuong, B. Abdullah, D.-V.N. Vo (2019), *Production of syngas from ethanol CO₂ reforming on La-doped Cu/Al₂O₃: Impact of promoter loading*, AIP Conference Proceedings, 2124(1), 020011.
5. **M.B. Bahari**, L.N. Jun, M.N.N. Shafiqah, F. Fayaz, D.-V.N. Vo (2018), *Ethylene glycol dry reforming on Ni/Al₂O₃ catalyst for syngas generation*, IOP Conference Series: Materials Science and Engineering, 446(1), 012013.

Book Chapter

1. F. Fayaz, **M. Bahari**, T.L.M. Pham, C. Nguyen-Huy, H.D. Setiabudi, B. Abdullah, D.-V.N. Vo (2018), *Hydrogen-Rich Syngas Production via Ethanol Dry Reforming over Rare-Earth Metal-Promoted Co-based Catalysts*. In: Sarangi

P., Nanda S., Mohanty P. (eds) Recent Advancements in Biofuels and Bioenergy Utilization. Springer, Singapore

Conferences

1. **Mahadi Bin Bahari**, Trinh Duy Nguyen, Sharanjit Singh, Tan Ji Siang, Mohd-Nasir Nor Shafiqah, Lau N. Jun, Pham T. T. Phuong, Nurul Ainirazali, Dai-Viet N. Vo, *Catalytic Performance of Yttrium-doped Co/Mesoporous Alumina Catalysts for Methane Dry Reforming*, The 8th International Conference on Environment (ICENV) 2018, December 11-13, 2018, Penang, Malaysia.
2. **Mahadi B. Bahari**, Mohd-Nasir Nor Shafiqah, Fahim Fayaz, Lau N. Jun, Sharanjit Singh, Tan Ji Siang, Nurul Ainirazali, Dai-Viet N. Vo, *Syngas Generation from Ethanol Dry Reforming over Alumina-supported Transition Metal Catalysts*, The 31st International Symposium on Chemical Engineering (ISChE 2018), November 30 - December 2, 2018, Chiang Mai, Thailand



اونيورسيتي ملايسيا قهغ

UNIVERSITI MALAYSIA PAHANG